Low-temperature specific heat of hyperaged and ultrastable glasses

— *Tomás Pérez Castañeda*

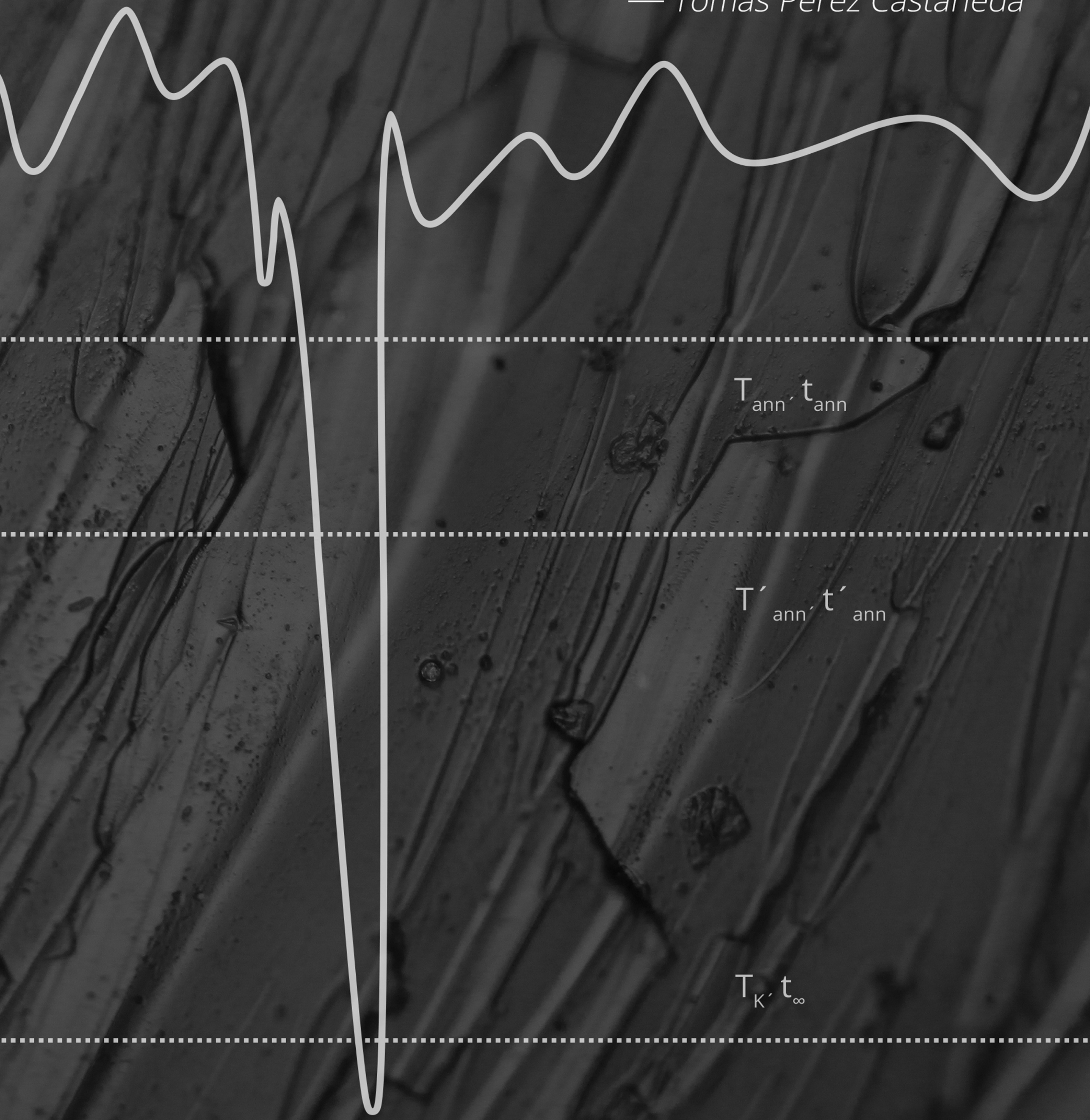

Cover: Photograph of the surface of a Spanish amber sample taken with an
optical microscope. On the front, a portion of the potential energy landscape,
where different combinations of temperature and time drive
the glass towards the ideal glassy state

LOW-TEMPERATURE SPECIFIC HEAT OF HYPERAGED AND ULTRASTABLE GLASSES

Thesis presented by

TOMÁS PÉREZ CASTAÑEDA

for the degree of Doctor in Physics by
Universidad Autónoma de Madrid

FACULTAD DE
CIENCIAS
UNIVERSIDAD AUTÓNOMA DE MADRID

Thesis Supervisor

Miguel Ángel Ramos Ruiz

Madrid, August 2013

A Cris,

mi chica yeyé

“Nuestra recompensa se encuentra
en el esfuerzo y no en el resultado.
Un esfuerzo total es una victoria completa”

Mahatma Gandhi

“Satisfaction lies in the effort,
not in the attainment.
Full effort is full victory.”

Mahatma Gandhi

AGRADECIMIENTOS

Quiero comenzar agradeciendo a mi director de tesis, Miguel Ángel Ramos, el apoyo y la confianza que me ha demostrado desde que nos conociéramos, hace ya cinco años. La búsqueda del trabajo científico meticuloso y bien hecho que de él he aprendido me ha guiado en mis primeros pasos por el mundo de la investigación. Gracias Miguel Ángel por la oportunidad de hacer esta tesis que tantas satisfacciones me ha dado.

En segundo lugar, quiero hacer constar mi más sincero agradecimiento a Gabino Rubio por darme la oportunidad de acceder a la física de muy bajas temperaturas. Por su paciente enseñanza del manejo del criostato de dilución y por la confianza que depositó en mí desde el primer momento.

Le agradezco a Sebastián Vieira la enseñanza que me diera en mis primeros pasos en el Laboratorio de Bajas Temperaturas sobre las cuestiones prácticas tan necesarias para un físico experimental. Gracias por inculcarme la pasión por el trabajo minucioso. Recordaré siempre con cariño nuestras incontables discusiones científicas que me han impulsado a la búsqueda de respuestas.

A José Gabriel Rodrigo le doy las gracias por sus siempre valiosos consejos sobre instrumentación, que sin duda me han ayudado a entender mejor los entresijos de la electrónica en mis experimentos. Por eso y por estar siempre dispuesto a dar su opinión constructiva.

No quiero olvidarme de Nicolás Agraït y de Herman Suderow, que también han ayudado a que mi paso por el Laboratorio de Bajas Temperaturas haya sido para mí tan fructífero y positivo.

Quiero agradecer al Departamento de Física de la Materia Condensada, sin olvidarme de ninguno de los profesores, postdocs, estudiantes… por haberme acogido durante estos años. Sin duda todos han aportado su granito de arena para que esta tesis se haga realidad.

A los técnicos del laboratorio, a Santiago, Andrés Buendía, Rosa, José Luis y Juanma, por su ayuda en los quehaceres del día a día, imprescindible para que la ciencia experimental siga adelante. A Santiago le agradezco su consejo, apoyo, y los cafés en buena compañía.

A María José de la Mata por su continua predisposición a ayudarme con las medidas de DSC del ámbar. Gracias por tu gran profesionalidad y por tu siempre valioso consejo.

A Carlos Gracia, por su amable dedicación a explicarme los detalles, las ventajas y la forma de optimizar los protocolos de medida en calorimetría diferencial.

A Elsa y Luisa por ayudarme con los papeleos siempre que lo he necesitado.

A Manolo, Javi, Jose y demás miembros del SEGAINVEX por todo su apoyo.

A Macarena, por tener siempre una sonrisa para todos.

A Fernando Moreno y Paco González (Dpto. de Física Aplicada de la Universidad de Cantabria), mis primeros maestros científicos, por ayudarme a cultivar el gusto por la ciencia.

A Rafael J. Jiménez Riobóo, con el que he tenido el placer de colaborar. Por sus siempre positivos y constructivos comentarios.

A Javier Rodríguez Viejo (Universidad Autónoma de Barcelona) por darme la oportunidad de investigar los vidrios ultraestables, que tantas preguntas han despertado en mí sobre la física de los sólidos amorfos. Gracias por tu motivación. A Cristian Rodríguez Tinoco (Universidad Autónoma de Barcelona) por tu ayuda y consejo en el estudio de la indometacina.

A Pilar Miranzo y Alicia Durán (Instituto de Cerámica y Vidrio CSIC), que no han dudado en recibirme siempre cuando he necesitado su ayuda.

A Idoia Rosales y César Menor Salván por proporcionarnos las muestras de ámbar español y discutir con nosotros sobre sus propiedades químicas e historia.

Ich wollte gerne Professor Christian Enss für seine Gastfreundschaft und für seine Einladung in Ihrem Labor danken. Ich danke allen im Kirchhoff Institut für ihre Hilfe während meines Aufenthaltes in Heidelberg. Quiero agradecerle muy especialmente a Marius Hempel su ayuda y compañerismo en el laboratorio.

A mis compañeros en el departamento. A Bisher y Merzak por ser los primeros en ayudarme en el laboratorio y a entender los vidrios. Merzak, muchas gracias por tu apoyo en las interminables semanas de medidas. A los de la antigua escuela, por su amistad y por ser para mí un gran ejemplo: A Andrés Castellanos por motivarme a dar lo mejor de mí y meterme el gusanillo de la ciencia. A Eduardo Anglada, gran amigo y mejor persona, por siempre estar dispuesto a echarme una mano (y leer y corregir todos los capítulos de esta tesis antes de ver la luz). A David Herranz, que me inculcó la filosofía del deporte y del buen humor: eres una persona Estée Lauder. A Guillermo Román, porque aunque todos tus amigos sean idiotas, me alegro de ser uno de ellos. A Ahmad Awad, que me ha incitado a no conformarme sólo con un punto de vista.

A Jose Augusto Galvis, por todos los buenos momentos que hemos pasado juntos en el laboratorio: gracias por tu alegría. A Juan Pedro Cascales, un genio y figura, gracias por la música y por tu amistad. A Jose Luis F. Cuñado, que me ha demostrado que el interés por aprender y superarse no tiene edad. A Roberto F. Lucas por su gran humor y compañerismo. A Manuel R. Osorio: sé que tus preguntas eran para que aprendiera más. A los jóvenes padawans Antón Fente, Edwin Herrera, Siya Sherif y Aday Molina. A Jon Azpeitia, mi primer discípulo, por darme la oportunidad de enseñarle calorimetría a un crack. A Charalambos Evangeli por aguantar pacientemente mi bomba y por nuestras conversaciones sobre la vida normal. A Isabel Guillamón, por tu siempre tranquilizador consejo cuando tenía alguna duda sobre el dilutor. A Curro Luque, Antonio Lara, Ana Maldonado, Vanesa Crespo, Carlos Arroyo, Michelle Fritz, Mohamed Moiaed y Amjad Taleb por contribuir a enriquecer mi experiencia en el departamento aún más.

A Pablo Molina, por tu amistad y por ser la mejor compañía para salir a recorrer Valdelatas y desconectar.

A mis amigos de la infancia, a Pito y a Joaquín, con los que tan buenos momentos he pasado. A Pito, por ser tan de verdad, y a Joaquín, tu recuerdo siempre irá conmigo.

A Pablín, porque no importa cuánto llevemos sin vernos o sin hablar, sé que una cerveza contigo basta para ponernos al día.

A la tropa de Físicas de Santander. A Rodrigo Alcaraz, gracias por tu amistad y porque siempre has sido un ejemplo para mí y una motivación por superarme: siempre nos quedará Berlín. A Jesica Sánchez, gran carácter y gran amiga. A Carlos Renero, Alejandro Moreno (Cucho), Lorena González, Cristina Pérez, Cristina Echevarría y Alberto Fernández (Peña): siempre es un placer estar con vosotros.

A los piscineros, que nos habéis hecho sentir como en casa estos años. Por los momentos chapuzón y los siempre geniales viernes de la Remonta.

A toda mi familia, que formáis parte de mi vida y de mis recuerdos. A mis abuelos, que aunque ya no estén, siempre tendré presentes.

A mi hermana, mi primera compañera de juegos y mi rubia favorita.

A Chefi y Guillermo, que desde el primer día me acogieron en su casa como a un hijo. A Aurora y Manolín, por su cariño y su vitalidad. A Will, porque aunque no hables mucho, tienes un gran corazón.

A Cris, mi princesa y mi compañera, quien me ha mostrado la verdadera felicidad. Gracias por ser mi apoyo desde que me levanto hasta que me acuesto. Tu amor es el mejor de mis descubrimientos.

A mis padres, María del Carmen y Enrique, los mejores que podría soñar. Vosotros me habéis ayudado a ser la persona que soy. De vosotros he aprendido la satisfacción por esforzarme y mejorar día a día. Por seguir siendo un apoyo incondicional y todo un ejemplo de humanidad.

GENERAL INDEX

APPENDICES

TABLES INDEX

Chapter 4: Hyperageing and the low-temperature anomalies in Dominican amber

Chapter 5: Hyperageing as a route to the ideal glass

FIGURES INDEX

Chapter 1: Brief introduction and motivation

Chapter 2: The physics of glasses

Chapter 3: Experimental techniques

Chapter 4: Hyperageing and the low-temperature anomalies in Dominican amber

Chapter 5: Hyperageing as a route to the ideal glass

Chapter 6: Vapor-deposited thin films ultrastable glasses

Appendix A: Differential Scanning Calorimetry measurements

Appendix B: Development of software for low-temperature calorimetry

ABSTRACT

Amorphous solids present a large number of differences with their crystalline counterparts which undoubtedly constitute a great challenge for the physicists dealing with glass forming systems. Since the entropy crisis was first stated by Kauzmann in 1948 [Kauz48], open questions on the phenomenology of supercooled liquids and glasses have steadily increased. More than twenty years later, the discovery of their anomalous behavior compared to the Debye prediction in the low-temperature thermal properties, observed by Zeller and Pohl in 1971 [ZePo71], meant a starting point in the race to understand the new phenomena hidden in disordered matter. Moreover, the universality of these low-temperature anomalies among the amorphous solids strongly demanded explanation. Only one year later this observation Anderson, Halperin and Varma [AnHV72] and Phillips [Phil72], independently gave an explanation for the excess density of states in amorphous solids below 1 K introducing the concept of the tunneling states. Although it successfully accounted for the deviations from the Debye-model predictions below 1 K, it failed in the understanding of the plateau in thermal conductivity and the maximum in the reduced specific heat representation C_P/T^3 at temperatures $2\text{ K} \leq T \leq 10\text{ K}$, typically. The so called *boson peak* is still in the present a topic of intense debate in the scientific community due to the lack of consensus on the origin of this excess in the Vibrational Density of States [GMPV03] [CMMC11] [BFMO09] [ZBCF11] [GuPS03][BGGP92]. Comprehension on the microscopic nature of the boson peak is needed, what will help us defining the key ingredients present in all amorphous solids which are responsible of their universal properties.

The access to this microscopic understanding is however arduous. The non-stable thermodynamic character of disordered systems further increases the difficulty to access a conclusion: it introduces the evolution with time to the physics of glasses. Many attempts have been done to identify the manner in which intermolecular forces originate the complex behavior in supercooled liquids and glasses: varying the route to obtain the glass [CoFR02], changing the thermal history [AYWC03][YuCJ02][Hodg95][UtDS00], the composition [JPRK09], using polymorphism and polyamorphism [GuGu03][SaPS01]…

Despite the exhaustive studies carried out in an endless list of non-crystalline solids in the last forty years, many of the findings done are far from being definite, and therefore susceptible to be interpreted in complete opposite directions depending on the theoretical view defended.

The application of extreme physical processes on glass forming systems and amorphous solids provides an extraordinary possibility to explore regions of the potential energy landscape never accessed before. This would shed light on the validity of the existing models and theories, which perhaps could have been developed and supported on the base of experimental observations far from being general.

The practical access to *extreme* amorphous solids has been conducted in this thesis in two different ways. The original idea we have pursued is studying glasses which have suffered an extraordinary stabilization process as a result of ageing. Given the geological character of *amber*, the well-known natural resin, which has stood the test of time for periods of several tens of millions or even over a hundred million years, is an unbeatable candidate to study the effects of extreme ageing or *hyperageing* in glasses. It gives us the chance to study for the first time the combined effects of extreme stabilization in the glass transition phenomenology and in the low-temperature universal anomalies of glasses.

In order to study the phenomenology of extremely stabilized glasses, two calorimetric techniques have been employed, the Differential Scanning Calorimetry and the low-temperature relaxation calorimetry. In this thesis we have also designed and built a versatile calorimeter for the low-temperature measurements which has allowed us to access the specific heat of glasses ranging from 50 mK up to 40 K or above. The elastic and acoustic properties of the glasses studied here have been also determined using a complementary technique like Brillouin scattering.

The access to the stability reached in amber glasses in laboratory time scales has only been possible in recent years with the discovery of ultrastable thin-film glasses grown by vapor deposition [SKMK07][KSEW08][LSGT10]. This has given us the chance to study a second system with extraordinary stability but which involves a completely different route to obtain it. The determination of the specific heat of indomethacin ultrastable glasses at very low temperatures done in this thesis entails the first approach to the study of the universal glassy anomalies of ultrastable thin films.

The joint research done in these two glassy systems which present the highest stability reached up to the date, and at the same time have quite different nature, leads to a new understanding of the microscopic origin of the excess density of states present in amorphous solids.

RESUMEN

Los sólidos amorfos o no cristalinos poseen incontables características que difieren de las de los cristales y que, sin lugar a duda, suponen un reto para los físicos que estudian estos sistemas. Desde que Kauzmann enunciara la crisis de entropía en su famoso trabajo de 1948 [Kauz48], la fenomenología conocida en torno a los líquidos sobreenfriados y los vidrios ha aumentado incesantemente, dando lugar a un sinfín de interrogantes. Veinte años después, los experimentos de Zeller y Pohl [ZePo71] pusieron de relieve la desviación de las propiedades térmicas de sólidos no cristalinos a bajas temperaturas con respecto a las predicciones hechas por Debye, que tan bien funcionan en sólidos cristalinos. Esto marcó un antes y un después en el interés de entender la nueva física presente en los sistemas desordenados. Además, la universalidad de las anomalías vítreas a bajas temperaturas hacía que la necesidad de encontrar respuestas fuese incluso más urgente. Sólo un año después parte de esas anomalías vítreas fueron explicadas por Anderson, Halperin y Varma [AnHV72] y Phillips [Phil72] en dos trabajos independientes. El modelo de sistemas de tuneleo (Tunneling Model en inglés) introducía los estados de dos niveles como el origen del exceso en la densidad de estados observada en los sólidos no cristalinos por debajo de 1 K. El modelo basado en sistemas de tuneleo fue capaz de explicar con éxito las denominadas anomalías vítreas que dominan a temperaturas por debajo de 1 K, pero fallaba al intentar entender otros fenómenos como el plateau en la conductividad térmica o el máximo del calor específico en la representación C_P/T^3 que aparecen a más altas temperaturas, típicamente en el rango $2\ \mathrm{K} \leq T \leq 10\ \mathrm{K}$. El denominado *pico bosónico* es aún hoy un tema de intenso debate dentro de la comunidad científica, debido a la falta de consenso que existe en cuanto al origen del exceso en la densidad vibracional de estados (VDOS por sus siglas en inglés) [GMPV03][CMMC11][BFMO09][ZBCF11][GuPS03][BGGP92]. Llegar a entender la naturaleza microscópica del pico bosónico es necesario, lo que nos

ayudará a definir los ingredientes fundamentales que son los responsables de las propiedades universales de los sólidos amorfos.

No obstante, poder hacernos una idea fiel de lo que ocurre a escala microscópica en los vidrios es una tarea difícil. Además, el hecho de que los sistemas desordenados sean no estables desde un punto de vista termodinámico, aumenta la dificultad: la no estabilidad introduce la variación con el tiempo de las propiedades vítreas. Para identificar el modo en que las fuerzas intermoleculares originan el comportamiento complejo de los líquidos sobreenfriados y los vidrios se han llevado a cabo numerosos estudios: variando la forma de obtener el vidrio [CoFR02], cambiando la historia térmica [AYWC03][YuCJ02][Hodg95][UtDS00], la composición [JPRK09], mediante el polimorfismo y el poliamorfismo [GuGu03][SaPS01]…

A pesar de los estudios exhaustivos que se han hecho en innumerables sólidos no cristalinos durante los últimos cuarenta años, gran parte de las conclusiones a las que se ha llegado distan mucho de ser definitivas. Esto las hace susceptibles de ser interpretadas de formas muy distintas dependiendo del punto de vista que se defiende en cada caso.

La aplicación de procesos físicos *extremos* en sistemas formadores de vidrios así como en sólidos amorfos, nos proporciona una posibilidad fantástica de explorar regiones del paisaje de energías que nunca antes han sido sondeadas. Esto nos serviría para dirimir sobre la validez de modelos y teorías que se han desarrollado hasta ahora, y que, podrían no tener un carácter general.

En la práctica, el acceso a sólidos amorfos extremos lo hemos hecho de dos formas distintas en esta tesis. La idea original que hemos buscado es la de estudiar vidrios que han sufrido extraordinarios procesos de estabilización como consecuencia del envejecimiento. Dado el carácter geológico del ámbar, la bien conocida resina natural, que ha resistido el paso del tiempo durante períodos de varias decenas en incluso superior a la centena de millones de años, este vidrio es un candidato inmejorable para estudiar los efectos del envejecimiento extremo o *hiperenvejecimiento* en vidrios. Este sistema nos da la posibilidad de estudiar por primera vez la conexión de los efectos que la estabilización extrema tiene en la transición vítrea y en las anomalías vítreas de bajas temperaturas.

El estudio de la fenomenología de vidrios extremos se ha hecho utilizando dos técnicas calorimétricas, la calorimetría diferencial o DSC (Differential Scanning Calorimetry) y la calorimetría de baja temperatura (mediante método de relajación). En esta tesis se llevado a cabo el diseñado y montaje de un calorímetro versátil de baja temperatura que nos ha permitido medir el calor específico de distintos vidrios en el rango de temperaturas desde 50 mK hasta 40 K. También se han determinado las propiedades elásticas y acústicas de los vidrios estudiados mediante una técnica complementaria como es la dispersión Brillouin.

Conseguir una estabilidad como la que se tiene en el ámbar, en escalas de tiempo de laboratorio, ha sido posible experimentalmente en los últimos años con el descubrimiento de las películas delgadas de vidrio ultraestables crecidas por deposición de la fase vapor [SKMK07][KSEW08][LSGT10]. El estudio del calor específico a bajas temperaturas de indometacina crecida por deposición en fase vapor nos ha permitido acceder a los efectos que una extrema estabilidad tiene en un sistema vítreo obtenido de una forma completamente distinta al hiperenvejecimiento del ámbar. Además, estas medidas suponen el primer acercamiento a las anomalías vítreas de baja temperatura en películas delgadas ultraestables.

La investigación que se ha hecho durante esta tesis en dos sistemas vítreos que tienen en común poseer las estabilidades más altas observadas hasta ahora en sólidos amorfos, y a la vez ser de naturaleza tan distinta, nos conduce a profundizar en la comprensión del origen microscópico del exceso en la densidad de estados presente en sólidos no cristalinos.

[AnHV72] P. W. Anderson, B. I. Halperin, and C. M. Varma, “Anomalous low-temperature thermal properties of glasses and spin glasses,” Philosophical magazine, vol. 25, no. 1, pp. 1–9, 1972.

[AYWC03] C. Angell, Y. Yue, L. Wang, J. R. Copley, S. Borick, and S. Mossa, “Potential energy, relaxation, vibrational dynamics and the boson peak, of hyperquenched glasses,” Journal of Physics: Condensed Matter, vol. 15, pp. 1051 – 1068, 2003.

[BFMO09] G. Baldi, A. Fontana, G. Monaco, L. Orsingher, S. Rols, F. Rossi, and B. Ruta, “Connection between Boson Peak and Elastic Properties in Silicate Glasses,” Physical Review Letters, vol. 102, no. 19, p. 195502, May 2009.

[BGGP92] U. Buchenau, Y. M. Galperin, V. L. Gurevich, D. A. Parshin, M. A. Ramos, and H. R. Schober, “Interaction of soft modes and sound waves in glasses,” Physical Review B, vol. 46, no. 5, pp. 2798 – 2808, 1992.

[CMMC11] A. I. Chumakov, G. Monaco, A. Monaco, W. a. Crichton, A. Bosak, R. Rüffer, A. Meyer, F. Kargl, L. Comez, D. Fioretto, H. Giefers, S. Roitsch, G. Wortmann, M. H. Manghnani, A. Hushur, Q. Williams, J. Balogh, K. Parliński, P. Jochym, and P. Piekarz, “Equivalence of the Boson Peak in Glasses to the Transverse Acoustic van Hove Singularity in Crystals,” Physical Review Letters, vol. 106, no. 22, p. 225501, May 2011.

[CoFR02] S. Corezzi, D. Fioretto, and P. Rolla, “Bond-controlled configurational entropy reduction in chemical vitrification,” Nature, vol. 420, no. 6916, pp. 653 – 656, Dec. 2002.

[GMPV03] T. Grigera, V. Martin-Mayor, G. Parisi, and P. Verrocchio, “Phonon interpretation of the ‘boson peak’in supercooled liquids,” Nature, vol. 422, pp. 289 – 292, 2003.

[GuGu03] B. Guillot and Y. Guissani, “Polyamorphism in low temperature water: A simulation study,” The Journal of Chemical Physics, vol. 119, no. 22, p. 11740, 2003.

[GuPS03] V. L. Gurevich, D. A. Parshin, and H. R. Schober, “Anharmonicity, vibrational instability, and the Boson peak in glasses,” Physical Review B, vol. 67, no. 9, p. 094203, Mar. 2003.

[Hodg95] I. M. Hodge, “Physical aging in polymer glasses.,” Science (New York, N.Y.), vol. 267, no. 5206, pp. 1945–7, Mar. 1995.

[JPRK09] R. J. Jiménez Riobóo, M. Philipp, M. A. Ramos, and J. K. Krüger, “Concentration and temperature dependence of the refractive index of ethanol-water mixtures: influence of intermolecular interactions.,” The European Physical Journal E, vol. 30, no. 1, pp. 19–26, Sep. 2009.

[Kauz48] W. Kauzmann, “The Nature of the Glassy State and the Behavior of Liquids at Low Temperatures,” Chemical Reviews, vol. 43, no. 2, pp. 219–256, 1948.

[KSEW08] K. L. Kearns, S. F. Swallen, M. D. Ediger, T. Wu, Y. Sun, and L. Yu, “Hiking down the energy landscape: progress toward the Kauzmann temperature via vapor deposition,” The Journal of Physical Chemistry B, vol. 112, no. 16, pp. 4934 – 4942, Apr. 2008.

[LSGT10] E. Leon-Gutierrez, A. Sepulveda, G. Garcia, M. Teresa Clavaguera-Mora, and J. Rodriguez-Viejo, “Stability of thin film glasses of toluene and ethylbenzene formed by vapor deposition: an in situ nanocalorimetric study,” Physical Chemistry Chemical Physics PCCP, vol. 12, no. 44, pp. 14693–14698, 2010.

[Phil72] W. A. Phillips, “Tunneling states in amorphous solids,” Journal of Low Temperature Physics, vol. 7, no. 3–4, pp. 351–360, 1972.

[SaPS01] I. Saika-Voivod, P. H. Poole, and F. Sciortino, “Fragile-to-strong transition and polyamorphism in the energy landscape of liquid silica.,” Nature, vol. 412, no. 6846, pp. 514–7, Aug. 2001.

[SKMK07] S. F. Swallen, K. L. Kearns, M. K. Mapes, Y. S. Kim, R. J. McMahon, M. D. Ediger, T. Wu, L. Yu, and S. Satija, “Organic glasses with exceptional thermodynamic and kinetic stability,” Science, vol. 315, no. 5810, pp. 353–6, Jan. 2007.

[UtDS00] M. Utz, P. Debenedetti, and F. Stillinger, “Atomistic simulation of aging and rejuvenation in glasses,” Physical review letters, vol. 84, no. 7, pp. 1471–4, Feb. 2000.

[YuCJ02] Y. Z. Yue, J. deC. Christiansen, and S. L. Jensen, “Determination of the fictive temperature for a hyperquenched glass,” Chemical Physics Letters, vol. 357, no. 1–2, pp. 20–24, May 2002.

[ZBCF11] M. Zanatta, G. Baldi, S. Caponi, A. Fontana, C. Petrillo, F. Rossi, and F. Sacchetti, “Debye to non-Debye scaling of the Boson peak dynamics: critical behavior and local disorder in vitreous germania.,” The Journal of chemical physics, vol. 135, no. 17, p. 174506, Nov. 2011.

[ZePo71] R. C. Zeller and R. O. Pohl, “Thermal conductivity and specific heat of noncrystalline solids,” Physical Review B, vol. 4, no. 6, 1971.

1

BRIEF INTRODUCTION AND MOTIVATION

When trying to explain why amorphous solids appear interesting today, we cannot forget mentioning the importance they have in technology. For a fundamental physicist, the exciting new phenomena found in glasses do themselves justify the existence of such an interest, although ignoring the benefits they introduce in modern life is impossible. From the window glass, known for thousands of years, to the polymers developed in the last century in food and textile industry, pharmaceuticals, telecommunication… a non-ending list of examples can be referred to in order to illustrate the power and presence of this state of matter, completely irreplaceable in its applications.

The physics of glasses has still many open questions which make research on amorphous and non-crystalline solids the focus of enormous effort and lively discussion nowadays. Since the topics which encompass these studies comprise a wide and rich variety of physical and chemical properties, choosing the subject becomes crucial if appreciable contribution is intended to be done. Attending to the temperature scale, three well defined ranges exist in which glasses show exciting universal phenomena, far away from the physics in crystalline solids. These relevant temperature ranges are defined by the supercooled liquid region near (above) T_g, the glass below T_g and the low-temperature anomalies at $0.1\ \mathrm{K} \leq T \leq 10\ \mathrm{K}$.

The first key point we find when cooling down from the liquid is the glass transition, where a kinetic arrest drives the supercooled liquid into the glassy state, as a consequence of the dramatic increase in the viscosity. When cooling the liquid, crystallization may happen at temperature T_m, hence producing a sudden decrease in the enthalpy/entropy of the system. In case the liquid can be driven below T_m without crystallizing, the system is called supercooled liquid: the system is in a metastable state (since the equilibrium state for a given temperature $T < T_m$ is the crystal phase), although it is commonly catalogued as equilibrium state as long as no crystal nuclei are present. If we further cool the liquid, its viscosity increases and the relaxation time rapidly surpasses 100 s (the arbitrary reference for the laboratory time scale to define the glass transition), entering the glassy region. The third aspect to be highlighted happens at low temperatures, to say at liquid helium and below, where glasses show an astonishing overall deviation from what would be “Debye-expected”. This deviation even goes in a numerical universality in the case of acoustic attenuation and thermal conductivity, which show similar values within an order of magnitude among very different amorphous solids [Pohl02]. The presence of an enhanced vibrational density of states causes the appearance of what has been called the Boson Peak –at temperatures in the range from 1 K up to 10 K-, which origin still remains unsolved. At lower temperatures, configurational degeneracy in glasses produces the appearance of the two-level systems: these are formed by a group of atoms which, in a cooperative way, can be found in two configurations very close in energy, separated by an energy barrier. The presence of these states introduces time dependence in the specific heat below 1 K.

This three-step illustration of the phenomenology in glasses is rather simplistic, but serves us to briefly introduce the two pillars of the study shown in the present work:

- Effects of lowering the free energy of a glass towards limits never reached before, and how the Kauzmann paradox is influenced.
- The influence these relaxation processes around the glass transition can have on the thermodynamic state and the universal low-temperature anomalies in glasses. And further, how configurational disorder connects to this phenomenology.

These two points serve us as the reference points in a roadmap: wherever the discussion is driven, remember that our final goal is finding the connection between the relaxation processes in glasses below (and far below) T_g and the resulting thermodynamic state with the low energy/temperature anomalies. So, once exposed, let us now focus on the phenomenology in the temperature ranges mentioned above as well as the samples we have chosen and the reasons why they can be useful for us.

1.1 Non-equilibrium and Glass transition

Upon cooling a liquid, this may crystallize at temperature T_m or below. This process is a first-order phase transition, in which the specific heat of the liquid drastically drops, producing a discontinuity in the enthalpy/entropy curve. Nevertheless, this process can be avoided –and should be avoided if our interest is studying glasses–, what is usually done in the laboratory by cooling at fast enough rates. Once the liquid surpasses the crystallization or melting point in Figure 1.1, it is called supercooled liquid, because of its metastable character, since it is no more the minimum free energy state. If the temperature of the supercooled liquid is further decreased, both viscosity and the structural relaxation time increase, producing a slowing down in the molecules motion that conform it. This slow motion involves a lack of equilibrium in the supercooled liquid, which progressively needs time scales much longer than those given in the cooling process. At a given temperature below T_m, time required for molecular rearrangements is so long that the supercooled liquid is ‘frozen’ in the experimental time scale. At this point the viscous liquid is called a glass, and the dynamic temperature so defined is T_g, the glass transition temperature [Ange95][EdAN96][Cava09]. Definition of T_g is then given in terms of viscosity, which controls rearrangements in the liquid: this makes the glass transition to depend on the cooling rate. It is important to say that the glass transition does not happen at a fixed temperature, but in a narrow range where molecular-rearrangement times reach values of the order of 100 s.

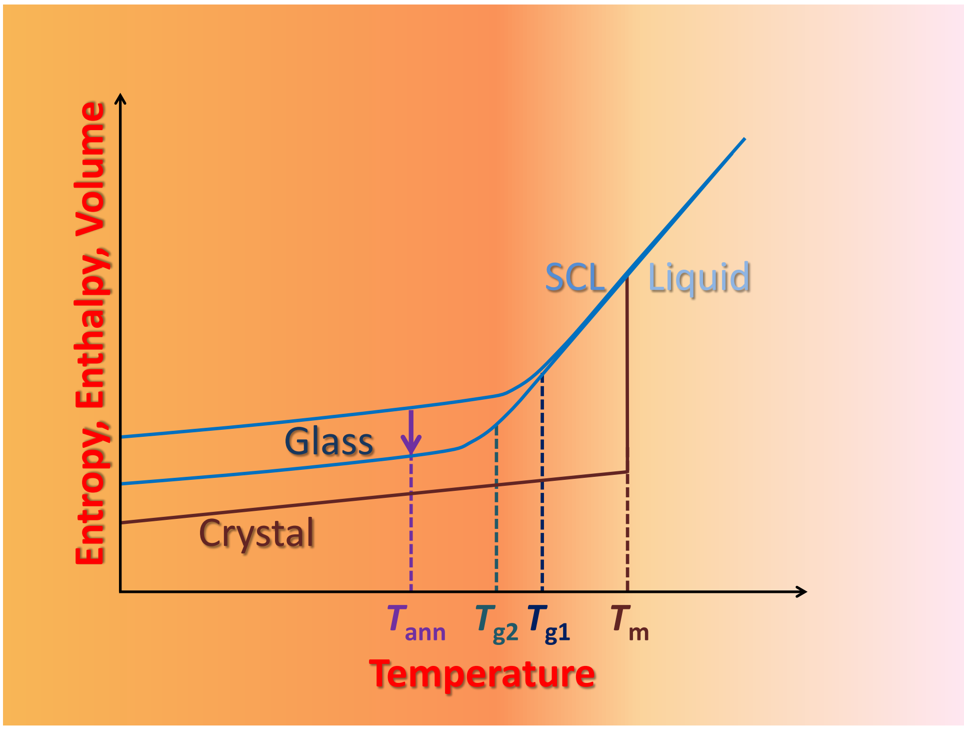

Figure 1.1 Schematic representation of the temperature dependence of entropy, enthalpy or specific volume of a liquid that can either crystallize or enter the supercooled liquid and later in the glass states, as the temperature is lowered. Different cooling rates result in different glasses, with their corresponding distinct glass transition temperatures. Since the glass is a frozen liquid in the experimental time scale, further relaxation processes take place below the glass transition. One of these processes is annealing, where relaxation happens at a constant temperature $T_{ann} < T_g$.

The glass transition observed in the laboratory, although so called, represents no thermodynamic transition but a kinetic one, since it is given by the intersection between molecular-rearrangements and the experimental time scales. Much discussion exists around the possibility that the glass transition is, indeed, a trace of an underlying phase transition that would take place at temperature T_0. There is not only one glass state, but a complete spectrum of them, and due to their out-of-equilibrium nature, they keep on relaxing below T_g. This process is called annealing, if isothermally and intentionally done, or ageing, in case it is the result of a natural process.

When crystallization occurs, a sudden reduction of the specific heat appears. But, in case the crystallization is avoided, the supercooled liquid keeps on cooling with higher specific heat than that of the crystal. This means that the entropy curve of the supercooled liquid decreases much faster than that of the crystal until the kinetic glass transition is reached, where its specific heat lowers down to values similar to the crystal. In case the entropy would not stabilize at T_g, this fast entropy decrease of the supercooled liquid would continue, eventually having the same value as that of the crystal. The temperature at which the extrapolated entropy of the liquid would meet that of the crystal is known as the *Kauzmann temperature* T_K, after Kauzmann first formulation in 1948 [Kauz48] (more about this topic will be discussed in section 2.1.2). Although counterintuitive, no law of thermodynamics is violated if the liquid would have lower entropy than the crystal. Thermodynamically speaking, the problem emerges in case the entropy would continue reducing fast enough, so that the zero-entropy value would be passed at finite temperature. Nevertheless, imaging a liquid with the same entropy (or even lower) as that of the crystal results in many aspects incredible, giving rise to the term *entropy crisis*. What happens in practice is that T_g always appears before T_K is reached, and thus a kinetic transition saves the thermodynamic entropy crisis.

The search for the definitive theory of the glass transition is far from being over. Instead, many different theoretical frameworks provide varied interpretations of the existing phenomenology. Among the most relevant and popular theories, the Adam-Gibbs theory [AdGi65], the Goldstein energy landscape scenario [Gold69], the Mode Coupling Theory (MCT) [BeGS84] [Leut84] and the Random First Order Transition (RFOT) theory [KiWo87][KiTh87][KiTW89][KiWo87] are found. For further theoretical views see Section 2.1.1.

The Adam-Gibbs theory introduced in 1965 is based on the connection between the relaxation time in the supercooled liquid and the configurational entropy given the so called Cooperative Rearranging Regions (CRR). The key concept lays on the increasing size of the CRRs (group of atoms or molecules) with decreasing temperature.

Goldstein formulation of the energy landscape scenario back in 1969 highlights the evolution of the system in the phase space (the space of all the configurational degrees of freedom). In the frame of this space, the total potential energy of the system is defined, and its surface is called the potential energy landscape. A configuration of the system is given by a point in the energy landscape. It is important to note that these configurations describe indeed ‘local’ configurations, since rearrangements in the system happen in a localized region, where the rest of the system acts as a rigid background, hence keeping the energy landscape stable (see Figure 1.2). Local minima correspond to locally stable configurations, and the absolute minimum is given by the ground state, this is, the crystal. In this potential energy landscape, local minima above the crystalline phase do exist, corresponding to defect crystals, polycrystals, and more importat for us, glassy configurations, this is, where the system lacks long-range order. The important idea introduced by Goldstein lays in the fact that, at low enough temperatures, the supercooled liquid explores the minima separated by energy barriers via activated jumps. Also important to be highlighted here is that the system is in equilibrium all the time, although the ground state is the crystal, hence conferring the supercooled liquid the metastable denomination.

In the Mode Coupling Theory, only the static observables are used to describe the equations, particularly the static structure factor. This astonishing aspect, since around the glass transition structural quantities do not show any peculiarity, is solved by the nonlinearity introduced in the interaction, thus giving the expected dependence between the static structure and dynamics.

The Random First Order Transition theory (RFOT) is developed from the same idea of local cooperative rearrangements introduced by the Adam-Gibbs theory and the energy landscape, for which a characteristic length-scale is defined. The concepts of an entropic force which drives rearrangements in the supercooled liquids and the existence of surface tension between cooperative regions entail the main contributions of this theory.

The glass transition temperature T_g, as already shown above in Figure 1.1, is lowered cooling the supercooled liquid slowly enough, or driving the glassy system into a more stable state by annealing and ageing. These are traditional ways to approach the *Kauzmann limit*, appearing in recent years a complete new route to achieve it: ultrastable glasses obtained from physical vapor deposition [SKMK07][KSEW08]. This technique has proven to successfully lower in a big amount the entropy of the glass in human time scales by optimizing the substrate temperature and deposition rate [KSEW07]. The drastic increase of the glass stability by applying one of the two ways described above opens a promising field to test the possible connection between the thermodynamic state and the low-temperature universal anomalies in glasses. The access to a wide range of states, from the ordinary glass to the extraordinary stable one (driven by extreme ageing in natural amber resins or enhanced two-dimensional mobility in vapor-deposited thin films), will allow us to answer old questions about the intrinsic ingredients of in disorder.

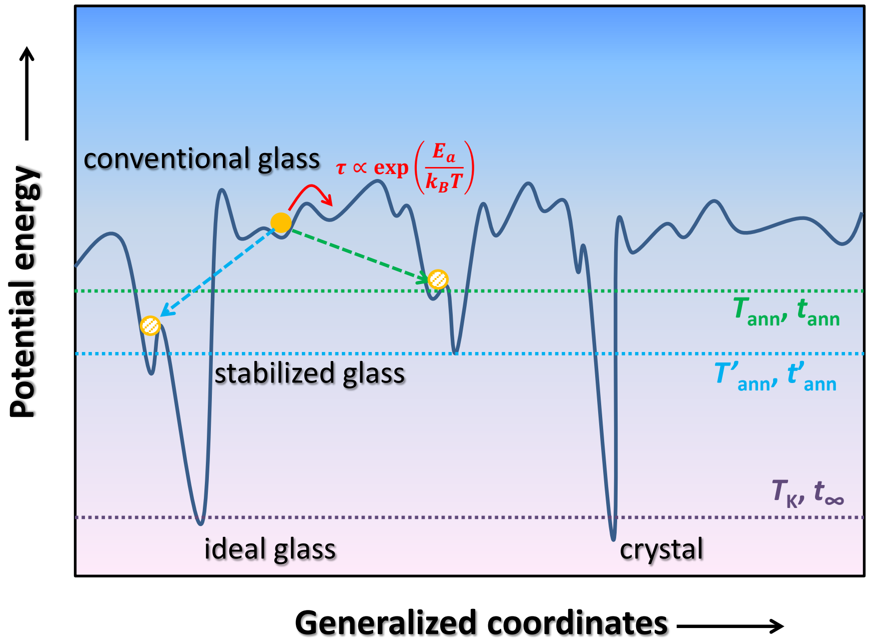

Figure 1.2 Energy landscape in the supercooled liquid and glass, together with the effects of structural relaxation processes induced in by annealing at different temperatures T_{ann}. The lowest energy configuration for a given annealing temperature is reached only if enough time is given to the system t_{ann}. Time necessary to overcome a barrier grows exponentially with decreasing temperature. In order to achieve the so called ideal glass configuration, this is, with glass transition temperature at T_K, infinite relaxation time t_∞ is needed.

The main strategy we have followed in our work is accessing extraordinary stable glasses which result from extreme relaxation processes. This is possible by using a well-known natural resin which has undergone a long ageing during tens or even hundred million years. We refer to amber, the geological glass

[LaPo02][Grim96]. Although the discussion about the formation of glasses has been addressed from the point of view of cooling the liquid, it is not the unique route to obtain a glass. Indeed, viscosity is the relevant macroscopic property which controls the transition from the liquid to the glass, and it can be increased in several ways, different from lowering the temperature, as for example via covalent bonds. This way, slowing down the motion of molecules which form the liquid is achieved by increasing the chemical bonds present in the system. It is a commonly used process in the polymeric glues employed in daily life, as for example the two-component epoxy resins. Because of this particularity they are commonly denominated chemical glasses, which have been proven to be a different way to produce glasses [CoFR02]. Once the amber resin is in its glassy state, natural ageing during million years at temperatures well below its glass transition –ranging from 115 ºC up to 165 ºC in the samples presented here– has driven amber to lower energy configurations. An important question to be solved is whether this natural ageing has been efficient enough, so that a *considerable* energy/entropy decrease is present in our amber samples (see Figure 1.2). In order to do this, quantification of how far in the journey towards the Kauzmann limit has our amber travelled must be done, for which determination of its *fictive temperature* T_f is needed [SKMK07], via specific heat.

As said before, physical vapor deposition has been proven to be an effective way lowering the glass in the energy landscape towards the Kauzmann temperature, since enhanced 2D mobility facilitates reaching a lower energy configuration. A complement to the investigations done on amber has been the study on the evolution of the low-temperature anomalies in indometathin thin films with increasing stability. This has provided us new insights about the interplay of extraordinary stability and dimensionality. While in the case of amber 3D rearrangements are needed, with annealing temperatures far away from T_g (typically T_g – 90 K), and hence exponentially increasing time scales from 10^3 to 10^9 years [KSEW08], ultraestable thin films exploit the ability of molecules to rapidly find extraordinary stable configurations in which two-dimensional rearrangements dominate. Amber also allows us to investigate the counter annealing process, this is, progressively annealing the glass at higher temperatures than that of the original ageing process, hence erasing its exceptional thermal history, and study its effects on enthalpy/entropy curves.

1.2 Low-temperature anomalies in amorphous solids

Before the work of Zeller and Pohl in the early 1970s [ZePo71], no exciting new phenomena were expected from the thermal properties of amorphous solids at low temperatures. Nevertheless, measurements on the thermal conductivity and specific heat in experiments by Zeller and Pohl showed intriguing properties in two ways: first, a deviation from the Debye model prediction in the noncrystalline dielectric solids, showing a marked linear dependence of the specific heat and an almost quadratic one in the thermal conductivity below 1 K; second, a universal behavior in the amorphous solids studied, even numerically in the case of thermal conductivity, since variations within a factor of 5 were observed among very different noncrystalline solids. The appearance of a plateau in thermal conductivity at temperatures between 1 K and 10 K and a broad peak in specific heat in the reduced C_p/T^3 representation appeared as new exciting phenomena, still not fully understood nowadays.

Two energy/temperature ranges are discussed when talking about the low-temperature anomalies in glasses: below 1 K, where the linear dependence in the specific heat as well as the quadratic dependence in thermal conductivity are originated by the presence of a quantum configurational degeneracy, the Two Level Systems (TLS) or tunneling states; above 1 K, where a plateau in thermal conductivity and a broad maximum in the specific heat in the C_p/T^3 representation known as the Boson Peak (BP) appear. Whereas broad consensus exists in the explanation introduced by the TLS, the BP is the focus of intense debate in recent years, as different theories compete in successfully clarifying this feature.

Soon after the low-temperature anomalies in glasses were exhaustively observed by Zeller and Pohl [ZePo71], Anderson *et al.* and Phillips independently developed in 1972 the Tunneling State Model [AnHV72][Phil72]. It successfully explained the phenomenology below 1 K (see Figure 1.3) in terms of a number of atoms (or group of atoms) that could occupy one of two local equilibrium positions, tunneling through the energy barrier that separate them, introducing the picture of the asymmetric double-well potential widely accepted nowadays. This model correctly predicts the linear temperature dependence of the specific heat as well as the $\sim T^2$ behavior in thermal conductivity. Besides, time dependence of the specific heat at high enough frequencies (in the time limit where not all tunneling states have relaxed) has been explained using this model as well.

In order to clarify the origin of the excess density of states above 1 K responsible of the appearance of the boson peak, neutron and Raman scattering performed in glasses (such as vitreous Silica and B_2O_3) have shown a clear crossover from vibrations in single-well potentials to thermally activated jumps in double-well potentials, when lowering the frequencies typically below 300 GHz ([RaBu98] and references therein). This effect has been experimentally observed as a marked non linearity in the inelastic scattering intensity versus energy gain as frequency is decreased. These observations suggest then the presence of quasi-localized modes in amorphous solids, in which low-frequency vibrational modes and relaxational modes (corresponding to double-well potentials with low barrier heights) exist.

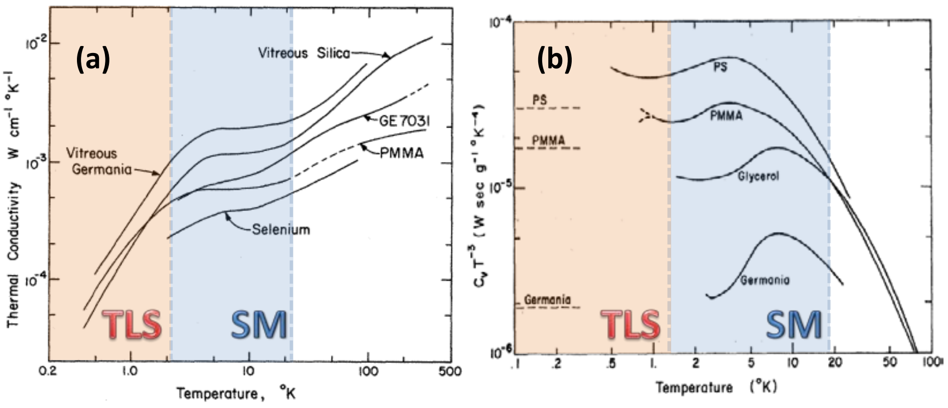

Figure 1.3 Low-temperature anomalies in the thermal properties of glasses after Zeller & Pohl [ZePo71]: (a) thermal conductivity and (b) specific heat. Red shadows indicate the Two Level Systems contributions below 1 K and blue shadows the so called *soft-modes* contribution which originates the Boson Peak in the reduced C_p/T^3 representation.

The Boson Peak is an excess in the vibrational density of states (VDOS) observed in glasses at frequencies ~ 1 THz, and correspondingly, at temperature ~ 10 K (see Figure 1.3). Extended agreement exists in seeing the BP as a vibrational consequence of the structural disorder present in glasses, although consensus in the origin of this feature is still far from being achieved. Nevertheless, existing boson peak interpretations can be categorized in two main dynamical models: (i) one based on harmonic elastic disorder as the source of the excess in the vibrational density of states at low frequencies [KaRB01][TLNE01][ScDG98]; (ii) a second model, in which extra –nonacoustic- quasi local vibrations at low frequencies give rise to the BP phenomenology [Pars94][KaKI83].

A remarkable aspect of the low-temperature anomalies presented here is their appearance in defective [KHSK11] and orientationally-disordered crystals [RaTV02][TRVC98] as well, which results from the increase of the soft modes contribution to the Vibrational Density of States (VDOS) with increasing disorder, regardless whether orientational or translational. This highlights the widespread presence of glassy behavior in condensed matter, together with the need of a deep understanding on the basic ingredients which give rise to disorder.

As briefly introduced above, many open questions in the low energy/temperature excitations in glasses do lack a good –and unified– explanation. Clarifying the origin of the excess in the vibrational density of states known as the boson peak can be highlighted as the main task to be addressed. Besides, description of the role played by configurational disorder frozen at the glass transition in the low-temperature anomalies is needed as well.

To this purpose, the low-temperature anomalies (BP and TLS) are exhaustively studied in glasses with extraordinary thermodynamic and kinetic stability obtained in two different ways: (i) as the result of hyperageing, this is, ageing process during million years, and (ii) in physical vapor-deposited thin film glasses showing enhanced stability under particular fabrication conditions [SKMK07][KSEW07][SLGR11].

[AdGi65] G. Adam and J. H. Gibbs, “On the temperature dependence of cooperative relaxation properties in glass-forming liquids”, The Journal of Chemical Physics, vol. 43, no. 1, pp. 139–146, 1965.

[Ange95] C. A. Angell, “Formation of glasses from liquids and biopolymers”, Science, vol. 267, no. 5206, pp. 1924–1935, 1995.

[AnHV72] P. W. Anderson, B. I. Halperin and C. M. Varma, “Anomalous low-temperature thermal properties of glasses and spin glasses”, Philosophical Magazine, vol. 25, no. 1, pp. 1–9, 1972.

[BeGS84] U. Bengtzelius, W. Götze and A. Sjölander, “Dynamics of supercooled liquids and the glass transition”, Journal of Physics C: Solid State Physics, vol. 17, pp. 5915 – 5934, 1984.

[Cava09] A. Cavagna, “Supercooled liquids for pedestrians”, Physics Reports, vol. 476, no. 4–6, pp. 51–124, 2009.

[CoFR02] S. Corezzi, D. Fioretto and P. Rolla, “Bond-controlled configurational entropy reduction in chemical vitrification”, Nature, vol. 420, no. 6916, pp. 653 – 656, 2002.

[EdAN96] M. Ediger, C. Angell and S. R. Nagel, “Supercooled liquids and glasses”, The Journal of Physical Chemistry, vol. 100, no. 31, pp. 13200–13212, 1996.

[Gold69] M. Goldstein, “Viscous Liquids and the Glass Transition: A Potential Energy Barrier Picture”, The Journal of Chemical Physics, vol. 51, no. 9, pp. 3728–3739, 1969.

[Grim96] D. A. Grimaldi, “The Age of Dominican Amber”, Amber, Resinite, and Fossil Resins, vol. 617, Chap. 11, American Chemical Society, 1996, pp. 11–203.

[KaKI83] V. G. Karpov, M. I. Klinger and F. N. Ignat’ev, “Theory of the low-temperature anomalies in the thermal properties of amorphous structures,” Zh. Eksp. Teor. Fiz, vol. 84, pp. 439 – 448, 1983.

[KaRB01] J. W. Kantelhardt, S. Russ and A. Bunde, “Excess modes in the vibrational spectrum of disordered systems and the boson peak”, Physical Review B, vol. 63, no. 6, p. 064302, 2001.

[Kauz48] W. Kauzmann, “The Nature of the Glassy State and the Behavior of Liquids at Low Temperatures”, Chemical Reviews, vol. 43, no. 2, pp. 219–256, 1948.

[KHSK11] A. I. Krivchikov, M. Hassaine, I. V. Sharapova, O. A. Korolyuk, R. J. Jiménez-Riobóo and M. A. Ramos, “Low-temperature properties of glassy and crystalline states of n-butanol,” Journal of Non-Crystalline Solids, vol. 357, no. 2, pp. 524–529, 2011.

[KiTh87] T. R. Kirkpatrick and D. Thirumalai, “Dynamics of the structural glass transition and the p-spin—interaction spin-glass model”, Physical Review Letters, vol. 58, no. 20, pp. 2091–2094, 1987.

[KiTW89] T. R. Kirkpatrick, D. Thirumalai and P. G. Wolynes, “Scaling concepts for the dynamics of viscous liquids near an ideal glassy state”, Physical Review A, vol. 40, no. 2, pp. 1045-1054, 1989.

[KiWo87] T. R. Kirkpatrick and P. G. Wolynes, “Connections between some kinetic and equilibrium theories of the glass transition”, Physical Review A, vol. 35, no. 7, pp. 3072–3080, 1987.

[KiWo87] T. R. Kirkpatrick and P. G. Wolynes, “Stable and metastable states in mean-field Potts and structural glasses”, Physical Review B, vol. 36, no. 16, pp. 8552–8564, 1987.

[KSEW07] K. L. Kearns, S. F. Swallen, M. D. Ediger, T. Wu and L. Yu, “Influence of substrate temperature on the stability of glasses prepared by vapor deposition”, The Journal of Chemical Physics, vol. 127, no. 15, p. 154702, 2007.

[KSEW08] K. L. Kearns, S. F. Swallen, M. D. Ediger, T. Wu, Y. Sun and L. Yu, “Hiking down the energy landscape: progress toward the Kauzmann temperature via vapor deposition”, The Journal of Physical Chemistry B, vol. 112, no. 16, pp. 4934 – 4942, 2008.

[LaPo02] J. B. Lambert and G. O. Poinar, “Amber: the organic gemstone”, Accounts of Chemical Research, vol. 35, no. 8, pp. 628–636, 2002.

[Leut84] E. Leutheusser, “Dynamical model of the liquid-glass transition”, Physical Review A, vol. 29, no. 5, 1984.

[Pars94] D. A. Parshin, “Soft-potential model and universal properties of glasses”, Physics of the Solid State, vol. 36, no. 7, pp. 991–1024, 1994.

[Phil72] W. A. Phillips, “Tunneling states in amorphous solids,” Journal of Low Temperature Physics, vol. 7, no. 3–4, pp. 351–360, 1972.

[Pohl02] R.O. Pohl, X. Liu and E. J. Thompson, Rev. Mod. Phys., vol. 74, pp. 991-1013 (2002).

[RaBu98] M. A. Ramos and U. Buchenau, “Beyond the standard tunneling model: The soft potential model”, in *Tunneling systems in amorphous and crystalline solids*, Chap. 9, edited by P. Esquinazi, Ed. Springer, 1998.

[RaTV02] M. A. Ramos, C. Talon and S. Vieira, “The Boson peak in structural and orientational glasses of simple alcohols: specific heat at low temperatures,” Journal of non-crystalline solids, vol. 307–310, pp. 80 – 86, 2002.

[ScDG98] W. Schirmacher, G. Diezemann and C. Ganter, “Harmonic vibrational excitations in disordered solids and the ‘boson peak’”, Physical Review Letters, vol. 81, no. 1, pp. 136 – 139, 1998.

[SKMK07] S. F. Swallen, K. L. Kearns, M. K. Mapes, Y. S. Kim, R. J. McMahon, M. D. Ediger, T. Wu, L. Yu and S. Satija, “Organic glasses with exceptional thermodynamic and kinetic stability”, Science, vol. 315, no. 5810, pp. 353–356, 2007.

[SLGR11] A. Sepúlveda, E. Leon-Gutierrez, M. Gonzalez-Silveira, C. Rodríguez-Tinoco, M. T. Clavaguera-Mora and J. Rodríguez-Viejo, “Accelerated Aging in Ultrathin Films of a Molecular Glass Former,” Physical Review Letters, vol. 107, no. 2, p. 025901, 2011.

[TLNE01] S. N. Taraskin, Y. L. Loh, G. Natarajan and S. Elliott, “Origin of the Boson Peak in Systems with Lattice Disorder”, Physical Review Letters, vol. 86, no. 7, pp. 1255–1258, 2001.

[TRVC98] C. Talón, M. A. Ramos, S. Vieira, G. J. Cuello, F. J. Bermejo, A. Criado, M. L. Senent, S. M. Bennington, H. E. Fischer and H. Schober, “Low-temperature specific heat and glassy dynamics of a polymorphic molecular solid,” Physical Review B, vol. 58, no. 2, pp. 745 – 755, 1998.

[ZePo71] R. C. Zeller and R. O. Pohl, “Thermal conductivity and specific heat of non-crystalline solids”, Physical Review B, vol. 4, no. 6, 1971.

2

THE PHYSICS OF GLASSES

Regardless of the particular state of the condensed matter we are interested in, all of them are the unavoidable result of interactions between the particles (ions, atoms, molecules) which constitute them. Liquids are the usual starting point of the game if our goal is obtaining a solid (without forgetting the routes which begin from the gas), and depending on the way we play our cards, we will end up with a crystalline or an amorphous phase. And within them, endless possibilities provided by polymorphism and polyamorphism. But let us start from the beginning.

When cooling a liquid the crystallization temperature is first reached, at which the system falls into the equilibrium phase via a sudden decrease in its enthalpy, entropy or volume (although counterexamples to the latter exist, like water). Instantaneous to the eye though, this first order transition is the consequence of microscopic crystalline-domains nucleation and growth. Nevertheless, for our joy one can avoid crystallization and further cool the liquid, thus entering the supercooled liquid region. Nothing special happens when going from the liquid into the supercooled liquid in terms of its thermodynamic properties, since they are the extrapolated properties of the liquid above T_m. The supercooled liquid is a metastable phase in which the system is at equilibrium, although not at the minimum energy. If we keep on cooling the supercooled liquid its viscosity increases, and so does the time necessary for the particles to reach the equilibrium in the liquid. Not far below T_m, times needed are so critically large that the particles no longer reach equilibrium in experimental time scales, and so the system is frozen to our purposes. The glass transition has occurred and the system is now in the glass phase, the central point of this chapter.

We will introduce here the basic aspects and phenomenology in glasses, together with the theoretical framework necessary to describe what happens to glasses at the glass transition, as well as their low-energy and low-temperature properties.

2.1 The glass transition

If we want to discuss about the phenomenology of supercooled liquids and glasses around the glass transition, first we have to give a suitable definition of it. It remains clear from the way we have announced the appearance of the glass when cooling the supercooled liquid, that the glass transition is a kinetic event determined by the crossing of the experimental time scale with that of the particle rearrangements in the liquid. The definition for T_g in terms of the relaxation or rearrangements time is conventionally chosen to be $\tau \approx 100$ s, first proposed by Laughlin and Uhlmann [LaUh72]. Despite being a dynamic transition, something dramatic happens at T_g, this is, the loss of ergodicity. The impossibility of particle rearrangement stops the phase-space sampling in the system, and so restricts the degrees of freedom accessible to the system. Broken ergodicity also appears in crystals, since particles occupy ordered equilibrium positions determined by the energy minimum, around which they vibrate but no more rearrange. But a critical difference exists between glass and crystal: the first is arrested off-equilibrium.

The result of lost ergodicity introduces a downfall in the specific heat of the supercooled liquid at the glass transition that almost reaches the value in the crystal, as schematically shown in Figure 2.1. This happens because once the rearrangements are suppressed, (almost) only vibrational contribution to the specific heat is left. We say *almost* referring to the glass, since particles vibrate around disordered equilibrium positions, and the possibility to rearrange weakly survives. This possibility makes $C_P(glass) \gtrsim C_P(crystal)$, as clearly reflected in Figure 2.1 below T_g.

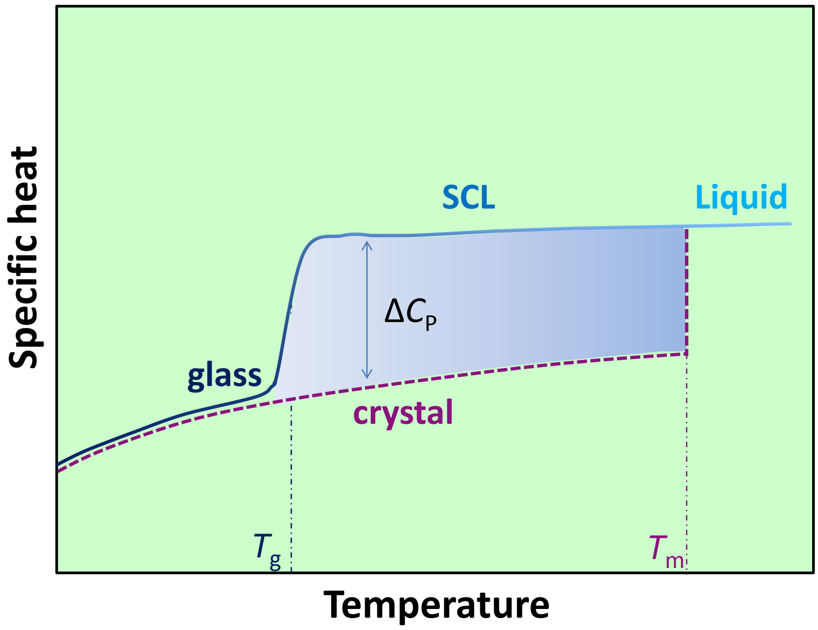

Figure 2.1 Specific heat curves of the liquid when falling into the crystal and of the supercooled liquid when freezing in the glass. The result of broken ergodicity in the crystal and the glass make their specific heat curves almost collapse, since (nearly) the only contribution left is vibrational in both cases.

Another widely used definition of the glass transition is given in terms of viscosity, a macroscopic property which relates to the ability of the liquid to flow. Once crystallization is avoided, the viscosity of the liquid starts rising much faster than it did before this point was reached. Furthermore, it has been empirically found that, typically, at the midpoint of the specific-heat jump in the glass transition the value for viscosity is $\eta \approx 10^{13}$ Poise, what directly connects to the relaxation times before mentioned. The specific-heat curve is used in general to determine the glass transition, as shown in Figure 2.1 for the supercooled liquid falling to the glass. Notice that no overshoot or sharp peak are observed at T_g and T_m, respectively, when lowering the temperature. In fact, these excesses in the specific heat are observed when measuring the C_p curve by increasing the temperature.

The question that comes to our head on observing the dynamical character of the glass transition is whether such a definition really makes sense. And the answer is *yes*, since the glass transition temperature depends on the available experimental time *weakly*. In many substances, the increase of the relaxation time when approaching the glass transition is so sharp that large variations on the cooling rate really make no difference in the T_g value. Considering an Arrhenius-like behavior of the shear-relaxation time in the vicinity of T_g, then

$$t_{\mathrm{exp}} = \tau_0 \exp\left(\frac{\Delta E_\mathrm{a}}{k_\mathrm{B} T_g}\right) \tag{2.1}$$

where ΔE_a stands for the characteristic energy barrier the system has to overcome in order to rearrange. Changes in the experimental time will induce then exponentially damped modifications in T_g, obtained from differentiation in both parts of Equation (2.1). And this in the case of Arrhenius dependence, which is weaker than that observed in most of the glass formers, which present a super-Arrhenius increase, derived from the fact that the energy barrier ΔE_a is temperature dependent, hence making T_g-variations even smaller.

We show in Figure 2.2 a widely used classification of glass formers depending on their temperature dependence of viscosity, first proposed by Angell [Ange91], which differentiates between Arrhenius- (linear in log(η) versus 1/T) and super-Arrhenius-behaved (exponential in liquids linear in log(η) versus 1/T) liquids. It allows us to bring into a single plot the viscosity data for many substances by scaling the temperature with T_g, discerning the so called strong (Arrhenius like) from the fragile (super-Arrhenius like) glass formers. Of course, this is not a black-or-white classification, since in the representation given in Figure 2.2 exists a continuous spectrum of substances going from the archetypical strong behavior (SiO_2 is the perfect example) to the fragile one (such as toluene), as shown by Angell in [Ange95], for example.

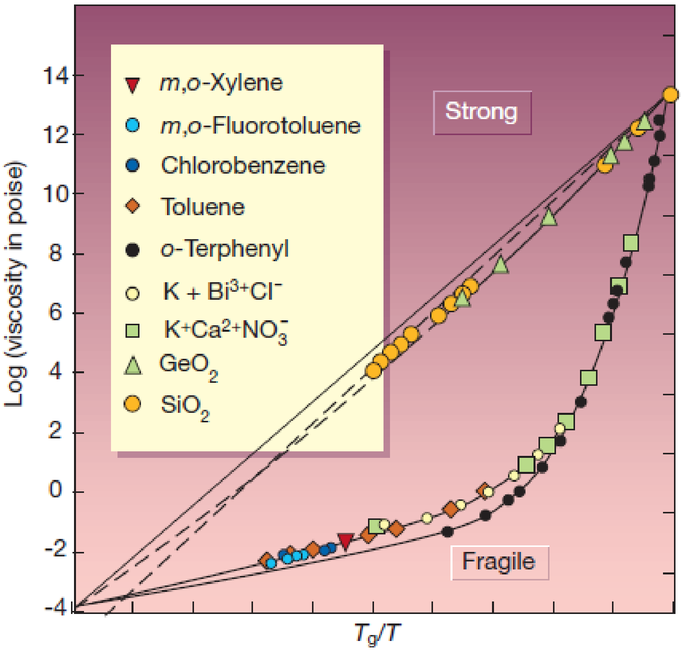

Figure 2.2 Angell's plot of the T_g-scaled Arrhenius behavior of the logarithm of viscosity in different glass formers. This representation markedly distinguishes between the Arrhenius-behaved systems, showing linear behavior (called *Strong* liquids), and super-Arrhenius-behaved ones, with viscosity increase sharper than exponential due to temperature dependence in the activation energy barrier ΔE_a (called *Fragile* liquids), from [DeSt01].

In order to account for the fragility quantitatively, a useful definition is given in terms of the slope of log(η) versus T_g/T at the glass transition. Strong liquids present a linear behavior in this representation, with slope close to 17. The higher the slope, the higher the fragility m

$$m = \left(\frac{d\log_{10}\langle\tau\rangle}{dT_g/T}\right)_{T=T_g} \tag{2.2}$$

It is interesting to remark the instructive vision on the glass transition that Figure 2.2 introduces: whereas for strong liquids T_g does not make a difference in terms of viscosity, in fragile glass formers something important really happens there, since in the vicinity of T_g viscosity increases dramatically and seems to diverge.

2.1.1 Theoretical views on the glass transition

Until now we have presented the phenomenology of the glass transition and the way it is observed in properties such as the specific heat or the viscosity. But let us go deeper in the understanding of what is known to date about the physics which govern the formation of glasses. For this purpose, we will briefly introduce some theoretical views on the glass transition which, to our understanding, better illustrate the most relevant events to us.

2.1.1.1 Adam-Gibbs theory

Adam and Gibbs developed in 1965 a theoretical framework in which the relaxation times in deeply supercooled liquids (near their glass transition) are inferred from entropy considerations [AdGi65]. In these conditions, they proposed that the relaxation comes from the rearrangement of an increasing number of particles with decreasing temperature. These groups of particles have to find the way to work together, hence defining a minimum –and indivisible– region in the system, called Cooperative Rearranging Regions (CRR). The existence of the CRR is explained as a signature of local events, since they evolve independently to their surroundings. The teamwork character of the CRR restricts the accessible microstates to them, and a statistical description of the states $\mathscr{N}$ in which the system can be found is easily derived as

$$\mathscr{N} = \Omega^{N/n} \tag{2.3}$$

with N the total number of particles in the system and n the average number of particles included in a CRR. These accessible configurations to the system give raise to the configurational entropy

$$S_c = \frac{\log \Omega}{n} \tag{2.4}$$

Adam and Gibbs considered that the number of local states Ω was temperature independent, and so the size of the CRR can be directly written in terms of the configurational entropy

$$n(T) = \frac{\log \Omega}{S_c(T)} \tag{2.5}$$

This way it is found quite straight forward that the size of the CRRs increases with decreasing configurational entropy. The energy barrier ΔE_a of the rearrangement was found in this context to scale with the particles included in the CRR, and so to be inversely proportional to the configurational entropy. Introducing this dependence in the Arrhenius equation for the relaxation time τ, we get the intended relation with the entropy

$$\tau = \tau_0 \exp\left(\frac{B}{TS_c}\right) \tag{2.6}$$

where τ_0 and B are constants.

Let us have a look now at the relation between the configurational entropy and the specific heat by going back to Figure 2.1. The excess entropy of the liquid above the crystal is defined as the configurational entropy, assuming that the glass has equal (vibrational) specific heat to the crystal, as observed below Tg in Figure 2.1. This excess specific heat is the contribution of relaxation processes, thus the relation

$$S_c(T) - S_c(T_K) = \int_{T_K}^{T} \frac{\Delta C_P}{T} \mathrm{d}T \tag{2.7}$$

being T_K a finite temperature below T_g where the configurational entropy vanishes (the Kauzmann temperature), and assuming that ΔC_P is temperature independent. We can rewrite Equation (2.7)

$$S_c(T) \sim \Delta C_P \frac{T - T_K}{T_K} \tag{2.8}$$

A more appealing approximation assumes a specific-heat dependence of the form $\Delta C_P \approx b/T$, from which the expression for the relaxation time in the vicinity of the glass transition is found to be

$$\tau = \tau_0 \exp\left(\frac{A}{T - T_K}\right) \tag{2.9}$$

which is the Vogel-Tamman-Fulcher relation (VFT).

2.1.1.2 Energy landscape scenario

The idea of describing the equilibrium dynamics in deeply supercooled liquids in terms of their evolution in the phase space of all configurational degrees of freedom was first proposed by Goldstein in 1969 [Gold69], which provides a helpful and simple insight to the physics of glass formers near the glass transition.

A particular configuration of the system is represented as a point in the phase space, and its dynamics is described by the motion of this point which drives the system to different configurations. The frontier or surface of the total potential energy of the system defines the potential energy landscape, in which local minima correspond to different stable configurations of the system. The absolute minimum is the crystalline state, in which possible defects and dislocations drive the system to surrounding local minima above the ground state. Apart from these local minima corresponding to the crystal with a different degree of disorder present in it, we have all the rest of minima given by the amorphous configurations of the system. These minima have potential energy values well above the crystal, and they are separated by potential energy barriers necessary to jump in order to reach different glassy configurations (see Figure 2.3c).

When cooling the liquid, we move from a corrugation-free region of the potential-energy landscape (given by point 1 in Figure 2.3) to another in which the system starts feeling the presence of the surface. The system still has energy enough to sample the whole phase space, but can already fall into the crystalline configuration (point 2 in Figure 2.3). If we keep cooling the liquid, the system gets confined inside one of the valleys in Figure 2.3c (called *basins*), and finally driven into a local minimum (point 5 in Figure 2.3). At this point, only activated jumps through energy barriers allow the system to access different configurations with average equal potential energy values. These rearrangements are not undergone by the N particles which make up the system, but rather have a local nature. It is a small group of n particles, then, which jointly rearrange in the real space to access a different configuration, with the particles far in the space playing no role. The larger the number of particles to rearrange the higher the energy barrier to jump is. Here lays a central aspect of activated dynamics, i.e. the dependence of rearrangement regions' size with temperature in supercooled liquids next to the glass transition, since an explanation on the increasing size n

with decreasing temperature conditions the construction of theories around the glass transition.

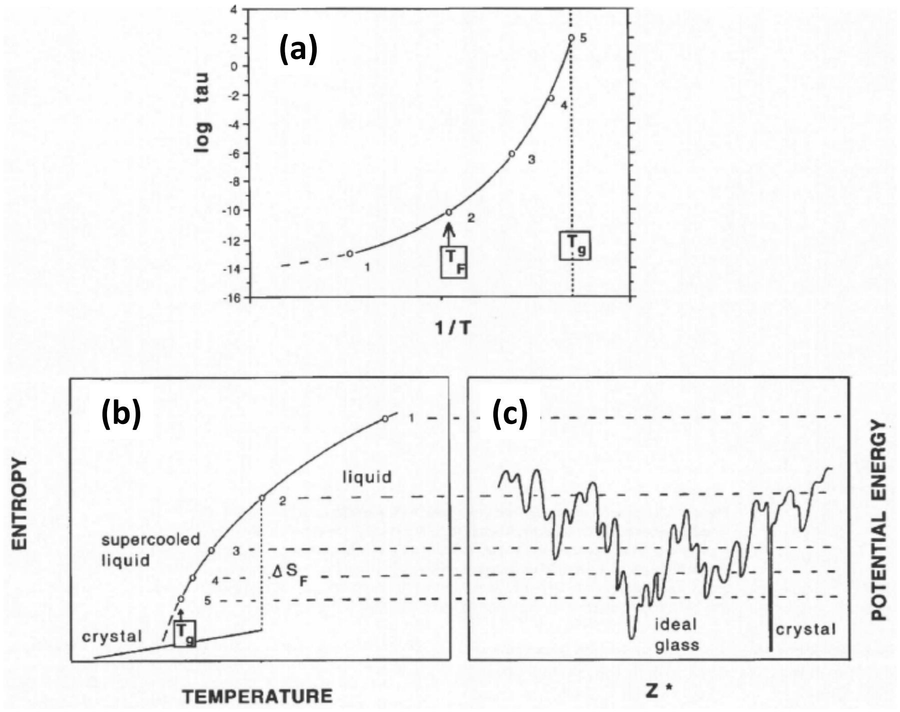

Figure 2.3 Description of the system evolution when cooling the liquid in (a) relaxation time, (b) entropy and (c) energy landscape scenario versus generalized coordinates Z^*. Correspondence between different configurations in the phase space and characteristic relaxation time scales and entropies are marked with numbers from 1 to 5. From [Ange97].

Of course, for high enough temperatures, the potential energy landscape does not govern any more the capability of the system to rearrange. If thermal energy k_BT is well above the surface of the potential energy landscape, the system is no more conditioned by energy barriers: the liquid is fluid. In the way from activated (where energy barriers matter) to non-activated regime, Goldstein defined a frontier temperature T_x, where the shear relaxation times are much faster than those at T_g, $\tau(T_g) \approx 10^2 – 10^3$ s, whereas $\tau(T_x) \approx 10^{-8}$ - 10^{-9} s (see region defined between points 2 and 3 in Figure 2.3). Although it seems a little arbitrary, this temperature divides the temperature range between the glass transition and the melting (the supercooled liquid region) in two equal parts $[T_g : T_x] \approx [T_x : T_m]$, and a deeper explanation was given by Goldstein. T_x is the temperature at which the shear relaxation time and the time needed for the system to rearrange intersect, thus providing it with a meaningful reason to exist. Below this temperature, two time scales appear: a fast one determined by vibrations of the system around a minimum in the potential energy landscape (see for example point 3 in Figure 2.3), and a slower one given by minimum-to-minimum jumps. These two scales may be seen as the experimental α- and β-relaxations observed in the dynamic correlation function. Two relaxation time scales are observed above T_x as well, but Goldstein view of vibrations and activation through energy barriers is not correct any more.

2.1.1.3 Mode coupling theory

The Mode Coupling Theory (MCT) bases its understanding of the supercooled liquid approaching the glass transition on the dynamical correlation function of density fluctuations $\Phi(t)$. Its decay with time can be written as a non-linear damped second-order differential equation, and after the simplifying approximations introduced in the theory, one can solve it numerically and even (in some qualitative studies) analytically. The handling of equations involved is quite complicated, and only a conceptual approximation is presented here.

The important idea to understand from the MCT is the fact that starting from static observables like the structure factor $S(\mathrm{q})$, we end up with a set of dynamical equations. This is possible by the non-linear character of interactions in MCT, which gives rise to a direct dependence between the static structure and the dynamics. The result of this is the appearance in the dynamical correlation function of two step relaxation at temperatures near the glass transition, what means dynamics in the supercooled liquid is divided into a ‘fast’ and a ‘slow’ one. A plateau emerges then, which increases with decreasing temperature (see Figure 2.4). This prediction of the MCT is in good agreement with what is observed in supercooled liquids, being the two-step relaxation a strong support to the acceptance of the theory.

But there are also failures in the prediction of the MCT, such as the diverging size of the plateau which is reached for a finite temperature T_C, meaning that the slow relaxation time diverge, thus frozen in at T_C. Such a divergence does not exist in real systems (see for example an extreme case in [ZhSM13] still showing a finite τ_R). The temperature T_C is found to be above T_g when fitting experimental data to the prediction of the MCT

$$\tau_R = \frac{1}{(T - T_C)^{\gamma}} \tag{2.10}$$

and the closer the data to TC the greater the difference with the value given by Equation (2.10), diverging at that critical temperature.

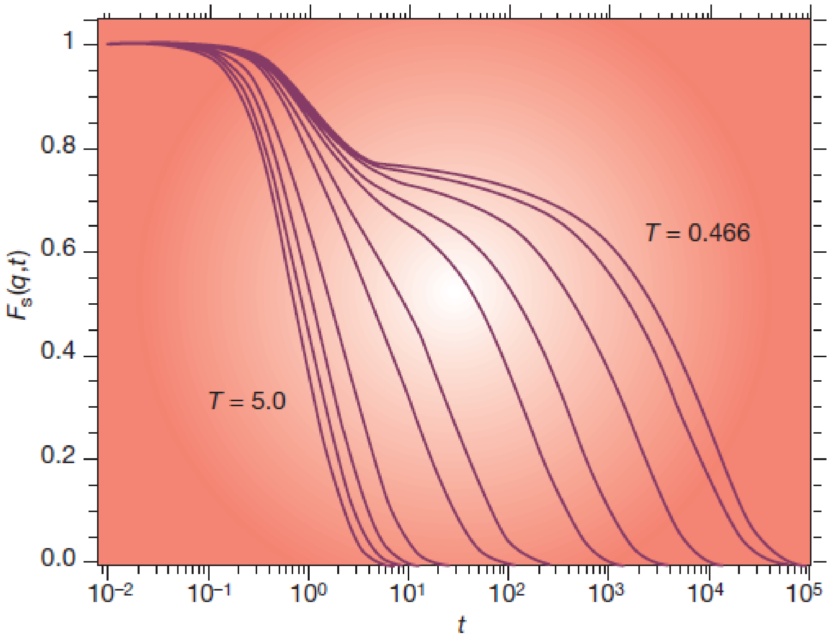

Figure 2.4 Evolution of the dynamical correlation function with temperature for a Lennard-Jones system, showing an exponential decay at high temperatures and developing a two-step relaxation behavior with decreasing T. The size of the plateau also increases when approaching the glass transition [KoAn95][Cava09].

This limits the validity of MCT to temperatures above the critical temperature T_C, what of course restricts its working range (well) above the glass transition. A possible explanation to this breakdown can be found in the relaxation mechanism which rules in MCT below T_g. MCT does not include activation through energy barriers, thus forcing the liquid not to relax below T_C, what in practice never happens. This critical temperature defines, then, the natural limit of MCT when lowering the temperature, what indeed seems quite analogous to the situation experienced by Goldstein in the opposite direction. Simply speaking, correspondence is found between T_C and T_x, what marks the transition from the activated to the non-activated (two-step) relaxation mechanisms.

2.1.1.4 Other theoretical views

Further theoretical views exist on the glass transition phenomenology which present interesting ideas in the understanding of some of its specific aspects. Nevertheless, due to the introductory character aimed for this Chapter, only some of the theories have been considered to appear. In order to give a broader vision on the field without extending much more, some additional models and theories are briefly mentioned here for completeness.

By historical appearance, the first theoretical view to be mentioned is the Free Volume model, originally developed by Cohen and Turnbull [CoTu59][TuCo61][TuCo70] for fluids assuming they were composed of hard spheres. The basic idea of the model is considering two different volumes in the liquid, the occupied one and the unoccupied or free volume. The latter allows the diffusive motion in the liquid. As the temperature is lowered, the system reaches some critical free volume value, below which this volume is ‘frozen-in’ in the locations they occupy, thus allowing no further diffusion and entering the glass.

A more recent theory, formulated in the late 80s by Kirkpatrick, Thirumalai and Wolynes, is the mosaic theory or the Random First Order Transition (RFOT) theory [KiTh87][KiWo87][KiWo87][KiTW89]. It considers the existence of many different states in a finite dimensional system, and so the interfaces between these amorphous configurations introduce *surface tension*. Although these amorphous states are different, they all look the same locally, thus making it impossible to distinguish them by using a standard local order parameter. This theory proposes the size of the rearranging regions to be determined by the balance between the surface tension cost and the thermodynamic gain. Beyond the differences the RFOT presents with the Adam-Gibbs theory, it recovers the main result from the latter one, namely, an increasing characteristic length scale with decreasing configurational entropy.

The Two-order Parameter model proposed by Tanaka to explain the glass transition [Tana99][Tana99] is based on the idea of two competing orderings in all the liquids: (i) the density ordering driving to crystallization and (ii) bond ordering which favors local symmetry (not always consistent with crystalline ordering). From this underlying concept, the liquid is thought to be composed of locally favored structures in a sea of normal-liquid structures.

For further details on the theories briefly discussed here, and others not included, see the review by A. Cavagna in [Cava09].

2.1.2 Entropy crisis

Below the melting temperature T_m, the specific heat of the liquid is larger than that of the crystal, as shown in Figure 2.1. If we recover the entropy definition in terms of the specific heat from Equation (2.7), we can easily calculate the excess entropy in the liquid compared to that of the crystal at temperature $T < T_\mathrm{m}$. If we decompose the temperature axis of Figure 2.1 in three parts: (i) $0 \leq T \leq T_\mathrm{g}$, (ii) $T_\mathrm{g} \leq T \leq T_\mathrm{m}$ and (iii) $T \geq T_\mathrm{m}$, we see that above T_m and below T_g the glass and crystal curves collapse. Hence we arrive to the relation

$$\Delta S_\mathrm{exc} = \Delta S_\mathrm{m} - \int_T^{T_\mathrm{m}} \frac{\Delta C_\mathrm{P}^\mathrm{liq}}{T} \mathrm{d}T \tag{2.11}$$

whcih states that the excess entropy in the liquid is consumed upon cooling it in the supercooled liquid region. The subtracting term in Equation (2.11) is nothing but the shaded area in Figure 2.1. Normalizing the excess entropy to that of the crystal and scaling the temperature to T_m, we can plot in the same graph many different substances for comparison. This was first done by Kauzmann in 1948 [Kauz48], who did a tentative extrapolation below T_g of the excess entropy curve in the liquid. He found that, for certain glass forming systems, the entropy excess is rapidly consumed, and the corresponding extrapolation leads to a zero value at finite temperatures, as shown in Figure 2.5, what entails an entropy crisis. The temperature at which the excess entropy vanishes is called Kauzmann temperature T_K. Although it can be argued that extrapolation of the liquid curve below T_g in Figure 2.5 lacks sense, together with the practical impossibility to equilibrate the system at T_K, it is the rapid approach of the entropy in some liquids to that of the crystal what really demands our attention.

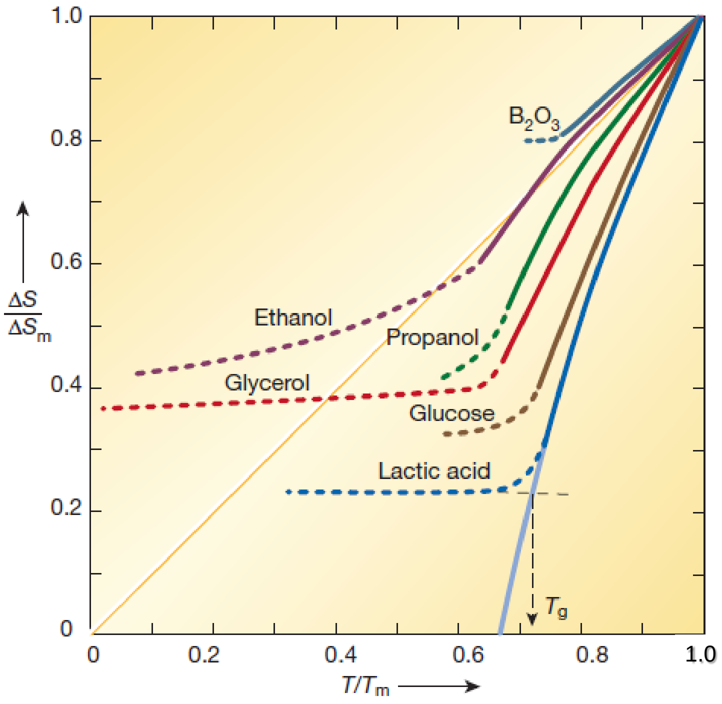

Figure 2.5 Excess entropy in the liquid normalized to that of the crystal for different substances [Kauz48][DeSt01]. Solid lines indicate the experimental data curves of the liquid, and dashed lines their extrapolation below T_g. Vanishing excess entropies are found in many systems at finite temperatures. The solid line in the diagonal of the graph is a guide to the eye, which separates liquids exhibiting normal behavior from those presenting an entropy crisis.

Recovering the idea exposed by Adam and Gibbs which assigns the excess entropy to the configurational contribution in the liquid, we find that the meaning of the Kauzmann paradox is decreasing configurational entropy as lowering the temperature. Let us go back to the view of Goldstein below T_x: the system lives most of the time vibrating around the minima in the potential energy landscape, and rarely jumps between minima. The clue is that the system is still ergodic, since we are describing the supercooled liquid, thus meaning that the system has enough time to sample the phase space, but visits less and less minima with decreasing temperature. This can be understood schematically by considering the decreasing potential energy of the system with decreasing T, and also that the number of energy minima is reduced the lower we go in the potential energy landscape. And the implication which derives from this situation when reaching T_K is that the system gets confined to a few (lowest) energy minima, of course above the crystal energy value. Whether this introduces or not a thermodynamic phase transition to the so called in the literature *ideal glass* is a matter of speculation.

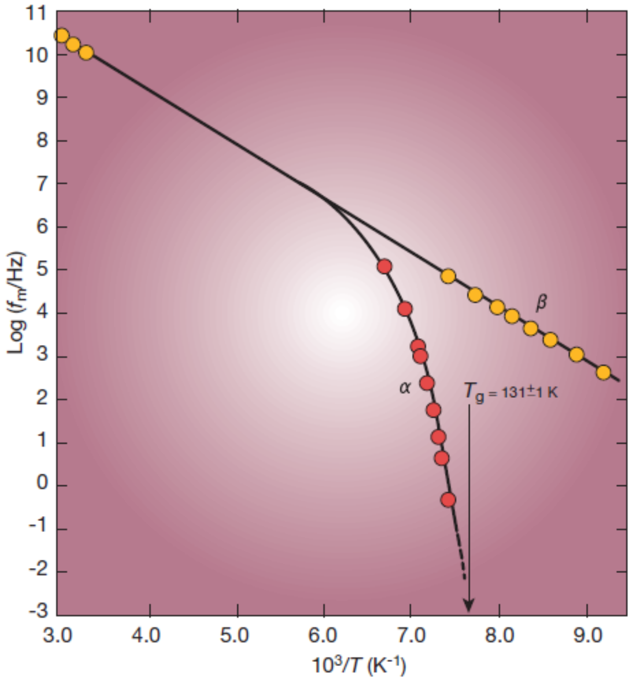

Figure 2.6 Decoupling of the relaxation processes near the glass transition at T_g as the liquid is cooled down, from [DeSt01] and references therein. The diffusive modes (α-relaxation or slow relaxation) vanish at T_g, whereas the fast modes (β-relaxation or fast relaxation) survive in the glass.

Let us remember that in the supercooled liquid, near the glass transition, the configurational changes which cause the relaxation increasingly slow down as temperature is decreased. A decoupling of the fast modes (β-relaxation) from the relaxational modes which involve diffusive motion (α-relaxation) appears as a result of the increasing viscosity of the fluid, as shown in Figure 2.6. The latter relaxation process vanishes at the glass transition, whereas the fast relaxation processes also take place in the glass, as will be reviewed in the next section.

2.1.3 Sub-T_g relaxation processes and the fictive temperature

We have already referred to the glass as a frozen liquid in the sense of a disordered solid which preserves the static structure of that in the liquid phase. But this statement goes beyond this innocent affirmation, since below the glass transition the system maintains structural relaxation mechanisms able to drive it towards lower potential energy minima in the Goldstein's view (see Figure 1.2 and Figure 2.3). This fact strengthens the idea that the glass is history-dependent, now knowing that *history* implies both the procedure to obtain the glass and the consequent route below T_g.

Three main (but not the only ones) relaxation processes can be listed to happen below the glass transition: (i) the β-relaxation (also called fast relaxation above), see Figure 2.4, which survives in the glass; (ii) the very-low-temperature anomalies, also known as the Two-Level-Systems mentioned in Section 1.2, more extensively discussed in Section 2.2.1; (iii) structural relaxations equivalent to the α-relaxation above T_g, which have been observed to produce time dependence in the thermal properties of some glass at temperatures as far as 200ºC below T_g.

The β-relaxation has associated times much shorter than the α-relaxation, and the activation energies involved are one or two orders of magnitude smaller (typically few thousandths up to some hundredths of eV). It is a local relaxation because it involves few atoms which are able to move in a relative long-range > 0.5 Å, localized and in a non-vibrational way. The origin of the β-relaxation lays on the thermal fluctuations in the liquid which are frozen in when entering the glassy phase. Thus, when the liquid is quenched, some atoms are trapped in configurations with potential energy high enough to jump between almost equivalent minima (with average equal energy values), and so to sample different configurations. In general, the β-relaxation introduces no significant contribution to the thermal properties of glasses, as no measurable effect is observed in their bulk thermodynamic properties.

We have also referred to relaxation processes far below T_g, at temperatures as low as 200ºC under the glass transition which cause structural change in the system. The energy associated to activation processes of these structural relaxations are on average one order of magnitude larger than those related to the β-relaxation, and two orders smaller than the energy related to viscous flow at T_g. It is worth saying that the times involved in these relaxations are much shorter, indeed many orders of magnitude smaller, than the extrapolations done using experimental data of shear viscosity above the glass transition. And these relaxations processes do affect the thermodynamical properties of the system, hence being observed when measuring, for example, the specific heat.

The ability of the system to seek for deeper stability below the glass transition temperature introduces an exciting phenomenon to the physics of amorphous solids: *annealing* and *ageing*. The difference between these two terms is conditioned by the human will in a way: annealing refers to processes intentionaly driven by the experimentalist, whereas ageing involves a natural process in which the conditions are not chosen by the scientist. In few words, these two mechanisms allow us to study the equivalent glasses we would obtain after infinitely slow-enough cooling of the liquid.

Liberation of enthalpy in the annealing and ageing processes is observed when driving the glass to T_g, since the enhanced stability achieved manifests as an increased specific heat in the surroundings of the glass transition. Although we have said above that the time scales of the structural relaxations far below T_g are much shorter than the extrapolations done with the supercooled liquid data, they increase with increasing annealing or ageing, this is, as the glass is further driven into more stable configurations.

A central concept of the physics in glasses that involves the relaxation processes is the *fictive temperature* T_f, which somehow quantifies the state of the glass, taking into account its behavior as a frozen liquid. It was first defined by A. Q. Tool in 1946 [Tool46] as the actual temperature at which a non-equilibrium state and its equilibrium (liquid) state have the same structure. It is built in terms of extrapolations of the glass and the fluid, since T_f is defined as the temperature at which the glass and the liquid would have the same structure. It is not a unique quantity when talking about different properties, and consequently one must strictly talk about the fictive temperature of the property under consideration. Nevertheless, it is quite extended to talk about the fictive temperature in general referred to that calculated from the enthalpy curves, as shown in Figure 2.7.

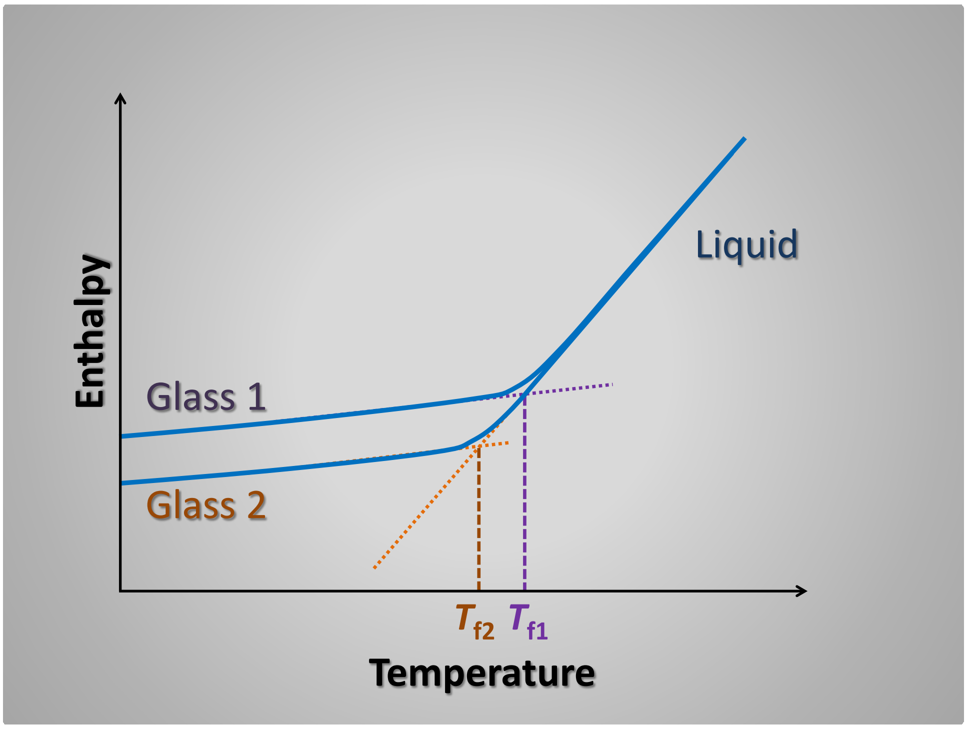

Figure 2.7 Fictive temperature determination in the enthalpy curve from the extrapolations of the glass and liquid curves far away from the glass transition. Different glasses have different fictive temperature as a result of their different configuration.

From a practical point of view, the fictive temperature is that at which, after equilibrating the supercooled liquid as long as required, we would quench it infinitely fast and have the equivalent frozen structure in the glass.

2.2 The low-temperature properties of glasses and amorphous solids

We already introduced in Chapter 1 a brief description of the phenomenology found in glasses at low-temperature/low-energy, as discovered in chronological order after 1970. In this section we will give theoretical groundings in order to understand these universal properties of glasses, together with a discussion about the different views on the topic.

The low-temperature universal properties of glasses are usually introduced differentiating two temperature ranges, below and above 1 K. We start with the description of the Tunneling Model (TM) and the derivation of the temperature dependence of the thermal and acoustic properties below 1 K in terms of the relevant parameters introduced in the model. Connected to some extent to the ideas of the TM, we discuss the Soft Potential Model and its predictions of the glassy properties above 1 K or frequencies in the THz range. This range corresponds to the boson peak regime, for which a theoretical framework (the Soft Potential Model) has been developed as an extension of the widely accepted Tunneling Model, used for the understanding of the physics in glasses below 1 K. Nevertheless, other theoretical views have appeared in the last two decades which try to explain the physics associated to the boson peak, a topic of intense debate in recent years. Further theories such as the Random Elastic Matrix Theory and the possible correspondence of the boson peak with the Ioffe-Regel limit are briefly discussed for completion.

2.2.1 The Two-Level Systems and the Tunneling Model

Low-temperature properties in glasses exhibit a universal deviation from the Debye prediction, which so successfully explains the physics in crystalline solids derived from the phonon behavior. At temperatures below 1 K, the specific heat of glasses decreases considerably more slowly than in crystals as shown in Figure 2.8, with a temperature dependence of the form

$$C_P(T) \approx aT + bT^3 \tag{2.12}$$

with a and b constants, b larger than the value predicted from the Debye model. Consistently with this, the thermal conductivity in glasses presents no peak at low temperatures as crystal do, but a monotonic decrease with decreasing temperature of the form $\kappa \sim T^2$. Besides, the thermal conductivity of glasses is always below their crystalline counterparts at low temperatures, as illustrated in Figure 2.8. Acoustic and dielectric losses in amorphous solids present high values, in contrast to their vanishing behavior in crystals below liquid helium temperatures.

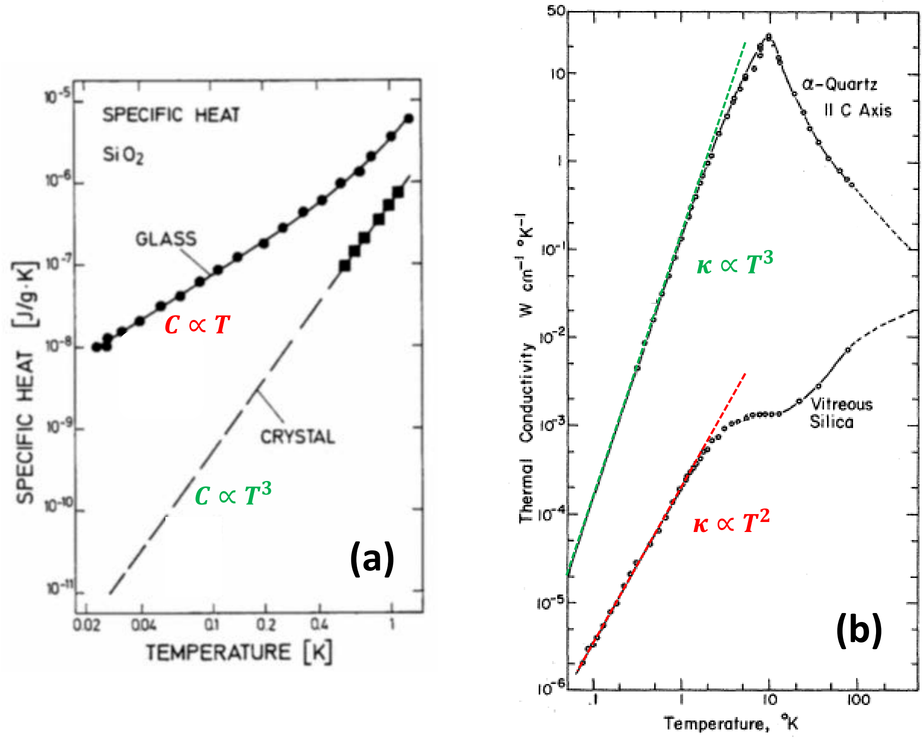

Figure 2.8 Comparison of the (a) specific heat and (b) thermal conductivity [ZePo71] in vitreous silica at low temperatures with quartz, its crystalline phase. The temperature dependence below 1 K due to two-level tunneling systems is highlighted on both (a) and (b).

In Figure 2.8a specific heat data of vitreous silica are compared to those of crystalline quartz. The excess in the specific heat shows a similar behavior to that of some dielectric crystals with defects, as for example in the mixed crystal KBr:KCl doped with KCN in [Wats95]. Although fundamental differences exist between both solids, it is the existence of tunneling systems which introduces the enhancement in their specific heat. In glasses, it is generally accepted that the low-temperature properties are determined by two-level tunneling systems, whose description is done in terms of a double-well potential as shown in Figure 2.9a.

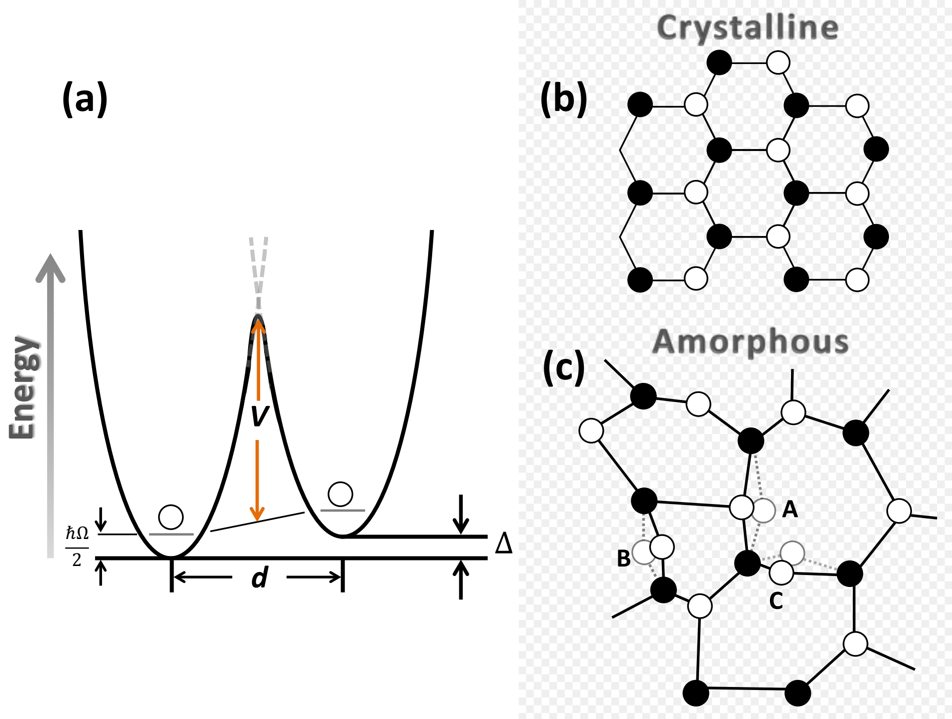

Figure 2.9 Two-level tunneling systems description in terms of the double-well potential (a) where the energy asymmetry Δ and the energy barrier *V* are presented. Particles involved may be formed by several atoms, thus *d* refers to a general coordinate. Two-dimensional description of the lattice in (b) crystalline silica, compared to (c) the disorder present in amorphous silica where different two-level tunneling sites. Solid circles correspond to silicon atoms and open circles to oxygen ones.

The requisite to find tunneling systems is the existence of some kind of disorder. Thus, they are also found in crystals which present dislocations or vacancies, for example, and in all amorphous solids. Nevertheless, the tunneling model predicts well the phenomenology only in amorphous solids. This results from the starting assumption of the tunneling model that the energy distribution of the two level systems is homogeneous, what does not apply to crystalline solids, in which dislocations are centered on an specific energy. They emerge from the possibility of an atom or a group of atoms to occupy two almost energetically equivalent positions in the disordered lattice, as those labeled as A, B and C in Figure 2.9c. In order to *jump* between the two configurations, the particle has to cross the energy barrier V in Figure 2.9a. Notice that we are using the term *particle* which can refer to individual atoms or groups of atoms, thus d is a general coordinate. An asymmetry Δ between the two configurations exists, which accounts for the energy difference between the two configurations. The two-level tunneling processes are not restricted to translational movements, but also rotations may appear.

Soon after the shocking results derived from the measurements on glasses at low temperatures by Zeller and Pohl [ZePo71] in 1971, Phillips [Phil72] and Anderson, Halperin and Varma [AnHV72] developed the phenomenological tunneling model in 1972. Having in mind the disordered lattice of amorphous solids in Figure 2.9c, we can consider a broad distribution in the asymmetry Δ as well as in the tunneling parameter λ

$$P(\Delta, \lambda)\ \mathrm{d}\Delta\ \mathrm{d}\lambda = P_0\ \mathrm{d}\Delta\ \mathrm{d}\lambda \tag{2.13}$$

where P_0 is constant and λ is given in terms of the energy-barrier parameters and the particle mass

$$\lambda \approx \frac{d}{2\hbar}\sqrt{2mV} \tag{2.14}$$

The two-level systems present in the solid coexist with the acoustic waves, which modify the double-well potential by changing the energy asymmetry Δ in Figure 2.9a. In order to evaluate this, the coupling between the asymmetry and tension ϵ_{j} generated by the elastic acoustic waves must be done, from which we have the coupling constant

$$\gamma_j = \frac{1}{2}\frac{\partial \Delta}{\partial \epsilon_j} \tag{2.15}$$

where *j* stands for the longitudinal *l* and transverse *t* acoustic waves.

We consider one-phonon processes, this is, the interaction of the two-level tunneling systems with the acoustic waves takes place with only one phonon at a time. The relaxation time of the tunneling state is then

$$\tau^{-1} = \left(\frac{\gamma_l^2}{v_l^2} + 2\frac{\gamma_t^2}{v_t^2}\right)\frac{E^3}{2\pi\rho\hbar^4}\left(\frac{\Delta_0}{E}\right)^2 \coth\left(\frac{E}{2k_\mathrm{B}T}\right) \tag{2.16}$$

with v_l and v_t the longitudinal and transverse sound velocities, respectively, and ρ the mass density of the solid.

We rewrite Equation (2.13) in terms of the energy $E = (\Delta^2 + \Delta_0^2)^{1/2}$ and the relaxation time τ, so that an expression for the specific heat can be calculated, and so direct comparison with the experiment is possible. This is done using a Jacobian transformation of Equation (2.13), and taking into account $\Delta_0 = \hbar\Omega\ \mathrm{e}^{-\lambda}$

$$P(E,\tau)\mathrm{d}\tau\ \mathrm{d}E = P(\Delta,\lambda)\left|\frac{\partial\Delta}{\partial E}\right|\left|\frac{\partial\lambda}{\partial\tau}\right|\mathrm{d}\tau\ \mathrm{d}E \tag{2.17}$$

and so results

$$P(E,\tau) = \frac{P_0}{2\tau\sqrt{1-\frac{\tau_\mathrm{min}(E)}{\tau}}} \tag{2.18}$$

As shown in Equation (2.16), the relaxation time τ depends on the ratio (E / Δ_0), which is minimum τ_min when asymmetry $\Delta = 0$, thus $(E / \Delta_0) = 1$, in the case of symmetric potentials in Figure 2.9a. On the other hand, τ can be infinitely high for increasing asymmetries.

When performing specific heat measurements we see only those tunneling systems with relaxation times faster than the experimental time t_0, and so the effective density of states taken into account is

$$D_{eff}(E,t_0) = \int_{\tau_\mathrm{min}}^{t_0} P(E,\tau)\mathrm{d}\tau = \frac{P_0}{2}\ln\left(\frac{4t_0}{\tau_\mathrm{min}}\right) \tag{2.19}$$

The free energy F of a two-level system is given as $F(E) = -k_B T \ln[\cosh(E/2k_B T)]$, and specific heat is derived from it as $-T(\partial^2 F/\partial T^2)$. Using the effective density of states in Equation (2.19), and integrating in the whole energy spectrum, we arrive to

$$C_\mathrm{p} \cong C_\mathrm{v} = \int_0^\infty D_{eff}(E,t_0)\frac{\left(\frac{E}{2k_BT}\right)^2}{\cosh^2\left(\frac{E}{2k_BT}\right)^2}dE = \frac{\pi^2}{12}P_0 k_B T\ \ln\left(\frac{4t_0}{\tau_\mathrm{min}}\right) \tag{2.20}$$

where the linear dependence with temperature observed in the experiments is already present. A weak logarithmic correction appears with increasing measuring time t_0.

Under some conditions the relaxation times distribution is not relevant, and thus only the energy of the two-level systems appears in the equations. Considering the energy density constant $n(E) \approx n_\mathrm{TLS}$, we reach a relation for the specific heat only in terms of the temperature

$$C_\mathrm{p} \cong C_\mathrm{v} = \frac{\pi^2}{6}P_0 k_B T \tag{2.21}$$

From the specific heat, together with the mean free path l at low temperature, we can further calculate the thermal conductivity κ, which, as shown in Figure 2.8b, presents a quadratic dependence with temperature. The mean free path in this temperature range is dominated by the resonant scattering of the phonons due to the presence of tunneling systems

$$l_{j,\mathrm{res}}^{-1}(\omega) = \frac{\pi\gamma_j^2\omega}{\rho v_j^3}P_0 \tanh\left(\frac{\hbar\omega}{2k_BT}\right) \tag{2.22}$$

where again j stands for the longitudinal and transverse modes. Taking Equation (2.22) in the thermal conductivity definition, we have

$$\kappa = \frac{1}{3}\sum_j \int_0^{\omega_{Debye}} C_{Debye}(\omega,T) v_j l_j(\omega)\,\mathrm{d}\omega =$$

$$= \frac{\rho k_B^3}{6\pi\hbar^2}\left(\sum_j \frac{v_j}{P_0\gamma_j^2}\right)T^2 \tag{2.23}$$

where the quadratic dependence with temperature appears straightforward.

2.2.2 The Soft-Potential Model

In order to account for the glassy anomalies above 1 K, i.e., the broad maximum in the C_P/T^3 representation of the specific heat as well as the plateau in thermal conductivity, further theoretical work was needed, since the Tunneling Model did not predict this behavior. This fact reveals that the existence of low-barrier relaxational modes alone is not enough to understand the excess modes at higher frequencies (around 1 THz) present in glasses. Two powerful reasons exist indeed to extend the standard tunneling model to higher temperatures. The first one has been already exposed: the breakdown of the model above 1 K. The second exploits the theoretical arguments of the tunneling model. It is quite hard to imagine in the frame of a disordered lattice the double-well potentials shown in Figure 2.9a not exhibiting energy barriers down to zero. On the one hand the barrier heights involved in these potentials have energies of $V \sim 100$ K, much lower than the thermal energy at the glass transition; on the other hand, the asymmetries between the two wells are restricted to energies $\Delta \leq 1$ K.

The soft-potential model was first proposed by Karpov, Klinger and Ignat'ev in 1983 [KaKI83] as an extension of the standard tunneling model, capable of explaining the observed deviations at higher temperatures. It was further developed in 1987 [IlKP87] by Il'in, Karpov and Parshin. The key assumption of the model is the existence of a large number of local modes with very small or even negative restoring force constant, from which the tunneling systems are only a minuscule part. As derived from the construction of the model, it provides a similar prediction for the anomalies in glasses below 1 K as the standard tunneling model. The crossover between the tunneling-states-dominated region and the soft-modes-dominated one is most clearly seen in the specific-heat measurements. In the reduced representation C_P/T^3 a decrease as T^{-2} (corresponding to $C \sim T$) is observed, followed by a minimum and a T^2 like increase (corresponding to a $C \sim T^5$), as shown in Figure 2.10. The Debye contribution calculated from the sound velocities has been subtracted, so only the excess specific heat due to the glassy anomalies is shown. The extrapolations of both temperature dependences intersect at T^* which corresponds to the temperature of the minimum T_{min} (except for the Suprasil W which still presents extra excitations that shift the minimum location towards higher temperature). The location of the minimum determines quantitatively the crossover between the two regions mentioned above.

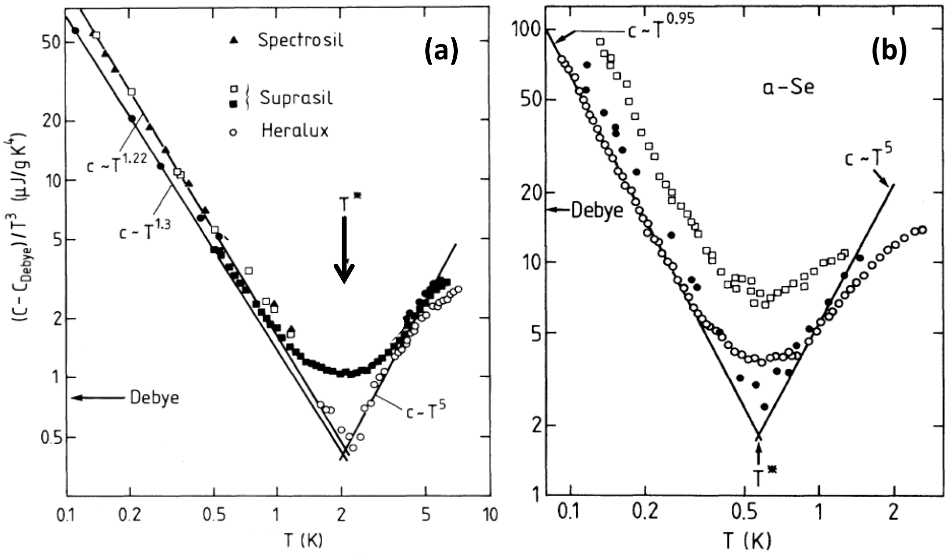

Figure 2.10 Specific heat of different (a) SiO_2 and (b) Se glasses shown in the C_P/T^3 representation with double logarithmic scale, where the Debye contribution C_{Debye} (indicated with the arrow on the left axis) has been subtracted. The temperature T^* indicates the minimum position in this representation. See [Ubuc91] and references therein.

Although not so clear, this crossover can be seen in the thermal conductivity as well shown in Figure 2.8b, given by the temperature at which the tendency changes from the T^2 dependence to the plateau region.

We have already proposed excess quasi-local vibrational modes as candidates to explain the excess in the specific heat above the crossover determined in Figure 2.10. And we have also introduced the idea of double-well potentials with energy-barrier distributions down to zero, what clearly invites us to think about anharmonic quartic potentials as candidates to describe these localized modes with very weak or even negative restoring force.

The atomic motion can be described by its eigenvector $\mathbf{e}_i$ in a local mode, with $i = 1,..N$ denoting the N atoms in the glass. This eigenvector fulfills the normalization conditions, thus $\Sigma_i\ \mathbf{e}_i^2 = 1$. We can then write the atomic displacement u_i of a particular atom I in terms of the mode amplitude A

$$\mathrm{u}_i = \sum_{i=1}^{N} \frac{\mathrm{e}_i}{\sqrt{M_i}} A \tag{2.24}$$

where Mi is the mass of the atom i. We have soft localized modes, so the displacements of the atoms will be large, thus the anharmonic terms have to be taken into account, which become even essential in the case of negative restoring forces in order to stabilize the mode. If we write the pure quartic potential

$$V(A) = \frac{v_4}{4} A^4 \tag{2.25}$$

Calculation of the zero-point energy in the quartic potential can be done equating the potential energy at a normal coordinate displacement A_0 to a kinetic confinement energy. This relation defines the first (and most relevant) parameter in the soft-potential model, the energy W, which determines the crossover between the tunneling and vibrational motion

$$\frac{\hbar^2}{2A_0^2} = \frac{v_4}{4} A_0^4 \equiv W \tag{2.26}$$

A generalized dimensionless coordinate $x = A/A_0$ is built in the soft-potential model. Introducing the restoring-force and the finite asymmetry in the potential, and neglecting higher order terms than the fourth order, we can write the potential due to the soft mode in terms of the displacement coordinate x as

$$V(x) = W(D_1 x + D_2 x^2 + x^4) \tag{2.27}$$

The origin is chosen so that the cubic term vanishes. D_1 determines the potential asymmetry and D_2 accounts for the small positive or negative restoring force. These two coefficients regulate whether we have a tunneling state, a soft vibration or a relaxational mode (jumping above the energy barrier instead of tunneling through it). This means that the D_1-D_2 space is separated in regions in which vibrations or tunneling states dominate, as shown in Figure 2.11

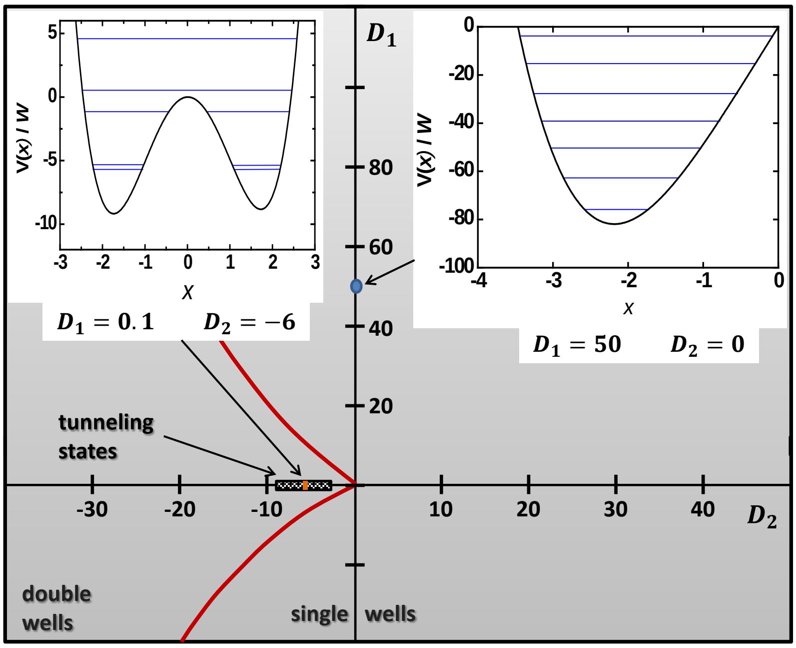

Figure 2.11 D_1-D_2 plane of the soft-potential model, where the regions of single- and double-well potentials are presented. Inserts show the typical form and energy level of the potential corresponding to (left) a tunneling state and (right) a vibrational state. [RGBB93][RaBu98].

The assumptions widely acknowledged by the scientists working with the soft-potential model can be enumerated in three points: (i) the soft modes can be characterized on average by a single energy W; (ii) the parameters D_1 and D_2 are randomly distributed around the origin of the D_1-D_2 plane in Figure 2.11, with density $P(D_1,D_2) = P(0,0) \equiv P_s$; (iii) the interaction between the soft modes and the sound waves is bilinear in the displacement of the soft mode and in the strain field of the sound wave. On average, the coupling can be described by the two coupling constants Λ_l and Λ_t, with $\delta V_l = \Lambda_l x \epsilon_l$ and $\delta V_t = \Lambda_t x \epsilon_t$ the modification in the energy and ϵ_j $j = l,t$ the longitudinal/shear strain field of a longitudinal/shear sound wave.

In order to calculate the total specific heat within the soft-potential model, the contributions due to the tunneling states and the vibrational states must be added to the phonons specific heat given by the Debye contribution

$$C_{\mathrm{Debye}} = \frac{2\pi^2}{5}\left(\frac{k_B^4}{\hbar^3 \rho v_D^3}\right) T^3 \tag{2.28}$$

with v_D the Debye-averaged sound velocity $1/v_D^3 = 1/3(1/v_L^3 + 2/v_T^3)$. Those low-energy excitations coexist with the lattice vibrations given in Equation (2.28).

The analytical description of the tunneling states in the soft-potential model is based on the concepts of the standard tunneling model. This means that similar results are obtained in the regions dominated by tunneling states. To write the density of tunneling states within the soft-potential mode, a very appropriate combination of variables to choose is that given by the total energy separation between levels E

$$E = \sqrt{\Delta_0^2 + \Delta^2} \tag{2.29}$$

And the dimensionless parameter

$$u = \frac{\Delta_0}{E} \tag{2.30}$$

Writing the energy splitting Δ_0 and the energy asymmetry Δ in terms of the soft-potential model parameters

$$\Delta_0 = W|D_2|^{3/2} \exp\left(1 - \frac{\sqrt{2}}{3}|D_2|^{3/2}\right) \tag{2.31}$$

$$\Delta = W D_1 \sqrt{2(|D_2| - 1)} \tag{2.32}$$

We have the density of tunneling states is found to be approximately [RGBB93][RaBu98]

$$P(E,u) \cong \left(\frac{2}{9}\right)^{1/3} \frac{P_s}{W} \frac{1}{u\sqrt{1-u^2}} \ln^{-2/3}(40W/Eu) \tag{2.33}$$

which has very weak energy dependence.

The specific heat contribution of the tunneling states in the frame of the soft-potential model is thus found to be

$$C_{\mathrm{P,TLS}}(T) \cong \frac{\pi^2}{6}\left(\frac{1}{9}\right)^{1/3}\frac{P_s}{W}k_B^2 T \ln^{1/3}\left(\frac{t_0}{\tau_{\min}(k_B T)}\right) \tag{2.34}$$

The additional contribution to the specific heat introduced by the harmonic vibrational soft modes in the single-well potentials described in the right side of Figure 2.11 is the most relevant prediction of the model. The density of states of these soft-modes can be found to be

$$g_s(h\nu) = \frac{P_s}{8W}\left(\frac{h\nu}{W}\right)^4 \tag{2.35}$$

Taking into account that the heat capacity C_h of a single harmonic oscillator is given by

$$C_h(x) = k_B \frac{x^2 e^{-x}}{(1-e^{-x})^2} \tag{2.36}$$

where here $x = \hbar\omega/k_\mathrm{B}T$. Integrating over the whole frequency spectrum, the specific heat of the quasi-harmonic soft-vibrations can be evaluated by

$$C_{\mathrm{P},s} = \int_0^\infty C_h(x)\, g_s(h\nu)\, \mathrm{d}\nu = \frac{2\pi^6}{21} P_\mathrm{s} k_B \left(\frac{k_B T}{W}\right)^5 \tag{2.37}$$

Putting together all the contributions introduced by the Soft-Potential Model given by the tunneling states in Equation (2.34), the Debye contribution in Equation (2.28) and the quasi-harmonic soft vibrations in Equation (2.37), the specific heat at low temperatures within the SPM is

$$C_\mathrm{P}(T) = c_\mathrm{TLS} T + c_\mathrm{D} T^3 + c_\mathrm{sm} T^5 \tag{2.38}$$

where c_TLS, c_D and c_sm include all the temperature-independent constants in the tunneling-systems, Debye and soft-modes contributions, respectively.

The Soft-Potential Model is able to predict the plateau in the thermal conductivity at temperatures T ~ 10 K as well. Taking again the definition of the thermal conductivity given in Equation (2.23), and considering that the phonon mean-free-path can be subdivided into the three contributions corresponding to sound-wave resonant scattering by tunneling states, quasi-localized soft-modes and classical relaxation processes [BGGP92][RaBu98]

$$l_j^{-1} = l_{\text{res,tunn}}^{-1} + l_{\text{rel,class}}^{-1} + l_{\text{res,vib}}^{-1} \tag{2.39}$$

Let us now describe the mean free path for each contribution. For the resonant scattering by the tunneling states we have

$$l_{\text{res,tunn}}^{-1} = \frac{\pi\omega C_j^{tunn}}{v_j} \tanh\left[\frac{\hbar\omega}{2k_BT}\right] \tag{2.40}$$

where *j* stands for *l* and *t*, longitudinal and transversal sound waves respectively, and with $C_j^{\text{tunn}} = P_0\gamma_j^2/\rho v_j^2$.

The mean free path of the sound waves influenced by the classical relaxation processes in asymmetric double-well potentials is given by

$$l_{\text{res,class}}^{-1} = \frac{\pi\omega C_j}{v_j}\left(\frac{k_BT}{W}\right)^{3/4} \ln^{-1/4}(1/\omega\tau_0) \tag{2.41}$$

where

$$C_j = \frac{P_s\Lambda_j^2}{W\rho v_j^2} \tag{2.42}$$

with $j = l,t$.

Finally, the mean free path for the resonant scattering from the localized vibrations follows the relation

$$l_{res,vib}^{-1} = \frac{\pi\omega C_j}{v_j}\frac{1}{8}\left(\frac{\hbar\omega}{W}\right)^3 \tag{2.43}$$

The number density of sound waves per unit volume and frequency interval dω is given by

$$n_l = \frac{\omega^2}{2\pi^2 v_l^3} \qquad n_t = \frac{\omega^2}{\pi^2 v_t^3} \tag{2.44}$$

Inserting this in Equation (2.23) we get

$$\kappa = \frac{1}{6\pi^2}\int_0^\infty \mathrm{d}\omega\,\omega^2 C_h(x)\left(\frac{l_l}{v_l^2} + \frac{2l_t}{v_t^2}\right) \tag{2.45}$$

Introducing Equations (2.40), (2.41) and (2.43) in Equation (2.45), using the dimensionless variables $x = \hbar\omega/k_\mathrm{B}T$ and $z = k_\mathrm{B}T/W$, we obtain

$$\kappa = \frac{2k_B}{3\pi}\left(\frac{W}{h}\right)^2\left(\frac{1}{C_l v_l} + \frac{2}{C_t v_t}\right)F(z) \tag{2.46}$$

with

$$F(z) = \int_0^\infty dx\,\frac{x^3 e^{-x}}{(1-e^{-x})}\,\frac{z^2}{1.1\tanh(x/2)+0.7z^{3/4}+x^3z^3/8} \tag{2.47}$$

that can be numerically evaluated, and is well approximated in the relevant range $k_\mathrm{B}T \leq 4W$ by

$$F(z) = \frac{9z^2}{1.1+0.7z+3z^2} \tag{2.48}$$

Defining an average $\bar{C}$

$$\bar{C} = \frac{1/v_l+2/v_t}{1/C_l v_l+2/C_t v_t} \tag{2.49}$$

the final equation for the thermal conductivity is reached

$$\kappa = \frac{6k_B}{\pi\bar{C}}\left(\frac{W}{h}\right)^2\left(\frac{1}{v_l} + \frac{2}{v_t}\right)\frac{9z^2}{1.1+0.7z+3z^2} \tag{2.50}$$

for which the plateau is reached roughly for $k_BT > 2W$. In order to determine the soft-potential parameter W from thermal conductivity data is to plot κ/T versus temperature and look for the maximum T_{max}, since

$$W \cong 1.6\ k_B T_{\mathrm{max},\kappa} \tag{2.51}$$

For further details and a complete introduction to the soft-potential model see [RaBu98].

2.2.3 Other theoretical views

We have discussed above two phenomenological models which are of great utility in the understanding of the low-temperature anomalies of glasses and provide a powerful tool to compare with the experimental data. Nevertheless, many other theoretical views on these properties do exist which are not introduced here. For completion, we enumerate some of the models or theories most commonly found in the literature of glasses nowadays, which try to explain the enhanced C_P/T^3 over the Debye level known as the boson peak. Although further explanations different to the standard tunneling model do exist, it is widely accepted and no such big controversy exists as that related to the boson peak. This hence justifies that only different views on the physics involved in the boson peak are taken into consideration here.

The Random Elastic Matrix Theory (REMT) developed by Schirmacher and coworkers in recent years [ScDG98][Schi06][ScRS07] is based on the assumption that the disorder leads to microscopic random spatial fluctuations on the transverse elastic constant (the shear modulus). Consequently, the excess density of states (DOS) arises from a band of disorder-induced irregular vibrational states. The onset of this band is found to approach lower frequencies the higher the disorder is.

Quite recently, an experimental work by Chumakov *et al.* [CMMC11] has been reported on one sodium silicate glass which presents a gradual transformation of the boson peak into the transverse acoustic van Hove singularity in the crystal. Although these results give support to the view introduced by the REMT, additional quasi-localized modes are not excluded to appear, which in the silicate glass appear as librations of SiO_2 tetrahedra.

Another related issue which has recently appeared is the Ioffe-Regel limit and its apparent relation to the boson-peak frequency. The Ioffe-Regel limit describes the phonon frequency at which the phonon mean-free path l has decreased to half the wavelength λ. Many authors claim to have found the $\omega^{\mathrm{IR}} \approx \omega^{\mathrm{BP}}$, what in some cases only stands for the transverse phonons [PaLa01][RGCV06][BWOF07][ShTa08].

The theory of *vibrational instability* of weakly-interacting quasilocal harmonic modes gives further support to the SPM views, and accounts for the appearance of the maximum in the reduced vibrational density of states (VDOS), this is, the boson peak.

[AdGi65] G. Adam and J. H. Gibbs, “On the Temperature Dependence of Cooperative Relaxation Properties in Glass-Forming Liquids,” The Journal of Chemical Physics, vol. 43, no. 1, pp. 139–146, 1965.

[Ange91] C. A. Angell, “Relaxation in liquids, polymers and plastic crystals—strong/fragile patterns and problems”, Journal of Non-Crystalline Solids, vol. 131, pp. 13–31, 1991.

[Ange95] C. A. Angell, “Formation of glasses from liquids and biopolymers”, Science, vol. 267, no. 5206, pp. 1924–35, Mar. 1995.

[Ange97] C. A. Angell, “Entropy and fragility in supercooling liquids”, Journal of Research of the National Institute of Standards and Technology, vol. 102, no. 2, p. 171, Mar. 1997.

[AnHV72] P. W. Anderson, B. I. Halperin and C. M. Varma, “Anomalous low-temperature thermal properties of glasses and spin glasses”, Philosophical Magazine, vol. 25, no. 1, pp. 1–9, 1972.

[BGGP92] U. Buchenau, Y. M. Galperin, V. L. Gurevich, D. A. Parshin, M. A. Ramos and H. R. Schober, “Interaction of soft modes and sound waves in glasses”, Physical Review B, vol. 46, no. 5, pp. 2798 – 2808, 1992.

[BWOF07] U. Buchenau, A Wischnewski, M. Ohl and E. Fabiani, “Neutron scattering evidence on the nature of the boson peak”, Journal of Physics: Condensed Matter, vol. 19, no. 20, p. 205106, 2007.

[Cava09] A. Cavagna, “Supercooled liquids for pedestrians”, Physics Reports, vol. 476, no. 4–6, pp. 51–124, 2009.

[CMMC11] A. I. Chumakov, G. Monaco, A. Monaco, W. A. Crichton, A. Bosak, R. Rüffer, A. Meyer, F. Kargl, L. Comez, D. Fioretto, H. Giefers, S. Roitsch, G. Wortmann, M. H. Manghnani, A. Hushur, Q. Williams, J. Balogh, K. Parliński, P. Jochym and P. Piekarz, “Equivalence of the Boson Peak in Glasses to the Transverse Acoustic van Hove Singularity in Crystals”, Physical Review Letters, vol. 106, no. 22, p. 225501, 2011.

[CoTu59] M. H. Cohen and D. Turnbull, “Molecular Transport in Liquids and Glasses”, The Journal of Chemical Physics, vol. 31, no. 5, pp. 1164–1169, 1959.

[DeSt01] P. G. Debenedetti and F. H. Stillinger, “Supercooled liquids and the glass transition”, Nature, vol. 410, no. 6825, pp. 259–67, 2001.

[Gold69] M. Goldstein, “Viscous Liquids and the Glass Transition: A Potential Energy Barrier Picture”, The Journal of Chemical Physics, vol. 51, no. 9, pp. 3728–3739, 1969.

[IlKP87] M. A. Ill’in, V. G. Karpov, and D. A. Parshin, “Parameters of soft atomic potentials in glasses”, Soviet Physics - JETP, vol. 65, no. 1, pp. 165–168, 1987.

[KaKI83] V. Karpov, M. Klinger, and F. Ignat’ev, “Theory of the low-temperature anomalies in the thermal properties of amorphous structures”, Zh. Eksp. Teor. Fiz, vol. 84, pp. 439 – 448, 1983.

[Kauz48] W. Kauzmann, “The Nature of the Glassy State and the Behavior of Liquids at Low Temperatures”, Chemical Reviews, vol. 43, no. 2, pp. 219–256, 1948.

[KiTh87] T. Kirkpatrick and D. Thirumalai, “Dynamics of the structural glass transition and the p-spin—interaction spin-glass model”, Physical Review Letters, vol. 58, no. 20, pp. 2091–2094, 1987.

[KiTW89] T. Kirkpatrick, D. Thirumalai and P. Wolynes, “Scaling concepts for the dynamics of viscous liquids near an ideal glassy state”, Physical Review A, vol. 40, no. 2, 1989.

[KiWo87] T. Kirkpatrick and P. Wolynes, “Connections between some kinetic and equilibrium theories of the glass transition”, Physical Review A, vol. 35, no. 7, pp. 3072–3080, 1987.

[KiWo87] T. Kirkpatrick and P. Wolynes, “Stable and metastable states in mean-field Potts and structural glasses”, Physical Review B, vol. 36, no. 16, pp. 8552–8564, 1987.

[KoAn95] W. Kob and H. Andersen, “Testing mode-coupling theory for a supercooled binary Lennard-Jones mixture. II. Intermediate scattering function and dynamic susceptibility”, Physical Review E, vol. 52, no. 4, 1995.

[LaUh72] W. T. Laughlin and D. R. Uhlmann, “Viscous flow in simple organic liquids”, The Journal of Physical Chemistry, vol. 76, no. 16, pp. 2317–2325, 1972.

[PaLa01] D. Parshin and C. Laermans, “Interaction of quasilocal harmonic modes and boson peak in glasses”, Physical Review B, vol. 63, no. 13, p. 132203, 2001.

[Phil72] W. A. Phillips, “Tunneling states in amorphous solids”, Journal of Low Temperature Physics, vol. 7, no. 3–4, pp. 351–360, 1972.

[RaBu98] M. A. Ramos and U. Buchenau, “Beyond the standard tunneling model: The soft potential model”, in *Tunneling systems in amorphous and crystalline solids*, P. Esquinazi, Ed. Springer, 1998.

[RGBB93] M. Ramos, L. Gil, A. Bringer and U. Buchenau, “The Density of Tunneling and Vibrational States of Glasses within the Soft-Potential Model”, Physica Status Solidi (a), vol. 135, no. 477, 1993.

[RGCV06] B. Rufflé, G. Guimbretière, E. Courtens, R. Vacher and G. Monaco, “Glass-Specific Behavior in the Damping of Acousticlike Vibrations”, Physical Review Letters, vol. 96, no. 4, p. 045502, 2006.

[ScDG98] W. Schirmacher, G. Diezemann and C. Ganter, “Harmonic vibrational excitations in disordered solids and the ‘boson peak’”, Physical Review Letters, vol. 81, no. 1, pp. 136 – 139, 1998.

[Schi06] W. Schirmacher, “Thermal conductivity of glassy materials and the ‘boson peak’”, Europhysics Letters (EPL), vol. 73, no. 6, pp. 892–898, 2006.

[ScRS07] W. Schirmacher, G. Ruocco and T. Scopigno, “Acoustic Attenuation in Glasses and its Relation with the Boson Peak”, Physical Review Letters, vol. 98, no. 2, p. 025501, 2007.

[ShTa08] H. Shintani and H. Tanaka, “Universal link between the boson peak and transverse phonons in glass”, Nature Materials, vol. 7, no. 11, pp. 870–877, 2008.

[Tana99] H. Tanaka, “Two-order-parameter description of liquids. I. A general model of glass transition covering its strong to fragile limit”, The Journal of Chemical Physics, vol. 111, no. 7, pp. 3163–3174, 1999.

[Tana99] H. Tanaka, “Two-order-parameter description of liquids. II. Criteria for vitrification and predictions of our model”, The Journal of Chemical Physics, vol. 111, no. 7, pp. 3175–3182, 1999.

[Tool46] A. Q. Tool, “Relation between inelastic deformability and thermal expansion of glass in its annealing range”, Journal of American Ceramics Society, vol. 29, no. 9, p. 240, 1946.

[TuCo61] D. Turnbull and M. H. Cohen, “Free-Volume Model of the Amorphous Phase: Glass Transition”, The Journal of Chemical Physics, vol. 34, no. 1, pp. 120–125, 1961.

[TuCo70] D. Turnbull and M. H. Cohen, “On the Free-Volume Model of the Liquid-Glass Transition”, The Journal of Chemical Physics, vol. 52, no. 6, pp. 3038–3041, 1970.

[Ubuc91] U. Buchenau, Yu. M. Galperin, V. L. Gurevich and H. R. Schober, “Anharmonic potentials and vibrational localization in glasses”, Physical Review B, vol. 43, no. 6, pp. 5039–5045, 1991.

[Wats95] S. Watson, “Tunneling states in crystals with large random strains,” Physical Review Letters, vol. 75, no. 10, pp. 1965–1968, 1995.

[ZePo71] R. C. Zeller and R. O. Pohl, “Thermal conductivity and specific heat of non-crystalline solids”, Physical Review B, vol. 4, no. 6, 1971.

[ZhSM13] J. Zhao, S. L. Simon and G. B. McKenna, “Using 20 Million Year Old Amber to Test the Super-Arrhenius Behavior of Glass Forming Systems”, Nature Communications, 2013.

3

EXPERIMENTAL TECHNIQUES

The experimental efforts of this thesis have been focused on the development of a versatile low-temperature calorimeter for solid samples, able to resolve down to tens of nJ/K at very low temperatures, and with a wide temperature working range from 50 mK up to 40 K typically, even with the possibility to measure up to room temperature. These features have allowed us to perform specific heat measurements on samples with masses down to few milligrams, and with a rich variety of physical properties, from dielectric glasses -which present enhanced difficulties in thermalizing at very low temperatures-, to semimetals or superconductors… Developing this experimental system comprises from the construction and calibration of thermometers to the programming of consistent Labview-based software in order to automate the acquisition and analysis of experimental data. In this chapter we introduce all the technical aspects required to assemble a powerful and reliable calorimetric set-up from the very beginning. Basic concepts on cryogenics, vacuum techniques and leak detection will also be revised.

3.1 Introduction

The low-temperature experimental physics has addressed up to date a vast amount of unknown new exciting features of nature. The observation of zero resistivity when lowering the temperature in superconductors [Onne11], the unusual behavior of ^{4}He [Kapi38] and ^{3}He [OsRL72] when the superfluid regime is achieved or the Debye model breakdown in amorphous materials [ZePo71] could serve as examples of this rich variety of phenomena. Among all the techniques used for the study of matter, calorimetry has always provided a powerful and valuable tool to determine the outstanding properties of materials, regardless whether the object of research is an insulator, a superconductor, a glass or a quasicrystal. This versatility has motivated the appearance of many different calorimetric techniques, depending on the temperature range and the special requirements of the issued phenomenology [NeLi11] [Gmel79][BaWh99].

The physics of this thesis lays on the connection, if any, between the stabilization processes that take place below (but next to) the glass transition T_g in amorphous materials, and their low-temperature properties. For this purpose, calorimetry has been chosen to be the main experimental tool, both at temperatures around T_g (typically in the range 370 K – 400 K) as well as at low (2 K – 40 K) and very-low (0.1 K – 2 K) temperatures. Two different calorimetric techniques have been used: commercial Differential Scanning Calorimetry [MeBr09][CrRe07], including the development of a measurement protocol to accurately determine absolute values of the specific heat (description and discussion on this protocol appears in Appendix A); and low-temperature non-commercial calorimetry for solid samples, which development and set-up comprise much of the technical efforts done in this thesis.

Specific heat gives us information about how much energy must be given to or removed from a material in order to increase or lower its temperature. As temperature is lowered, the properties of materials become *simpler*, say, “thermal noise” disappears and behavior can be better understood by *easier* models [Pobe96][BaWh99]. Nevertheless, low-temperature calorimeters comprise a large number of technical difficulties to be resolved, mainly coming from the fact that characteristic energy values are reduced up to 10^5 times when cooling from room temperatures down to ^{4}He, ^{3}He or ^{3}He/^{4}He mixture temperatures. Radiation, the lack of internal equilibrium, a controlled heat exchange with the environment, or efficiently cooling the cell space are some of the hardest problems that appear when designing these experimental set-ups. These setbacks have been addressed historically by different methods. The first one to be used was the adiabatic calorimeter introduced by Nernst early in the 20th century [NeLi11] [Gmel79], in which an extremely good thermal isolation is needed. It therefore allows a simple calculation of the heat capacity involved: the power applied P over a time Δt produces a temperature increase ΔT that relates to the sought heat capacity C as $C = (P \cdot \Delta t) / \Delta T$. This thermal isolation is the source of many technical difficulties as well, since cooling down the sample to the lowest temperature requires a thermal contact with the *switch-off* possibility when desired. Also, big samples must be employed so that the undesired heat-leak effects are minimized when calculating the heat capacity. On the other hand, good accuracy is achieved when using this method. In order to improve some of the demerits of the adiabatic method, different techniques have been developed. AC-calorimetry appears as a likely method to obtain high-precision measurements [SuSe68] using small samples (down to a few milligrams), although the accuracy of the experimental data does not improve those obtained by other methods. This technique appears to be very appropriate in the vicinity of phase transitions [SiSa74]. Sample response to small oscillations in temperature with constant frequency ω directly relates to its heat capacity, but considerations on the internal equilibrium of sample and the sensors used make this technique quite sophisticated. Relaxation techniques [Schu74][PéRa07], where a non-ideal thermal contact between the calorimetric cell and the sink is designed, so that internal equilibrium times τ_{in} within and between sample and sensors are much faster than those needed to equilibrate with the reservoir $\tau_{\mathrm{in}} << \tau_{\mathrm{rel}}$. Variations of this method have been developed to accomplish good accuracy and precision when heat capacity, and consequently typical relaxation times, increase [PéRa07]. A quasi-adiabatic continuous method that also uses poor thermal links to the sink, and thereby can be applied in the same calorimeter employed for relaxation techniques has been designed, built and exhaustively tested with different samples in this thesis [PAHF13]. Good accuracy and precision are obtained in the temperature range 2 K – 100 K with short time requirements (typically a few hours). Heat losses must be calibrated for every single experiment, as cooling power enters the equation to calculate the heat capacity of the cell *C*.

We describe next the low-temperature systems employed in this thesis; the construction and calibration of low-temperature thermometers; vacuum systems and leak detection for cryogenics; the experimental calorimetric cell; calorimetric methods used and a brief description of the software developed.

3.2 Low-temperature systems

In this section we will discuss all the aspects involved when working at liquid ^{4}He and ^{3}He/^{4}He liquid mixture temperatures. This thesis has been completed using two different cryogenic systems: a ^{4}He cryostat, in which specific heat measurements down to 1.8 K were performed; and an Oxford Instruments MX400 dilution refrigerator for measurements from 3 K down to 50 mK. A detailed description of the work done in preparing these two systems for calorimetric meaurements is presented, as well as the critical factors to take into account when using them for a more general purpose.

3.2.1 ^{4}He cryostat

A double-chamber insert together with a 10-liter ^{4}He dewar was employed in the specific heat measurements from room temperature down to 1.8 K (see schematic description in Figure 3.1). The dewar for liquid ^{4}He is made up of an inner 102 mm-in-diameter and 130 cm-in-height space, where the insert is immersed in the cryogenic bath. Both liquid N_2 and ^{4}He can be used as cryogenic bath. Concentric to the inner chamber, a high-vacuum jacket 7.5 cm thick is located. A high density of mylar film mechanically attached to the inner space wall is used as super-isolator. This super-isolator has two objectives: 1) it works as radiation shield and 2) adsorbs gas particles that could induce thermal contact between the bath space and the environment. Two security valves are located in the dewar to prevent from risks derived from possible overpressure. No optical access into the cryogenic bath exists once the insert is placed inside the dewar for the experiments, and so a superconductor probe is used as level meter to monitor the bath liquid ^{4}He level (see Figure 3.2c).

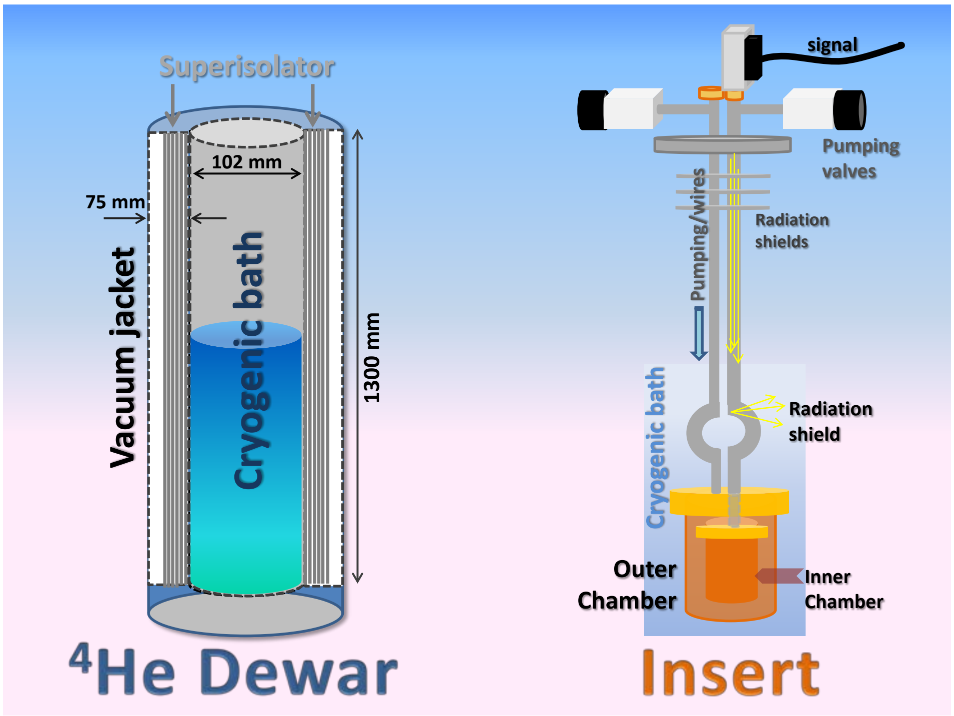

Figure 3.1 Schematic description of ^{4}He dewar and double-chamber insert used in the low-temperature specific heat measurements, where all important elements are shown.

When using liquid ^{4}He as cryogenic bath, the dewar is connected to a *recovery* line in order to store the ^{4}He gas and further liquefy it again in the university liquefaction facilities. A general view of the experimental set-up is shown in Figure 3.2. Recording of evaporated gas is done using a gas counter attached to the recovery line coming from our cryostat, with which control on the helium consumption is possible (see Figure 3.2b). A set of valves allows us to work in two modes: using recovery pressure $P \approx 1$ atm as reference; or lower the bath pressure by pumping it using an auxiliary rotary pump. This allows us to further cool down the system down to 1.8 K. Helium gas pumped is sent through gas filters back to the recovery line, to prevent possible contamination of the line with oil, water or others. A manometer is used to monitor the bath-pressure in the pumping mode.

The insert is composed of two concentric and separated chambers (see sketch in Figure 3.1). The inner chamber, where the experimental cell is located, is under high-vacuum conditions $P \leq 10^{-7}$ mbar. An indium-sealed copper pot separates the inner and outer chambers, as well as the outer chamber and cryogenic bath. The second chamber is under low helium gas pressure (typically $P \approx 1$ mbar), what is used for tuning the cooling power to the calorimetric cell. This second copper pot also serves as radiation shield for the experiment. Wiring of the experimental cell into the inner chamber comes through a thin-walled stainless-steel pipe. The same pipe is used to access the experimental place when pumping. A second pipe goes into the outer chamber. Further shields inside the stainless-steel pipes are used to prevent direct 300 K radiation to enter the experimental space. In the upper part of the pipes, vacuum-sealed-fiber-glass walls serves as connection for the wires (see details in Figure 3.1). A ‘T’ of the pipes allows a second access to the inner chamber with a valve, through which pumping is done (Figure 3.1).

Vacuum system employed to pump the experimental chamber is made up of rotary and diffusion pumps. Using the rotary pump, pressures down to 10^{-2} mbar are reached, as a previous step before using the diffusion pump. With the latter one, values down to 10^{-7} mbar are achieved within 2-3 hours.

Leak detection is seldom needed, only in case uncontrolled ^{4}He going inside the insert is observed as experiments are performed. For this purpose, a *Pfeiffer Vacuum Smarttest* allows us, by previously doing high vacuum where we are interested in running the test, to detect ^{4}He or ^{3}He flows into the system down to 10^{-9} - 10^{-10} mbar · l / s.

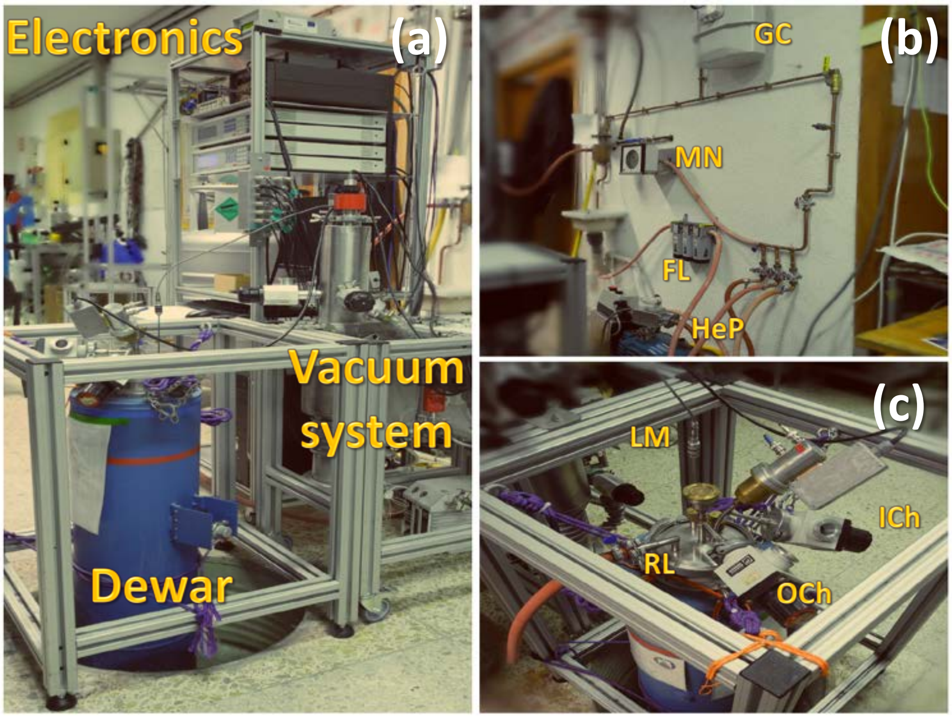

Figure 3.2 Experimental set-up for the low-temperature specific heat measurements down to 1.8 K. (a) Low-temperature experimental configuration. (b) Gas handling set-up in the recovery line: (FL) helium filters, (MN) bath manometer, (GC) gas counter and (HeP) helium pump. (c) Details in top of insert where manual valves to inner chamber (ICh), outer chamber (OCh), recovery line conecction (RL) and (LM) level meter are accessed.

3.2.2 Dilution refrigerator

Heat capacity measurements down to 50 mK have been performed in a dilution refrigerator Oxford Instruments MX400, with base temperature 7 mK and 400 μW cooling power at 100 mK. A 72-liters of total volume (50 liters useful) dewar with the possibility of applying magnetic fields up to 9 T was used (see Figure 3.3). Total amount of the ^{3}He/^{4}He mixture is 71 liters at 1 atm and room temperature. Partial volume of ^{3}He is 19 liters.

The different parts involved in the mixture handling procedure are: insert, ^{3}He rotary pump, roots pump, gas cabinet, liquid nitrogen trap and liquid helium trap (see Figure 3.6). The parallel circuit for the 1K pot cooling includes a second rotary pump.

When a mixture of the stable isotopes of helium is cooled down below a critical temperature $T_c \approx 0.86$ K, it separates into two phases. The lighter *concentrated* phase is rich in ^{3}He, and the heavier *diluted* phase is rich in ^{4}He. The difference in enthalpy from having an atom of ^{3}He in the concentrated or in the diluted phase provides us with a cooling power. This is accessed by ‘evaporating’ ^{3}He from the concentrated into the diluted phase. It is in the mixing chamber (MC) of the dilution refrigerator where this process takes place. ^{3}He atoms are injected to the MC, after passing through a number of stages (as described in Figure 3.5), in order to progressively cool down the ^{3}He to base temperature. These stages are located between room temperature and the MC temperature (7 mK at minimum), where cooling power of the ^{3}He being pumped (going out) is used to cool down the ^{3}He being injected (going in). ^{3}He, before being injected into the refrigerator, goes through the liquid nitrogen and the liquid helium traps, in order to purify it and prevent the system from possible blockades due to water or oil, for example.

When going into the dilution refrigerator, the ^{3}He/^{4}He mixture is precooled under 2 K with the 1K pot (see Figure 3.5). Typical operation temperatures of constant-flux 1K pots are 1.5 K – 1.7 K. From now on we will always refer to the ^{3}He/^{4}He mixture, and so only ‘diluted’ (if poor in ^{3}He) or ‘concentrated’ (if rich in ^{3}He) phase distinctions will be done. This temperature is not enough to separate the two phases (going down to 0.86 K is necessary as shown in Figure 3.4), what is achieved by pumping the ^{3}He from the still. After the 1K pot, the concentrated phase suffers Joule-Thomson expansion and further cools down below 1.4 K. Then, the ingoing mixture goes in thermal contact with the still stage, where it goes to temperatures below 0.6 K - 0.7 K. This happens before the concentrated phase is driven through the continuous heat exchangers. At this point, diluted phase going out is passed through a spiral. Inside this spiral, a smaller and denser spiral is located in counter direction, where the concentrated phase flows. This enhances thermal contact between the two phases and lowers concentrated phase temperature below 50 mK.

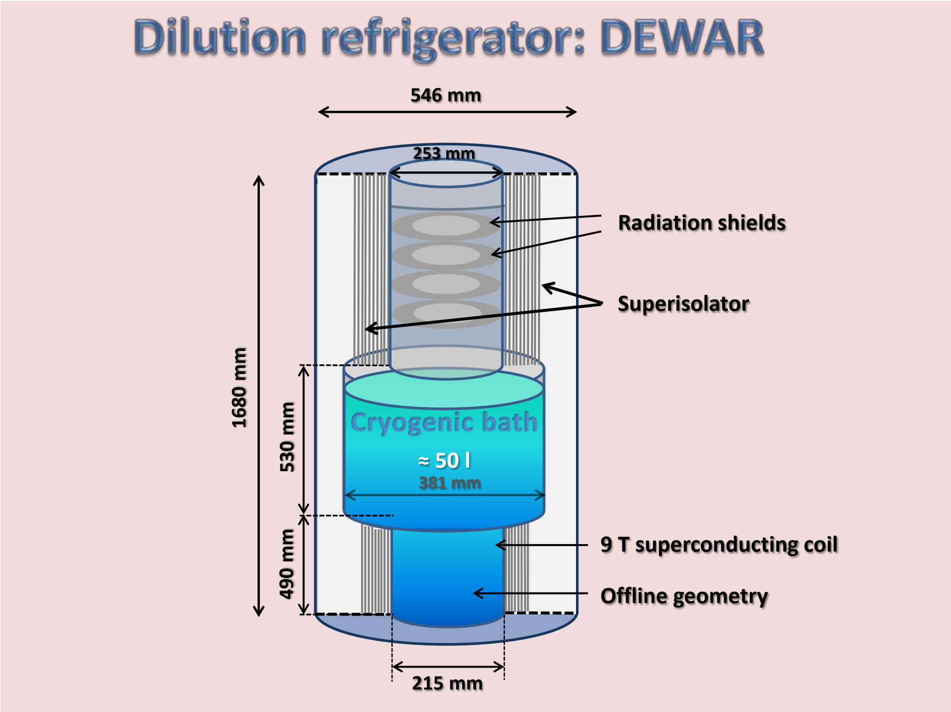

Figure 3.3 Schematic drawing of the liquid helium dewar with its basic elements employed for the dilution refrigerator. Total volume of the dewar is 72 l, useful space for cryogenic liquid is 50 l.

At this temperature, Kapitza resistance between mixture and solids becomes dramatically high –up to 10^4 W/K depending on the solid– (we remind that Kapitza boundary resistance increases approximately as T^3), and so thermal contact activation must be done by exponentially rising contact area. This is obtained using the discrete heat exchangers, where the two phases are thermally contacted mediated by sintered silver walls, what counteracts boundary resistance. After this point the concentrated phase goes into the MC, where a 7 mK base temperature is achieved.

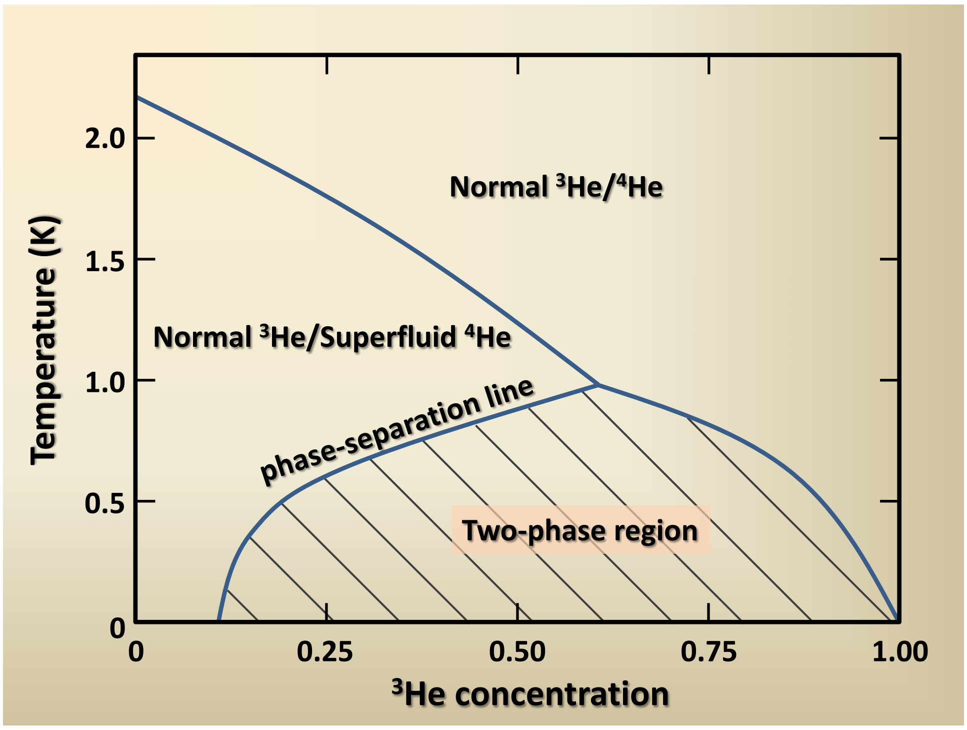

Figure 3.4 Phase diagram of the ^{3}He – ^{4}He mixture at low temperature as a function of the ^{3}He concentration.

As said above, ^{3}He atoms are pumped from the still, which is partially filled by the diluted phase (see Figure 3.5). This produces a reduction in the ^{3}He concentration in the diluted phase at this point, creating an osmotic pressure that pushes *hot* ^{3}He atoms up from the MC. A pumping rate is necessary in order to establish a cooling power in the dilutor. For this purpose a heater is located at the still to regulate the ^{3}He evaporation rate, and hence the dilution of ^{3}He atoms from the concentrated phase to the diluted one, in the MC. From what is said above, we deduce that minimum temperature is conditioned by the pumping rate of ^{3}He we are able to achieve in the still. Two pumps are devoted to this task: rotary and roots pumps in Figure 3.6b. They are located one after the other, so that rotary pump is always working, but the roots pump is only used to achieve the lowest temperature (pumping pressure below some mbar is necessary for this pump to work properly).

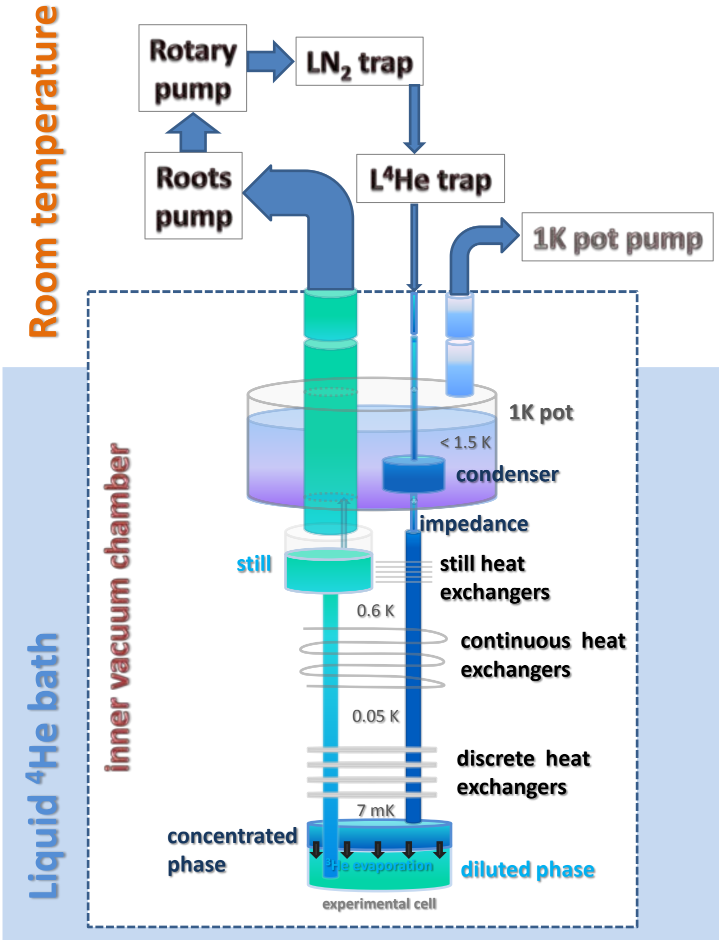

Figure 3.5 Schematic description of dilution refrigerator performance with all elements involved. Inner vacuum chamber delimits the insert space immersed in liquid ^{4}He bath. The parts of the circuitry located at room temperature are out of the dashed line. Arrows indicate ^{3}He flow.

A gas handling cabinet in the MX400 (Figure 3.6d) allows monitoring pressure, temperature and power values in the mixture circuit, as well as controlling the whole mixture operation procedure, included the 1K pot performance.

Dilution refrigerator provides a continuous cold point, which can be conveniently controlled in order to move from 7 mK up to 4 K. In the standard circulation mode, temperature is varied in the range 0.007 K – 0.86 K. In an alternative mode, where only a fraction of the total mixture from the dump is circulated (around 10% of total), control on temperature from 0.6 K up to 4 K is achieved.

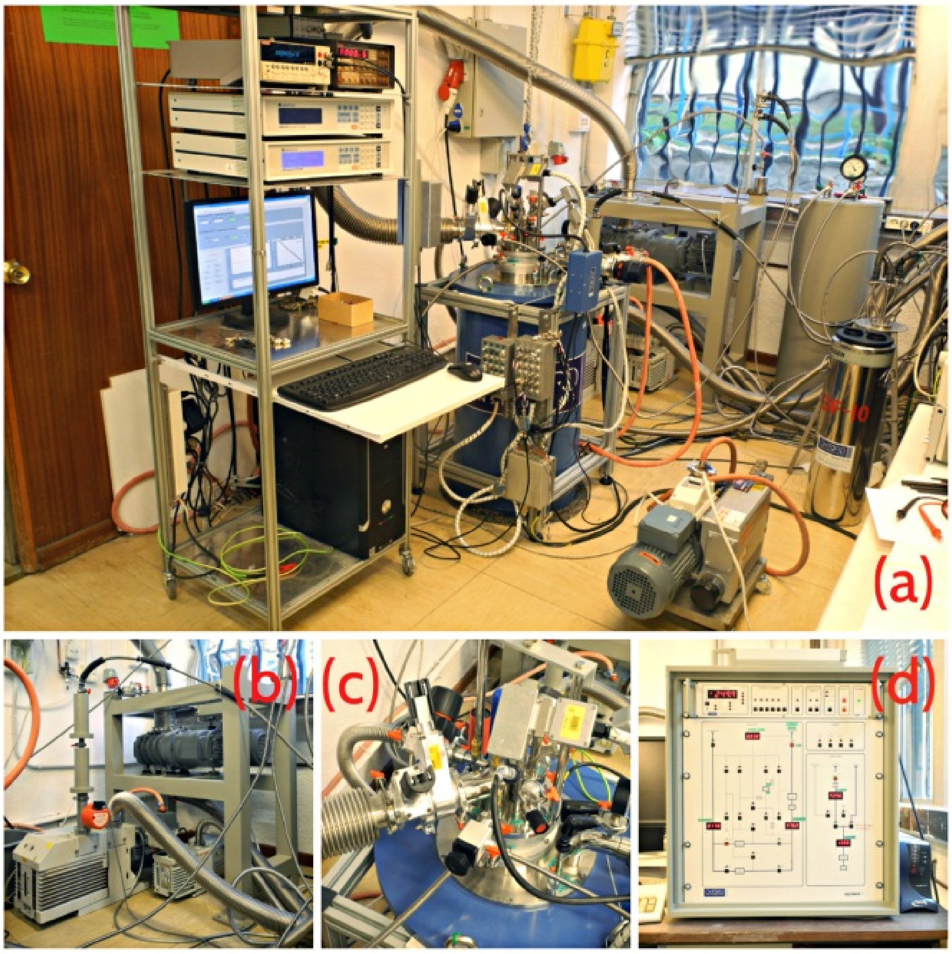

Figure 3.6 Dilution refrigerator set up used for the specific heat measurements. (a) Overview of the elements in the mixture circuit; (b) pumps in the dilution unit for the mixture and 1K pot; (c) details in the top of the dilution refrigerator and (d) gas handling cabinet.

3.3 Thermometry

Thermometry plays a major role in the low-temperature experimental techniques, especially if thermal properties are going to be measured. In this section we will introduce thermometers involved in the measurement of specific heat at ^{4}He and ^{3}He/^{4}He mixture temperatures. Operation of these sensors, calibration using primary and secondary thermometers as reference, electronics requirements and some other important details to consider when choosing thermometers for calorimetric experiments at low temperatures are discussed.

In order to measure temperature we need a physical property directly connected to it by a physical law. This way, determination of the temperature depends on how accurately we can measure the given physical property and how appropriate the physical law results. Two different groups of thermometers can be differentiated in terms of the law connecting the physical property with temperature: *primary thermometers* for which a good enough knowledge on the physical law describing the connection to the thermodynamic temperature exists, and hence no prior calibration is needed; *secondary thermometers* which lack a direct connection between the physical property and temperature, so previous calibration is needed using primary thermometry, fixed points or secondary thermometers already calibrated. In this thesis secondary thermometers have been mostly used, but also assembly of a resistor and calibration using a primary thermometer (noise thermometer) has been done.

For accurate temperature measurements in the calorimetric cells, resistance thermometry was always employed. To monitor and control intermediate stages silicon diodes (with standard calibration curve) were sometimes used, for which voltage drop in the diode is related to temperature. In the case of the resistance thermometers, we had three types depending on the temperature range and dimensions: (1) RuO_2 chips made up of a mixture of conducting RuO_2, $BiRuO_2$ and a lead silicate glass (heated above its glass transition), with sensor mass < 1 mg, for the temperature range $0.05\ \mathrm{K} \leq T \leq 4\ \mathrm{K}$; (2) cernox sensors (here mounted on a small sapphire plate and hermetically sealed), where zirconium nitride conductor is embedded in a zirconium oxide nonconducting matrix, with validity in the range $0.1\ \mathrm{K} \leq T \leq 100\ \mathrm{K}$ (for more details consult [Cryo00]); (3)

germanium sensors, in which a doping using As (‘n-type’) or Ga (‘p-type’) is done, and typical working range is 0.3 K $\leq T \leq$ 40 K.

Appropriate use of thermometry at low temperatures implies several considerations to have in mind, which are increased when this thermometry is to be employed in a calorimetric cell. In order to have an accurate reading of temperature (i.e. of the sample, or a stage in the cryostat), good thermal contact between the thermometer and the element is crucial. By means of mechanical fixing and cryogenic grease or varnish, thermalization of the thermometer is achieved. When working at low temperatures, special care of the contact surface between the sensor and the place where it is fixed must be taken into account, what sometimes implies removal of possible oxide by polishing. Important to have in mind is the fact that, once we do vacuum in the experimental chamber, most of the space between two surfaces will be in vacuum. To activate thermal contact (vacuum is a perfect isolator), cryogenic grease as apiezon or varnish are used. Not only the sensor must be in good thermal contact with that element to monitor, but also wires coming to the thermometer must be properly thermalized next to that element. To this purpose, different elements are employed: high-thermal-conducting cylinders (i.e. cooper cylinders), plates where wires are trapped in between, etc.

A third question is the electrical excitation of the thermometers for temperature reading. Compromise here between self-heating effects and good accuracy/precision is necessary. Let us remember that the sensors we use to monitor the temperature are resistive, what means heat dissipation by Joule effect happens when circulating current through the thermometer. If excitation is too high, thermal contact with the stage is not fast enough and sensor’s temperature decouples from that where it is fixed. Temperature reading then exceeds that of interest. If excitation is too low, sensitivity decreases, and so does precision, what implies a worse temperature definition. So, at a given temperature, maximum excitation without self-heating effects must be chosen, in order to have an accurate and precise reading. Electronics choice is a key point in the temperature reading, as stable and low-noise signals are required. Two possibilities are chosen, depending on the temperature range: for temperature above 1 K, DC-signal electronics with current range down to 10 – 100 nA are commonly used (voltage drop below 10 mV), where square-shaped signals (including polarity change) are applied to the sensor; in the range 0.02 K – 1 K AC-signal electronics where a lock-in amplifier together with a resistance bridge allows us to read the sensor temperature by applying a sinusoidal-shaped excitation with frequency ω and determine resistance by comparing with a reference value (see for instance chapter 12 of [Pobe96]). Power dissipated in the sensor is drastically reduced to pW or even fW at the lowest temperatures.

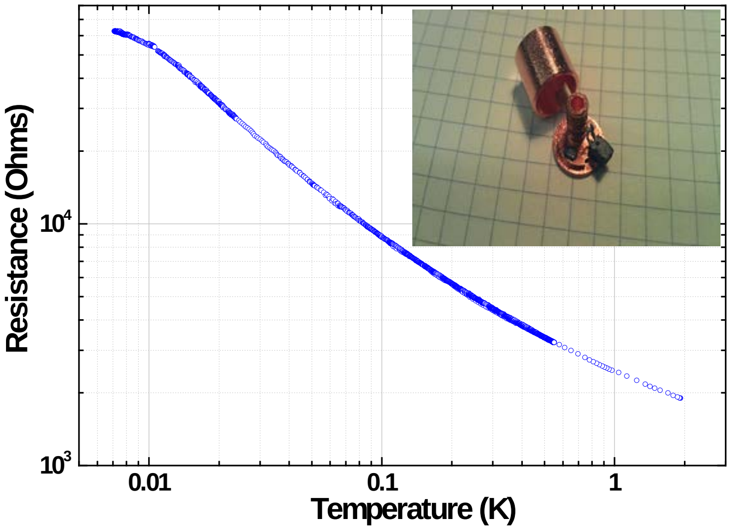

Figure 3.7 Resistance versus temperature for a RuO_2 sensor in the temperature range 0.007 K – 2 K, calibrated using –primary- noise thermometry and a second –commercially calibrated- RuO_2 as references. Inset shows robust mounting details of the RuO_2 sensor in a copper (oxygen free) capsule, with thermalized NbTi wires for the signal.

In Figure 3.7 an example of calibration curve for a RuO_2 is shown, where noise thermometry was used as reference in the range 0.007 K – 0.6 K (using a dilution refrigerator with base temperature 0.006 K), and further calibration with a –commercially calibrated- second RuO_2 sensor in the range 0.1 K – 2 K was performed. Frequency bandwidth to calculate noise temperature was 100 Hz – 10 kHz. In order to check the thermodynamic temperature given by the noise thermometer, a CMN paramagnetic salt with fixed points given by nine superconducting transitions in the range 0.01 K – 1 K was used.

Noise thermometry takes advantage of the electrical noise in a resistive element, where a relation between the noise voltage, resistance and temperature was first found by Johnson and Nyquist in 1928 [John28][Nyqu28]. This relation tells us that, when measuring in a frequency bandwith $\Delta\nu$ at a temperature T in a resistance R, voltage noise is proportional –and uniquely determined- to these quantities in the form

$$< u^2 > = 4k_B RT\Delta\nu \tag{3.1}$$

Specific mechanical mounting is usually required for thermometer calibration, as perfect thermal contact between the sensor and the reference is required in order to obtain an accurate calibration curve. When designing this kind of cells, differences in the expansion coefficients between sensor materials and that of the mounting can derive in a poor thermal contact when lowering the temperature. To avoid this problem, usage of springs, for example, can be of much help in order to keep surfaces in good mechanical contact, regardless the temperature.

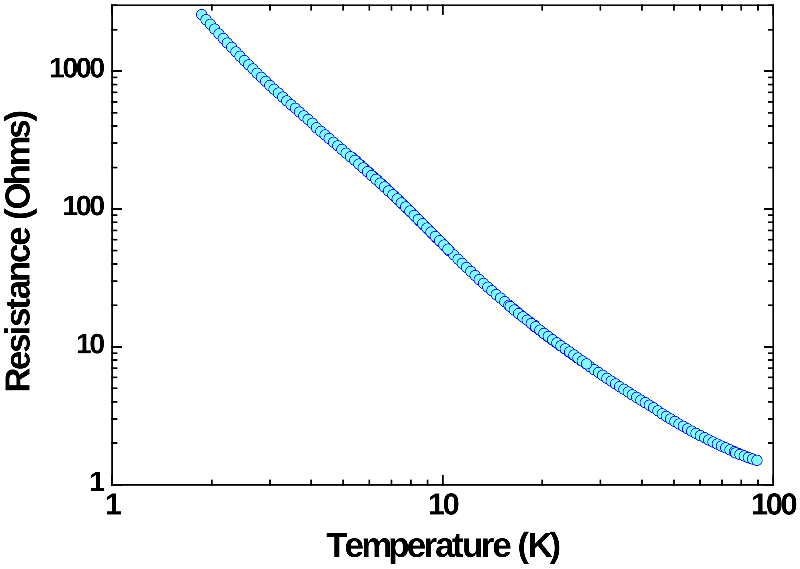

Figure 3.8 Calibration of resistance versus temperature of a Germanium sensor in the temperature range 2 K – 90 K, using as reference a commercial Cernox sensor.

At higher temperatures, to say, above 2 K, excitation and thermalization are not so critical, and calibration of thermometers can be easily achieved up to 100 K typically by using commercial thermometry as reference, as shown in Figure 3.8. Calibration curve is then built and uploaded to the thermometry electronics, so that direct reading of the temperature is obtained in future experiments.

3.4 Vacuum techniques

High-vacuum environment is an important requirement when reaching and maintaining low-temperature conditions. Factors like contamination of the sample, adsorption of gases or unwanted heat conduction are some of the major problems introduced by poor vacuum conditions in cryogenics. Vacuum level requirement in cryogenics is usually of the order 10^{-6} mbar, and thus high-vacuum equipment is needed to achieve this value. This pumping equipment is made up in our case of a mechanical pump and a diffusion pump. The mechanical pump serves as a backing and fore-pump for the diffusion one. It is a rotating-vane pump that sweeps gas from a cylindrical chamber and expels it into the atmosphere. The minimum vacuum level reached by this pump is 0.01 mbar. These pumps work in a compressive action, and are not effective in pumping out condensable gases such as water. To help them in this respect, they are assisted by a gas ballast valve, which admits a controlled volume of air going into the compression stage.

The diffusion pump works using the oil vapor produced by heating the bottom, where a fixed amount of low-vapor-pressure oil is located. This oil pressure travels up the diffusion pump until it is deflected at the top, trapping the gas molecules and trapping them towards the lower part, where they are pumped by the rotary pump (see diagram in Figure 3.9).

The different pumping configurations are allowed by the valves distributed in the vacuum system (named from V1 to V4 in Figure 3.9). Connection with the cryostat is done using flexible pumping lines. The vacuum level is monitored by three gauges in the system. Two of them (G1 and G2) are low vacuum detectors –reading range 0.001 – 10^{3} mbar-, and the third one is a Penning detector, with working range 10^{-8} – 10^{-3} mbar. The diffusion pump efficiency is abruptly enhanced by the liquid nitrogen trap located at the top of it, as gas molecules are kept in the oil vapor working volume.

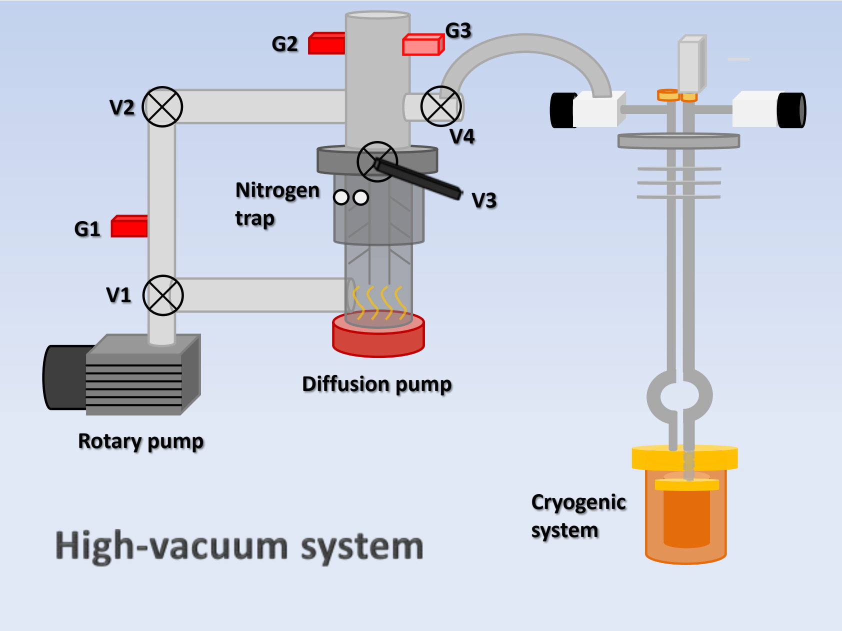

Figure 3.9 Schematic diagram of the high-vacuum system employed in cryogenics. Rotary pump serves either as a backing or fore-pump for the diffusion pump. Typical vacuum values achieved with the rotary pump are 0.01 mbar, whereas the diffusion pump reaches vacuum level down to 10^{-7} mbar.

3.5 Calorimeters

Specific heat measurements at low-temperatures require an amount of details and specifications to be kept in mind, which are introduced in this section. Of course, these specifications change depending on the method to be employed, as well as the temperature range in which the measurement is done. Two different calorimeters have been used in the work presented here, attending to the temperature region in which they work. At temperatures from 50 mK to 40 K – which have been seldom extended up to 300 K in the ^{4}He cryostat- using a low-temperature solid-sample calorimeter; and those measurements above room temperature, from 280 K – 480 K with a Differential Scanning Calorimeter (DSC).

The main technical development addressed in this thesis has been the design, mounting and successful performance of a versatile solid sample calorimeter. This calorimeter allows us to measure specific heat from 50 mK up to 40 K, by alternating the dilution refrigerator and the ^{4}He cryostat –described already in sections 3.2.1 and 3.2.2- depending on the temperature range. Heat capacity resolution down to nJ / K at the lowest temperature is achieved, what has allowed us to study glasses of few mg in mass down to 50 mK. Complete automation of the measurement process has also been done by a parallel development of software in Labview language, which results in a powerful tool to exhaustively study and accurately determine specific heat in a wide range of samples (compounds presenting magnetic or superconducting transitions to glasses or different graphite specimens have been studied). Discussion on the design and mounting –including technical problems faced in the first stages of performance- are presented, with comparison to other heat capacity techniques. Regarding the DSC measurements, commercial equipment was used, but specific protocol developed for the quantitative study of relaxation processes around the glass transition is introduced in Appendix A.

3.5.1 Low-temperature calorimeter

Introducing low-temperature calorimetry must be done first mentioning the changes induced in matter when lowering the temperature down to some tens of millikelvin: a drastic reduction in the characteristic energy scale of up to 10^4 happens from room temperature down to liquid helium temperatures, which further decreases a 10^3 factor at ^{3}He/^{4}He mixture temperature [Gmel79][Pobe96][Loun74][BaWh99]. A parallel reduction in the heat conduction is present –in approximately the same order of magnitude-, the enemy of thermal equilibrium as well as of cooling. This reduced energy scale makes heat capacity measurements sensitive to really small heat contributions – insignificant at higher temperatures– of some nW (or even fW when going to tens of millikelvin), introduced by vibrations, radiation or other heat influxes from the surroundings [Whit79]. These non-desired –of unknown amount in principle– heat contributions introduce uncertainty in the heat capacity determination. Reduction of these spurious energy supplies, activation of thermal link between all the elements in the calorimetric cell or requirements on the sample internal equilibrium are some of the hardest problems to solve in the low-temperature calorimetry.

The first calorimeter developed in history is the Nernst or adiabatic calorimeter, at the beginning of the 20th century [NeLi11], in which heat capacity is determined given no heat contributions from the surroundings, as well as a finite and controlled energy amount ΔQ from the heater placed at the sample (see page 85 for further details). Direct application of the heat capacity definition is used under these adiabatic conditions, since an increase in temperature ΔT is driven by ΔQ, only opposed by the heat capacity of the sample. This means a perfect isolation between cell –sample plus addenda- and its environment is necessary, what is never fulfilled (radiation is always present, for example). The sample is attached to a substrate, where a sensor and a heater are glued, in order to monitor the temperature and produce the heat pulses $\Delta Q = P \cdot \Delta t$ (of the order of 1% in the temperature increase). The calorimeter has a surrounding shield that is kept at the same temperature as the cell –slightly lower after the heat pulse- in order to minimize thermal drift. This –small negative– thermal drift is always present in the sample temperature due to non-perfect isolation. Determination of the experimental point temperature is given by calculating the mean value from temperatures before and after the heat pulse.

A continuous-heating operation mode is possible under the adiabatic conditions described above, since, increasing power supplied, temperatures changes much higher than 1% are achieved. Taking instantaneous derivatives of temperature versus time (instead of the absolute change mentioned before), and monitoring the power applied, determination of heat capacity is done [BKPS89].

In general, three kinds of calorimeters can be differentiated in terms of the thermodynamic conditions which apply in each case: adiabatic (as described above), in which no heat transfer ideally exists between the calorimeter and surroundings; isoperibol, with fixed temperature of the surroundings, but different to that of the calorimeter –a controlled thermal resistance is located between both-; and isothermal, where calorimeter and surroundings are kept at the same temperature. The calorimeter developed in this thesis lies in the isoperibol classification, since a finite thermal resistance is designed and placed in order to decouple the calorimeter from its surroundings – with typical relaxation times of one minute typically at liquid helium temperatures-.

An isoperibol calorimeter has been designed and further improved to end up with a versatile low-temperature calorimeter, with which heat capacity measurements in the temperature range 0.05 K – 300 K can be performed.

In Figure 3.10 a simplified sketch of our isoperibol calorimeter for solid samples is shown, where the entire elements configuration is displayed, both in the cell –where sample is attached- and thermal reservoir –controlled temperature focus-. Signals wiring do not appear for clearance.

When building an isoperibol calorimeter for solid samples, the first element to be chosen is the substrate where sample will be attached to. Three conditions have to be taken into account: good thermal conduction, low specific heat and robustness. Among possible candidates, sapphire –crystalline Al_2O_3- presents a good compromise between these three requirements. Monocrystalline sapphire discs are easily purchased in different diameters and thicknesses, depending on the geometry of our calorimeter. Sapphire has a high Debye temperature Θ_{Debye} = 1035 K [BaWh99], and it is a non-metallic solid, what makes its specific heat very low: $C_p \approx 6$ µJ/g·K at liquid helium temperature . The absence of magnetic impurities makes it also very appropriate for the ^{3}H/^{4}He mixture temperatures, since no extra contribution appears at even lower temperatures. It has also a high thermal conductivity $\kappa_{th} \approx 1$ W/cm·K at 4 K [Pobe96], what gives a very good thermal-conductivity-to-specific-heat ratio at low temperatures. At 0.1 K thermal conductivity is $\kappa_{th} \approx 20$ µW/cm·K and specific heat $C_p \approx 0.1$ nJ/g·K. Further, holes can be easily machined in sapphire using diamond drills, and so mechanical attachment to the thermal reservoir is done with nylon wires in 120º geometry –to optimize stability-. Two different sapphire disc geometries have been employed in this thesis: 25 mm diameter/0.5 mm thick for big samples –mass above one hundred milligrams-, and a 12 mm diameter/0.5 mm thick for samples of few milligrams. Machining on these smaller sapphire discs (they are easily cracked) becomes rather difficult, and fixing the nylon wires to the disc can be done using a small amount < 1mg of araldite epoxy (see Figure 3.11b).

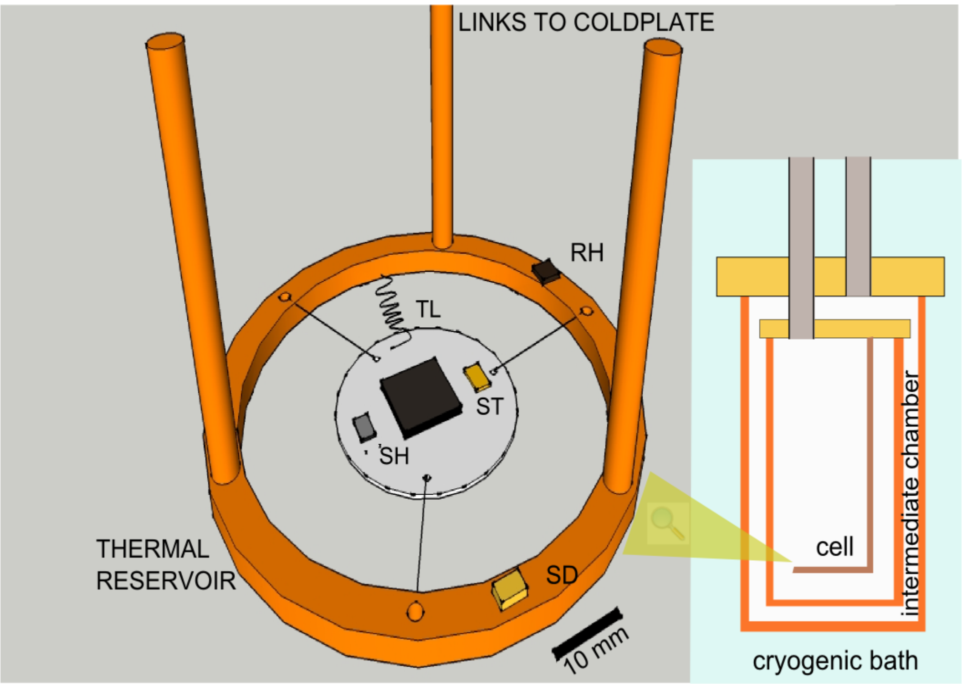

Figure 3.10 Simplified sketch of isoperibol calorimeter for solid samples designed and built for the low-temperature heat capacity measurements in this thesis, with all basic elements necessary both in cell and thermal reservoir. Sample is attached in the center of sapphire disc (in the center), with sample thermometer ST and sample heater SH in good thermal contact with it. Finite thermal link between sample and thermal reservoir TL determines calorimeter relaxation times. Temperature in the thermal reservoir is controlled using close loop PID between thermometer SD and heater RH. Inset shows location of the calorimeter in the double-chamber insert used in ^{4}He cryostat (see Figure 3.3). In the very-low temperature measurements, the calorimeter is attached to the cold plate of the dilution refrigerator (see Figure 3.5).

Nylon wires are used for the mechanical attachment of the sapphire disc to the copper ring because of its low thermal conductivity $\kappa_{th} = 4{\cdot}10^{-4}$ W/cm·K at 4 K and flexibility. Three 0.18 mm-in-diameter and 2 cm-long nylon wires fix the sapphire disc to the thermal reservoir, what gives a total thermal conductance of 50 nW/K at 4 K (negligible compared to that of the thermal link). This thermal conductance goes down to 1 nW/K at 0.1 K. On the bottom face of the sapphire disc, a RuO_2 chip $< 1mm^3$ and mass below 1mg is glued using araldite epoxy (see Figure 3.11b). Resistance values at room temperatures for these sensors are typically 1 kΩ, increasing with decreasing temperature (see Figure 3.7). A commercial-thick-film resistor is also attached to the sapphire disc, diametrically opposed to the thermometer, using araldite. This resistor is used as sample heater, and typical values are between 100 Ω and 1 kΩ at room temperature (and quite temperature independent). Thin resistive films are evaporated on top of 8 mg alumina substrates in this kind of chips. In order to lower heat capacity contributions at low temperature, these heaters can be easily polished down to < 1 mg, without compromising their mechanical resistance. Electrical connections of both thermometer and heater are done in two-terminal configuration with 0.05 mm diameter NbTi wires –superconducting under 9 K- for the dilution refrigerator experiments, and in four-terminal configuration using manganine wires for experiments above 2 K. Low-mass welding in the sensor electrodes is done with tin paste –made up of micrometer size tin spheres-. The opposite end of NbTi wires are welded to the multi-socket connector attached to the copper ring.

In between both sensors, the thermal link is fixed using a small amount of cryogenic varnish. Choice of this link must be carefully done, so that heat conduction through it is dominant among all contacts with the sink, in the whole temperature range the calorimeter operates. *Dominant* here means that this conduction channel is required to be above several tens stronger than the rest of channels –electrical connections to the sensors for example-. As will be shown in the next section, relaxation method is mostly used for the low-temperature heat capacity measurements, where time constants of the order of one minute at 4 K are usually desired. This value, together with a low-enough heat capacity contribution, gives us the clue for choosing the optimal thermal link. Imagine, for example, we want to calibrate our empty cell heat capacity –to subtract it from future measurements-. With the configuration given in Figure 3.11, heat capacity values for the empty cell at 4 K are $C \approx 10^{-5}$ J/K. Depending on the sensor and heater dimensions, heat capacity can increase up to 10^{-4} J/K at this temperature. Imposing relaxation time at this temperature to be $\tau = 60$ s, a heat conduction $\kappa = C / \tau = 0.2 – 2$ μW/K is needed. Looking at the thermal heat conductivities of commonly used materials at low temperatures [Loun74][Pobe96], a wide variety of metals and alloys appear, ranging from some mW/K up to some W/K at 4 K.

Here enters another important factor when selecting a thermal contact: geometry matters. Whatever material used for thermal contact, it must have a manageable shape and length. Too long (various tens of centimeters) or too thin (few micrometers diameter) wires make working with them a very tedious or even unaffordable task. Given electrolytic copper $\kappa_{th} \approx 2$ W/cm·K at 4 K, and 0.07 mm diameter wire, then required length for 60 s time constant for $C = 10^{-5}$ J/K would be L > 600 cm! Hundred times geometrical reduction should be reached to make this wire appropriate. This must be done by changing the material: compounds like constantan or manganine present thermal conductivities two orders lower than electrolytic copper, what would allow us using a reasonable geometry. A precaution must be taken into account when reaching temperatures below 0.3 K, where these two compounds present magnetic contributions to the specific heat [Pobe96][Loun74], and an increase with decreasing temperature, what makes them useless for our purpose. For temperatures in the range 0.05 K up to 2 K compounds like Pt-W are recommended, since thermal conductivity is the same order as those for constantan or manganine, but specific heat goes two orders below them, around 0.6 mJ / mol·K at 0.1 K (see [Pobe96]). This compound also presents some magnetic contributions, nevertheless, well below 0.1 K, what makes it ideal for our measurements. In our low-temperature calorimeters, Pt-W wires 50 μm in diameter and copper wires 70 μm / 50 μm in diameter have been employed. Lengths were chosen depending on the total heat capacities to be measured in each case.

The example given above tries to illustrate the difficulties which emerge in designing the optimal thermal link between sample and thermal reservoir. Although many recommendations have been given, in many cases only experience drives to the appropriate choice, what sometimes implies using the wrong material in the way. Acquisition of these metals or compounds is not an easy task as well, since the fabrication processes can modify thermal conductivity more than one order of magnitude in the low temperature range –depending, for example, if the wire is annealed or stretched-.

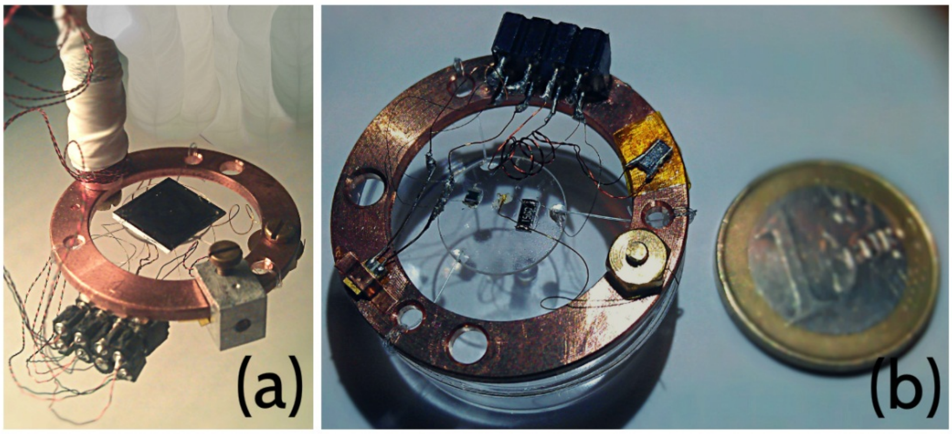

Figure 3.11 Set-up of our isoperibol low-temperature calorimeter for solid samples. (a) Calorimeter mounted in the cryostat with an indometathin sample. Elements on sapphire are all glued to one face of the sapphire disc, so that the opposite one is free for attaching the sample. Electrical connection on the copper ring using socket connectors allows calorimeter versatile configuration and on-table-sample attachment. (b) Photograph of the calorimeter upside down and one euro coin for size comparison.

Once the sample holder and sensors have been described in detail, and the thermal link conveniently chosen, the next step is properly controlling the temperature in the thermal reservoir. To do this, a thermometer and a heater are located in the copper ring which holds the sapphire disc. The chosen geometry is diametrically opposed, so that the reading of thermometer is not screened by the heater proximity (see Figure 3.11b). Depending on the temperature range, a second RuO_2, a Cernox, a Germanium or a silicon diode can be used. A thick-film-chip resistor with 50 Ω resistance at room temperature acts as heater. Feedback between heater output and thermometer reading, via Proportional Integral Differential (PID) control, is done, what provides high thermal stabilities – below μK/s at liquid helium temperatures, and down to few tens of nK/s at 0.1 K-.

Accurate temperature readings of the sample and thermal reservoir must be ensured, by good thermal anchoring of sensors in the substrate, adequate thermalization of wires going to thermometer and convenient excitation. In the case of heaters, as powers up to some tens of mW are dissipated, robust enough fixing to the substrate is demanded. Mechanical attachment is highly recommended for the heater in thermal reservoir, where power released is maximal.

Thermal resistances in the calorimeter appears as the result of boundaries, the use of epoxies and the high vacuum environment in which the experiment is performed (see Figure 3.12). Also internal resistance in materials has to be considered, what can be crucial, as happens in glasses for example. This sometimes forces us to high surface-volume ratio in the samples, in order to compensate this effect. These thermal resistances translate into relaxation times, which must fulfill some conditions so that heat capacity is correctly determined.

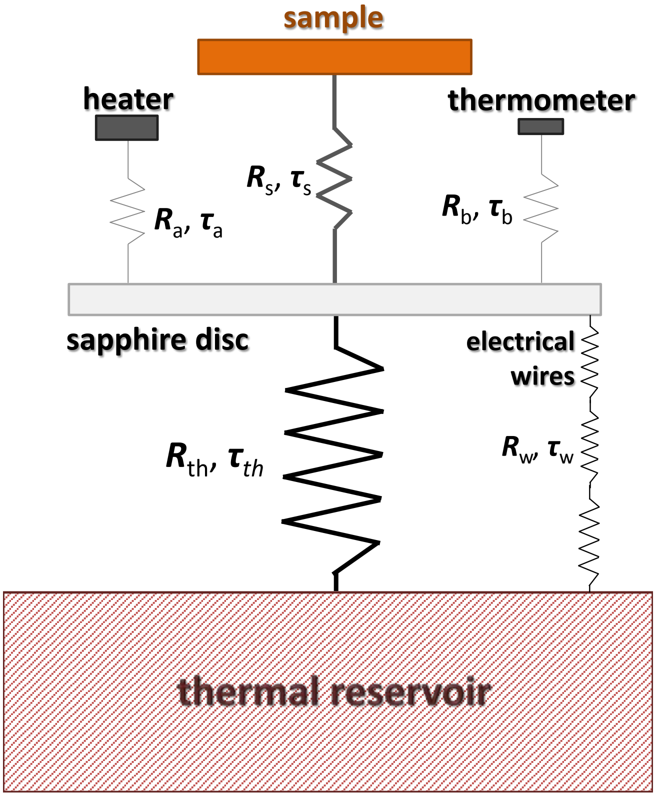

Figure 3.12 Thermal resistance distribution in the calorimeter between all the elements given in Figure 3.10. R_w and τ_w refer to residual thermal conductance due to electrical wiring. Thermometer and heater -in the copper ring to which sapphire disc is attached to- are considered as part of the thermal reservoir.

In Figure 3.12, a schematic representation of the most important resistances is shown. The dominant relaxation time in calorimeter must be that given by the thermal link between sample + sensor + substrate and the reservoir. It means that all resistances, both in parallel -due to electrical connections for example- or in series –between sample and substrate, thermometer and substrate, heater and substrate, or within sample- with thermal link resistance, must be much larger $\tau_w >> \tau_{th}$ or much smaller $\tau_a \approx \tau_s \approx \tau_b << \tau_{th}$. Another requirement for the relaxation time through the thermal link to the reservoir τ_{th}, is that it must be much smaller that the experimental time scale $\tau_{th} << \tau_{exp}$.

The whole calorimeter is mechanically fixed to the cold plate of the cryostat using copper cylinders, in which thermal anchoring of the wires is also done by gluing them with cryogenic varnish. In order to optimize thermalization, wires length is maximized in the anchoring stage.

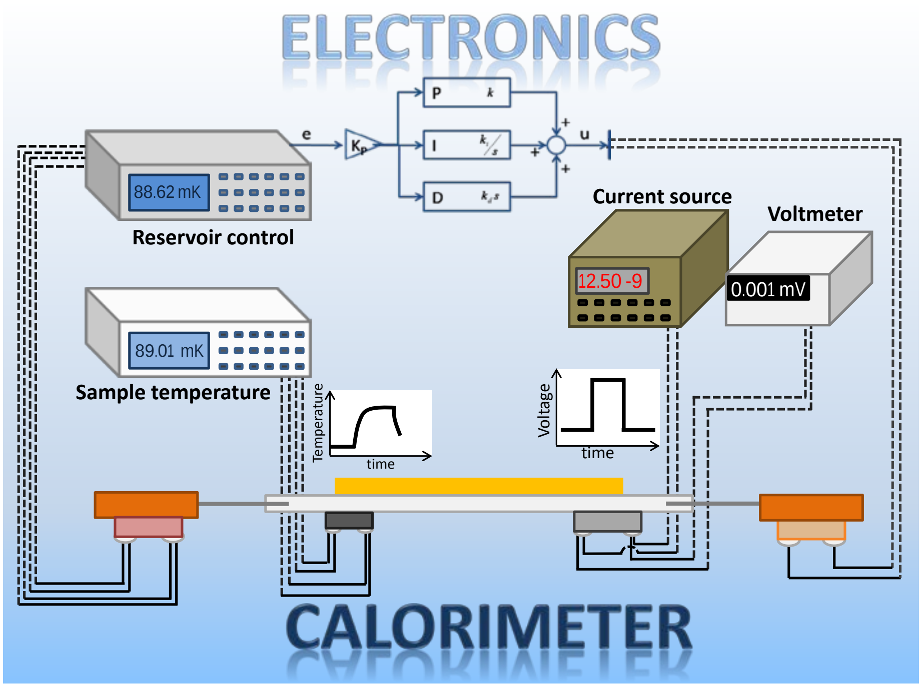

Figure 3.13 Schematic description of the calorimeter control with electronic equipment. Dashed lines correspond to room-temperature electrical wiring, solid lines for low-temperature ones.

In order to control temperature in the thermal reservoir, to monitor the sample temperature and to apply heating power to it, a set of electronic equipment was employed (see Figure 3.13). This electronics varies depending on the temperature range, what implies different excitation ranges for currents and voltages applied, as well as different requirements in the noise level allowed into the experiment –which produces self-heating in sensors, loss of accuracy, etc.–. For the measurements in the ^{4}He cryostat, a Lakeshore 336 Temperature Controller was used both for the reservoir temperature control (with PID feedback between thermometer and heater in thermal reservoir) and reading of the sample temperature. Heating pulses in the sample are done by applying current to the heater fixed to the sapphire disc with either a Keithley 224 or a home-made current source. Power applied is measured determining voltage drop in the heater with a Keithley 2000 multimeter. In the dilution refrigerator, temperature of the sample is independently monitored using a Lakeshore 370 AC Bridge, which provides AC excitation with amplitude down to 2 µV, lowering power dissipation in sample thermometer to some tens of fW. Temperature control of the reservoir is again performed using Lakeshore Temperature Controllers 336 or 350.

3.5.2 Differential scanning calorimeter

Differential scanning calorimetry (DSC) is the most extended technique in thermal analysis. It obtains its name from the work by Perkin-Elmer, when they marketed their first instrument as DSC-1 in 1963, which indeed came to be the first DSC. What is common among all techniques under the DSC label is the possibility to determine a number of characteristic properties in the sample at constant heating or cooling rates. Some of these relevant properties are heat capacity, the glass transition temperature, melting and crystallization temperature, heat of fusion, for example. A huge application of these techniques on polymers and pharmaceuticals has been done in the last decades, with a constant development that has benefited other fields like organic or inorganic chemistry, and even the food industry [CrRe07][Kops95].

In the measurements presented here from room temperature up to 480 K, a commercial differential scanning calorimeter (DSC) from TA Instruments –model Q100- has been employed [Inst00]. These DSC measurements have been performed in the SIdI facilities (*Servicio Interdepartamental de Investigación*). DSC, as it name shows, uses differential measurement from a given reference to extract the sample heat capacity. Two –approximately- identical pans are located in two separate platforms (see schematic description in Figure 3.14). Inside one of the pans we put the sample. A heater is used to increase the temperature of the two platforms, and three thermometers –thermocouples- located in both platforms –the sample and reference ones- and in the block where these two last are attached. Before starting the experiment, the two platforms (calorimeters) are at equilibrium, since they are kept at the same temperature $T_{bl} = T_s = T_r$, with T_{bl} the block temperature, T_s and T_r the sample and reference temperatures, respectively. After this, we start the heating scan, in which the block temperature is heated up in a linear rate, and hence temperature in the reference and sample platforms is increased as well. But temperature in both calorimeters has a lag with the block temperature: this lag is different in the platforms, since the sample is in only one of them. This means, the lag in the sample platform is larger than that in the reference one, and so $T_s < T_r$. Assuming both pans are identical, temperature difference with the block temperature is proportional to the sample heat capacity. This temperature difference T_s - T_r is related to the sample heat capacity and the heating/cooling rates. Calibration routine is performed to determine the heat flows between platforms, and platforms with the block, what determine the time constants in the calorimeters, τ_r and τ_s.

Heating and cooling rates in the DSC play a key role in the heat capacity determination. High heating/cooling rates ~ 10 K/min – 100 K/min can be used to save experimental time, but this is achieved loosing resolution in the way. For high resolution measurements, slow heating rates – of a few Kelvin per minute- and small masses –few milligrams- are desirable, as thermal equilibrium in the sample is enhanced. Nevertheless, by doing this, experimental times drastically increase for achieving good resolution.

Typical sample mass used in experiments shown in this work are between 3 mg and 10 mg. When running preliminary characterization curves, in which only the glass transition temperature and the presence of enthalpy release signal around it were sought, small amounts of sample –next to 3 mg- were used. For the accurate and reproducible determination of specific heat –for enthalpy and entropy curves calculation-, sample mass was always next to – slightly above- 10 mg. Masses above this value could induce poor sample thermal equilibrium, what would lower heat capacity accuracy.

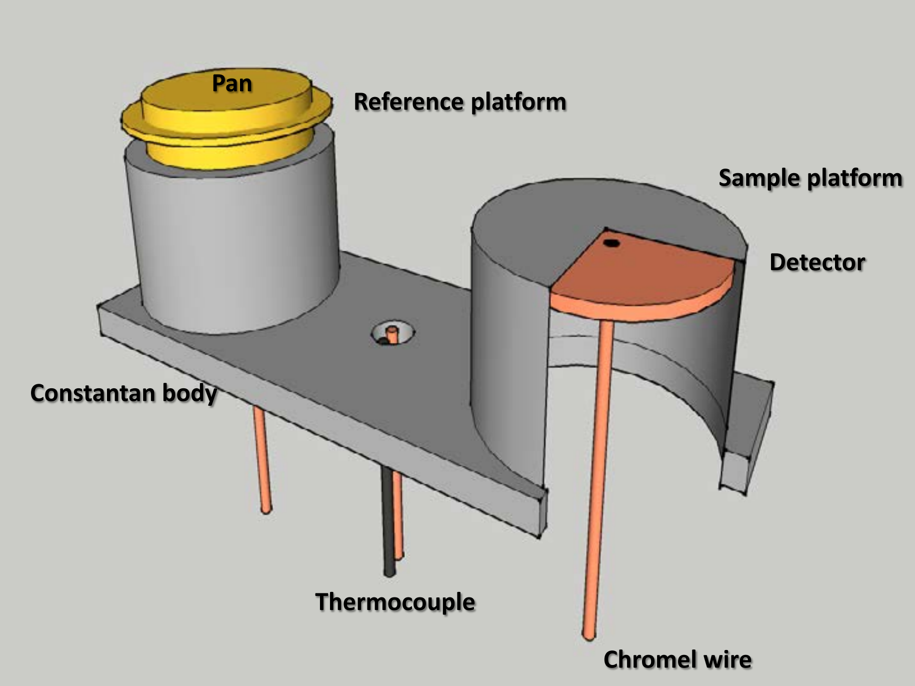

Figure 3.14 Differential scanning calorimeter description, with the two platforms design for reference signal. Three temperature sensors are located in platforms and between them, in order to monitor heat flow in the cell.

As previously said, during the experiment the sample is contained in DSC pans, which are made of high purity metals – like Al, Pt or Ag -. Different kind of pans can be used, depending on the measurement purpose and nature of the sample. Standard aluminum pans are the most commonly used, but sealed pans are preferred to prevent sample mass loss, in case it contains volatiles, for example. Experiments run here were always performed using standard aluminum pans, with masses around 20 mg.

Two different ways have been used to measure heat capacity in amber samples in this work: (i) traditional DSC and (ii) Modulated-Temperature DSC in quasi-isothermal mode (MT-DSC).

Determination of heat capacity using the traditional DSC is done by performing two different runs: a blank run (in which both pans in the platforms are empty), a calibration run (this means a standard material is used, usually sapphire above room temperature), and the sample run (with the sample we are interested in). At the beginning of the run, the DSC cell is held isothermally at temperature T_1 for a short time, and then the control starts producing a constant heating rate. At the final temperature T_2, the heating is stopped and cell is kept isothermally. In the process, DSC signal is exponential shaped, as a consequence of the 'charging' process in the cell. All three curves for the runs mentioned above have the same 'background' shape, and so to determine heat capacity only the difference amplitude between the sample run and the empty pans run need to be measured. Of course, this process is valid having a reference curve (sapphire DSC curve), which is used as the calibration curve. This process is qualitatively shown in Figure 3.15.

The more the conditions in the experiments are kept identical –equal pan masses for reference, sapphire and sample down to 0.1%, constant environment conditions during the experiment, etc. – the higher the accuracy, which can reach values of ±1% in the best scenario.

The second protocol here to measure heat capacity is performed with the Modulated-Temperature DSC (MT-DSC) one, which was first used during the early 1990s by [ReEH93][GiSR93] as an extension of the conventional DSC technique. Changes introduced by this evolution lay in the introduction of a small perturbation on the traditional heating program, by a low-amplitude sinusoidal signal mounted on the heating/cooling scans. This procedure enables deconvoluting two parts of the sample response: the reversing component and a thermal-history-dependent (non-reversing) component, whereas the traditional DSC gives only the total response. The amplitude of the modulated heat flow is used for determination of reversing heat capacity as follows

$$C_{\mathrm{p,rev}} = \frac{heat\ flow\ amplitude}{heating\ rate\ amplitude} K\left(C_{\mathrm{p,rev}}\right) \tag{3.2}$$

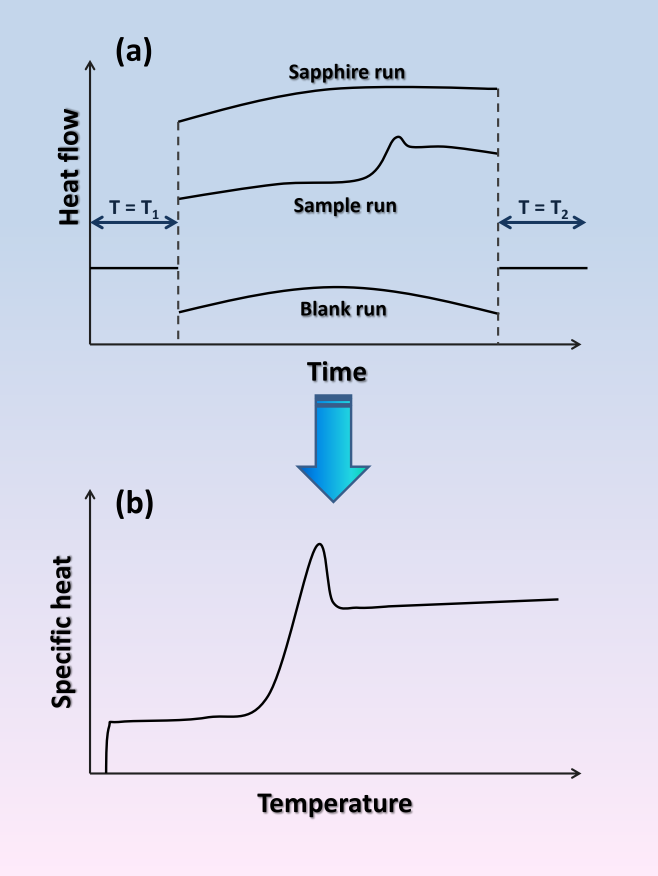

Figure 3.15 Qualitative description of the heat capacity measurement using the traditional DSC method. (a) DSC heat flow signal obtained in calibration, blank and sample runs. Notice blank run has the same initial and final heat flow values, as empty pans are located in both platforms. At the beginning and end of the heating rate, signal shift appears, seen in the jump from and to constant heat flow values during T_1 and T_2 isothermals. (b) Specific heat curve for the sample after convolution of the three heating curves [MeBr09].

where $K(C_{\mathrm{p,rev}})$ is the calibration constant for the reversing heat capacity. In the determination of the heat capacity using this modulated method, low modulation amplitudes –in this work 0.5 K/min– and periods –from 60 s up to 100 s– must be carefully chosen. For the measurement of heat capacity using MT-DSC with high accuracy, a strict protocol has been developed in this thesis, in order to quantitatively describe the effects of the hyperageing in the amber samples –in the enthalpy and entropy curves, fictive temperatures, etc.-. For clarity and to avoid too extensive and detailed description of the method here, the reader is referred to Appendix A for a deep discussion and some examples.

3.6 Low-temperature calorimetric methods

The design and construction of a versatile low-temperature calorimeter has already been introduced in section 3.5.1, with discussion about all critical aspects to take into account. As it can be easily understood, it is the calorimetric method choice what determines the design and construction of the calorimeter, as well as the electronics involved in the measurement. It is no surprise then the three calorimetric methods chosen for the low-temperature heat capacity measurements: (I) standard relaxation method, (II) an alternative ‘fast’ relaxation method, and (III) a quasi-adiabatic continuous method –which has been employed for the first time at liquid helium temperatures in this work–. All these three methods are quasi-adiabatic, in the sense that a finite and moderately large relaxation time constant is always present between the sample and the thermal sink. Actually, one of the figures of merit in the work developed here is the versatile character of the calorimeter, allowing the implementation of these three methods in situ. This aspect exponentially enhances the measurement power of our set-up, providing measurements from 50 mK up 40 K (and even room temperature in some cases), in a highly automated process. In order to contextualize the methods employed here, and discuss the particular advantages and drawbacks of these techniques, we start with a brief review of the existing low-temperature calorimetric methods and their possibilities.

Attending to the historical development of calorimetry, the first method to be introduced was the adiabatic one by Nernst in the beginning of 20th century, in which, as already mentioned in 3.5.1, an ‘infinite’ –high in practice– thermal resistance between sample and thermal reservoir is employed [NeLi11]. Because of curves obtained by this method, it is called a step technique (see Figure 3.16), where given an energy amount supplied to the sample $\Delta Q = P \cdot \Delta t$, a jump in temperature ΔT is obtained, directly proportional to heat capacity C

$$C_{\mathrm{p}}(T) = \lim_{\Delta T \to 0} \left(\frac{\Delta Q}{\Delta T}\right)_{\mathrm{p}} \tag{3.3}$$

The temperature assigned to an experimental point is $T_{\mathrm{med}} = (T_{\mathrm{i}} + T_{\mathrm{f}}) / 2$, with T_{i} and T_{f} initial and final temperatures respectively, taking into account thermal drift (see Figure 3.16). This method has been successfully implemented in temperatures from 0.3 K up to above 300 K [HaSS77], and typical accuracy is below 1% (depending on sample contribution to the total heat capacity, this is sample plus addenda).

The large mass sample requirement of this method to achieve good accuracy, as well as the difficulties derived from the adiabatic conditions, gave rise to other techniques like AC-Temperature calorimetry. In this technique the sample is heated by passing an AC current through the heater, with angular frequency $\omega/2$. The corresponding peak-to-peak temperature response T_{ac} is measured by applying an AC voltage to the thermometer and synchronously detecting it with a lock-in amplifier. Choosing the adequate conditions, heat capacity calculation is given by the simple expression

$$C_{\mathrm{p}}(T) \approx \frac{\dot{Q}_0}{2\omega T_{\mathrm{ac}}} \tag{3.4}$$

where $\dot{Q}_0$ is the amplitude of the sinusoidal heating signal (see Figure 3.16). Adequate conditions here mean sample and addenda response time constants much smaller than $1/\omega$, and sample to bath time constant much bigger than $1/\omega$.

Another possibility when measuring heat capacity at low temperature in the adiabatic configuration, as already introduced in section 3.5.1, is the adiabatic continuous method. In this method, heat pulses are chosen to be higher than those used in the step method, and so temperature increase goes well above the usual 1% jump. Instead of accounting for the heat capacity using the complete step, use of the temperature derivative with time allows ‘instantaneous’ determination of $C_{\mathrm{p}}(T)$ at every measuring point, since, taking infinitesimal changes in Eq (3.3) we have

$$C_{\mathrm{p}}(T) = \frac{V(T)\cdot I}{\frac{\mathrm{d}T}{\mathrm{d}t}(T)} \tag{3.5}$$

where the current applied to the heater I is kept constant during a run, and voltage drop is recorded as a function of temperature $V(T)$.

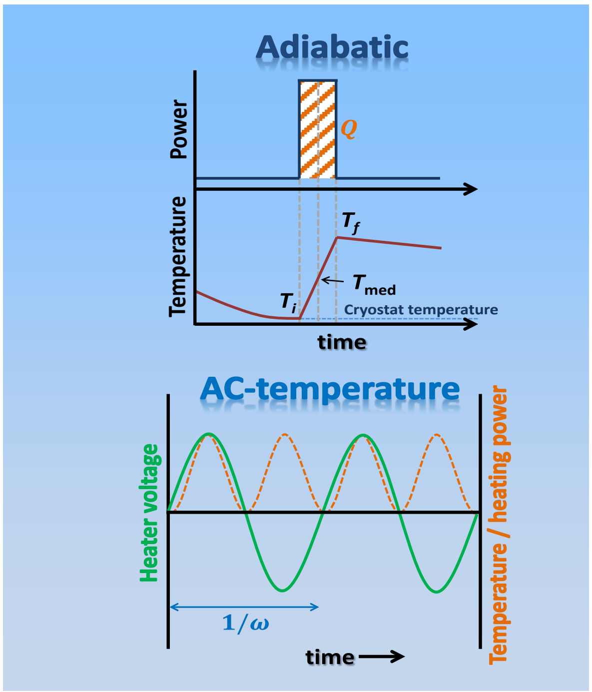

Figure 3.16 Signals description in the adiabatic and AC-temperature methods. Measurement temperature T_{med} in adiabatic technique is calculated taking into account thermal drift correction. In AC-temperature technique heating is applied in AC mode with low excitation amplitude $\Delta T/T < 1\%$.

We move now to the low-temperature techniques employed in this work, as said before, two versions of the relaxation method and a fast quasi-adiabatic continuous one. An exhaustive discussion on the implementation and results obtained by these methods is presented below, with details and key aspects which push accuracy to optimal values.

3.6.1 Relaxation methods

We start with the first and most broadly used method, the standard relaxation [Gmel79][BaWh99][PéRa07]. In this method, the system is driven to the initial temperature T_{i} using the control in the thermal reservoir (copper ring in Figure 3.10 and Figure 3.11). After equilibrium is reached –what means thermal drifts below 1 μK/s at liquid helium temperatures, and some tens of nK/s at ^{3}He/^{4}He mixture temperatures–, heating power to the sample is started. Using the heater attached to sapphire disc (see Figure 3.10), sample and addenda are driven to a second equilibrium state at temperature $T_i + \Delta T_\infty$, with $\Delta T_\infty / T \approx 1\%$ –so that most parameters can be considered constant without introducing error–. Again, equilibrium state is given by conditions imposed to thermal drift, which is forced to be parallel to the initial one within typically 2 – 4% in absolute value, and in any case lower than a given value –similar to those in the first equilibrium state–. Once the second equilibrium state is reached, heating power is switched off, and hence sample and addenda relax to the first equilibrium state. Heating and cooling curves obey an exponential dependence with time, respectively:

$$\Delta T(t) = \frac{P}{\kappa_\mathrm{H}} \cdot \left(1 - \exp\left(-\frac{t}{\tau}\right)\right) \tag{3.6}$$

$$T(t) = T_0(t) + \Delta T_\infty \cdot \exp\left(-\frac{t}{\tau}\right) \tag{3.7}$$

and are related to the heat conductance κ_H of the thermal link (TL) and the relaxation time constant τ, from which the total heat capacity C_p (T) is easily derived as given by Eq (3.8) and Eq (3.9)

$$\kappa_H = {}^{P}\!/_{\Delta T_\infty} \tag{3.8}$$

$$C_P = \kappa_H \cdot \tau \tag{3.9}$$

where τ is obtained by fitting the relaxation exponential curve. As can be seen in Figure 3.17a, ΔT_∞ is the temperature jump given by extrapolating the thermal drift from the initial equilibrium state, calculating the difference with the temperature value when power is switched off.

In our alternative relaxation method [PéRa07], the stationary state is not reached, but the power applied is switched off at some time during the heating process as shown in Figure 3.17b (usually when $\Delta T/T \approx 1\%$). Again the total heat capacity is calculated after obtaining τ from the relaxation curve, and κ_H by a fit of the heating curves given by Eq (3.6). Using these two methods, specific-heat measurements in the temperature range from, say, 0.1 K up to 30 K can be easily performed. An example of these two methods applied to the low-temperature specific heat measurement in Highly Oriented Pyrolytic Graphite (HOPG) is shown in Figure 3.17.

In principle, the standard relaxation method (Figure 3.17a) is employed with lower heat capacity values, what implies smaller relaxation time constants (usually below 2 minutes), whereas the alternative relaxation method (Figure 3.17b) is applied when heat capacity increases more rapidly than the thermal link conductance (usually at higher temperatures) and consequently τ grows above several minutes. In both methods, the relaxation time constant τ is straightforwardly obtained from linear fits in semilogarithmic plots, such as those in Figure 3.17c for the corresponding points in Figure 3.17a and Figure 3.17b. The inset in Figure 3.17shows the additional T vs $(1 - e^{-t/\tau})$ plot to determine the value of ΔT_∞ in the alternative relaxation method. Notice that the excellent linearity in all these curves of Figure 3.17c is a clear evidence of the quality of the conducted experimental method and of the assumptions made.

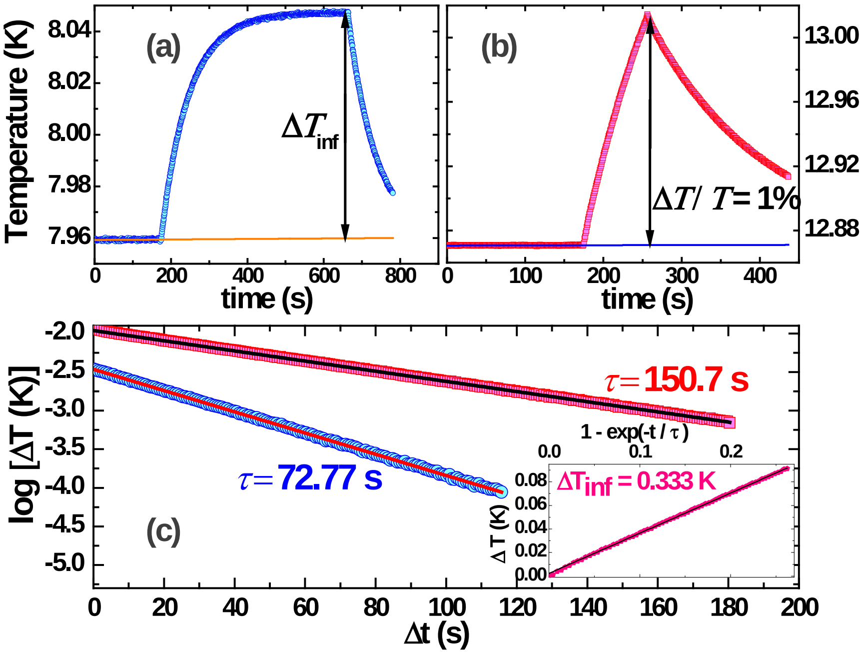

Figure 3.17 Real example of acquisition points (temperature versus time) obtained in HOPG graphite when using (a) standard relaxation method and (b) alternative relaxation method. (c) Semilogarithmic plot for the corresponding points in (a) and (b) to extract the time constant τ. Inset: Temperature increase versus $(1 - e^{-t/\tau})$ to determine ΔT_∞ in the alternative relaxation method.

3.6.2 Quasi-adiabatic continuous method

A much faster calorimetric method, though usually less accurate, is the already mentioned continuous heating method [Gmel79][BaWh99]. The simplest and most traditional version is the ideal adiabatic one, where the simple relation given in Eq (3.5) is assumed. This method has been usually employed at relatively high temperatures, though experiments down to 15 K have also been conducted [WaPJ01]. An opposite version of this technique is exhaustively discussed in [PlWJ02], where an accurate determination of the heat flux to the sample using commercial Peltier elements is performed. This version needs only a constant-reference temperature from the thermal bath, as well as a weak thermal contact between cell and bath (τ of the order of few tens of seconds). The use of a thermometer and a heater for the sample in four-terminal configuration is needed, in order to monitor the applied-power evolution with time/temperature. Heat losses calibration is performed in every experiment by simply recording the sample temperature evolution $T(\mathrm{t})$ with time by switching off the heating power at a given temperature $T(\mathrm{t}_0)$.

In the laboratory, a new (*quasi-adiabatic*) version [PéRa07] of the continuous method has been developed, using a different approach to those two mentioned above, though likely closer to the former one. However, the non-perfect adiabaticity of the real calorimeter is physically taken into account by using a more realistic equation of heat. Furthermore, our versatile calorimetric set-up allows us to choose between this quasi-adiabatic continuous method, two thermal relaxation methods and even the adiabatic one for the low-temperature specific-heat measurements, using the very same experimental set-up.

We will discuss now the quasi-adiabatic continuous method [PéRa07], which we have used here for the first time at liquid-helium temperatures. As already described above, our calorimetric cell has a fixed weak thermal contact with the thermal sink, given by a copper, Pt/W or manganine wire(plus any other parallel thermal conduction mechanism that might contribute in a much lower amount) that results in relaxation time constants of the order of $\tau \sim$ 30-60 s at liquid helium temperatures. The basic idea of the method is that there will always be an effective and measurable cooling power for the cell $P_{\mathrm{cool}}(T)$ as a function of temperature for a given sample, *provided we keep fixed the temperature of the thermal sink*. All this means that the heat transport equation has to take into account both cooling and heating power terms:

$$C_{\mathrm{p}}(T) \cdot \frac{dT}{dt}(T) = P_{heat}(T) + P_{cool}(T) = V_h(T) \cdot I_{\mathrm{h}} + C_{\mathrm{p}}(T) \cdot \Theta(T) \qquad (3.10)$$

where $\Theta(T) = dT/dt$ accounts for the intrinsic *negative* thermal drift of the system measured by spontaneous or “standard” cooling ($I_{\mathrm{h}} = 0$), this is, at zero applied heating power. The thermal sink is easily fixed (and monitored) at either 4.2 K (if helium bath is used), or 77 K (if liquid nitrogen, as in previous works [PéRa07][HJSK09][TMRR06]). The thermal drift of the system $\Theta(T)$ is determined for every single experiment, as it can vary depending on the total heat capacity of the cell (sample plus addenda). The heat capacity is hence determined by

$$C_{\mathrm{p}}(T) = \frac{V_h(T) \cdot I_{\mathrm{h}}}{\frac{dT}{dt}(T) - \Theta(T)} \qquad (3.11)$$

Eq (3.11) shows that, in order to calculate the heat capacity curve, both the heating *dT/dt* and cooling $\Theta(T)$ curves need to be combined together. Here comes a significant difference with other methods in the literature [PlWJ02][WaPJ01], where heating and cooling curves provide two “*independent*” heat capacity curves. Applied current to the heater I_{h} is selected so that *dT/dt* is slow enough (typically < 3 K/min) to ensure good internal equilibrium in the cell. The empty-cell heat capacity is measured in a different run to subtract the addenda contribution.

At this point it is important to highlight the main difference that makes this method a fast and reliable tool to measure specific heat: whereas in the relaxation method the experimental time scale is governed by the thermal link between reservoir and cell, in the continuous method only internal thermal equilibrium in the cell is required to be fast compared to all other characteristic times, which at low temperatures is of the order of some tens of milliseconds. A thermal link between the cell and the sink is used so that the relaxation time constant τ is always of the order from half to one minute at liquid helium temperatures. This is a second important variance with earlier applied continuous methods, where thermal connection of the sample to the surroundings is chosen to be either extremely bad (τ >> 1 min) [Gmel79][BaWh99] or extremely good (τ << 1 s) [PlWJ02]. As can be seen, our low-temperature version of the quasi-adiabatic continuous method has something in common with the thermal relaxation one. An effective weak thermal link is needed to have an effective and measurable cooling rate given by the standard cooling $\Theta(T)$ (i.e., zero heating power), what allows us to employ *the same experimental set-up* for both thermal relaxation and quasi-adiabatic continuous techniques. Heating rates must be chosen carefully, usually below 2–3 K/min, to ensure that internal equilibrium is fulfilled at every single temperature among all the components in the experimental cell (see Figure 3.10). Heating and cooling must also be done above some critical rate, since when making derivatives too low, uncertainties start dominating Eq (3.11). A remarkable aspect is that the density of data points in the heat capacity versus temperature plot can be enhanced by increasing the reading frequency of the electronics used for the sensors. This makes the method even more suitable for specific heat studies on systems with first order transitions, as the resolution of the peaks can be much better than with other methods. With the experimental cell described in this work, *dT/dt* on heating and cooling can also be directly used as valuable thermograms to monitor transitions such as those present in $CeSb_2$, as shown in Figure 3.18.

To illustrate how our continuous method works, we show in Figure 3.18 different thermograms obtained to measure the specific heat of the $CeSb_2$ sample. The three magnetic transitions in $CeSb_2$ are clearly observed in the figure (on grey shadows), both in heating (Figure 3.18a) and cooling (Figure 3.18c) curves, hence also giving an estimation of the uncertainty in the determination of the transition temperature. On the other hand, *dT/dt* curves on heating for different applied currents (powers) (see Figure 3.18a and Figure 3.18b) can be used to check the reproducibility of the measurement. For the empty cell, heating (Figure 3.18b) and cooling (Figure 3.18d) smooth curves with no sharp features are observed, as expected. In fact, the heating and cooling rates used for the empty cell measurement are typically higher than those employed with the sample, due to its lower total heat capacity. These faster rates carry no problem, as internal equilibrium is more easily fulfilled for the addenda measurements.

As already described above, the heat capacity curve is determined via Eq (3.11) from both the heating *dT/dt* and cooling $\Theta(T)$ curves, taken under the very same experimental conditions, i.e., with the thermal sink at its fixed temperature. During the heating curve, the heater voltage is recorded as a function of temperature to take into account possible variations of its resistance with temperature. Although we usually measure the spontaneous cooling of the system $\Theta(T) = dT/dt$ at zero applied heating power ($I_h = 0$), Eq (3.11) is also valid if cooling slower with a small applied current, by changing in the numerator the heating power by the net power difference.

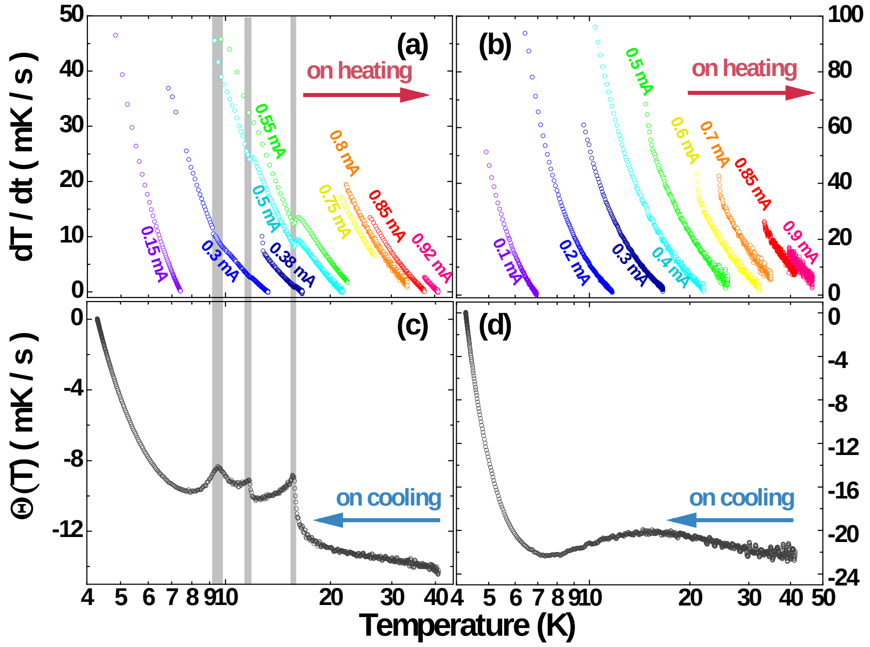

Figure 3.18 Temperature derivatives with time on heating *dT/dt* [panels (a) and (b)] and on cooling $\Theta(T)$ [panels (c) and (d)]: (a) $CeSb_2$ and (b) empty cell, in both cases by heating with different applied currents; (c) $CeSb_2$ and (d) empty cell, by standard cooling at $I_h = 0$. The three magnetic transitions in $CeSb_2$ measurements [panels (a) and (c)] are highlighted with grey shadows at 9.5 K, 11.7 K and 15.6 K.

Finally, to obtain the specific heat of the given substance, the heat capacity of the addenda is measured using the same procedure (e.g., panels (b) and (d) in Figure 3.18) and then it is subtracted from the total heat capacity measured. For this case of the $CeSb_2$ sample, the corresponding heat capacity curves are shown in Figure 3.19.

Moreover, we can see in Fig. 4 that the different heating runs, obtained using different currents, previously shown in Figure 3.18 (a) and (b), merge very well into corresponding single curves of heat capacity, with differences well below 3% in absolute values.

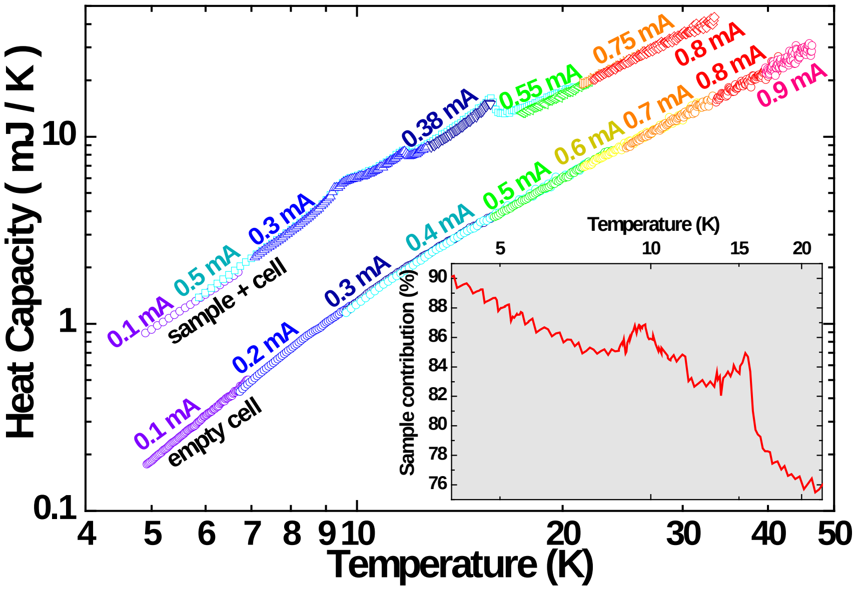

Figure 3.19 Heat capacity comparison among the different applied currents using the continuous method, calculated from the data in Figure 3.18 with Equation 3.7, for both the 'empty cell' and 'sample + empty cell'. Inset: Relative $CeSb_2$ contribution to the total heat capacity.

3.7 Calorimetry software

In the design and construction of our low-temperature calorimeter, much work has also been done in order to end up with a user-friendly environment for the heat capacity measurements. For this purpose, a complete set of programs using Labview language has been developed, which allows a full automation of the experiment. All three methods are available and interchangeable, with a complete control on the experimental set-up, so that in situ comparison of data obtained by the different techniques is easily done. Since describing in detail these programs exceeds the scope of this chapter, readers interested in the calorimetry software are referred to Apendix B, where a deep description of the programs structure is presented.

3.8 Conclusions

In this third chapter, an extensive and detailed discussion on all the aspects involved in the development of a low-temperature calorimeter as well as in the employment of a commercial DSC technique at higher temperatures has been presented.

The low-temperature calorimeter combines the ability to perform heat capacity measurements on solid samples of a few milligrams, and the versatility to operate in a vast temperature range: from 0.05 K up to 100 K or even room temperature. A big technical effort has been done in order to make this calorimeter not only powerful, but also easy to use with a friendly software interface for the user. The requirement of using two different cryostats to cover the whole temperature range has driven us to a plug and play calorimeter, with an easy table-top sample mounting procedure. Sensitivity down to nJ/K is achieved at the lowest temperatures, and thermal stabilities of the order of some tens of nK/s. In the way to construct this calorimeter, experience on the low-temperature techniques has been gained, since working with liquid ^{4}He cryostats has required from the leak testing to the complete wiring of the experimental insert. The dilution refrigerator, which has allowed us performing calorimetric measurements down to 50 mK, provided a peerless possibility to build and calibrate our own thermometry using different primary thermometers as well. But our technical endeavour has also given as result the successful implementation and validation of a quasi-adiabatic continuous method at low temperatures, which, together with the relaxation methods, provides our calorimeter with high accuracy in short experimental times.

Further, the search of connection between stabilization processes around the glass transition and the low-temperature properties of glasses has made DSC and MT-DSC the second key techniques used in this work. Although commercial equipment has been employed to characterize our hyperaged amber glasses, the design of a protocol to precisely determine and compare the specific heat of our samples with accuracy next to 1% comprises also an important part in the experimental work presented here.

[BaWh99] T. H. K. Barron and G. K. White, *Heat Capacity and Thermal Expansion at Low Temperatures*. Kluwer Academic/Plenum, 1999.

[BKPS89] V. G. Bessergenev, Y. A. Kovalevskaya, I. E. Paukov, and Y. A. Shkredov, "Heat capacity measurements under continuous heating and cooling using vacuum adiabatic calorimetry," *Thermochimica Acta*, vol. 139, no. 1, pp. 245–256, 1989.

[CrRe07] D. Q. M. Craig and M. Reading, *Thermal Analysis of Pharmaceuticals*. Taylor & Francis Group, 2007, p. 400.

[Cryo00] Lakeshore Cryotronics, "www.lakeshore.com".

[GiSR93] P. S. Gill, S. R. Sauerbrunn, and M. Reading, "Modulated differential scanning calorimetry," *Journal of thermal analysis*, vol. 40, no. 3, pp. 931–939, 1993.

[Gmel79] E. Gmelin, "Modern low-temperature calorimetry," *Thermochimica Acta*, vol. 29, no. 1, pp. 1–39, 1979.

[HaSS77] O. Haida, H. Suga, and S. Seki, "Calorimetric study of the glassy state XII. Plural glass-transition phenomena of ethanol," *The Journal of Chemical Thermodynamics*, vol. 9, no. 12, pp. 1133–1148, 1977.

[HJSK09] M. Hassaine, R. J. Jiménez-Riobóo, I. V Sharapova, O. A Korolyuk, A. I. Krivchikov, and M. A. Ramos, "Thermal properties and Brillouin-scattering study of glass, crystal, and 'glacial' states in n-butanol.," *The Journal of chemical physics*, vol. 131, no. 17, p. 174508, 2009.

[Inst00] TA Instruments *www.tainstruments.com*.

[John28] J. B. Johnson, "Thermal agitation of electricity in conductors", *Physical Review*, vol. 32, pp. 97 – 109, 1928.

[Kapi38] P. Kapitza, "Viscosity of Liquid Helium below the lambda-Point," *Nature*, vol. 141, no. 74 & 75, 1938.

[Kops95] H. Kopsch, *Thermal Methods in Petroleum Analysis*, Wiley, 1995.

[Loun74] O. V. Lounasmaa, *Experimental Principles and Methods Below 1 K*, Academic Press, 1974.

[MeBr09] J. D. Menczel and R. Bruce Prime, *Thermal Analysis of Polymers: Fundamentals and Applications*, (1st Edition) Wiley & Sons, 2009.

[NeLi11] W. Nernst and F. A. Lindemann, “Spezifische Wärme und Quantentheorie,” *Zeitschrift für Elektrochemie und angewandte physikalische Chemie*, vol. 17, no. 18, pp. 817–827, 1911.

[Nyqu28] H. Nyquist, “Thermal agitation of electricity in conductors”, *Physical Review*, vol. 32, pp. 110 – 113, 1928.

[Onne11] K. Onnes, " On the change of electric resistance of pure metals at very low temperatures", *Proceeding of Royal Netherlands Academy of Arts and Sciences (KNAW)*, vol. 13 II, pp. 1274–1276, 1911.

[OsRL72] D. D. Osheroff, R. C. Richardson, and D. M. Lee, “Evidence for a new phase of solid He3”, *Physical Review Letters*, vol. 28, no. 14, pp. 885–888, 1972.

[PAHF13] T. Pérez-Castañeda, J. Azpeitia, J. Hanko, A. Fente, H. Suderow, and M. A. Ramos, “Low-temperature specific heat of graphite and CeSb2: Validation of a quasi-adiabatic continuous method,” vol. 173, pp. 4 – 20, 2013.

[PéRa07] E. Pérez-Enciso and M. A. Ramos, “Low-temperature calorimetry on molecular glasses and crystals,” *Thermochimica Acta*, vol. 461, no. 1–2, pp. 50–56, 2007.

[PlWJ02] T. Plackowski, Y. Wang, and A. Junod, “Specific heat and magnetocaloric effect measurements using commercial heat-flow sensors,” *Review of Scientific Instruments*, vol. 73, no. 7, pp. 2755 – 2765, 2002.

[Pobe96] F. Pobell, *Matter and methods at low temperatures*, (2^{cnd} Edition) Springer, 1996.

[ReEH93] M. Reading, D. Elliott, and V. L. Hill, “A new approach to the calorimetric investigation of physical and chemical transitions,” *Journal of thermal analysis*, vol. 40, no. 3, pp. 949–955, 1993.

[Schu74] R. J. Schutz, “Thermal relaxation calorimetry below 1 K,” *Review of Scientific Instruments*, vol. 45, no. 4, pp. 548–551, 1974.

[SiSa74] D. S. Simons and M. B. Salamon, “Specific heat and resistivity of gadolinium near the Curie point in external magnetic fields,” *Physical Review B*, vol. 10, no. 11, p. 4680, 1974.

[SuSe68] P. Sullivan and G. Seidel, “Steady-state, ac-temperature calorimetry,” *Physical Review*, vol. 173, no. 3, pp. 679 – 685, 1968.

[TMRR06] A. Triolo, A. Mandanici, O. Russina, V. Rodriguez-Mora, M. Cutroni, C. Hardacre, M. Nieuwenhuyzen, H. J. Bleif, L. Keller, and M. A. Ramos, “Thermodynamics, structure, and dynamics in room temperature ionic liquids: the case of 1-butyl-3-methyl imidazolium hexafluorophosphate ([bmim][PF6]).,” *The journal of physical chemistry. B*, vol. 110, no. 42, pp. 21357–64, 2006.

[WaPJ01] Y. Wang, T. Plackowski, and A. Junod, “Specific heat in the superconducting and normal state (2–300 K, 0–16 T), and magnetic susceptibility of the 38 K superconductor MgB2: evidence for a multicomponent gap,” *Physica C*, vol. 355, no. 179, pp. 1–17, 2001.

[Whit79] G. K. White, *Experimental Techniques in Low Temperature Physics*, (4th Edition) OUP Oxford, 2002.

[ZePo71] R. C. Zeller and R. O. Pohl, “Thermal conductivity and specific heat of noncrystalline solids”, *Physical Review B*, vol. 4, no. 6, 1971.

4

HYPERAGEING AND THE LOW-TEMPERATURE ANOMALIES IN DOMINICAN AMBER

Amber is a fossilized tree resin which has undergone a maturation process for a period of time that can vary from several thousand years up to above hundred million years. *Amber* is, as well, the etymological origin of the modern word electron, coming from its Greek meaning. It was Thales of Miletus who first observed the effects of electrical charge by rubbing an amber bar with a cloth, after what it was able to attract light objects. From the chemical point of view, amber is a macromolecule result of molecular polymerization, isomerization reactions and cyclation from precursors of the labdane family (like communic acid). Starting with units of the form $C_{20}H_{32}$, the maturation processes build the organic chain, driving the liquid resin into the glassy gemstone. The formation of amber needs of the presence of high pressures produced by deposited sediments on top of it and temperatures above 30 ºC. Its successful natural fabrication is highly susceptible to fail because of physical and biological processes (sunlight-activated reactions, microorganisms, etc.). All trees produce resins, but only those resistant to disintegration survive until our days, some of which end up forming amber. It is not only time what matters when producing amber, but its combination with temperature and pressure. The joint effect of these three physical parameters produces what is called *maturation*.

Amber has been greatly appreciated from ancient as decorative stone, incense or even adhesive. The use of amber and other fossil resins are first found in the Paleolithic, around twelve thousand years B.C., and trade of this organic gemstone was already quite extended around eight thousand years B.C. [LaPo02].

Only two resins exist with the potential capability to fossilize, terpenoids, which are produced by conifers and angiosperms, and phenolic resins from angiosperms. A classification of ambers into five different types exists, based on their chemical and structural composition [AnBo93][Ande94]. The most abundant class is that in which Baltic and Dominican ambers are included (named as class I [AnWB92]). The former one is mainly based on succinic acid, whereas the latter is basically composed of enantio-labdatrienonic acids and lacks the succinic one [AnWB92].

Attending to the physical properties of amber, it is an amorphous polymer. Although originated from well-defined units, the result is a nonperiodic group of chains (originated by covalent bonding), with weaker bonds between chains (as van der Waals forces or hydrogen bonds), which confer amber its viscosity. The liquid resin is driven into the glassy state as the covalent bonds are progressively formed, hence reducing molecular mobility and increasing its viscosity. This route to obtain a glass has been widely studied [CoFR02][CCFF09], and is known as chemical vitrification, since molecular arrest is produced by chemical bonds instead of by lowering the temperature or increasing the pressure, as commonly done. Molecular arrest in the ‘fresh’ resin takes place in times of the order of days, and thus a solid precursor is obtained. After maturation the solid precursor transforms into amber. Maturation means further polymerization, isomerization, crosslinking and cyclization under convenient conditions of pressure and time. When amber is heated, the glass transition is reached (typically at temperatures ranging from 100 ºC up to 170 ºC) and chain mobility is enhanced. Above 200 ºC amber starts decomposing, and if temperatures up to 400 ºC – 500 ºC are reached, it burns completely.

Maturation in amber entails the ageing process present in glasses, which drives the system to lower energy minima in the potential energy landscape, as a consequence of the enthalpy/entropy loss. This makes amber a glass with promising kinetic and thermodynamic stability, as long as the ageing process has been efficient enough.

4.1 Introduction

Amorphous materials surround us in daily life. They are present in basic products such as pharmaceuticals, plastics, the fiber used in telecommunications or window glasses. In recent years a rising interest in producing these materials with exceptional properties, such as enhanced kinetic and thermodynamic stability, has appeared. Controlling these properties means producing glasses with potentially improved characteristics compared to the conventional ones.

The glass is always in a thermodynamic state of nonequilibrium, and hence continuous structural relaxation happens in this system below T_g. These relaxation processes drive glasses towards lower energy states in the energy landscape (see Figure 1.2), where plenty of local minima exist. The final limit the glass can reach is the metastable thermodynamic state the supercooled liquid would have at such temperature [Braw85]. But accessing this limit is also matter of at least an exponentially increasing time with decreasing annealing temperature below T_g [ANMM00]. Much work has been done in the past to study the effects of annealing/ageing in different glassy substances [LaGM81][WaSM06][BLLB12], but human time scales have been found to be too short to produce efficient enough stabilizations in bulk glasses, compared to the accelerated ageing obtained in thin and ultrathin films of organic ultrastable glasses [SKMK07]. Ageing times going from 10^3 to 10^9 years would be needed in order to access a similar stabilization to those achieved in ultrastable thin films starting from a conventional glass [KSEW08].

As already discussed in the first two chapters, many open questions exist in the physics of glasses that need deep understanding, to the point that no consensual theory exists on the phenomenology of the glass transition or the origin of the low-temperature/energy anomaly known as the boson peak. Besides, clarification about the role played in the low-temperature anomalies by configurational disorder frozen-in at the glass transition needs to be addressed. Although the extra excitations in glasses at temperatures below 1 K are quite well explained in terms of the so-called Tunneling Model (TM) [Phil72][AnHV72] introduced by Phillips and by Anderson *et al.* soon after the experimental observations of Zeller and Pohl [ZePo71], a general feeling still exists of misunderstanding around the universal low-temperature glassy anomalies and their connection with the processes present at the glass transition.

For this purpose we have chosen a glass like amber, which presents extreme ageing effects that may have driven it deep in the potential energy landscape, and undoubtedly much further than any other human-scale annealing process has been able to do up to now. It represents a model system in order to study the connection between the relaxation present in all glasses below the glass transition and the low-temperature additional excitations. Many answers could be found if a clear correlation between the sub-T_g phenomenology and the excess in the density of states at low energies is observed. Not only this, but also the validity of many models and theories proposed up to the present could be tested, allowing us to take a step forward in the understanding of the physics of glasses.

In order to perform the analysis of our experimental data, the Soft Potential Model (SPM) will be employed [Pars94][KaKI83][BGGP92][RaBu98], which extends and somehow generalizes the TM. The idea of additional (non-acoustic) quasi-local vibrations is the basis of this model, which can be modeled by asymmetric quartic potentials, including –and extending– the double-well potentials of the TM. It has been shown [BGGP92][RaBu97] that the SPM correctly accounts for the low-temperature and low-frequency glassy properties up to the boson peak energies. The recent theory of *vibrational instability*, further supports and extents the view given by the SPM [GuPS03][PaSG07], predicting the appearance of the maximum of the boson peak derived from interacting quasi-local harmonic modes.

4.2 Kinetic and thermodynamic stability in Dominican amber

Amber is a peculiar glassy system, since beginning with a conventional 3D glass (chemical glass as already explained) the unusually long ageing process is expected to drive the system into an extraordinary stable glassy state, both from the kinetic and thermodynamic point of view. We call this extreme ageing process *hyperageing*, which in amber involves times of the order of tens of millions of years at temperatures ~ T_g – 90 K. Dominican amber samples studied here present ageing processes of around 20 million years (depending on the deposits Dominican amber goes from 15 to 45 million years [LaPo02][Grim96])

Using standard chemical analysis, the composition of the samples was found to be 78.6 % C, 9.9 % H and 11 % O in mass, in reasonable agreement with other values found in the literature [WWSL89]. Nitrogen content is ~ 0.1 % and sulfur impurities below 0.2 %. Mass density of the samples was measured using a Mettler Toledo AB 265-S balance by means of the Archimedes method, with bidistilled water as fluid. The pristine sample has mass density $\rho = 1.08 \pm 0.03$ g / cm^3 and the rejuvenated sample $\rho = 1.05 \pm 0.02$ g / cm^3. The rejuvenated sample was obtained after heating the pristine hyperaged sample and isothermally annealing at 395 K for three hours under vacuum conditions $P \leq 10^{-2}$ mbar. A densification process of around 2.8 % (though with admittedly large experimental error) is undergone by the sample during the stabilization, what agrees well with values reported by Zhao *et al.* [ZhSM13] in Dominican amber. A parallel effect is found in other glasses with extraordinary kinetic and thermodynamic stability such as physically-vapor-deposited IMC thin films [SKMK07], where densifications up to almost 2 % are reported. It is important to measure the same sample when quantifying densification in amber in order to minimize possible contributions due to heterogeneities or impurities among the samples.

The pristine samples may have accessed an extremely stabilized glassy state. Qualitative and quantitative study of the ageing process is done determining the specific heat curve around the glass transition in amber. Enthalpy relaxation processes like ageing manifest as overshoots around the glass transition, which reflect the previous entropy loss due to this natural stabilization. Similar effects emerge in glasses obtained from slowly supercooled liquids, being the overshoot proportional to the difference between the heating rate (of the measurement) and the cooling one when the glass was formed [JaGB99].

Modulated Differential Scanning Calorimetry (MT-DSC) on Dominican amber samples was performed using a commercial TA Instruments Q100 model (see Section 3.5.2 for further details). Using the MT-DSC technique it is possible to evaluate separately the reversing and non-reversing (thermal history dependent) processes involved in the specific heat.

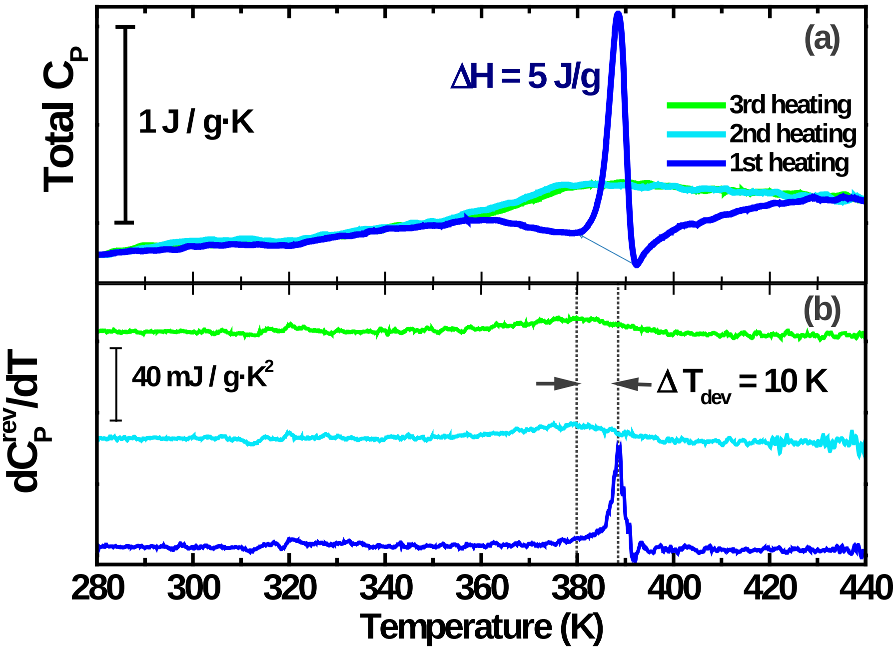

Figure 4.1 MT-DSC measurements on the pristine Dominican amber. Specific heat study for each sample includes three consecutive heating scans at a constant rate 1.5 K/min and modulating signal 1 K every 60 s. (a) Total specific heat where a huge overshoot is observed in the first heating scan, corresponding to the extraordinary ageing present in the pristine amber. (b) Temperature derivative of the reversing part of specific heat, in which the position of the maximum determines the temperature of devitrification. The shift ΔT_{dev} = 10 K towards lower temperature manifests a decrease in kinetic stability from the hyperaged to the conventional amber glass. Curves are shifted 60 mJ/g K^2 for clarity.

Standard aluminum pans of empty mass $m \approx 20$ mg were employed as sample holders, N_2 was used as purging gas and to enhance thermal contact. Amber samples were manually milled using an agate mortar until homogeneous particle size of some tens of microns was achieved. Typical masses of the samples employed were $m \approx 4$ mg. Calibration in temperature and enthalpy of the system was done using certified indium. Measurements on every sample were conducted at heating/cooling rates of ± 1.5 K/min and with modulating amplitude 1 K every

60 s, in the temperature range 273 K $\leq T \leq$ 450 K. All samples were measured with three heating and three cooling scans in total, from which the heating curves were taken for the numerical analysis. Three heating curves are needed in order to check reproducibility and differences between the first scan and the two others.

The pristine Dominican amber presents a huge peak of $\Delta H \approx$ 5 J/g around the devitrification temperature at T_{dev} = 389 K in the specific heat curve, as seen in Figure 4.1a, as a consequence of the extraordinary stabilization process undergone by the Dominican amber sample. We will use the convention to name devitrification temperature T_{dev} the calorimetric feature at the glass transition measured in the heating curve, defined as the position of the maximum in $\mathrm{d}C_{\mathrm{P}}^{\mathrm{rev}}/\mathrm{d}T$, in order to avoid confusion with the canonical definition of the glass transition temperature T_{g} at standard coooling rates. The second and third scans show no further feature, and reproducibility among them warrant that ageing signal is completely erased after the first run.

From the analysis of the reversible contribution to the specific heat in Figure 4.1b, the glass transition evolution is accessed independently from the thermal history. A clear decrease of the devitrification temperature ΔT_{dev} = 10 K appears after the hyperaged sample is first heated above 389 K, similar to what is observed in ultrastable thin films [SKMK07]. This increase in T_{dev} due to stabilization of the glass is referred to as *kinetic stability*. Besides, the stabilized glass shows a narrow step-like devitrification within 15 K, whereas in the conventional glass it broadens up to 35 K.

The conventional glass is accessed by heating the pristine Dominican amber to 395 K and isothermally annealing it at this temperature for three hours. After this counter-annealing process, removal of the ageing signal is completely done, as seen in the total specific heat curve of Figure 4.2a. The three scans in the rejuvenated sample are identical, what reflects complete removal of any thermal history effect. The temperature derivative of the reversible specific heat in Figure 4.2b shows a broad peak in a temperature window of 35 K, equal to the second and third scans of the pristine sample (which also correspond to the conventional state). This drastically contrasts with the curve corresponding to the first heating signal of the pristine sample in Figure 4.1b, which presents a sharp peak of height $(dC_P^{rev} / dT)_{max} \approx 60$ mJ/g·K^2.

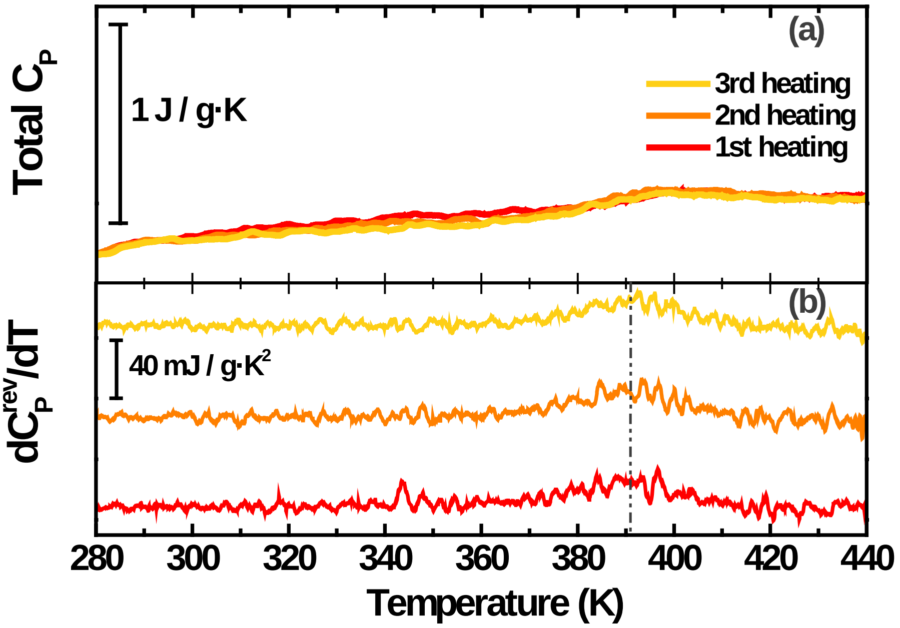

Figure 4.2 MT-DSC measurements on the rejuvenated Dominican amber after isothermal annealing at 395 K for three hours. Three consecutive heating scans at a constant rate 1.5 K/min and modulating signal 1 K every 60 s. (a) Total specific heat where complete reproducibility is observed among the three scans. (b) Temperature derivative of the reversing part of specific heat, in which the position of the maximum determines T_{dev}, with no variation after the first heating. Curves are shifted 60 mJ/g K^2 for clarity.

4.3 Effects of hyperageing on the low-temperature specific heat

The central phenomenology which motivates this thesis lays on the possible connection between enhanced stabilization in glasses and their low-temperature universal anomalies. To this purpose, after characterizing the result of the ageing process of 20 million years on Dominican amber, we analogously studied the low-temperature specific heat of these samples in the temperature range 0.6 K ≤

$T \leq 26$ K, in order to find possible correlations between relaxation processes below T_g and excess in the vibrational density of states (VDOS) at low energies/temperatures.

Although a general consensus has not been reached yet on the origin of the excess in the VDOS in glasses at temperatures 2 K – 10 K, as already discussed in the first two chapters, to account for possible differences in the low-temperature specific heat between the samples studied here, experimental data are analyzed in the framework of the basic Soft Potential Model (SPM) [BGGP92][Pars94][RaBu98]. This version of the SPM does not account for the boson peak (BP) and other glassy properties at higher temperatures, which are included in more recent extensions of this model [GuPS03][PaSG07]. In the basic SPM the low-frequency dynamics of glasses is assumed to be governed by the coexistence of acoustic –phononlike– lattice vibrations and some additional quasilocalized vibrations (usually called ‘soft modes’). This behavior is described in terms of asymmetric quartic potentials (see section 2.2.2), from which the derived specific heat is found to be approximately linear in temperature for $k_B T << W$, being W the average energy of the soft modes. This behavior recovers the limit where the Two-Level-Systems (TLS) contribution dominates $T < 1$ K, hence agreeing with the Tunneling Model (TM) prediction. Given the reduced C_P/T^3 representation, the TLS region is followed by a minimum and a rapid increase $C_P \sim T^5$ produced by the quasi-harmonic soft-mode vibrations, which correspond to the lower energy vibrations of the boson peak. From these considerations, the most reasonable fit of the low-temperature specific heat is given by a quadratic polynomial in the C_P/T versus T^2 representation [Ramo04], taking into account the SPM prediction

$$C_p(T) = c_{TLS}T + c_D T^3 + c_{sm}T^5 \tag{4.1}$$

with the coefficients in Equation (4.1) corresponding to the TLS contribution c_{TLS}, the Debye lattice contribution c_D and the quasiharmonic soft modes c_{sm}, respectively. The temperature range to apply this fit is $0 < T < 3/2\, T_{min}$, being T_{min} the position of the minimum in the C_P/T^3 representation, in order to obtain meaningful estimations.

Two possibilities exist to make this fit. The direct way, as already mentioned, is performing a quadratic polynomial fit in C_P/T versus T^2, thus obtaining an estimation for the three coefficients in Equation (4.1). The second possibility is determining the Debye contribution independently, using High Resolution Brillouin Spectroscopy (HRBS), and fixing c_D to the value so calculated. From this, a linear fit of $(C_P - C_{Debye})/T$ versus T^4 provides the other two contributions in Equation (4.1), with $C_{Debye} \equiv c_D \cdot T^3$. The first calculation is discussed in this section, while the second method is introduced in section 4.4 after the Brillouin data, together with a comparison between the two estimations.

We observe no qualitative change in the specific heat $C_P(T)$ curve as a result of rejuvenating the pristine Dominican amber. This is clearly reflected in the C_P/T^3 representation shown in Figure 4.3, in which position of the maximum at 3.7 K and the minimum at 1.3 K remain unaltered after the extraordinary ageing process of 20 million years

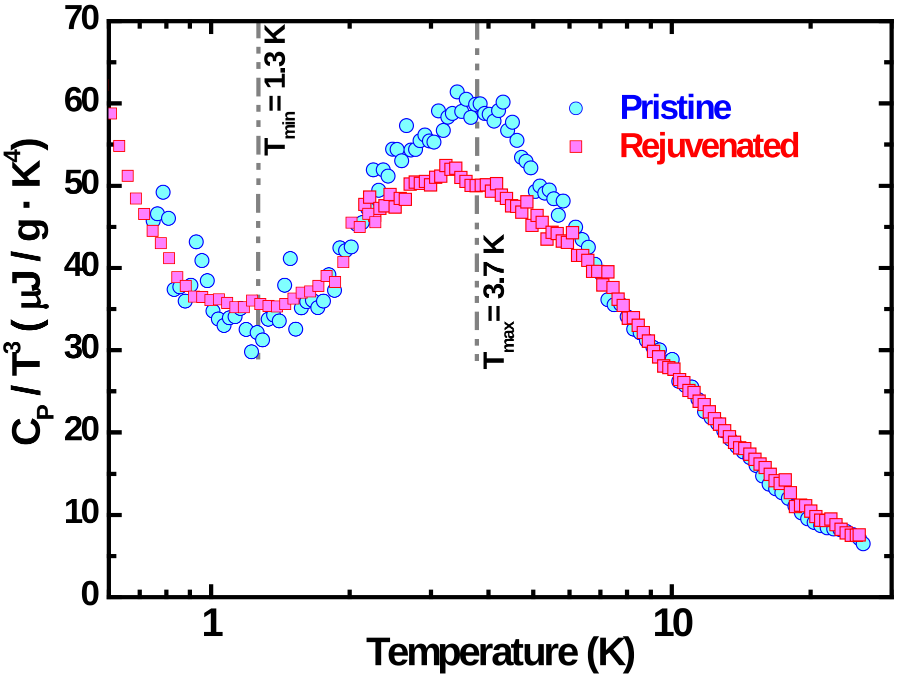

Figure 4.3 Reduced C_P/T^3 representation of the specific heat for the Dominican amber. Comparison between the pristine *hyperaged* sample and the rejuvenated *conventional* one. Positions of the minimum T_{min} = 1.3 K and the maximum T_{max} = 3.7 K remain unaltered after the extraordinary stabilization process of ageing during ~ 20 million years.

We would like to stress the fact that the pristine Dominican amber presents a big boson peak, even appreciably higher ~ 11% than that in the rejuvenated sample. A clear explanation on this point is still missing, although possible connection with further polymerization processes taking place above T_g when first heating the pristine sample may exist (see Figure 4.1a). Nevertheless, in order to discard any possible artifact in the measurements, we measured the specific heat of a second Dominican amber sample of the same batch in the temperature range of the boson peak, again both in the *hyperaged* (pristine) and the *conventional* (rejuvenated) state. The same behavior was found, with 11% decrease of the maximum of the boson peak after removing the ageing (see Figure 4.4).

But even more surprising is the equality between both samples at temperatures below the maximum of the boson peak. Pristine Dominican amber specific-heat data reveal a height at the minimum of the C_P/T^3 representation slightly smaller ~ 10% than after driving the sample to the conventional glassy state. This reflects a softening in the lattice, what means a lowering in the sound velocity and, hence, an increase in the Debye contribution to the specific heat after removing the ageing.

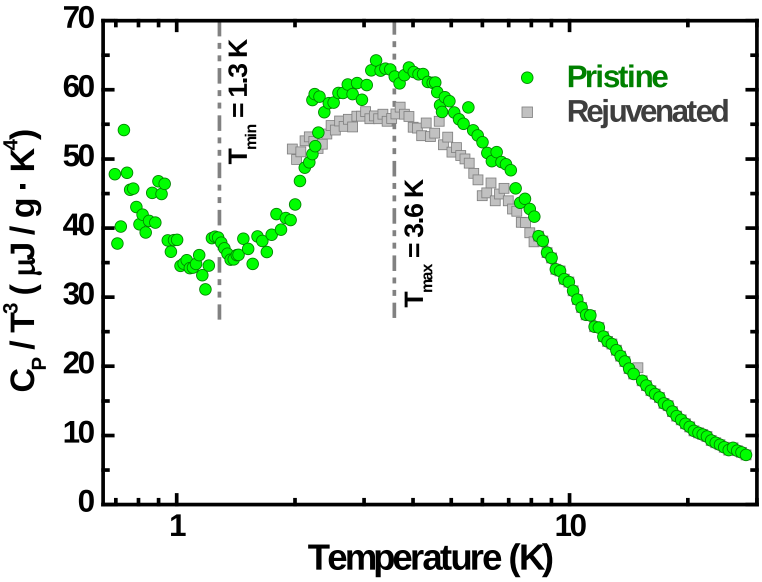

Figure 4.4 Reduced C_P/T^3 representation of the specific heat for a second sample of Dominican amber from the same batch as the sample in Figure 4.3. Reproducibility is clearly observed in the minimum and maximum positions, as well as in the 11% decrease of the boson peak height.

Calculations of the contributions to the specific heat given in Equation (4.1) are done by fitting experimental data from the pristine and rejuvenated samples shown in Figure 4.3 in the C_P/T versus T^2 representation, using a quadratic polynomial fit. Comparison between the fits for both samples in Figure 4.5 reveals no important modification in the low-temperature anomalies of the glass as a consequence of the hyperageing process. Only a small decrease of the Debye contribution in the pristine sample, which can be understood in terms of the ~ 2.5 – 3.0 % densification derived from the extraordinary stabilization.

Taking into account the phonon-like contributions to the low-temperature specific heat in pristine $c_D^{prs} = 14$ μJ / g · K^4 and rejuvenated $c_D^{rej} = 16.1$ μJ / g · K^4 Dominican amber, it remains clear that the presence of quasi-localized modes is not affected by the sub-T_g relaxation processes in our amber samples.

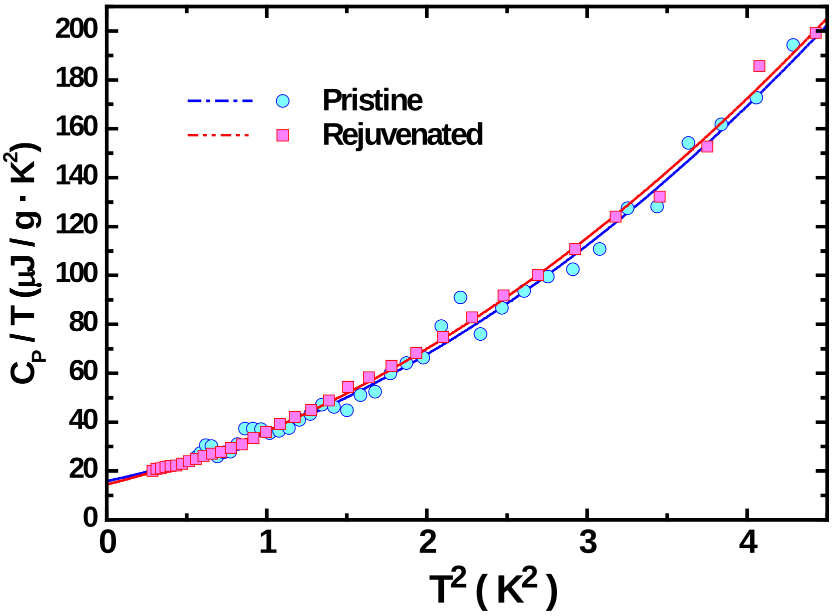

Figure 4.5 C_P/T versus T^2 representation for the Dominican amber samples in Figure 4.3. Solid blue circles and solid red squares correspond to the pristine and rejuvenated amber samples, respectively. Quadratic polynomial fits using Equation (4.1) provide TLS, Debye lattice vibrations and quasiharmonic soft modes contributions in Table 4.1.

Amber glass	$T_{\min}$ (K)	$T_{\max}$ (K)	c_D (μJ/g·K^4)	c_{TLS} (μJ/g·K^2)	c_{sm} (μJ/g·K^6)
Pristine	1.3	3.7	14 ± 4	15.9 ± 3.8	6.2 ± 0.9
Rejuvenated	1.3	3.7	16.1 ± 1.5	14.5 ± 1.1	5.8 ± 0.4

Table 4.1 Comparison of the low-temperature parameters obtained from the specific heat of the Dominican amber samples in Figure 4.3, using quadratic fits shown in Figure 4.5 in the C_P/T versus T^2 representation. Minimum $T_{\min}$ and maximum $T_{\max}$ positions in the C_P/T^3 representation marked in Figure 4.3, c_D Debye lattice vibrations, c_{TLS} TLS and c_{sm} quasiharmonic soft modes contributions.

4.4 Elasto-acoustic properties determined from Brillouin measurements

High Resolution Brillouin Spectroscopy (HRBS) measurements were performed on Dominican amber samples, in collaboration with Dr. Rafael J. Jiménez Rioboó at the ICMM-CSIC Institute[1], in order to obtain direct information about the propagation velocity of acoustic modes at hypersonic frequencies and refractive index of these samples. This technique allows us to access to the Debye-like phonon contribution to the low-temperature specific heat.

Dominican amber samples were mechanically cut down to < 2mm thick using a water-refrigerated slow-rotational (~30-60 rpm) cutter machine together with a diamond disc, so that sample temperature was not dramatically increased. Afterwards, amber slabs were manually polished down to approximately 1 mm thickness, and several flat surfaces were obtained. The sample was placed inside an Oxford Instruments Optistat CF cryostat. An ITC 4 Temperature Controller (Oxford Instruments) was used, providing a temperature stability of ± 0.05 K. Liquid nitrogen was used as cryogenic bath to obtain temperatures down to 80 K. The Brillouin spectrometer is integrated by a 2060 Beamlock Spectra Physics Ar+ laser (λ_0 = 514.5 nm) as monochromatic light source; a Sandercock-type 3+3 tandem Fabry-Pérot interferometerwas used to analyze the scattered light. No

---

[1] Instituto de Ciencia de Materiales de Madrid, Consejo Superior de Investigaciones Científicas (ICMM-CSIC), E-28049 Madrid, Spain.

polarization analysis was made of the scattered light. Both backscattering (180º) and right-angle (90º) geometries were simultaneously used [Krüg89], the latter allowing the observation of the (weak) transverse sound peak. The 90º scattering geometry is refractive-index independent, whereas the backscattering geometry (180º) involves a refractive-index dependent acoustic wave vector, as follows

$$\mathrm{q}^{90\mathrm{A}} = \frac{4\pi\sqrt{2}}{\lambda_0} \qquad \mathrm{q}^{180} = \frac{4\pi n_i}{\lambda_0} \tag{4.2}$$

where λ_0 stands for the (laser) excitation wavelength and n_i for the refractive index of the sample. The sound propagation velocity v is obtained from the combination of the Brillouin frequency shift *f* and the corresponding wave vector from Equation (4.2)

$$\mathrm{v}^{90\mathrm{A}} = \frac{f^{90A}\lambda_0}{\sqrt{2}} \qquad \mathrm{v}^{180} = \frac{f^{180}\lambda_0}{2n_i} \tag{4.3}$$

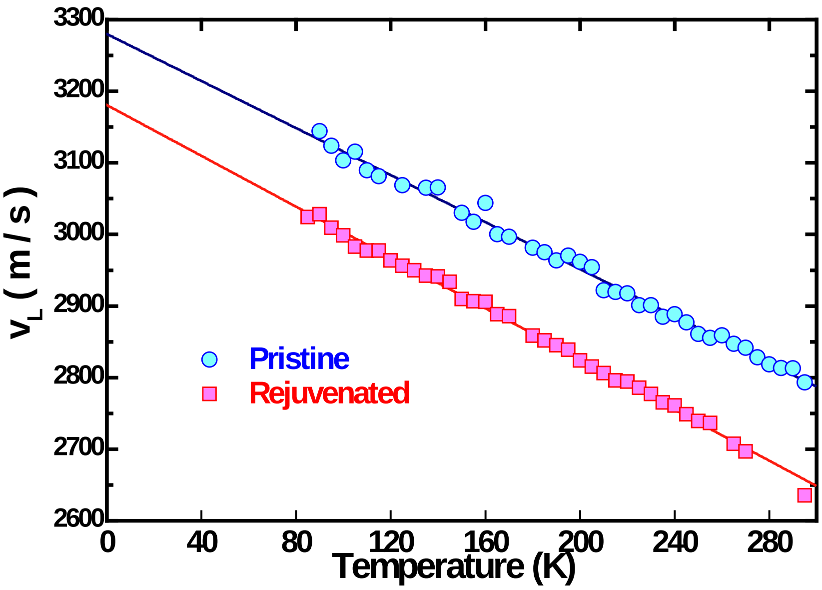

Figure 4.6 Temperature dependence of the longitudinal sound velocity in Dominican amber. Comparison between the pristine hyperaged (solid blue circles) and the rejuvenated conventional (solid red squares) samples. Linear extrapolation to 0 K using experimental data in 80 K ≤ *T* ≤ 300 K provide zero-temperature values $v_L^{prs}(0\ \mathrm{K}) = 3280 \pm 30$ m/s and $v_L^{rej}(0\ \mathrm{K}) = 3180 \pm 10$ m/s.

The longitudinal sound velocity dependence with temperature was measured for the Dominican amber samples for 80 K ≤ T ≤ 300 K, as illustrated in Figure 4.6. They show a clear decrease $|\Delta v_L(T)|/v_L^{prs}(T) \approx 3.3$ % when the pristine Dominican amber sample is driven to the conventional state by thermal treatment. A linear fit of the data was used to extrapolate longitudinal sound velocities to 0 K. The transverse sound velocities were only accessed at room temperature, since the extreme weakness of its Brillouin peak made it necessary integration times greater than forty hours. Values for the pristine v_T^{prs}(300 K) = 1403 ± 7 m/s and rejuvenated v_T^{rej}(300 K) = 1320 ± 40 m/s Dominican amber samples reveal an enhanced softening of the transverse modes of ~ 5.7 % compared to the softening in the longitudinal ones. Nevertheless, a generalized Cauchy-like relation has been proposed by Krüger *et al.* for isotropic solids such as glasses and polymers, which is very well fulfilled in all the systems studied. They showed that the ideal Cauchy relation between longitudinal c_{11} and shear c_{44} modulus given as $c_{11} = 3c_{44}$ should be replaced by a generalized Cauchy relation that should include and additive constant term, hence making the longitudinal and transverse sound velocities to be directly related at any temperature –and ageing in the case of polymers– by [KBBC02]

$$v_L^2(T) = A + 3 \cdot v_T^2(T) \tag{4.4}$$

This way, using Equation (4.4) it is possible to obtain the zero-temperature limit for the transverse sound velocity, since A is a constant of the sample. For the pristine sample we get v_T^{prs}(0 K) = 1722 m/s, and for the rejuvenated one v_T^{rej}(0 K) = 1667 m/s. Average Debye velocities are then v_D^{prs} = 1926 m/s and v_D^{rej} = 1865 m/s for the pristine and rejuvenated amber, respectively.

To calculate the Debye coefficient c_D from the Brillouin measurements, the zero-temperature mass density is needed as well, which can be calculated using the Lorenz-Lorentz relation between mass density and the refractive index of a transparent medium

$$\frac{n^2(T)-1}{n^2(T)+1} \cdot \frac{1}{\rho(T)} = const \tag{4.5}$$

in which $n(T)$ stands for the refractive index and $\rho(T)$ for the mass density. As indicated in Table 4.1, the room temperature values of the mass density are $\rho_{\mathrm{prs}}(300\ \mathrm{K}) = 1.058\ \mathrm{g/cm^3}$ for the pristine and $\rho_{\mathrm{rej}}(300\ \mathrm{K}) = 1.028\ \mathrm{g/cm^3}$ for the rejuvenated Dominican amber samples. Temperature dependence of the refractive index was measured for both samples in the range $80\ \mathrm{K} \leq T \leq 300\ \mathrm{K}$, as shown in Figure 4.7. A change in the behavior is observed after removing the ageing from the pristine sample, which shows an increase from the room-temperature value to the zero-temperature value of 1.5 %, whereas in the rejuvenated sample it remains equal within the experimental error.

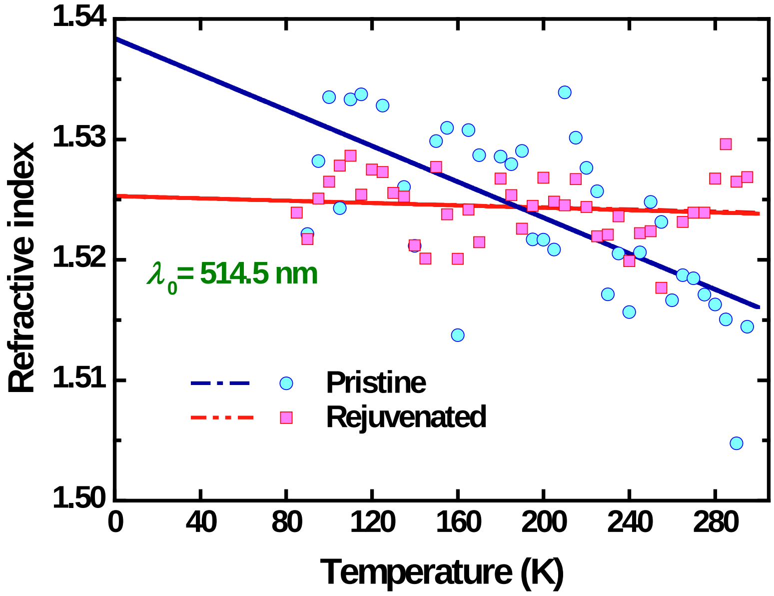

Figure 4.7 Temperature dependence $80\ \mathrm{K} \leq T \leq 300\ \mathrm{K}$ of the refractive index in Dominican amber for the pristine hyperaged (solid blue circles) and the rejuvenated conventional (solid red squares) samples, for incident wavelength $\lambda = 514.5$ nm. Zero-temperature extrapolation using a linear fit of the experimental data provide values $n^{\mathrm{prs}}(0\ \mathrm{K}) = 1.538 \pm 0.004$, $n^{\mathrm{rej}}(0\ \mathrm{K}) = 1.526 \pm 0.002$.

Using the relation given in Equation (4.5), the zero-temperature mass density is calculated, with $\rho_{\mathrm{prs}}\ (0\ \mathrm{K}) = 1.090\ \mathrm{g/cm^3}$ and $\rho_{\mathrm{rej}}\ (0\ \mathrm{K}) = 1.031\ \mathrm{g/cm^3}$.

With the average Debye velocities and the zero-temperature mass density, an estimation of the Debye contribution to the specific heat c_{D}, independent to that calculated from the low-temperature specific-heat measurements can be performed using its definition

$$c_D = \frac{2\pi^2}{5}\left(\frac{k_B^4}{\hbar^3 \rho v_D^3}\right) \tag{4.6}$$

We obtain $c_D^{prs} = 15.5 \pm 0.8$ μJ/g·K^4 for the pristine and $c_D^{rej} = 18.0 \pm 0.9$ μJ/g·K^4 for the rejuvenated amber samples, what shows the same softening behavior in the conventional glass, and coherent values with those calculated from quadratic polynomial fit of C_P/T versus T^2 given in Table 4.1.

4.5 Low-temperature universal anomalies in Dominican amber glasses

In the previous section we have evaluated the phonon-like vibrations contribution to the low-temperature specific heat using Brillouin spectroscopy, what shows in our samples good agreement with the values calculated from the specific heat given in Table 4.1, in agreement to the behavior for a number of different systems reported by Ramos [Ramo04]. This allows us to estimate the TLS and the quasi harmonic soft modes contribution in the low-temperature specific heat in a different way, by fixing the Debye coefficient to that obtain from HRBS results, thus directly obtaining comparison of the low-temperature anomalies in an extraordinary stabilized glass (pristine) and a conventional one (rejuvenated) with only two fitting parameters, the procedure followed in [HRKS12] for butanol.

In Figure 4.8 the linear fit of $(C_P - C_{Debye}) / T$ versus T^4 is shown for both the pristine and rejuvenated Dominican amber samples, where $C_{Debye} \equiv c_D \cdot T^3$ obtained from the HRBS measurements. We fix the elastoacoustic c_D coefficient value, and the excess specific heat (those indeed revealing the anomalous glassy properties) is manifested after subtracting the Debye (cubic) contribution $C_{Debye} = c_D \cdot T^3$. Plotting $(C_P - C_{Debye}) / T$ versus T^4, the T and T^5 terms are directly accesed, hence obtaining the coefficients from simple straight-linear fits, as shown in Figure 4.8, and the values included in Table 4.2. See that the linear behavior of the data below 2 K clearly shown in Figure 4.8 manifests the convenience and validity of the SPM, despite the larger data dispersion due to the very sensitive scale chosen.

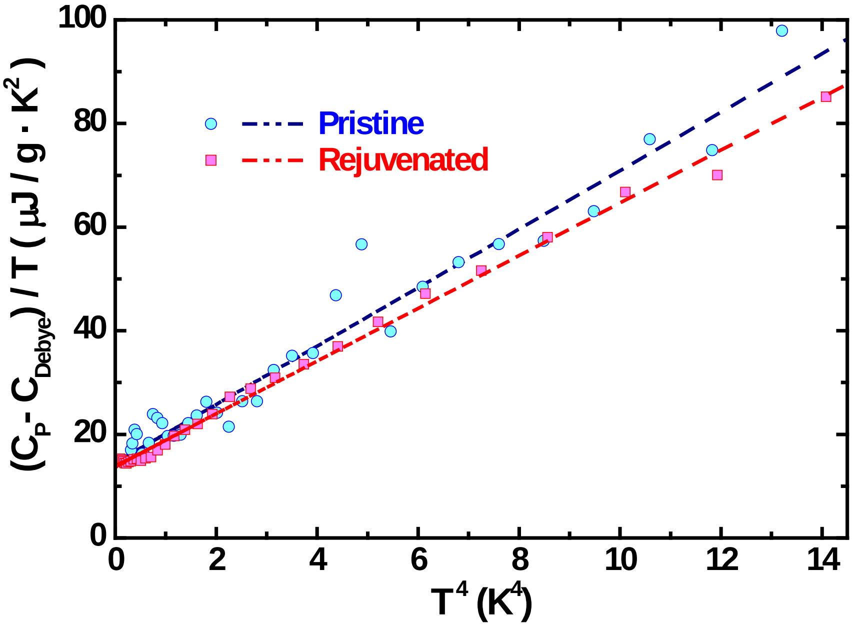

Figure 4.8 Linear fit of the low-temperature specific heat in the (C_P − C_{Debye}) / T versus T^4 representation, where $C_{Debye} \equiv c_D T^3$, c_D fixed to the value obtained from the HRBS measurements. Pristine (solid blue circles) and rejuvenated (solid red squares) Dominican amber samples, together with their least square fits (dashed blue line and dashed red line for the pristine and rejuvenated samples, respectively).

All information obtained from the elastoacoustic measurements of amber, together with the estimated contributions to the specific heat of the TLS and the quasi harmonic soft modes using the SPM are summarized in Table 4.2 and further shown in Figure 4.9, in which the Debye level for each sample is shown (thick solid lines).

ELASTIC DATA					SPM FIT OF $(C_P\text{-}C_{Debye})/T$ vs T^4	
Amber	ρ_{300K} (g/cm^3)	ρ_{0K} (g/cm^3)	v_D (km/s)	c_D (μJ/g·K^4)	c_{TLS} (μJ/g·K^2)	c_{sm} (μJ/g·K^6)
Pristine	1.058	1.090	1926	15.5 ± 0.8	14.7 ± 1.0	5.7 ± 0.2
Rejuvenated	1.028	1.031	1865	18.0 ± 0.9	13.8 ± 0.3	5.09 ± 0.06

Table 4.2 Elastic data determined by HRBS and mass density measurements, together with the anomalous glassy contributions in the low-temperature specific heat obtained from the SPM fit of $(C_P - C_{Debye})\ /\ T$ versus T^4, for both the pristine and rejuvenated Dominican amber samples. Mass density values at room temperature ρ_{300K} and extrapolation to 0 K ρ_{0K} using Equation (4.5) and temperature dependence of refractive index in Figure 4.7; Average Debye velocity v_D; Debye phonon-like contribution c_D calculated using Equation (4.6); two-level-systems c_{TLS} and quasi harmonic soft modes c_{sm} contribution to the specific heat estimated using the SPM.

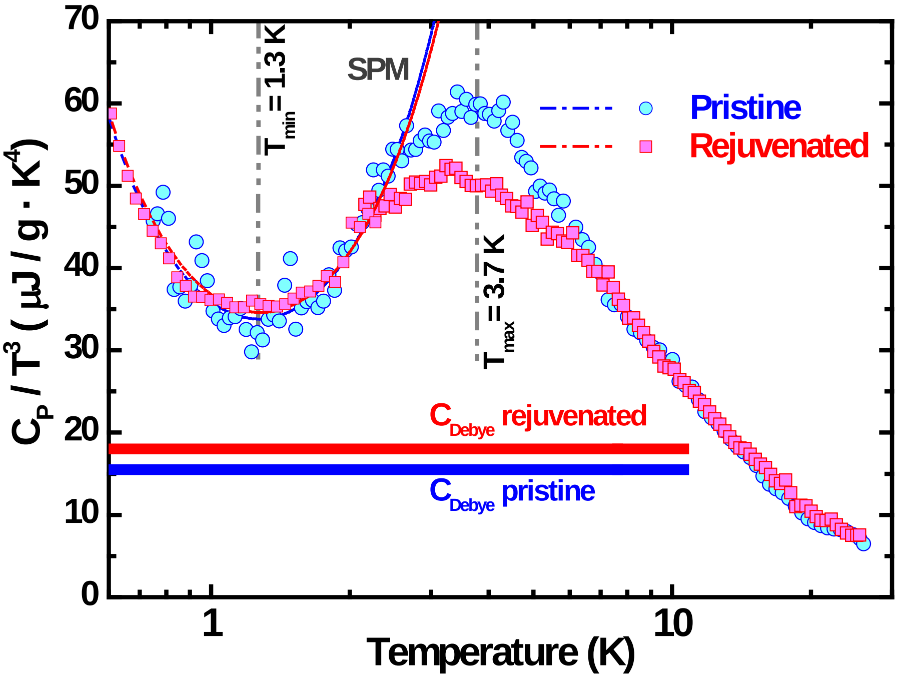

Figure 4.9 C_P/T^3 representation for the Dominican amber data, both in the pristine *hyperaged* and the rejuvenated *conventional* states, together with the phonon-like Debye contribution and the best SPM fit done in Figure 4.8 using Equation (4.1) and fixing c_D to the value independently determined by elastoacoustic measurements.

From Figures 4.8 and 4.9 and Table 4.2 it appears very clear that the *hyperaged*, highly densified amber retains all the low-temperature glassy excitations present in the *conventional* non-densified sample, not only qualitatively but also quantitatively. Besides, the boson peak slightly decreases in height after rejuvenation, although keeping the same maximum position, what appears certainly striking (as well as reproducible in our amber samples), clearly contradicting the Debye scaling suggested elsewhere [Monaco06][Baldi09] (and references therein).

This astonishing behavior of the low-temperature anomalies in our samples is, nevertheless, shared by previous low-temperature thermal-conductivity data $\kappa(T)$ reported by Love and Anderson [LoAn91] in Dominican amber. Although their Dominican amber samples present a lower glass transition temperature than in our samples, what is totally compatible with the heterogeinity present among different provenances and batches, thermal conductivity is not very sensitive to material parameters [Phil81], so that a joint analysis can be done. We focus our interest on the parameter W/k_B which in the SPM defines the crossover from a TLS-dominated region to a *single-well* soft-modes-dominated one. This crossover is observed in the specific heat as the minimum in C_P/T^3, and determined by T_{min}, being $W/k_B \approx 1.6\ T_{min}$ from analytical derivations [BGGS91], also found $W/k_B \approx 1.8\ T_{min}$ numerically [RGBB93][RaBu98]. In the thermal conductivity the crossover appears as a bend from the quadratic temperature dependence at the lowest temperatures to the plateau region (see Sections 2.2.1 and 2.2.2), thus introducing a maximum in the κ/T representation, with $W \approx 1.6\ T_{max}$. This means, in few words, that the SPM predicts that the minimum T_{min} in C_P/T^3 and the maximum T_{max} in κ/T should occur at the same temperature.

In Figure 4.10 we depict the low-temperature thermal-conductivity data $\kappa(T)$ measured by Love and Anderson for pristine (as received) and rejuvenated (at 370 K) amber samples. The inset of Figure 4.10 shows that for the pristine Dominican amber sample T_{max} = 1.3 K, what makes W = 2.1 K, in nice agreement with our minimum in C_P/T^3 of T_{min} = 1.3 K. Furthermore, the thermal conductivity of the rejuvenated amber (although not provided in the whole temperature range [LoAn91]) is again very similar to that of the pristine sample, as seen in Figure 4.10. This undoubtedly supports our statement that the hyperaged glass retains the universal glassy properties at low temperatures, which is even quantitative when compared to its rejuvenated state, hence meaning that the low-temperature glassy anomalies are not affected by this dramatic structural and thermodynamic relaxation.

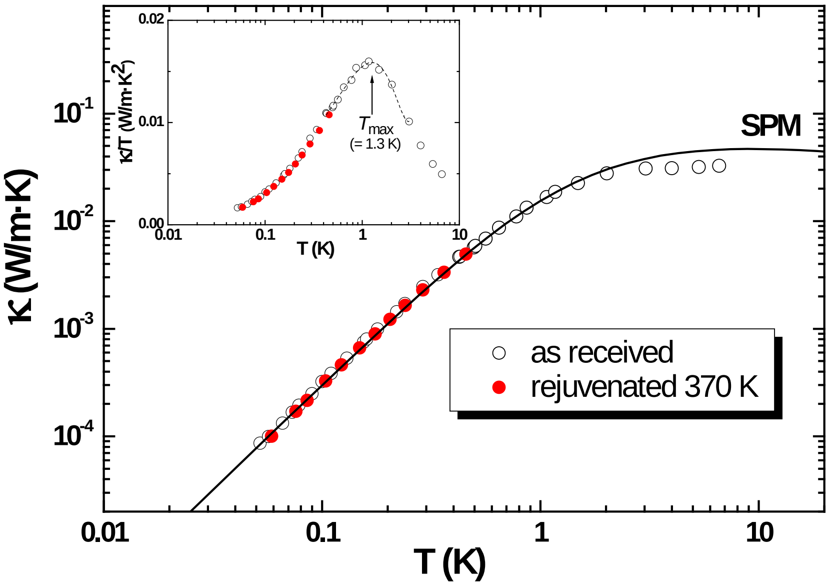

Figure 4.10 Thermal conductivity κ versus temperature measured by Love and Anderson [LoAn91] for (different) pristine and rejuvenated (at 370 K) Dominican amber samples, presenting the crossover (determined by W) from the quadratic-temperature-dependence (TLS-dominated) region to the (soft-modes) plateau one. The inset shows the same data in the κ/T versus T representation, in order to determine the maximum position T_{max} and, consequently, $W \approx 1.6\ T_{max}$, following the SPM prediction. The solid line in the κ versus T representation is the SPM predicted curved for the fitted W in the inset.

4.6 Conclusions

In this chapter we have presented amber as a model system to study the effects of extraordinary sub-T_g relaxations in bulk glasses on the universal low-temperature anomalies present in amorphous solids. Characterization of Dominican amber samples using Modulated Differential Scanning Calorimetry (MT-DSC) has allowed us to access the huge ageing signal present in the specific-heat curve at the glass transition T_g = 389 K of the pristine hyperaged sample. After a thermal counter-annealing (rejuvenation) of the pristine sample, the extreme overshoot in C_P completely disappears, revealing that the initial hyperaged Dominican amber is transformed into the conventional (unrelaxed) glass.

Low-temperature calorimetry, together with High Resolution Brillouin Spectroscopy (HRBS), has been used to track the evolution of the low-temperature glassy anomalies with hyperageing. In particular, the Two-Level-Systems and the soft-modes contributions have been directly determined by linearly fitting the excess (above the Debye-predicted) specific heat $(C_P - C_{Debye})/T$ versus T^4, using the prediction given by the basic SPM. Whereas a clear increase in the Debye level is observed after rejuvenating the pristine Dominican amber, as a consequence of the lattice softening induced by the reduction in the mass density of the sample, no changes are observed in the glassy anomalies. A slightly reduced boson peak height in the rejuvenated sample appears, although the position of the maximum is kept unaltered.

The results obtained on Dominican amber evidence the preservation of the low-temperature glassy anomalies in extremely relaxed amorphous systems due to hyperageing processes. A decrease in the phonon-like contribution to the specific heat in the extraordinarily stabilized amber is introduced by the 2.5 – 3% densification of the sample (due to loss of volatiles, hardening of the lattices, etc.), what favors the sound propagation. This clearly contradicts the Debye scaling proposed [Monaco06][Baldi09] (and references therein) as a consequence of the apparent shift of the boson peak in temperature due to changes in the local elastic constants between neighboring atoms.

[AnBo93] K. B. Anderson and R. E. Botto, “The nature and fate of natural resins in the geosphere—III. Re-evaluation of the structure and composition of Highgate Copalite and Glessite”, Organic Geochemistry, vol. 20, no. 7, pp. 1027–1038, 1993.

[Ande94] K. B. Anderson, “The nature and fate of natural resins in the geosphere—IV. Middle and Upper Cretaceous amber from the Taimyr Peninsula, Siberia—evidence for a new form of polylabdanoid of resinite and revision of the classification of Class I resinites”, Organic Geochemistry, vol. 21, no. 2, pp. 209–212, 1994.

[AnHV72] P. W. Anderson, B. I. Halperin and C. M. Varma, “Anomalous low-temperature thermal properties of glasses and spin glasses”, Philosophical magazine, vol. 25, no. 1, pp. 1–9, 1972.

[ANMM00] C. A. Angell, K. L. Ngai, G. B. McKenna, P. F. McMillan and S. W. Martin, “Relaxation in glassforming liquids and amorphous solids”, Journal of Applied Physics, vol. 88, no. 6, p. 3113, 2000.

[AnWB92] K. B. Anderson, R. E. Winans and R. E. Botto, “The nature and fate of natural resins in the geosphere—II. Identification, classification and nomenclature of resinites”, Organic Geochemistry, vol. 18, no. 6, pp. 829–841, 1992.

[Baldi09] G. Baldi, A. Fontana, G. Monaco, L. Orsingher, S. Rols, F. Rossi and B. Ruta, “Connection between Boson Peak and Elastic Properties in Silicate Glasses”**,** Physical Review Letters, vol. 102, 195502, 2009.

[BGGP92] U. Buchenau, Y. M. Galperin, V. L. Gurevich, D. A. Parshin, M. A. Ramos and H. R. Schober, “Interaction of soft modes and sound waves in glasses”, Physical Review B, vol. 46, no. 5, pp. 2798 – 2808, 1992.

[BGGS91] U. Buchenau, Y. M. Galperin, V. L. Gurevich and H. R. Schober, “Anharmonic potentials and vibrational localization in glasses”, Physical Review B, vol. 43, no. 6, pp. 5039–5045, 1991.

[BLLB12] C. Brun, F. Ladieu, D. L’Hôte, G. Biroli and J.-P. Bouchaud, “Evidence of Growing Spatial Correlations during the Aging of Glassy Glycerol”, Physical Review Letters, vol. 109, no. 17, pp. 1–5, 2012.

[Braw85] S. Brawer, “Relaxation in viscous liquids and glasses”, American Ceramic Society, 1985.

[CCFF09] S. Caponi, S. Corezzi, D. Fioretto, A. Fontana, G. Monaco and F. Rossi, “Raman-Scattering Measurements of the Vibrational Density of States of a Reactive Mixture During Polymerization: Effect on the Boson Peak”, Physical Review Letters, vol. 102, no. 2, p. 027402, 2009.

[CoFR02] S. Corezzi, D. Fioretto and P. Rolla, “Bond-controlled configurational entropy reduction in chemical vitrification”, Nature, vol. 420, no. 6916, pp. 653 – 656, 2002.

[GMPV03] T. S. Grigera, V. Martin-Mayor, G. Parisi and P. Verrocchio, “Phonon interpretation of the ‘boson peak’in supercooled liquids”, Nature, vol. 422, pp. 289 – 292, 2003.

[Grim96] David A. Grimaldi, “The Age of Dominican Amber”, in Amber, Resinite, and Fossil Resins, vol. 617, American Chemical Society, pp. 11–203, 1996.

[GuPS03] V. L. Gurevich, D. A. Parshin, and H. R. Schober, “Anharmonicity, vibrational instability, and the Boson peak in glasses”, Physical Review B, vol. 67, no. 9, p. 094203, 2003.

[HRKS12] M. Hassaine, M. A. Ramos, A. I. Krivchikov, I. V. Sharapova, O. A. Korolyuk and R. J. Jiménez-Riobóo, “Low-temperature thermal and elastoacoustic properties of butanol glasses: Study of position isomerism effects around the boson peak”, Physical Review B, vol. 85, no. 10, p. 104206, 2012.

[JaGB99] P. Jablonski, a Golloch and W. Borchard, “DSC-Measurements of amber and resin samples”, Thermochimica Acta, vol. 333, no. 1, pp. 87–93, 1999.

[KaKI83] V. G. Karpov, M. I. Klinger and F. N. Ignat’ev, “Theory of the low-temperature anomalies in the thermal properties of amorphous structures”, Zh. Eksp. Teor. Fiz, vol. 84, pp. 439 – 448, 1983.

[KBBC02] J. K. Krüger, J. Baller, T. Britz, A. le Coutre, R. Peter, R. Bactavatchalou and J. Schreiber, “Cauchy-like relation between elastic constants in amorphous materials”, Physical Review B, vol. 66, no. 1, p. 012206, 2002.

[Krüg89] J. K. Krüger, “Brillouin spectroscopy and its application to polymers”, in Optical Techniques to Characterize Polymer Systems, Studies in Polymer Science, vol. 5, H. Bässler, Ed. Elsevier, pp. 429–534, 1989.

[KSEW08] K. L. Kearns, S. F. Swallen, M. D. Ediger, T. Wu, Y. Sun and L. Yu, “Hiking down the energy landscape: progress toward the Kauzmann temperature via vapor deposition”, The Journal of Physical Chemistry B, vol. 112, no. 16, pp. 4934 – 4942, 2008.

[LaGM81] J. P. Larmagnac, J. Grenet and P. Michon, “Glass transition temperature dependence on heating rate and on ageing for amorphous selenium films”, Journal of Non-Crystalline Solids, vol. 45, no. 2, pp. 157–168, 1981.

[LaPo02] J. B. Lambert and G. O. Poinar, “Amber: the organic gemstone”, Accounts of Chemical Research, vol. 35, no. 8, pp. 628–36, 2002.

[LoAn91] M. S. Love and A. C. Anderson, “Influence of structural relaxation on the low-temperature thermal conductivity of ancient natural glasses”, Journal of Low Temperature Physics, vol. 84, no. 1–2, pp. 19–36, 1991.

[Monaco06] A. Monaco, A. I. Chumakov, Y-Z Yue, G. Monaco, L. Comez, D. Fioretto, W. A. Crichton and R. Rüffer, “Density of Vibrational States of a Hyperquenched Glass”, Physical Review Letters, vol. 96, 205502, 2006.

[Pars94] D. A. Parshin, “Soft-potential model and universal properties of glasses”, Physics of the Solid State, vol. 36, no. 7, pp. 991–1024, 1994.

[PaSG07] D. A. Parshin, H. R. Schober and V. L. Gurevich, “Vibrational instability, two-level systems, and the boson peak in glasses”, Physical Review B, vol. 76, no. 6, p. 064206, 2007.

[Phil72] W. A. Phillips, “Tunneling states in amorphous solids”, Journal of Low Temperature Physics, vol. 7, no. 3–4, pp. 351–360, 1972.

[Phil81] W. A. Phillips, “Amorphous solids: low-temperature properties”, Topics in Current Physics vol. 24, Ed. Springer, 1981.

[RaBu97] M. A. Ramos and U. Buchenau, “Low-temperature thermal conductivity of glasses within the soft-potential model”, Physical Review B, vol. 55, no. 9, pp. 5749 – 5754, 1997.

[RaBu98] M. A. Ramos and U. Buchenau, “Beyond the standard tunneling model: The soft potential model”, in Tunneling systems in amorphous and crystalline solids, P. Esquinazi, Ed. Springer, 1998.

[Ramo04] M. A. Ramos, “Are the calorimetric and elastic Debye temperatures of glasses really different?”, Philosophical Magazine, vol. 84, no. 13–16, pp. 1313 – 1321, 2004.

[RGBB93] M. A. Ramos, L. Gil, A. Bringer and U. Buchenau, “The Density of Tunneling and Vibrational States of Glasses within the Soft-Potential Model”, physica status solidi (a), vol. 135, no. 477, 1993.

[SiEP13] S. Singh, M. D. Ediger and J. J. de Pablo, “Ultrastable glasses from in silico vapour deposition”, Nature Materials, vol. 12, no. 1, pp. 1–6, 2013.

[SKMK07] S. F. Swallen, K. L. Kearns, M. K. Mapes, Y. S. Kim, R. J. McMahon, M. D. Ediger, T. Wu, L. Yu and S. Satija, “Organic glasses with exceptional thermodynamic and kinetic stability”, Science, vol. 315, no. 5810, pp. 353–6, 2007.

[WaSM06] P. Wang, C. Song, and H. A. Makse, “Dynamic particle tracking reveals the ageing temperature of a colloidal glass”, Nature Physics, vol. 2, no. 8, pp. 526–531, 2006.

[WWSL89] C. A. Wert, M. Weller, D. Schlee and H. Ledbetter, “The macromolecular character of amber”, Journal of Applied Physics, vol. 65, no. 6, pp. 2493 – 2499, 1989.

[ZePo71] R. C. Zeller and R. O. Pohl, “Thermal conductivity and specific heat of noncrystalline solids”, Physical Review B, vol. 4, no. 6, 1971.

[ZhSM13] J. Zhao, S. L. Simon and G. B. McKenna, “Using 20-million-year-old amber to test the super-Arrhenius behaviour of glass-forming systems”, Nature Communications, vol. 4, p. 1783, 2013.

5

SPANISH AMBER: HYPERAGEING AS A ROUTE TO THE IDEAL GLASS

We have discussed in the previous Chapter 4 some of the effects that hyperageing produces on glasses, as shown from the results obtained in 20 million year Dominican amber. In the present Chapter, we further seek the possible impact that extraordinary thermodynamic and kinetic stability have on the low-temperature universal anomalies of glasses. For this purpose, about 110-million-year Spanish amber has been chosen, since it represents the most-stabilized glass to our knowledge that can be studied in the laboratory. Continuing with the research started in the Dominican amber, our main goal is again to find out whether the amount of low-temperature anomalies in glasses are correlated to the amount of disorder frozen in at the glass transition, or rather they are an intrinsic consequence of the non-crystalline dynamics.

5.1 Introduction

In recent years the discovery of amber deposits in northern Spain has provided a big amount of this fossil resin, yielding a large number of bioinclusions for paleontological research. In the deposit of *El Soplao*, in north

Spain (Cantabria), amber similar to other Spanish Cretaceous specimens has been found. The origin of this amber has been determined to be the extinct conifer genus Frenelopsis (Cheirolepidiaceae). This amber bearing deposit is included within the *Las Peñosas* formation, dated as a Lower Albian unit, 112-110 million years age. Two different types of amber have been reported to appear in this deposit [MNVR10][NPRP09] as shown in Figure 5.1. Type A amber samples are characterized by a strong blue-purple color under sun light and purple-reddish under artificial light; type B samples, less abundant, present yellow-honey color under artificial light and honey with a bluish tinge in the sun light.

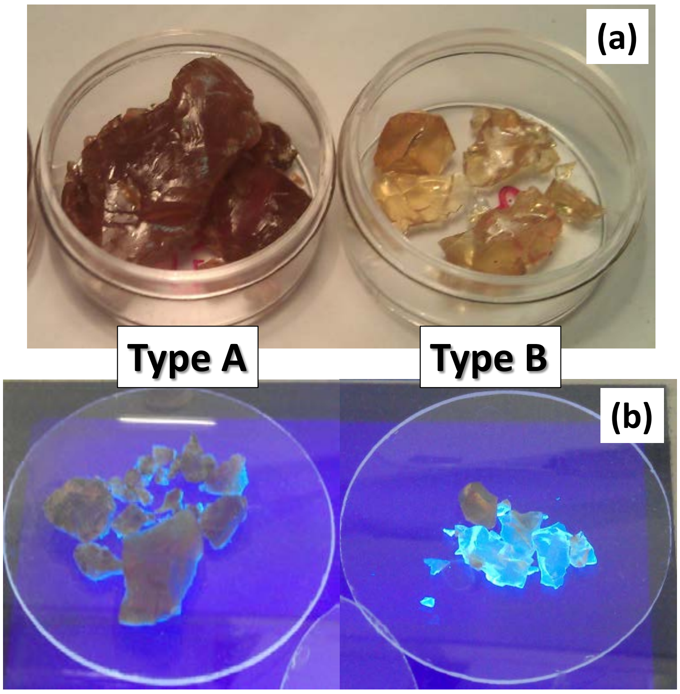

Figure 5.1 Spanish amber samples from El Soplao. The difference between samples is visible to the naked eye (a). Type A amber presents a strong purple-reddish color under artificial light, whereas type B samples present a yellow-honey color. (b) Under ultraviolet illumination, type A amber presents a strong blue-purple color, and type B amber a honey tonality with a bluish tinge.

In Figure 5.2 the geographical location and age of Spanish amber studied in this Chapter, from *El Soplao* deposit are presented, as determined in [NPRP09].

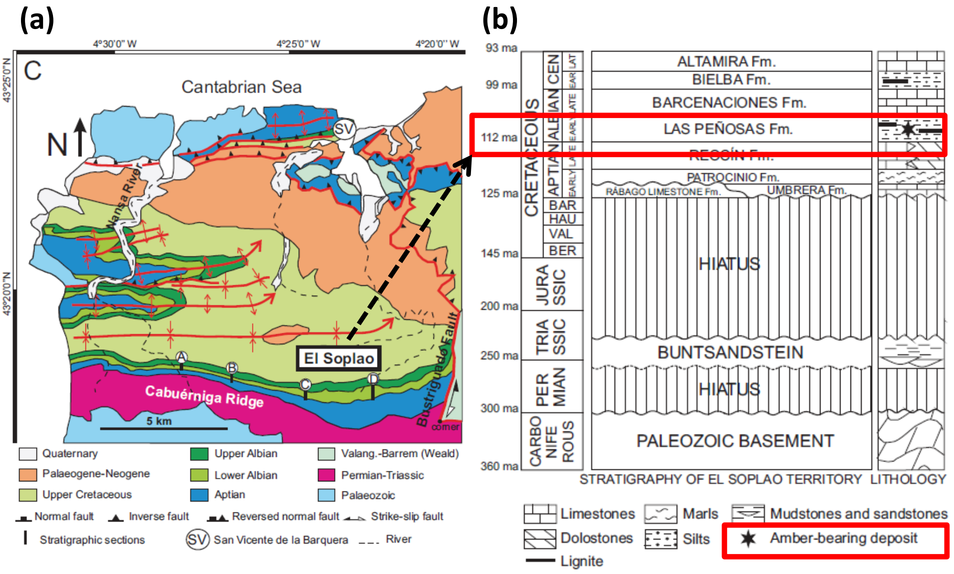

Figure 5.2 Origin of the Spanish amber from *El Soplao*. (a) Geographical location of the amber deposit *El Soplao* in Cantabria, north Spain; (b) age of the Spanish amber from *El Soplao* deposit, which is included within the Las Peñosas Formation, after [NPRP09].

The two types of amber samples shown in Figure 5.1 above indicate the existence of two resin producers which contribute to the deposit. The chemical composition among them varies, but both samples have been used for the study on the thermodynamic and kinetic stability produced by hyperageing processes.

However, in order to look for a possible correspondence between the stability in amber and the excess density of states at low temperatures, only type B samples have been used, due to their homogeneity and less amount of impurities. An exhaustive characterization of the ageing effects around the glass transition using Modulated Differential Scanning Calorimetry (MT-DSC) has been done, nevertheless, in both types A and B, to check possible effects of impurities in the thermodynamic and kinetic stability. Low-temperature calorimetry and High Resolution Brillouin Scattering (HRBS) was performed in type B amber, together with the MT-DSC measurements.

5.2 Extraordinary kinetic and thermodynamic stability in hyperaged Spanish amber

Amber is a fossil resin which solidifies as a consequence of the molecular arrest driven by the formation of covalent bonds. This mechanism, the chemical vitrification, entails a complete different route to produce glasses from the usual cooling of a liquid (commonly known as physical glasses), which has been studied in recent years [CoFR02][CCFF09]. Nevertheless, chemical glasses share the same glassy behavior as those obtained by physical processes, and structural relaxations take place analogously to those happening in physical glasses. Most of the polymers which vitrify follow the chemical route, hence amber is not an exception. The striking property of amber which makes it so interesting for a physicist studying glasses is its capability to resist degradation and disintegration, attending to its organic composition. This incredible feature, together with the fact that its glass transition is located at temperatures not far from room temperature (typically from 100 ºC to 160 ºC), makes amber a perfect candidate to investigate extreme annealing in glasses.

5.2.1 Glass transition and kinetic stability in *type B* amber

Quantification of the effectiveness that this ageing process has introduced in amber can be performed using MT-DSC (see Section 3.5.2 for more details) around the glass transition, where extra exothermic signals are observed as a consequence of the enthalpy released due to stabilization (see Section 2.1.3 and [LaGM81][Hay95] for example). The more effective the ageing, the larger the enthalpy signal. In the case of amber, the pristine sample is the most stabilized glass, due to the extreme ageing process, which we call *hyperageing*. Any thermal annealing performed near the glass transition to the pristine amber drives the system into less stable states. This allows us to stepwise transform the initial hyperaged amber into the conventional glass by applying consecutive thermal treatments.

The MT-DSC measurements on Spanish amber from *El Soplao* were done following a similar procedure as for the Dominican amber samples presented in Chapter 4. Nevertheless, in order to optimize the resolution of the calorimeter and the quantitative reproducibility in all the samples studied, the protocol was further improved, as described in Appendix A. For every single sample measured, three heating curves (with the corresponding three cooling curves) were done at rates ± 1 K/min, and with modulating amplitudes ± 0.5 K/min every 80 s. As an example of the reproducibility and precision in the specific heat curves presented here, the three heatings for the pristine sample are presented in Figure 5.3.

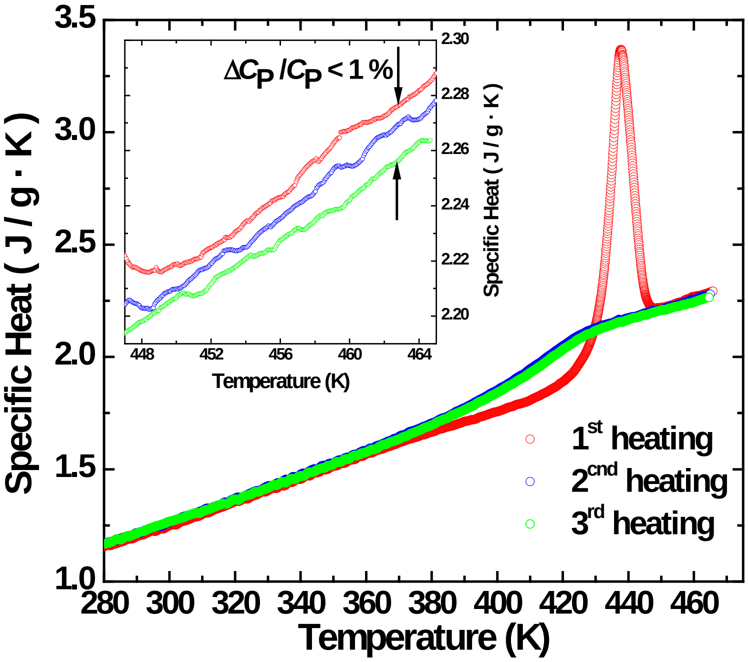

Figure 5.3 Specific heat of the pristine amber sample of type B. The curves correspond to the three heating ramps done for every sample measurement. The first one presents the huge relaxation signal at the glass transition due to hyperageing. The second and third heatings are indistinguishable and correspond to the rejuvenated (conventional) amber glass. The inset shows a zoom in the liquid region, where the reproducibility between curves is determined < 1-2%.

The huge relaxation signal in the pristine amber sample of type B as a consequence of hyperageing is clearly seen in the first heating curve of Figure 5.3. After the amber sample is first heated above the glass transition at 438 K, the relaxation signal is completely removed, evidenced by the complete reproducibility among the second and third heating curves. An approximate quantification of the precision in the MT-DSC measurements is given by the maximum difference among the C_P curves in the liquid region, as shown in the inset of Figure 5.3.

In Figure 5.4 the specific heat of amber type B from *El Soplao* is shown as thermodynamic and kinetic stability is decreased, starting from the pristine hyperaged sample, which has the devitrification temperature T_{dev} at 438 K (again defined as the position of the maximum in dC_P^{rev}/dT, like in Chapter 4). Thermal annealings to the pristine sample are applied by heating it to a temperature T_{ann} and keeping isothermally at that temperature for a period of time, as shown in the legend of Figure 5.4.

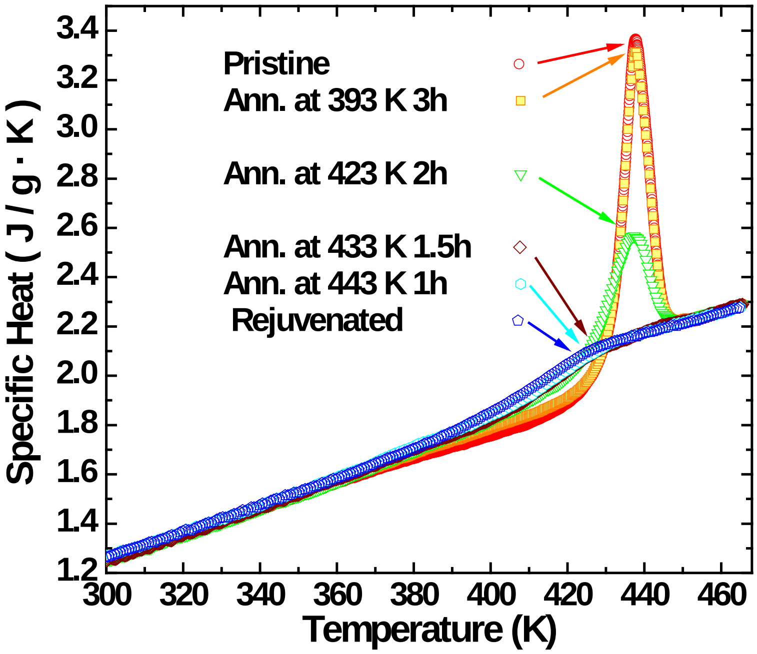

Figure 5.4 Specific heat curves of amber from *El Soplao* type B at different states. The devitrification temperature of the pristine sample is located at 438 K, and decreases with decreasing stability. The ageing signal is clearly seen as a huge exothermic peak at the glass transition, which is maximal in the case of the pristine sample. Reduction of the stability in amber was done stepwise by applying thermal treatments to the pristine sample near the glass transition. Temperatures of the partial thermal treatments applied to the hyperaged sample appear in the legend. Heating rates are 1 K/min, modulating amplitude ± 0.5 K/min every 80 s. Only the first heating curves of each sample (see Figure 5.3) measurement are presented.

The annealing temperatures chosen below T_{dev} range from 393 K up to 433 K. MT-DSC measurements for every single sample studied comprise three heating ramps with heating rates 1 K/min, modulating amplitude ± 0.5 K/min and period 80 s. The reasons to do three heating ramps per sample are mainly two: (i) observe the differences between the first heating (in which the ageing signal appears) with the second heating (which corresponds to the conventional glass); and (ii) check the reproducibility between the second and the third heatings, i.e., that no further process takes place when heating the sample the second time, meaning that the thermal history has been completely removed in the first heating to 465 K. For a detailed explanation of the measurement protocol see Appendix A.

Analyzing the specific heat curves in Figure 5.4 we see that applying a thermal treatment well below the glass transition, at 393 K for three hours produces a slight change in the pristine sample. No change in the height of the maximum within the experimental error is seen. If we increase the annealing temperature, approaching it to the glass transition, the consequences are more obvious. The enthalpy released gradually decreases until it completely disappears for the thermal annealing at 433 K, whereas the specific heat curve below T_{dev} increases until it collapses with the curve of the conventional glass.

After the amber was rejuvenated, i.e., the pristine sample was driven into the conventional state (the overshoot in the specific heat at T_{dev} is completely removed) by heating the sample above the glass transition, further thermal treatments were done. Quenching the liquid at 50 K/min introduced no difference from the conventional glass in the specific heat curve, as can be seen in Figure 5.5. Annealing the conventional glass for two hours at 423 K produces negligible effects on the stability of the system, as derived from the slight overshoot developed at the glass transition in the specific heat curve in Figure 5.5.

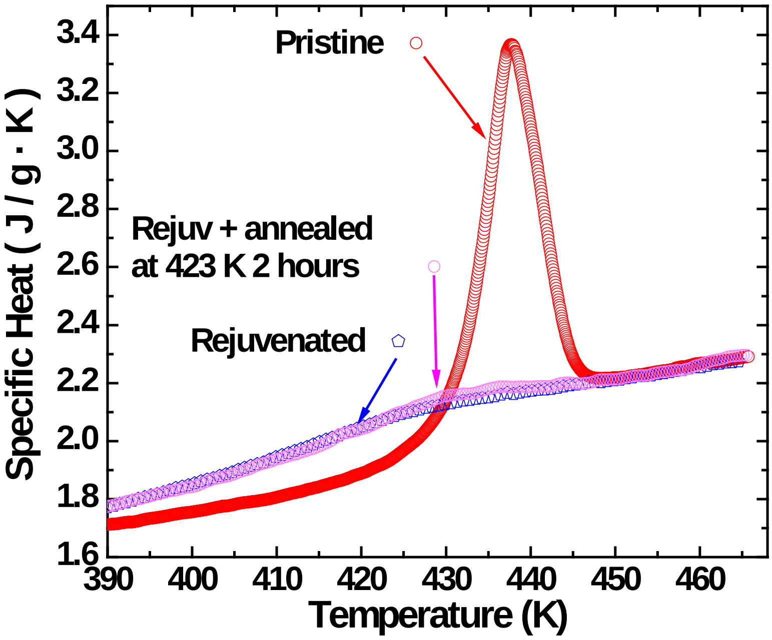

Figure 5.5 Specific heat curves corresponding to the quenched and ‘rejuvenated + thermal annealed’ amber samples of type B compared to the hyperaged and conventional glassy state. The arrow indicates the appearance of a slight overshoot in the annealed amber after rejuvenation, as a consequence of a negligible stabilization process compared to the effect of hyperageing.

Attending to the gradual decrease of the stability that the amber glass undergoes with the thermal annealings near the glass transition in Figure 5.4, we can trace its successive positions in the potential energy landscape (for an extensive discussion see Section 2.1.1.2), as schematically illustrated in Figure 5.6. There, the pristine *hyperaged* amber (red circle) is at a minimum with potential energy deep below the conventional glass (purple circle), but still not at the ideal glassy state. The hyperageing process in the Spanish amber from El Soplao took place with temperatures far below its glass transition (temperatures from 300 K up to 340 K). This means that its configurational energy has gradually decreased during ~ 110 million years to the value of a minimum well below those which can be accessed at higher annealing temperatures for shorter annealing times. Hence, the thermal treatments done in the laboratory to the pristine sample drive it uniquely towards minima at higher potential energy values (represented with the orange, green and blue circles in Figure 5.6). The rejuvenated amber glass, after heating the pristine sample above T_g, corresponds to the conventional glass, located in the minima of higher potential energy in the landscape scenario. Human scale annealings to the conventional glass can only bring it to minima slightly below the conventional glass (illustrated with the purple and violet circles in Figure 5.6).

Comparison between the sample annealed in the laboratory for two hours at 423 K and the pristine amber reveals the effectiveness of the hyperageing process, hence supporting the idea of relaxation processes in glasses far below the glass transition. But let us go beyond this qualitative description of the enhanced stability in amber and try to quantify it in terms of kinetic and thermodynamic parameters.

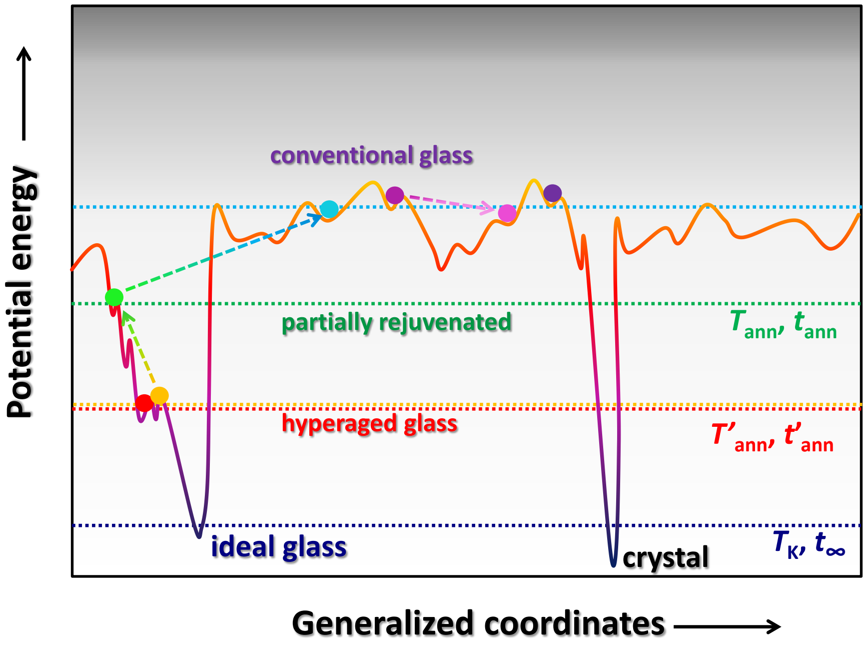

Figure 5.6 Potential energy landscape scenario of Spanish amber from *El Soplao***.** The successive states obtained with the gradual thermal treatments to the pristine sample are illustrated with the path described by the circles and the arrows, which correspond to the specific heat curves in Figure 5.4 and Figure 5.5, as the ageing signal at the glass transition decreases. After the conventional state is reached, human scale annealings only produce slight decreases in the potential energy landscape.

In order to perform a quantitative analysis of the stability in amber glasses, the devitrification temperature T_{dev} (defined as the maximum in $\mathrm{d}C_{\mathrm{P}}^{\mathrm{rev}}/\mathrm{d}T$) and the fictive temperature T_{f} are of great interest. The former gives us information on the kinetic stability of the glass: the more stable the glass is, the higher T_{dev} is, since a larger amount of energy is necessary in order to force the molecules in the system to flow.

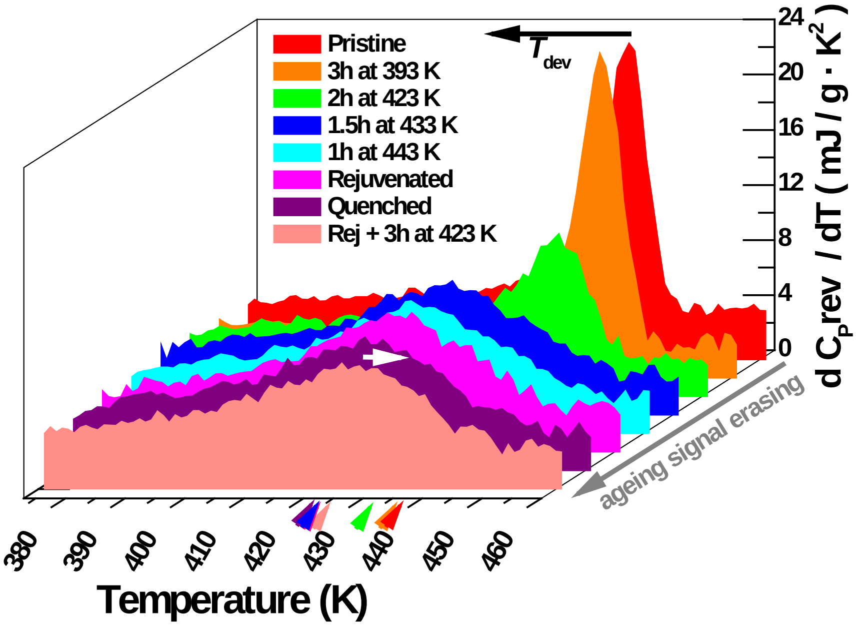

Figure 5.7 Temperature derivative of the reversing part of the specific heat for the Spanish type B amber in Figure 5.4 and Figure 5.5. The maximum of the derivative determines the devitrification temperature. A shift towards lower temperatures of T_{dev} is observed as the stability of the sample is decreased (black arrow) from 438 K (pristine amber) to 423 K (conventional or rejuvenated sample). After complete rejuvenation, thermal annealing at 423 K for two hours produces a negligible increase on the stability of the conventional glass, observed as a slight increase in T_{dev}.

From the MT-DSC measurements, we obtain separately the reversing and non-reversing contributions to the specific heat. The reversing part is a measure of the specific heat of the sample in thermal equilibrium, whereas the non-reversing specific heat includes the history-dependent processes, this is, the ageing signal in our amber samples. Analyzing the reversible specific heat, quantification of the shift in the devitrification temperature, as stability is decreased from the initial pristine sample to the conventional glass, can be done. In Figure 5.7 the evolution of the devitrification temperature with decreasing stability is shown. Determination of T_{dev} is done using the maximum in the temperature derivative of the reversible specific heat $\mathrm{d}C_{\mathrm{P}}^{\mathrm{rev}}/\mathrm{d}T$, which in the case of the conventional glass corresponds to the total specific heat $C_{\mathrm{P}}^{\mathrm{rev}} \equiv C_{\mathrm{P}}^{\mathrm{tot}}$(since no thermal history contribution exists). A gradual decrease in T_{dev} is produced when annealing the pristine hyperaged amber near $T_{\mathrm{g}} = 423$ K. A maximum shift $\Delta T_{\mathrm{dev}} = 15$ K when going from the initial hyperaged sample to the final rejuvenated glass is measured. Quenching the liquid at 50 K/min introduces no shift in T_{dev}, whereas annealing of the conventional glass at its glass transition $T_{\mathrm{g}}^{\mathrm{conv}} = 423$ K for two hours produces a negligble increase of its T_{dev} of ~ 1 K, indicated by the white arrow in Figure 5.7.

5.2.2 Fictive temperature and thermodynamic stability in *type B* amber

We have seen how hyperageing in amber samples produces an increase in the kinetic stability, as seen in the shift of 15 K in the devitrification temperature from the conventional amber glass to the extremely stabilized one. In parallel, the effects of this hyperageing in the thermodynamic stability of the amber glass can be determined. For this purpose, the fictive temperature T_{f} calculated from the enthalpy curves provides insight of the thermodynamic state of the glass. It is lower the higher the stability, since (as introduced in Section 2.1) it is equivalent to quenching the thermodynamically equilibrated liquid at that temperature.

The enthalpy curves of the amber samples are directly calculated from the specific heat curves in Figure 5.4 and Figure 5.5, through

$$H(T) = \int_{T_0}^{T} C_P(T)\,\mathrm{d}T \tag{5.1}$$

where T_0 denotes a reference temperature in the liquid state, and C_{P} the total specific heat (the reversing plus the nonreversing contribution). Fixing T_0 well above the glass transition, where the system is ergodic, and calculating numerically Equation (5.1) for every curve in Figure 5.4, we obtain the total enthalpy evolution as thermal treatments are applied to the pristine amber sample of type B, shown in Figure 5.8

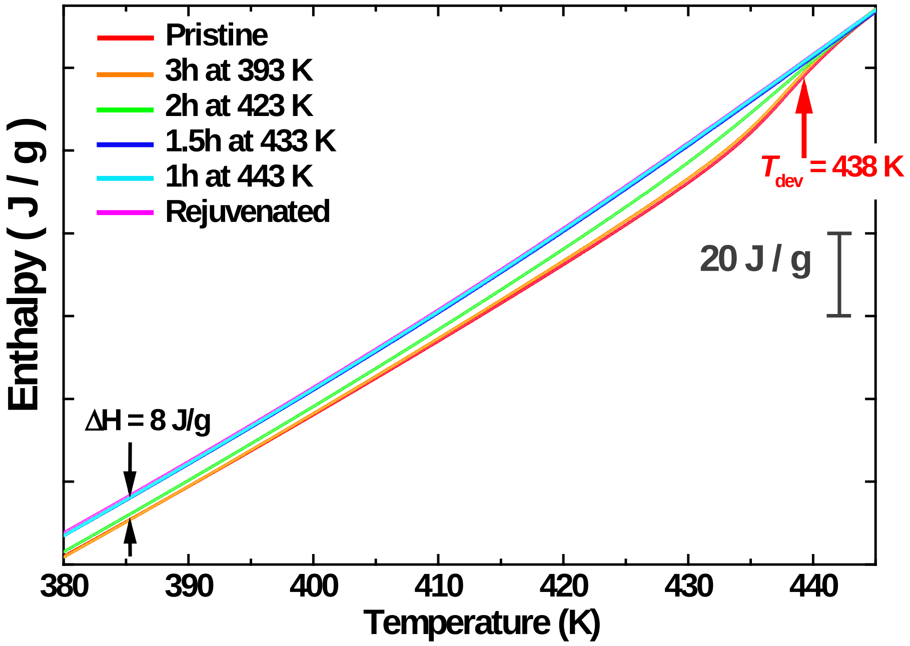

Figure 5.8 Total enthalpy versus temperature curves for type B amber samples from *El Soplao*. Evolution of the pristine amber enthalpy with different thermal treatments next to the devitrification temperature T_{dev} are shown, calculated from the specific heat curves in Figure 5.4. The enthalpy decrease due to hyperageing is ΔH = 8 J/g, calculated from the difference between the rejuvenated (conventional) amber and the pristine sample. The enthalpy scale is indicated with a vertical bar on the left axis. The devitrification temperature T_{dev} = 438 K corresponds to the pristine amber sample.

The enthalpy curves for type B amber samples from *El Soplao* in Figure 5.8 show a clear evolution towards higher values when thermal treatments near the devitrification temperature are applied to the pristine sample. A total difference ΔH = 8 J/g is observed between the hyperaged amber and the conventional glass, after rejuvenation of the pristine sample. This high value of the enthalpy released in the pristine sample reveals the great thermodynamic stability induced by the extreme ageing process. Besides, this effect is comparable to that observed in ultrastable thin films [SKMK07][KSEW07][LSGT10], in which physical vapor deposition is used to grow extraordinary stable glasses, playing with the substrate temperature and the evaporation rate.

In order to account for the thermodynamic stability of the amber samples, as well as its evolution with the thermal treatments applied to the hyperaged sample, we will determine the fictive temperature T_f from the enthalpy curves. Calculation of this parameter can be done in several ways, depending on the criterion used. In fact, different methods conduct to different T_f values, and hence can lead to different estimations of the shift due to the stabilization processes. Discussion of some of the methods that could be employed in our case is presented below, together with a comparison of the values provided by each of them.

5.2.2.1 Methods for the estimation of the fictive temperature

From the enthalpy curves corresponding to the pristine and rejuvenated amber samples in Figure 5.8 we will illustrate some of the methods which can be frequently found in the literature to determine the fictive temperature. We will discuss three different procedures which can be summarized as follows:

A. The fictive temperature is calculated by extrapolating the enthalpy of the liquid and finding the point where it intersects the enthalpy of the glass.

B. The fictive temperature is determined by the intersection of both extrapolations from the enthalpy of the liquid and the glass, far from the glass transition.

C. Assuming that well below the glass transition only the vibrational contribution to the specific heat persists, calculation of the fictive temperature is done in terms of the configurational enthalpy (calculated from the specific-heat difference between the total C_P and the extrapolation from the liquid, as shown in Figure 5.11).

Let us begin with the A method, for which only the extrapolation for the liquid of the enthalpy is needed. In our case, attending to the linearly increasing specific heat of amber far from T_g, a quadratic fit of the enthalpy curve is needed. Fitting the enthalpy curve in the liquid region (i.e. in the temperature range 452 K $\leq T \leq$ 465 K) the fictive temperatures for the pristine and rejuvenated type B amber samples are shown in Figure 5.9

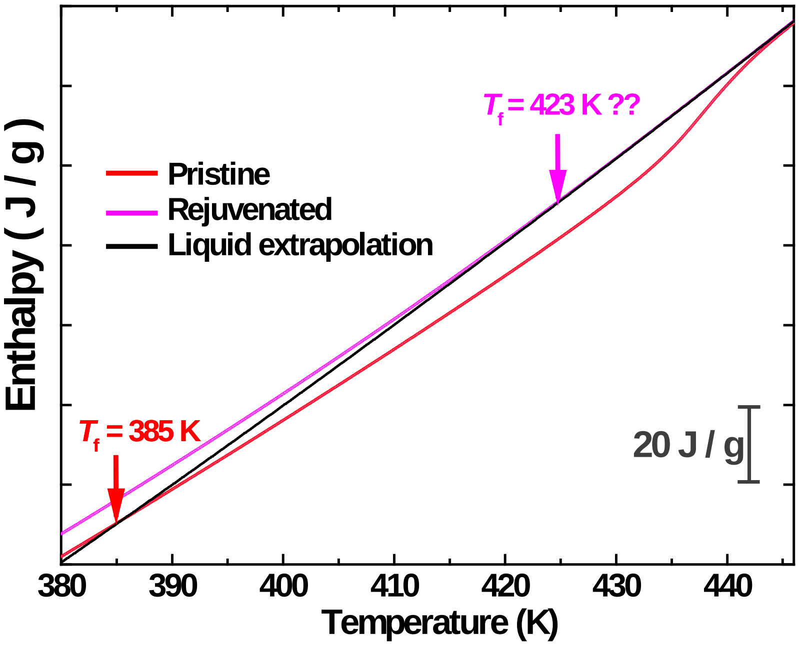

Figure 5.9 Fictive temperature determination for the pristine and rejuvenated (type B) amber samples from *El Soplao*, applying method A to the total enthalpy curve. Extrapolation of the enthalpy curve from the liquid is done using a quadratic fit in the temperature range 452 K ≤ T ≤ 465 K. Fictive temperature for the pristine sample is found to be T_f = 385 K, whereas the intersection of the extrapolated liquid curve with the rejuvenated sample is not clear. The maximal fictive temperature for the conventional glass would be then T_f = 423 K.

From Figure 5.9 a problem in the determination of the fictive temperature for the conventional glass appears, since the extrapolated curve from the liquid appears overlapping that of the conventional glass in a wide temperature range. The fictive temperature T_f = 423 K corresponds to the case of the rejuvenated sample, in which this value would be maximum, hence $T_f^{rej} = T_g^{rej}$. Nevertheless, the uncertainty in T_f for the conventional glass makes this method inadequate in our case.

The second method implies calculating in addition to the liquid extrapolation, the glass extrapolation for the enthalpy curve far below the glass transition. By doing this, again using a quadratic fit for the enthalpy fits, in the temperature range (for the glass) 320 K ≤ T ≤ 355 K, we find the fictive temperature shown in Figure 5.10

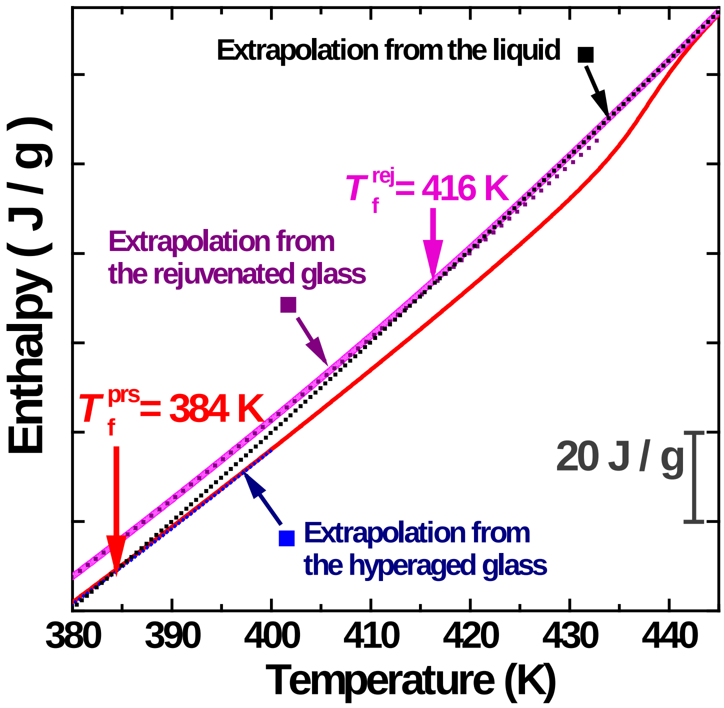

Figure 5.10 Fictive temperature determination from the enthalpy curves of the pristine and rejuvenated (type B) amber samples, using method B. Intersections between the extrapolations from the liquid and the glass far from the glass transition are used to calculate T_f. A total fictive temperature shift ΔT_f = 32 K is observed between the extremely stabilized amber and the rejuvenated one.

Determination of the fictive temperature using extrapolations both from the liquid and the glass resolves the problem with the conventional glass, found when applying *Method A* in Figure 5.9. Besides, the value calculated for the pristine amber presents only a small variation ~ 1 K to that using only the liquid extrapolation. This small difference derives from the fact that the extrapolated and the glass curves in the range of interest are almost indistinguishable of each other, since T_f is far below the glass transition. All these aspects support the convenience of using *Method B* instead of only the liquid extrapolation, so that the fictive temperatures near T_g can be properly resolved.

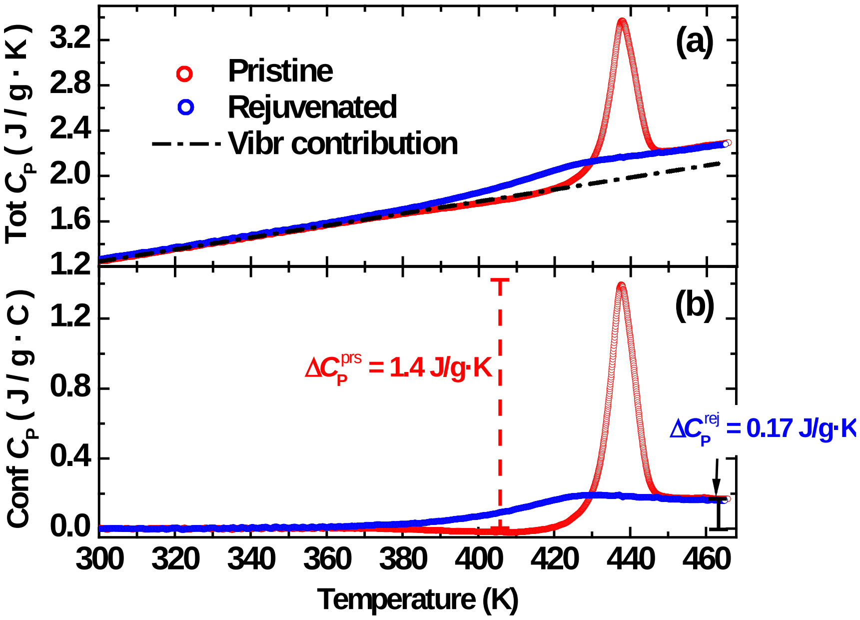

Figure 5.11 Specific heat for the pristine and rejuvenated (type B) amber samples from *El Soplao*. (a) Total specific heat together with the vibrational contribution calculated as the linear fit from the C_P curve in the temperature range 300 K $\leq T \leq$ 350 K. (b) Configurational specific heat curves after subtracting the vibrational contribution to the total specific heat in (a). Comparison between the jump in the pristine and rejuvenated samples is shown, where ΔC_P^{prs} = 1.4 J/g·K and ΔC_P^{rej} = 0.17 J/g·K.

The third method (method C) consists of calculating the fictive temperature from the configurational enthalpy instead of using the total enthalpy curve. To do this, it is supposed that the specific heat of the glass is mainly vibrational.

Assuming this, the configurational contribution to the specific heat is obtained from the difference between the liquid and the extrapolation from the glass, as presented in Figure 5.11.

Assuming that well below the glass transition the contribution to the specific heat is all of vibrational nature, we can fit C_P far from T_g and, extrapolating it to higher temperatures, subtract the vibrational part in the range of interest. Looking at the C_P curves in Figure 5.3, a linear fit in the temperature range $300\ \mathrm{K} \leq T \leq 350\ \mathrm{K}$ accounts well for the specific heat behavior, and can be used to extrapolate the vibrational contribution for temperatures > 350 K, as shown in Figure 5.11a. Subtracting this part to the total specific heat, the configurational contribution is calculated, as illustrated in Figure 5.11b. By doing this, the magnitude of the relaxation signal induced by the hyperageing appears clear. From direct comparison of the height of the overshoot in the pristine sample with the jump in the rejuvenated (conventional) glass in Figure 5.11b, we find the relation $\Delta C_P^{prs}/\Delta C_P^{rej} > 8$. This is a further evidence of the huge release of configurational enthalpy (or entropy) occurring at T_g for the hyperaged glass.

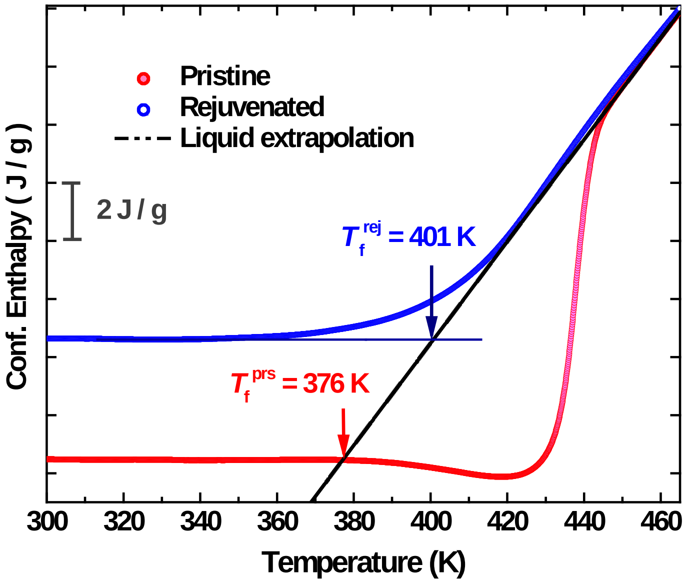

Figure 5.12 Configurational enthalpy curves for the pristine and rejuvenated (type B) amber samples from *El Soplao*, after integration of the configurational specific heat in Figure 11b. The fictive temperature is determined with the intersection form the extrapolated enthalpy of the liquid and the glass, analogous to Figure 5.10. The enthalpy scale is indicated with a bar on the left axis.

From Figure 5.11b we find that the extrapolation (at T_g and above) done for the specific heat of the glass from the data well below T_g perhaps overestimates its contribution, given the discrepancy with the values obtained from the total enthalpy curve in Figure 5.10. Ignoring this important aspect for the moment, and calculating the corresponding configurational enthalpy, we find the fictive temperatures estimation using *Method C*, as shown in Figure 5.12. The total shift in the fictive temperature due to the hyperageing is reduced to $\Delta T_f = 25$ K, and the values for both samples appear at lower temperatures. It seems very surprising the low fictive temperature value for the rejuvenated sample, far below the glass transition $T_g = 423$ K. This consideration, together with the questionable assumption that only vibrational contribution appears in the specific heat below T_g (illustrated in the striking negative C_P^{conf} for the pristine sample in Figure 5.11b) confirms the election of *Method B* to determine T_f.

5.2.2.2 Fictive temperature evolution with hyperageing

After comparing some of the possible methods to calculate the fictive temperature from the enthalpy curve, and finding *Method B* as the optimal choice for our study, we can already determine T_f for all the amber glasses studied in Figure 5.4 and Figure 5.5. By doing the respective extrapolations from the glass enthalpy far below T_g, their intersection with the enthalpy of the liquid determines T_f for amber (type B) samples going from the pristine back to the rejuvenated one, as shown in Figure 5.13. It is clear that the extreme thermodynamic stability is progressively reduced as partial treatments at higher temperatures (near T_g) are applied to the pristine sample. The total shift in the fictive temperature from the hyperaged to the conventional glass is very high $\Delta T_f = 32$ K, comparable to the effect observed in ultraestable thin films of organic glasses [SKMK07][KSEW08][SLGR11]. On the other hand, quenching the liquid introduces an inappreciable effect in the fictive temperature, similarly to the invariance in T_{dev} seen in Figure 5.7.

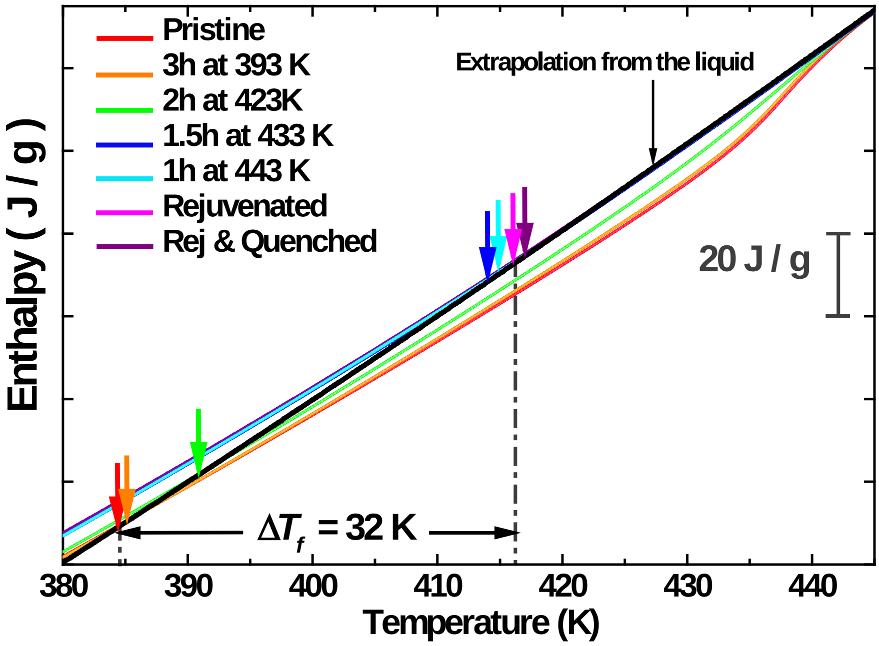

Figure 5.13 Fictive temperature evolution for the type B amber from El Soplao from the initial hyperaged (extraordinary stable) state to the rejuvenated (conventional) glass, applying gradual thermal treatments near T_g to the pristine sample. The quenched sample was obtained after heating the pristine sample above its T_{dev} = 438 K and cooling at 50 K/min. The quadratic fits (calculated in Figure 5.10) of the glasses are not shown for clarity.

5.2.3 Kinetic versus thermodynamic stability in *type B* amber from *El Soplao*

We have already analyzed separately the kinetic and thermodynamic stability in the Spanish amber type B samples from *El Soplao* as a function of its thermal history. Let us now bring together the evolution of the devitrification temperature and the fictive temperature, so that a quantity of how far our sample has traveled in the journey towards the ideal glass can be given. Although we do not have an estimation of the Kauzmann temperature for our amber glass, to which the fictive temperature of the hyperaged sample could be directly compared, we can define the following stabilization factor *s*

$$s = \frac{T_g - T_f}{T_g} \tag{5.2}$$

where T_g = 423 K and T_f denote the glass transition temperature and the fictive temperature, respectively. In Table 5.1 we summarize T_{dev}, T_f and s for all the thermal histories in the type B amber from El Soplao, shown in Figure 5.7 and Figure 5.13

Thermal history	T_{dev} **(K)**	T_f **(K)**	$s = \frac{T_g - T_f}{T_g}$
Hyperaged	438	384	9.2%
3 hours at 393 K	438	385	9.0%
2 hours at 423 K	436	391	7.6%
1.5 hours at 433 K	423	413	2.4%
1 hour at 443 K	423	415	1.9%
Rejuvenated	423	416	1.7%
Quenched	423	417	1.4%
Rej. + 2 hours at 423 K	424	416	1.7%

Table 5.1 Summary of the stability parameters for the Spanish amber type B from *El Soplao* as a function of its thermal history. The devitrification temperature T_{dev} is calculated from the maximum in dC_P^{rev} / dT shown in Figure 5.7. The fictive temperature T_f determined from the intersection between the liquid and glass enthalpy extrapolations in Figure 5.13. The stabilization factor is given from Equation (5.2) in (%). The glass transition temperature for the type B Spanish amber is T_g = 423 K.

The stability factor measures how far the fictive- and glass- transition temperatures are from each other, normalized to T_g. The closer they are, the higher the system is in the potential energy landscape (see Figure 5.6), up to the limit of the conventional glass, for which $T_f \equiv T_g$. Comparing to the values obtained for ultrastable samples of organic molecules like IMC (indomethacin) or TNB (1,3-bis-(1-naphthyl)-5-(2-naphthyl)benzene), which have stabilization factors s_{IMC} = 6.4% from the data in [KSEW07] and s_{TNB} = 9% from data in [SKMK07], we find that the stabilization in our Spanish amber samples is similar or even higher to that in these vapor-deposited thin films. For B_2O_3 (which is extremely sensitive to annealing processes) annealed for one week at 480 K from [Ramos97] s_{B2O3} = 6.8%; for o-terphenyl and selenium from [Kearns10] and references therein, we find stabilization factors $s_{o\text{-}ter}$ = 0.8% and s_{Se} = 1%, respectively, far from the values obtained for our hyperaged amber glass.

5.2.4 Kinetic versus thermodynamic stability in *type A* amber from *El Soplao*

Until now we have discussed the enhanced stability, both kinetic and thermodynamic, of Spanish type B amber (see Figure 5.1) from *El Soplao* due to hyperageing. Nevertheless, the existence of two ambers which share geographical origin and present differing chemical compositions [NPRP09][MNVR10] allows us to investigate the possible different effects of the same extreme ageing process in different polymer glasses. For this purpose, an analogous study to that presented in Sections 5.2.1 and 5.2.2 for the type B amber is introduced here for type A amber (the purple-blue amber in Figure 5.1).

The specific heat curves obtained by MT-DSC measurements on type A amber followed the same scheme of three heating ramps at 1 K/min and modulating amplitude ± 0.5 K every 80 s. For further details about the measurement protocol see *Appendix A*. The specific heat curves in Figure 5.14 obtained for samples presenting different thermal histories, from the hyperaged to the rejuvenated (conventional) glass, show the huge overshoot due to the relaxation processes, which decreases as thermal treatments are applied to the pristine sample. The first point to mention in the specific heat curves of type A amber is its glass transition temperature at 402 K, 21 K lower than in the type B amber. Another aspect to highlight is that the relaxation signal due to hyperageing appears here in a broad temperature range of 40 K, much wider than in the case of type B amber with 20 K-wide relaxation signal. Besides, the height of the relaxation signal (normalized to the C_p jump due to the glass transition) in type A amber is approximately half of that in type B amber.

Apart from the T_g location and the wider relaxation signal in type A amber, the effects of the thermal treatments on the pristine sample are analogous to those induced in type B amber, with a gradual decrease with increasing annealing temperature.

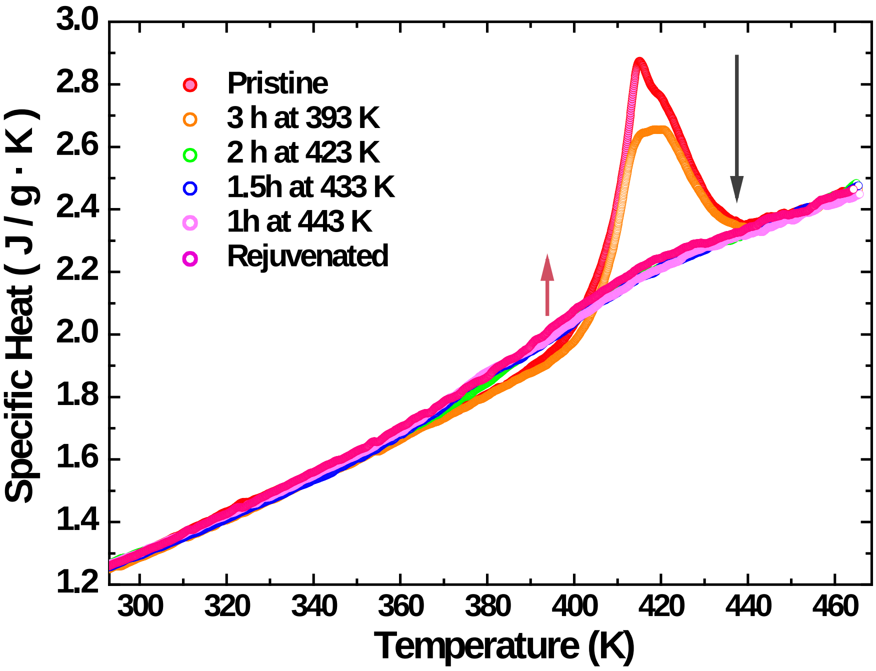

Figure 5.14 Specific heat evolution with thermal history for the Spanish amber type A samples from El Soplao. The devitrification temperature of the pristine sample is at 418 K, and decreases with increasing annealing temperature. The ageing signal appears as a broad and high endothermic peak at the devitrification, gradually disappearing with the thermal treatments. Temperatures of the partial thermal treatments appear in the legend, $T_g = 402$ K. Heating rates are 1 K/min, modulating amplitude ± 0.5 K/min every 80 s. Only the first heating curves of each sample (see Figure 5.3) measurement are presented.

Let us go now to the analysis of the glass transition evolution due to decreasing kinetic stability, as the ageing effect is stepwise erased. Taking the reversible contribution to the specific heat curves in Figure 5.14 and calculating its temperature derivative, we can evaluate T_{dev} as the position of the maximum in dC_p^{rev} / dT, as shown in Figure 5.15.

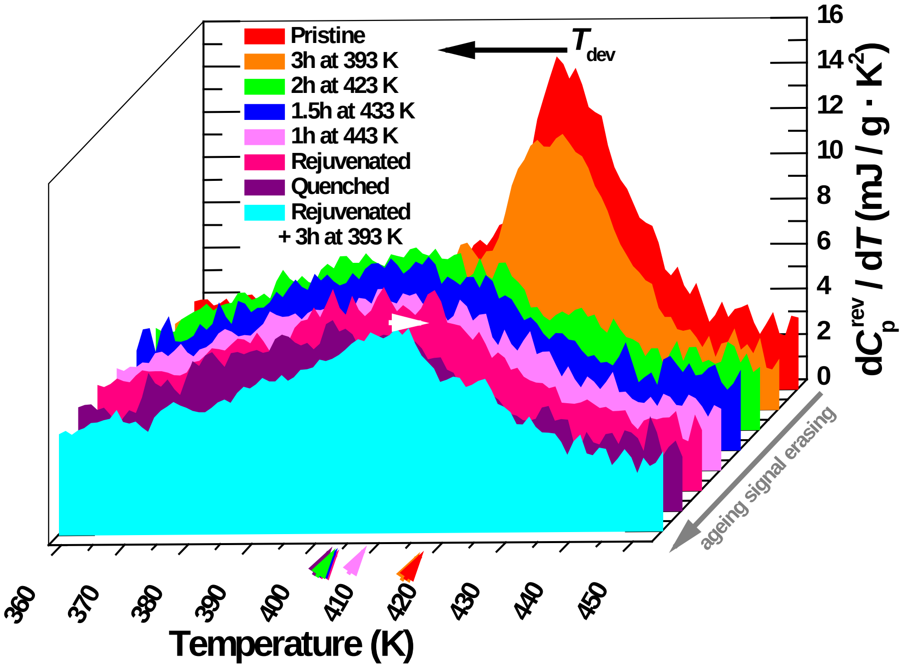

Figure 5.15 Temperature derivative of the reversing part of specific heat for the Spanish amber type A from *El Soplao* with decreasing stability (ageing signal). The maximum in dC_p^{rev} / dT provides the devitrification temperature T_{dev}, which evolves towards lower values (black arrow) with the partial thermal treatments applied to the pristine sample. After rejuvenating the sample, thermal annealings below T_g produce negligible increase of the kinetic stability, as shown with the white arrow.

A decrease in T_{dev} from 418 K in the pristine amber type A sample to 402 K in the rejuvenated one is observed, similar to the glass transition shift in type B amber from *El Soplao*. Although the glass transition temperature T_g in the pristine type A sample is 21 K lower than that of the type B amber, the effects of enhanced kinetic stability are analogous, with total shifts ΔT_{dev} = 15 - 16 K in both cases. Furthermore, the two samples evolve from a very sharp devitrification process to a broad one with decreasing stability, as illustrated in the reduction and widening of the dC_p^{rev} / dT (indicated with the black arrow) in Figure 5.15. After the sample is rejuvenated, thermal treatments induced negligible changes in T_{dev} (marked with the white arrow in Figure 5.15).

The enthalpy curves for the type A amber samples with different thermal histories in Figure 5.16 are calculated by directly integrating the specific heat curves in Figure 5.14, using Equation (5.1).

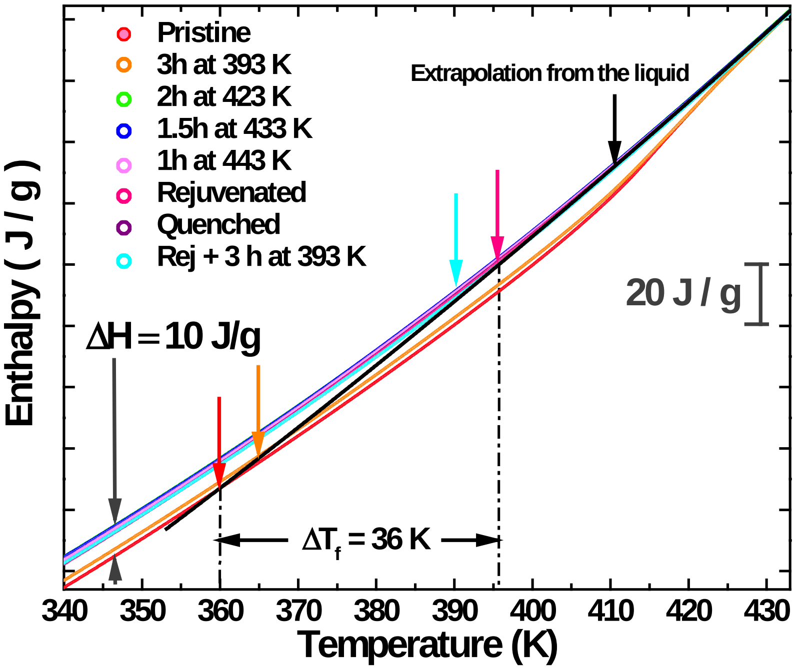

Figure 5.16 Enthalpy curves for the Spanish amber type A from El Soplao with different thermal histories from the pristine (hyperaged) amber to the rejuvenated (conventional) one. The colored arrows indicate the fictive temperature positions for the pristine (red), thermally annealed at 393 K (orange), rejuvenated (pink) and annealed at 393 K after rejuvenation (light blue). The total enthalpy difference due to hyperageing ΔH = 10 J/g and fictive temperature shift ΔT_f = 36 K is calculated taking the pristine and rejuvenated amber curves. The enthalpy scale is shown with a vertical bar on the right axis. Calculations of the fictive temperatures are done using extrapolations both from the liquid and the glass. Only extrapolation of the liquid is shown for clarity.

An analogous behavior to that exhibited by type B amber samples is observed with decreasing stability, when gradually annealing the pristine samples at temperatures closer to the glass transition temperature. Enthalpy release ΔH = 10 J/g, calculated from the difference between the pristine and rejuvenated samples, is similar to the value observed in type B amber. The fictive temperature shift ΔT_f = 36 K clearly shows the extraordinary thermodynamic stability induced by hyperageing.

A summary of the devitrification and fictive temperatures for type A Spanish amber, T_g = 402 K, together with the stabilization factor calculated using Equation (5.2) is shown in Table 5.2.

Thermal history	T_{dev} **(K)**	T_f **(K)**	$s = \frac{T_g - T_f}{T_g}$
Hyperaged	418	360	10.4%
3 hours at 393 K	417	367	9.2%
2 hours at 423 K	402	396	1.5%
1.5 hours at 433 K	402	396	1.5%
1 hour at 443 K	402	396	1.5%
Rejuvenated	402	396	1.5%
Quenched	402	396	1.5%
Rej. + 3 hours at 393 K	407	390	3.0%

Table 5.2 Summary of the stability parameters for the Spanish amber type A from *El Soplao* as a function of its thermal history. The devitrification temperature T_{dev} is calculated from the maximum in dC_P^{rev} / dT shown in Figure 5.15. The fictive temperature T_f determined from the intersection between the liquid and glass enthalpy extrapolations in Figure 5.16. The stabilization factor s is calculated from Equation (5.2).

Again, as in the case of the type B amber, the stability drastically decreases when annealing the pristine sample near the glass transition. The thermal treatments applied to the rejuvenated amber show poor efficiency if compared to the strong effects of the hyperageing. Notice that the hyperageing has decreased the fictive temperature of type A amber more than 10% the value of T_g, clearly surpassing the values reached up to date in other highly stable glasses.

5.3 Universal low-temperature anomalies in Spanish amber glasses from *El Soplao*

We have characterized in the previous sections the extraordinary thermodynamic and kinetic stability present in pristine Spanish amber samples from *El Soplao* as a consequence of the hyperageing process. MT-DSC measurements have provided us with the enthalpy values associated to the relaxations undergone in two different samples (type A and type B), together with the shifts in the fictive- and glass-transition temperatures. Applying thermal annealings to the pristine amber samples, gradual reduction of the stability have been observed. Further stabilization attempts done in the laboratory after complete rejuvenation of the amber samples have evidenced the extreme relaxation present in the pristine samples compared to annealing processes near T_g done in human-scale times.

In this section we present the consequences of the hyperageing in the Spanish type B amber from *El Soplao* on the universal low-temperature anomalies of glasses, i.e., the tunneling states and the boson peak. This study is analogous to that performed in Chapter 4 for the Dominican amber. The low-temperature specific heat of the pristine, a partially rejuvenated and the (completely) rejuvenated type B Spanish amber has been measured in the temperature range 0.07 K – 35 K, as shown in Figure 5.17. The partially rejuvenated amber corresponds to the pristine type B sample annealed at 423 K for 2 hours (see Figure 5.4). This study was done using a ^{3}He/^{4}He dilution refrigerator together with a ^{4}He cryostat. In parallel, the Debye level was determined using High Resolution Brillouin Scattering (HRBS) (described in Section 4.4), in order to quantify the phonon contribution independently. Determination of the mass density for the three samples measured at low-temperatures was done using the Archimedes method with a microbalance.

5.3.1 Elasto-acoustic measurements

We have determined the zero-temperature values of the longitudinal and transversal sound velocities for the three Spanish type B amber samples studied at low-temperatures, using HRBS, analogously to what we did for the Dominican amber in Section 4.4. By doing this, we calculate the Debye limit of the sound velocity. Besides, the mass densities of these samples were measured at room temperature, and extrapolated to 0 K using the Lorenz-Lorentz relation given in Equation (4.5). With these two values, v_{Debye} and $\rho_{0\,\mathrm{K}}$, we can estimate the Debye contribution to the specific heat in the Spanish amber.

In Figure 5.17 the temperature dependence of the longitudinal sound velocities of Spanish type B amber is shown, together with the best linear fit used to extrapolate their zero-temperature value.

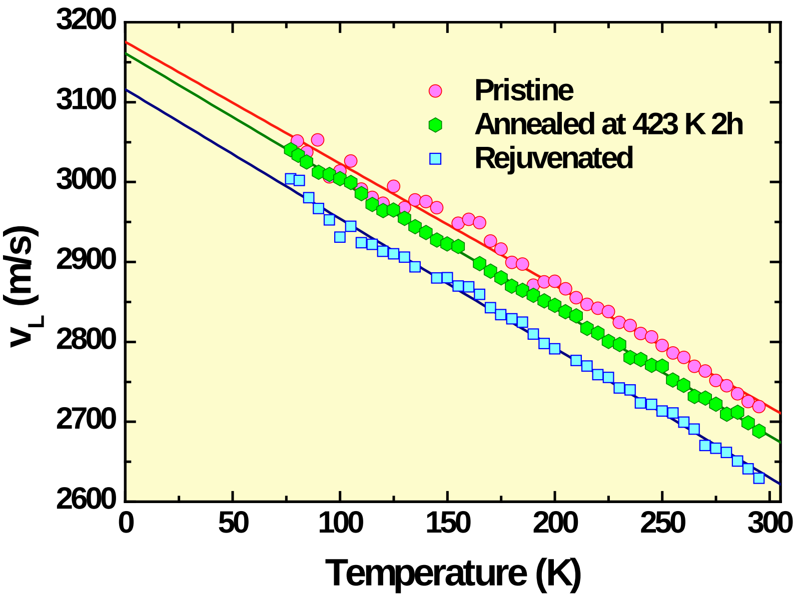

Figure 5.17 Temperature dependence of the longitudinal sound velocities in Spanish type B amber with decreasing stability. The linear fits provide zero-temperature values $v_L^{prs}(0K) = 3175$ m/s, $v_L^{ann}(0K) = 3160$ m/s and $v_L^{rej}(0K) = 3115$ m/s.

Let us notice the gradual decrease of the longitudinal sound velocities for the three samples studied with decreasing stability, as a result of the thermal treatments applied progressively to the hyperaged amber. This behavior is the expected for a softening of the lattice when removing the ageing signal present in the pristine sample. It is also worth mentioning that the temperature dependence of v_L is almost the same in the three samples, as evidenced by the parallelism of the experimental data in the range 77 K $\leq T \leq$ 300 K. A total decrease of 1.9% from the pristine to the rejuvenated sample is observed, whereas the partial rejuvenation shows a small decrease of around 0.5%.

From the longitudinal sound velocities at 0 K, we have calculated the transversal sound-velocity values using the generalized Cauchy relation given in Equation (4.4). In the case of the Spanish amber, the values at room temperature of v_T could not be accessed due to the strong luminescence of the samples for the excitation wavelength used λ_0 = 514.5 nm. We estimated v_T(0K) by considering that the relation between longitudinal and transversal sound velocities is equal to that in the Dominican amber samples, this is v_T^2(0K)/ v_L^2(0K) = const. We calculated this value for the two Dominican amber samples studied, obtaining a relation factor of 0.276. Then we used it to calculate v_T(0K) for the Spanish amber, finding v_T^{prs}(0K) = 1666 m/s, v_T^{ann}(0K) = 1658 m/s and v_T^{rej}(0K) = 1634 m/s.

The mass density at room temperature of the three samples used in the low-temperature specific heat studies was determined by means of the Archimedes method. The values obtained are ρ_{prs}(300K) = 1.044 g/cm^3, ρ_{ann}(300K) = 1.038 g/cm^3 and ρ_{rej}(300K) = 1.024 g/cm^3. In order to calculate the 0 K extrapolation of the mass density using the Lorenz-Lorentz relation, the temperature dependence of the refractive index was measured between 77 K and 300 K. A linear fit of all the experimental data for the three samples measured in this range provided an estimation of the temperature dependence of the refractive index $n(T)$ = 1.553 – (2.619·10^{-5} K^{-1}) · T. The 0 K values for the mass density calculated are hence ρ_{prs}(0K) = 1.055 g/cm^3, ρ_{ann}(0K) = 1.049 g/cm^3 and ρ_{rej}(0K) = 1.035 g/cm^3.

From the average Debye sound velocities and the 0 K mass densities, we calculate the Debye contribution $C_{Debye} \equiv c_D \cdot T^3$ to the specific heat using Equation (4.6). In Table 5.3 we summarize the evolution of c_D with decreasing stability, as well as the elastic parameters used to estimate it.

Amber	ρ_{300K} (g/cm^3)	ρ_{0K} (g/cm^3)	v_L(300K) (km/s)	v_L(0K) (km/s)	v_T(0K) (km/s)	v_D (km/s)	c_D (μJ/g·K^4)
Pristine	1.045	1.055	2715	3175	1666	1863	17.7
Part. rejuv	1.038	1.049	2683	3160	1658	1854	18.1
Rejuvenated	1.024	1.035	2630	3115	1634	1828	19.1

Table 5.3 Elastic data determined by HRBS and mass density measurements for the three Spanish amber samples used for the low-temperature specific heat study, namely, the hyperaged (pristine), the partially rejuvenated (the pristine sample after annealing at 423 K for two hours) and the rejuvenated samples. Mass density values at room temperature ρ_{300K} and extrapolation to 0 K ρ_{0K} using Equation (4.5) and temperature dependence of refractive index $n(T) = 1.553 - (2.619\cdot10^{-5}\ \mathrm{K}^{-1})\cdot T$; Average Debye velocity v_D; Debye phonon-like contribution c_D calculated using Equation (4.6).

According to the data in Table 5.3 when removing the ageing signal (from the pristine to the rejuvenated sample), we see a considerable density reduction of 1.9%, in parallel with a decrease in the average Debye sound velocity of 1.9%. The combined reduction of ρ_{0K} and v_D produces a moderate increase of the Debye contribution to the specific heat c_D of 8% after rejuvenating the hyperaged amber glass, and of 2% when partially removing the ageing.

5.3.2 Low-temperature specific heat

The low-temperature specific heat measurements enables us to quantify separately the contribution of the tunneling states (TLS), the phonon-like vibrations (independently determined from the elasto-acoustic measurements) and the soft modes within the Soft Potential Model, as already discussed in Section 4.3. In such a way, we can study the evolution of the universal low-temperature anomalies in glasses as a function of the thermodynamic and kinetic stability.

In order to determine the specific heat of our Spanish amber samples in the temperature range 0.07 K – 30 K we have used two cryogenic systems (see Section 3.2), the ^{4}He cryostat for the range 1.8 K – 30 K and the ^{3}He-^{4}He dilution refrigerator for the range 0.07 K – 2.5 K. Two calorimetric cells have been employed (one in each cryostat). Comparison of the heat capacity contribution of the empty cell, and the cell plus the sample (with mass m = 44.2 mg) are shown in Figure 5.18 for the measurements in both cryostats.

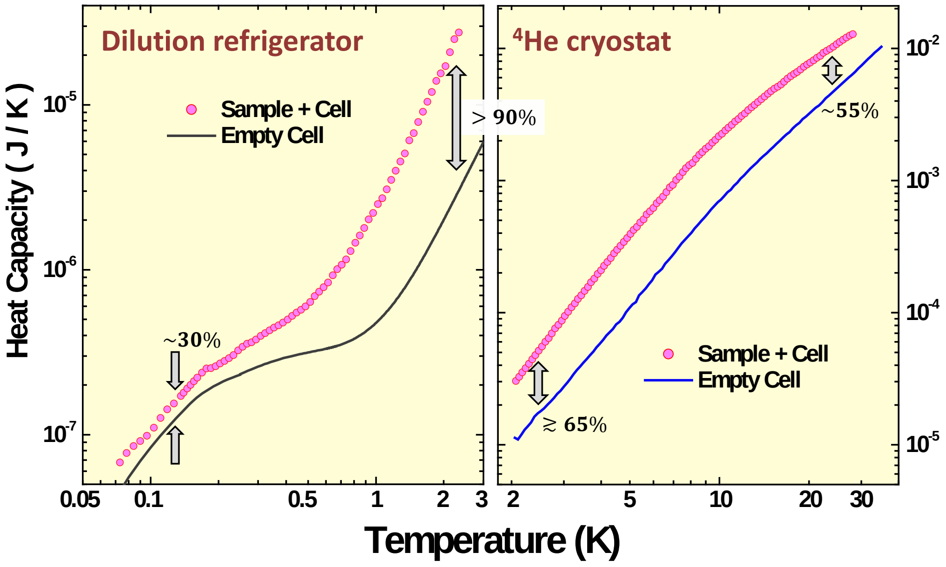

Figure 5.18 Comparison of the typical total heat capacity (sample + cell) measured for the Spanish amber samples (with mass m = 44.2 mg) both in the ^{3}He-^{4}He dilution refrigerator and the ^{4}He cryostat, with the heat capacity of the corresponding empty cell. The arrows indicate the sample contribution to the total heat capacity in the regions where this is maximum/minimum.

From Figure 5.18 we can estimate the contribution of the sample to the total heat capacity in the whole temperature range of our measurements. By doing this, we see that the minimum contribution of the empty cell is below 10%, whereas its maximum is of about 70%. The lower the contribution of the empty cell, the lower the dispersion in the final specific-heat data of the sample. Nevertheless, in the temperature range where this contribution is high, a higher density of the experimental data counteracts this effect to a large degree. Typical numbers of the points measured in the experiment are: 100 - 140 in the range 0.07 K - 2.5 K (equispaced in the logarithmic scale), 150 – 180 in the range 1.8 K – 30 K. After statistical analysis, the number of points in the whole range varies from 140 to 160, typically.

After subtracting the empty cell contribution to the heat capacity, we calculate the specific heat of our amber samples, as shown in Figure 5.19, where additional data at higher temperatures 30 K – 90 K are included as well.

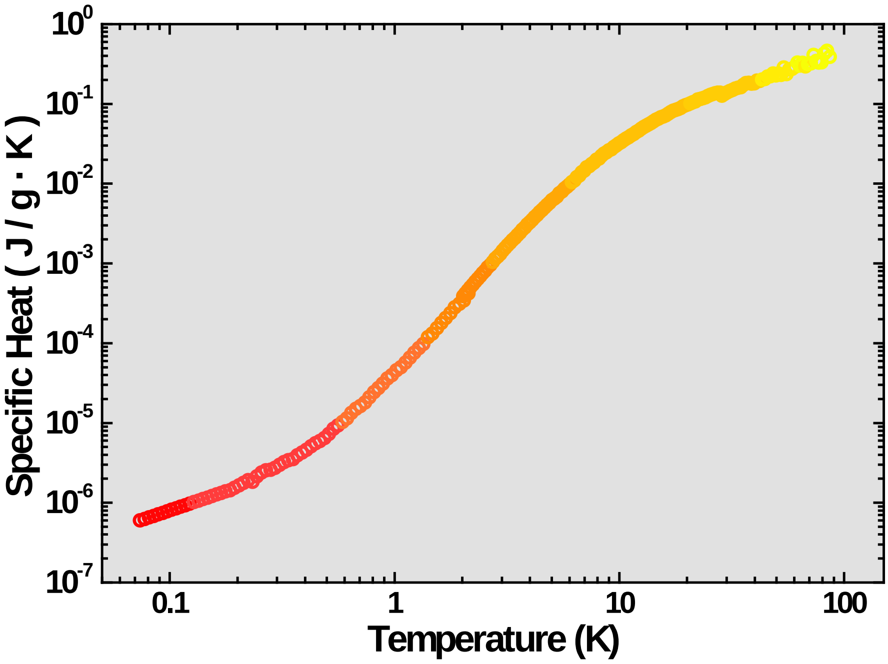

Figure 5.19 Low-temperature specific heat of the pristine Spanish amber type B from *El Soplao*, showing the overall temperature range measured using both the ^{3}He/^{4}He dilution refrigerator and the ^{4}He cryostat.

In Figure 5.19 the specific heat of the pristine amber type B sample from *El Soplao* is presented in the temperature range from 70 mK to 100 K, where the quasi linear dependence at very low temperatures (below 0.5 K) is clearly observed. The contribution of both the tunneling states and the soft modes are responsible for this marked departure from the $C_P \sim T^3$ behavior observed in crystals at low temperatures. This is more clearly seen in the typical reduced representation C_P/T^3 versus temperature of Figure 5.20, in a double logarithmic scale, after subtracting the Debye contribution determined from the elastic data in Table 5.3. The two relevant temperature ranges of the universal anomalies in glasses are highlighted in Figure 5.20. Below 1 K, the quasi linear dependence of the specific heat with temperature appears, and above 1 K the boson peak introduces a roughly $C_P \sim T^5$ increase immediately after the minimum, as shown in Figure 2.10 for SiO_2 and Se glasses.

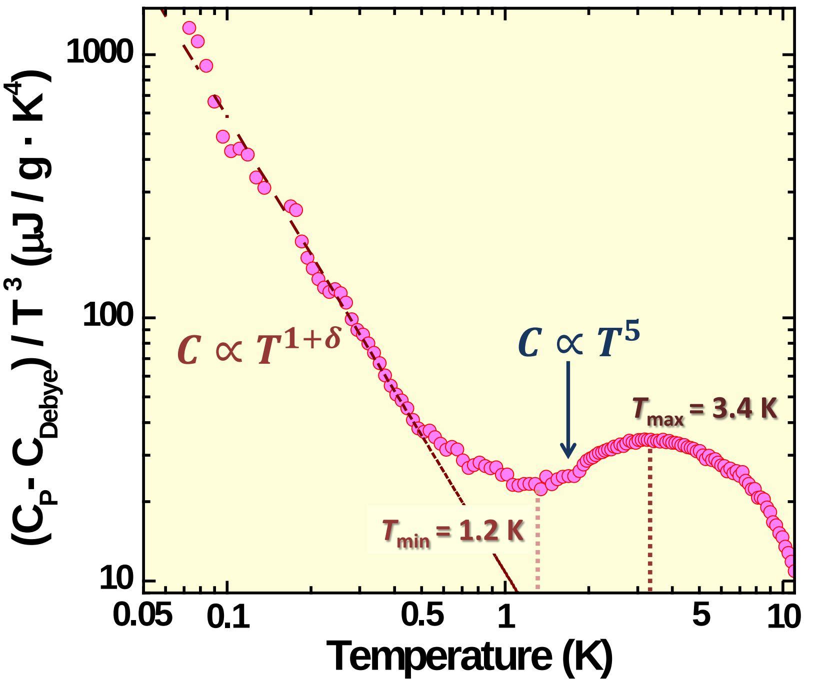

Figure 5.20 Reduced C_P/T^3 versus T representation (after subtracting the Debye contribution) in a double logarithmic scale for the pristine Spanish type B amber from *El Soplao*. This corresponds to the (hyperaged) extremely stable state. The quasi linear dependence with temperature $C_P \sim T^{1+\delta}$ below 1 K introduced by the tunneling states and the $C_P \sim T^5$ immediately above the minimum due to the left tail of the boson peak are highlighted. The minimum and the maximum positions in the C_P/T^3 representation are located at T_{min} = 1.2 K and T_{max} = 3.4 K, respectively.

The reduced C_P/T^3 representation, after subtracting the Debye contribution, of the specific heat for the hyperaged amber sample clearly presents the universal properties of glasses and amorphous solids at low temperatures, with the minimum (which marks the frontier between the TLS-dominated region to the vibrational-dominated one) at T_{min} = 1.2 K, and the maximum of the boson peak at T_{max} = 3.4 K. Let us notice that these temperatures are slightly lower than the values found for the Dominican amber in Chapter 4, which had the minimum and maximum positions at 1.3 K and 3.7 K, respectively.

After confirming that the universal glassy properties remain in a glass which has suffered an extreme stabilization process, the next step is to quantify the effect of hyperageing in the contribution of both the TLS and the soft modes. For this purpose, we have studied the evolution of the low-temperature specific heat when gradually rejuvenating the pristine amber sample. In Figure 5.21 we present the specific heat data in the C_P/T^3 representation for the pristine, the partially rejuvenated and the completely rejuvenated Spanish amber (type B) samples, together with their corresponding Debye level obtained from the elasto-acoustic measurements in Table 5.3.

There are three main aspects to be highlighted in Figure 5.21: (i) the moderate increase (~ 25%) of the boson peak height when completely removing the stability to the hyperaged sample, (ii) the collapse of the three curves at very low temperatures, what evidences equal TLS density of states in the three glasses, and (iii) the invariable position of the minimum and the maximum at T_{min} = 1.2 K and T_{max} = 3.4 K repectively, regardless of the stability of the sample.

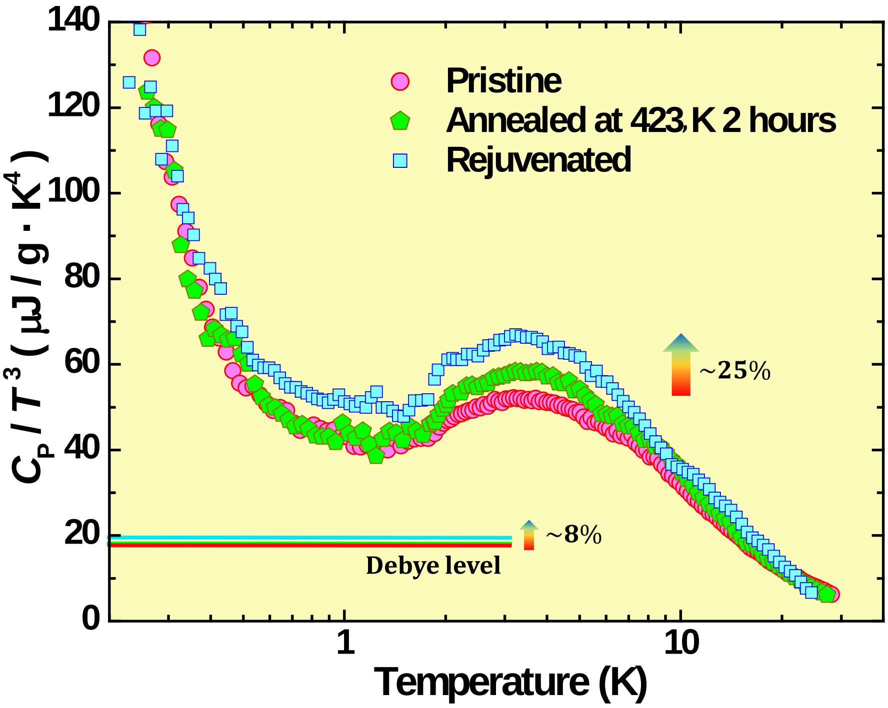

Figure 5.21 Evolution of the low-temperature properties of the hyperaged Spanish amber in the C_P/T^3 representation with decreasing stability in the range 0.2 K – 30 K. The curves for the pristine (solid red circles), the partially rejuvenated (solid green pentagons) and the completely rejuvenated (solid blue squares) samples are shown, together with their corresponding Debye level determined from the elastic data in Table 5.3. A 25% increase in the height of the boson peak is observed when removing the ageing, but no shift within the experimental error appears in the minimum and maximum positions T_{min} = 1.2 K and T_{max} = 3.4 K, respectively. The three curves collapse both at T < 0.4 K and T > 10 K.

We analyze the glassy properties of the Spanish amber in two steps: we focus first our attention on the contribution to the specific heat due to the tunneling states, given by the quasi linear temperature dependence at temperatures below 1 K. The second step is analyzing the excess vibrational density of states observed above 1 K, namely, the boson peak. In Figure 5.22 we show the specific heat curves for the three amber samples in the very low-temperature range 0.05 K – 2 K, in a double-logarithmic scale.

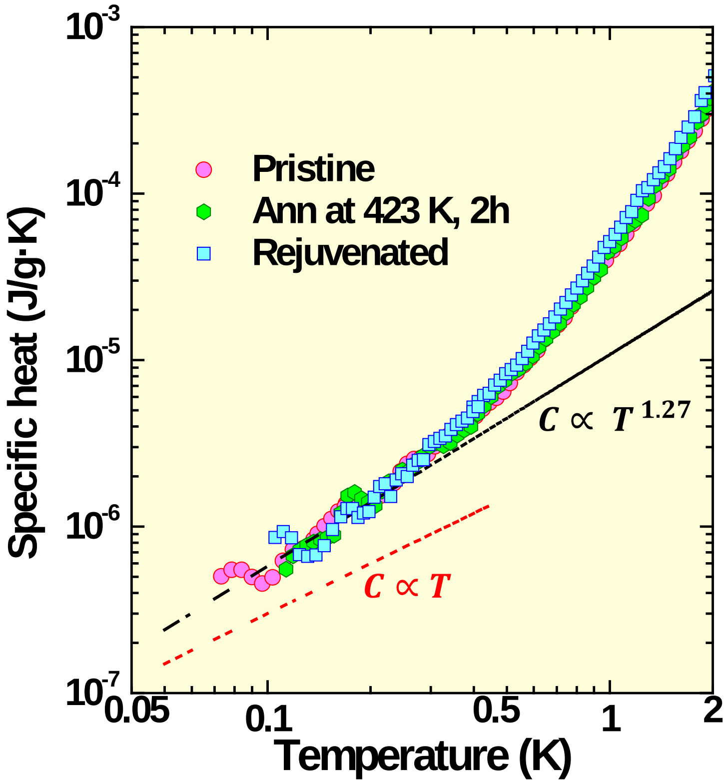

Figure 5.22 Comparison of the specific heat curves for the three Spanish amber samples at very low temperatures 0.05 K – 2 K. The collapsing of the three experimental curves within the experimental error below 0.5 K evidences the unchanged density of tunneling states when removing the hyperageing to the pristine sample. The dashed black line shows the best quasi linear fit to the experimental data given by $C \sim T^{1.27}$, which decreases faster with decreasing temperature than the linear dependence reflected by the dashed red line.

The very low temperature specific heat data in Figure 5.22 show a quasi linear dependence $C \sim T^{1.27}$, ascribed to the two-level systems in glasses as predicted by the tunneling model [Phil72] [AnHV72]. By fitting the specific heat curves of the three samples (after subtracting the Debye contribution $c_D \cdot T^3$) in the range 0.07 K – 0.45 K, we find the evolution of the TLS contribution with decreasing stability: c_{TLS}^{prs} = (10.8 ± 0.7) μJ/g·K$^{1.73}$, c_{TLS}^{ann} = (10.3 ± 0.9) μJ/g·K$^{1.73}$, c_{TLS}^{rej} = (10.5 ± 1.2) μJ/g·K$^{1.73}$. From these coefficients the equality of the TLS contribution within the experimental error in the three samples is evident, and hence the density of tunneling states remains constant after the extreme loss of stability in the sample when rejuvenating the hyperaged glass.

After calculating the TLS contribution to the specific heat, and using the Debye contribution determined from the acoustic and mass-density data, we can do an estimation of the soft modes contribution by assuming that

$$C_\mathrm{P}(T) = c_\mathrm{tunn} \cdot T^{1.27} + c_\mathrm{D} \cdot T^3 + c_\mathrm{sm} \cdot T^5 \tag{5.3}$$

holds up to 2 K, this is, in the boson peak region. In these conditions, we are able to evaluate c_sm by doing a linear fit of C_P-C_Debye-C_TLS versus T^5 in the temperature range $T_\mathrm{min} < T \leq (3/2)\ T_\mathrm{min}$, as shown in Figure 5.23

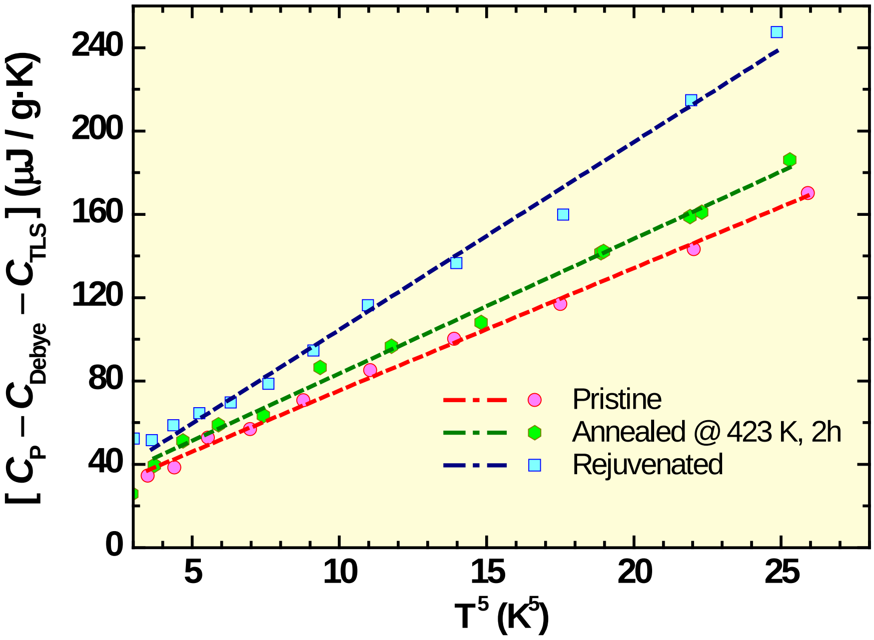

Figure 5.23 Calculation of the soft modes contribution c_sm to the specific heat by fitting $(C_\mathrm{P} - C_\mathrm{Debye} - C_\mathrm{TLS})$ versus T^5 in the range 3 $\mathrm{K}^5 < T^5 \leq 25\ \mathrm{K}^5$, for the three Spanish amber samples studied: the pristine amber (solid red circles) $c_\mathrm{sm}^\mathrm{prs} = 5.90 \pm 0.13$ μJ/g·K^6, the partially rejuvenated sample (solid green hexagons) $c_\mathrm{sm}^\mathrm{ann} = 6.50 \pm 0.15$ μJ/g·K^6 and the completely rejuvenated sample (solid blue squares) $c_\mathrm{sm}^\mathrm{rej} = 9.0 \pm 0.3$ μJ/g·K^6.

From the values obtained for c_{sm} in Figure 5.23 we would estimate almost a 50% increase of the soft modes contribution when rejuvenating the hyperaged amber. Nevertheless, ascribing the increase in the height of the boson peak to an increase in the excess vibrational density of states (the soft modes) would be rather simplistic. Comparing the pristine and rejuvenated amber samples, we clearly see in Figure 5.21 that the increase in C_P/T^3 is almost the same ~ 20-25% in the region of the minimum and the maximum, when rejuvenating the hyperaged glass. This rise in the range of the minimum cannot be explained as well only in terms of the increase of the Debye contribution ~ 8%. In Figure 5.24 the *excess* specific heat above the Debye level is shown in the C_P/T^3 representation, where this parallel increase of the curves in the range 0.8 K – 5 K is even more clearly observed.

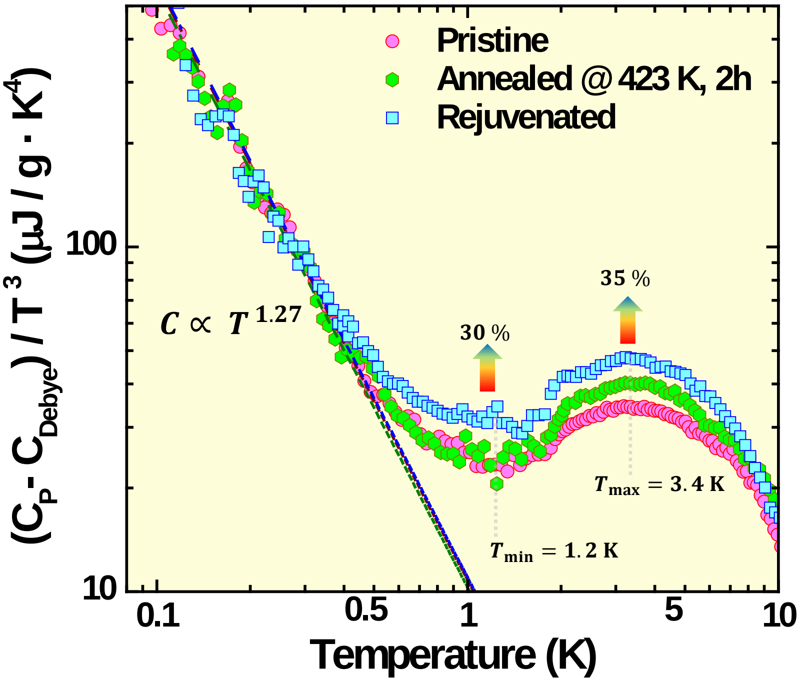

Figure 5.24 Excess specific heat in the C_P/T^3 representation for the three Spanish amber samples, after subtracting the Debye contribution $C_{Debye} \equiv c_D \cdot T^3$, determined from the elastic and mass density data in Table 5.3. The parallel increase in the regions of the minimum and the maximum when rejuvenating the hyperaged glass are indicated by the arrows. The three (almos indistinguishable) quasi linear fits in the very low-temperature range are shown in dashed lines. No shift in the position of the minimum and the maximum $T_{min} = 1.2$ K and $T_{max} = 3.4$ K are observed, within the experimental error.

These two aspects support the idea that the specific heat in this temperature region is a convolution of both the acoustic waves and the excess vibrational modes (due to the disorder) of the glass, which could interact or hybridize up to a frequency range in which the sound waves would become overdamped or quasilocalized, giving rise to the maximum of the boson peak (and the plateau in the thermal conductivity) [PaSG07]. Hence, it is senseless trying to separately analyze the contribution of the acoustic and the excess vibrational states in this higher temperature range, since the total specific heat is not a simple addition of these terms, as reflected in the overall increase in the range of the minimum and the maximum in Figure 5.24.

5.4 Conclusions

We have presented in this Chapter a model system like Spanish amber from El Soplao which is 112 million years old, to study the effects of an extreme ageing process in the thermodynamic and kinetic stability of a glass. Accurate MT-DSC measurements have provided us insight in the evolution of both the glass-transition temperature and the fictive temperature with increasing stability by independently analyzing the reversible and total specific heat change. A continuous increase of the devitrification temperature with ageing has been found, with a maximum T_{dev}-difference between the pristine and rejuvenated amber samples of 16 K. On the other hand, the fictive temperature was observed to steadily decrease with ageing, up to a maximum difference in T_{f} of 36 K. These values are the highest T_{dev} and T_{f} shifts observed in bulk glasses as a consequence of ageing up to date, and strongly support the idea of using natural amber in order to study the effects of extreme stabilization processes in glasses. The enthalpy released in this hyperageing has been found to be from 8 J/g to 10 J/g, comparable to the values obtained in ultrastable thin-film glasses grown by physical vapor deposition [SKMK07][SLGR11], which may be rather seen as 2D systems [SiEP13].

The existence of two types of Spanish amber from *El Soplao* (labeled as type A and type B), well studied in the bibliography [MNVR10][NPRP09], have also provided us insight on how the chemical composition shifts the glass transition temperature, and how the presence of inhomogenities broadens the ageing signal around the devitrification temperature. Nevertheless, the analysis of the kinetic and thermodynamic stability shows a similar behavior of the two amber types, since the thermal history is identical in both glasses.

After the exhaustive study on the phenomenology of these hyperaged glasses around their glass transition, we have investigated how the low-temperature properties of the Spanish type B amber glass evolve with increasing stability. The first point to be highlighted is that the universal glassy properties remain in an extremely stabilized glass. Besides, we have been able to determine how the universal excess density of states varies separately (the TLS and the soft modes), by measuring the low-temperature specific heat of three amber samples with different thermal history: the pristine amber, partially-rejuvenated pristine amber and a rejuvenated one. A first inspection of the specific heat evolution, in the C_P/T^3 representation, when removing the ageing, evidenced the invariability of C_P at temperatures below 0.5 K. This is associated to a constant density of tunneling states regardless of the thermodynamic and kinetic stability of the sample. The independent determination of the sound velocities by HRBS and of the mass density showed an expected moderate increase in the Debye level of about 8% when rejuvenating the hyperaged sample. The persistence of the excess low-temperature excitations in glasses, as shown in the invariability of the two-level systems, the moderate increase of the boson peak and the absence of shift in the position of the minimum and maximum in the C_P/T^3 representation, prove as well the independence of the excess vibrational states with the sample stability. This latter aspect contradicts the Debye scaling of the boson peak suggested by other authors [Baldi09][Monaco06].

The combined study done on the thermodynamic and kinetic stability of a hyperaged glass, its evolution when removing the ageing, and in parallel, the determination of the low-temperature specific heat and the elastic constants, support the following conclusions:

(i) Bulk hyperaged glasses of amber exhibit and extraordinary stability, which is the highest up to date comparing with other annealed glasses and even with the ultrastable glasses obtained from vapor deposition [Kearns10][SKMK07] [KSEW07][SLGR11].

(ii) The universal (anomalous) properties at low temperatures have been found to be essentialy independent of both the different amounts of disorder frozen in at the glass transition (entropy) and the energy reduction or stabilization (enthalpy).

[AnHV72] P. W. Anderson, B. I. Halperin and C. M. Varma, “Anomalous low-temperature thermal properties of glasses and spin glasses”, Philosophical Magazine, vol. 25, no. 1, pp. 1–9, 1972.

[Baldi09] G. Baldi, A. Fontana, G. Monaco, L. Orsingher, S. Rols, F. Rossi and B. Ruta, “Connection between Boson Peak and Elastic Properties in Silicate Glasses”**,** Physical Review Letters, vol. 102, 195502, 2009.

[CCFF09] S. Caponi, S. Corezzi, D. Fioretto, A. Fontana, G. Monaco and F. Rossi, “Raman-scattering measurements of the vibrational density of states of a reactive mixture during polymerization: Effect on the boson peak”, Physical Review Letters, vol. 102, no. 2, p. 27402, 2009.

[CoFR02] S. Corezzi, D. Fioretto and P. Rolla, “Bond-controlled configurational entropy reduction in chemical vitrification”, Nature, vol. 420, no. 6916, pp. 653 – 656, 2002.

[GMPV03] T. Grigera, V. Martin-Mayor, G. Parisi and P. Verrocchio, “Phonon interpretation of the ‘boson peak’in supercooled liquids”, Nature, vol. 422, pp. 289 – 292, 2003.

[Hay95] J. N. Hay, “The physical ageing of amorphous and crystalline polymers”, Pure and applied chemistry, vol. 67, no. 11, p. 1855, 1995.

[KSEW07] K. L. Kearns, S. F. Swallen, M. D. Ediger, T. Wu and L. Yu, “Influence of substrate temperature on the stability of glasses prepared by vapor deposition”, The Journal of Chemical Physics, vol. 127, no. 15, p. 154702, 2007.

[KSEW08] K. L. Kearns, S. F. Swallen, M. D. Ediger, T. Wu, Y. Sun and L. Yu, “Hiking down the energy landscape: progress toward the Kauzmann temperature via vapor deposition”, The Journal of Physical Chemistry B, vol. 112, no. 16, pp. 4934 – 4942, 2008.

[Kearns10] K. L. Kearns, K. R. Whitaker, M. D. Ediger, H. Huth and C Schick, “Observation of low heat capacities for vapor-deposited glasses of indomethacin as determined by AC nanocalorimetry”, The Journal of Chemical Physics, vol. 133, 014702 (2010).

[LaGM81] J. P. Larmagnac, J. Grenet and P. Michon, “Glass transition temperature dependence on heating rate and on ageing for amorphous selenium films”, Journal of Non-Crystalline Solids, vol. 45, no. 2, pp. 157–168, 1981.

[LSGT10] E. Leon-Gutierrez, A. Sepulveda, G. Garcia, M. Teresa Clavaguera-Mora and J. Rodriguez-Viejo, “Stability of thin film glasses of toluene and ethylbenzene formed by vapor deposition: an in situ nanocalorimetric study”, Physical Chemistry Chemical Physics PCCP, vol. 12, no. 44, pp. 14693–14698, 2010.

[MNVR10] C. Menor-Salván, M. Najarro, F. Velasco, I. Rosales, F. Tornos and B. R. T. Simoneit, “Terpenoids in extracts of Lower Cretaceous ambers from the Basque-Cantabrian Basin (El Soplao, Cantabria, Spain): Paleochemotaxonomic aspects”, Organic Geochemistry, vol. 41, no. 10, pp. 1089–1103, 2010.

[Monaco06] A. Monaco, A. I. Chumakov, Y-Z Yue, G. Monaco, L. Comez, D. Fioretto, W. A. Crichton and R. Rüffer, “Density of Vibrational States of a Hyperquenched Glass”, Physical Review Letters, vol. 96, 205502, 2006.

[MSFR13] A. Marruzzo, W. Schirmacher, A. Fratalocchi and G. Ruocco, “Heterogeneous shear elasticity of glasses: the origin of the boson peak”, Scientific Reports, vol. 3, p. 1407, 2013.

[NPRP09] M. Najarro, E. Peñalver, I. Rosales, R. Pérez-de la Fuente, V. Daviero-Gomez, B. Gomez and X. Delclòs, “Unusual concentration of Early Albian arthropod-bearing amber in the Basque-Cantabrian Basin (El Soplao , Cantabria , Northern Spain): Palaeoenvironmental and palaeobiological implications”, Geologica Acta, vol. 7, no. 3, pp. 363–387, 2009.

[Phil72] W. A. Phillips, “Tunneling states in amorphous solids”, Journal of Low Temperature Physics, vol. 7, no. 3–4, pp. 351–360, 1972.

[Ramo04] M. A. Ramos, “Are the calorimetric and elastic Debye temperatures of glasses really different?”, Philosophical Magazine, vol. 84, no. 13–16, pp. 1313 – 1321, 2004.

[Ramos97] M. A. Ramos, J. A. Moreno, S. Vieira, C. Prieto and J. F. Fernández, “Correlation of elastic, acoustic and thermodynamic properties of B_2O_3 glasses”, Journal of Non-Crystalline Solids, vol. 221, pp. 170-180 (1997).

[SiEP13] S. Singh, M. D. Ediger and J. J. de Pablo, “Ultrastable glasses from in silico vapour deposition”, Nature Materials, vol. 12, no. 1, pp. 1–6, 2013.

[SKMK07] S. F. Swallen, K. L. Kearns, M. K. Mapes, Y. S. Kim, R. J. McMahon, M. D. Ediger, T. Wu, L. Yu and S. Satija, “Organic glasses with exceptional thermodynamic and kinetic stability”, Science, vol. 315, no. 5810, pp. 353–356, 2007.

[SLGR11] A. Sepúlveda, E. Leon-Gutierrez, M. Gonzalez-Silveira, C. Rodríguez-Tinoco, M. Clavaguera-Mora and J. Rodríguez-Viejo, “Accelerated Aging in Ultrathin Films of a Molecular Glass Former”, Physical Review Letters, vol. 107, no. 2, p. 025901, 2011.

BIBLIOGRAPHY

6

VAPOR-DEPOSITED THIN FILMS OF ULTRASTABLE GLASSES

In recent years a great interest in organic glasses grown using vapor deposition has emerged due to the possibility to access extraordinary kinetic and thermodynamic stability in short time scales. This way to obtain glasses with very peculiar properties such as the above mentioned ultrastability, together with the quasi-two-dimensional character of the samples thus grown, enables us studying the effects that these factors have on the properties properties of glasses [SKMK07][KSEW07][KSEW08]. A big effort has been done to characterize the phenomenology related to these samples in the vicinity of their glass transition, as well as to understand the aspects involved in the efficient attaining of low energy configurations within short times [SLGR11].

Despite the enormous possibilities of these samples, no study has been performed to access the effects that this new phenomenology introduces on the universal low-temperature anomalies of amorphous solids up to date. In this chapter we present for the first time to our knowledge, how the tunneling states and the soft modes, characteristic of the amorphous solids, are modified (if so) in vapor deposited thin films. For this purpose, the low-temperature specific heat of indomethacin has been measured in three different samples, namely, the ordinary or conventional glass, the crystal, and the ultrastable glass. The samples were grown and characterized by Cristian Rodríguez-Tinoco in the group of Prof.

Javier Rodríguez Viejo, in the Laboratory of Nanomaterials and Microsystems at Universitat Autònoma de Barcelona. Characterization of the samples has been done using Differential Scanning Calorimetry (DSC) around the glass transition and melting temperatures in order to check the phase and stabilities of the vapor deposited samples.

In Chapters 4 and 5 we have presented an exhaustive study on the effects of an extreme ageing process of tens or even hundred million years (*hyperageing*) in two amber glasses far below their glass transition. There we have shown that low-energy configurations are accessed in the potential energy landscape, as indicated by the huge enthalpy release observed in the specific heat around T_g, due to the sub-T_g relaxation over periods of time of the order of $10^6 – 10^8$ years. Natural amber resins from the Dominican Republic (~ 20 million years) and Spain (~110 million years) were used in the study. Gradual removal of the kinetic and thermodynamic stabilities were obtained applying thermal treatments to the pristine samples, finally driving the glasses to the conventional state, also called rejuvenated because of the procedure used. By doing this we were able to trace the evolution of the low-temperature anomalies of glasses with increasing/decreasing stability, manifesting great independence of the tunneling and soft modes with the thermodynamic and kinetic stability. Evaluation of the extra modes contribution to the low-temperature specific heat was directly accessed thanks to the independent quantification of the Debye level using High Resolution Brillouin Scattering.

Here we will have the opportunity to trace the evolution of the universal low-temperature anomalies with stability in completely different samples. Both the hyperaged amber samples and the ultrastable vapor-deposited thin films possess extraordinary thermodynamic and kinetic stability, but differences among them are numerous. This will provide us with insight into the key aspects which imply the existence of the so extensively studied glassy anomalies.

6.1 Introduction

The interest in amorphous solids and glasses goes beyond the mere wisdom to answer fundamental questions which remain unsolved. Understanding the properties of disordered matter has an even more beneficial outcome in our daily life, since a great number of the materials used in food, technology, pharmaceuticals… are amorphous. The ability to control their properties at will undoubtedly opens to us the possibility to optimize their performance.

The non-stable character of amorphous solids implies, as already introduced in Chapters 1 and 2, the remediless process of ageing. And ageing means that the original material once obtained to respond to a need will not behave very long time as it was intended to be. Thin-film amorphous solids with enhanced stability accelerates ageing as shown in [SLGR11] and references therein, what makes these products robust against future ageing processes, hence ensuring their correct long-term operation.

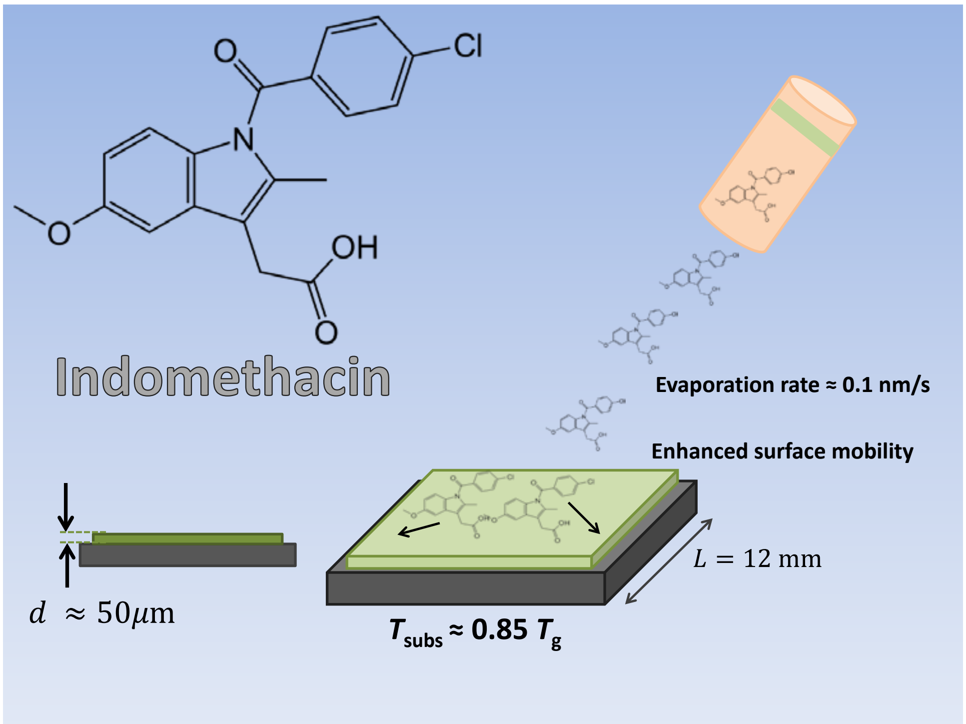

Figure 6.1 Description of the vapor deposition of the indomethacin molecule to produce ultrastable thin films. On the left upper corner the chemical composition of the molecule is presented. Typical thicknesses of the films used for the low-temperature specific-heat measurements are 50 µm.

Indomethacin is a clear example of an amorphous solid employed in our daily life. It is an organic molecule with anti-inflammatory properties commonly used as a drug to reduce fever, pain, swelling and stiffness.

A few years ago it was observed that some organic molecules, as indomethacin or toluene, vapor-deposited at rates of few nanometers per second (as illustrated in Figure 6.1) onto substrates at temperatures 15 – 20 % below their glass transition, produced a strong enhancement of the thermodynamic and kinetic stability of the glass so grown [SKMK07][KSEW07]. The drastic increase of mobility in the surface of these glasses has been proven to be responsible of the effective decrease in the energy landscape [KSEW08] and accelerated ageing [PEBT05][Prie09][PRBR10][SLGR11]. Such stability could only be accessed via ageing processes on the bulk glass given time scales ranging from thousands to tens of millions years [KSEW08]. This extrapolation directly matches with the observations found in bulk amber glasses shown in Chapters 4 and 5, which present enthalpy releases of the order of 8 – 10 J/g.

6.2 Sample growing and characterization

The conventional (bulk) glass of indomethacin is easily grown by cooling the liquid at a rate of 10 K/min. Its glass transition is located at 315 K, measured by DSC at the standard heating rate of 10 K/min, as shown in Figure 6.2, using a Perkin Elmer DSC7. The glass transition temperature is determined here using the onset temperature, as done in previous works in these samples [SKMK07][KSEW07], which is given in the heat flow curve by the intersection between the extrapolations of the glass and the jump due to the transition, as indicated in the inset of Figure 6.2. The crystal is grown by heating the liquid to 390 K and keeping it isothermally for one hour at that temperature. It is quite easy to differentiate between the glass and crystal phases of indomethacin by eye, since the crystal presents an opaque white color, whereas the glass has a transparent yellowish-green appearance. The melting temperature of the crystal, measured at 10 K/min using DSC as well, is T_m = 430 K, as illustrated in Figure 6.2. The measurement procedure in Figure 6.2 was as follows: the crystal was grown from the liquid, and cooled to 280 K. After this, the DSC curve of the crystalline phase was measured at 10 K/min up to 455 K. The liquid was again cooled at rate 10 K/min to 280 K and the conventional glass was obtained. The DSC curve for the conventional glass was measured from 280 K up to 455 K, in order to compare the reproducibility in the liquid state with the curve corresponding to the crystal. The growth of the conventional glass and the crystal is done under controlled atmosphere (N_2 or vacuum conditions) in order to avoid possible contamination (like water impurities).

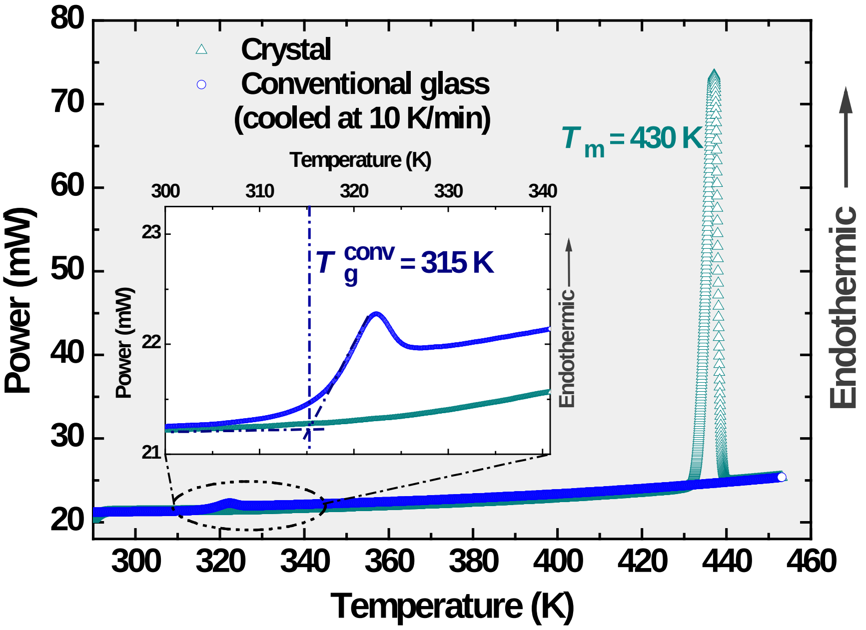

Figure 6.2 Differential Scanning Calorimetry of the crystal and ordinary (conventional) glassy phase of indomethacin. The melting of the crystal is located at T_m = 430 K. After melting the crystal, the liquid was cooled at rate 10 K/min to obtain the conventional glass, with glass transition at T_g = 315 K. The inset shows a zoom on the glass transition of the conventional glass, determined by the onset in the heat flow curve, in the temperature range 300 K – 340 K.

The fabrication of the ultrastable glass of indomethacin was done under ultrahigh-vacuum (UHV) conditions P < 10^{-8} mbar, by vapor-depositing the organic molecule onto a silicon substrate kept isothermally at temperature T_{subs} = 0.85 T_g = 266 K (for further details see Ref. [LGLF08]). The deposition rate for the samples presented here was kept constant at ~0.1 nm/s, which was observed to produce samples with optimal stability.

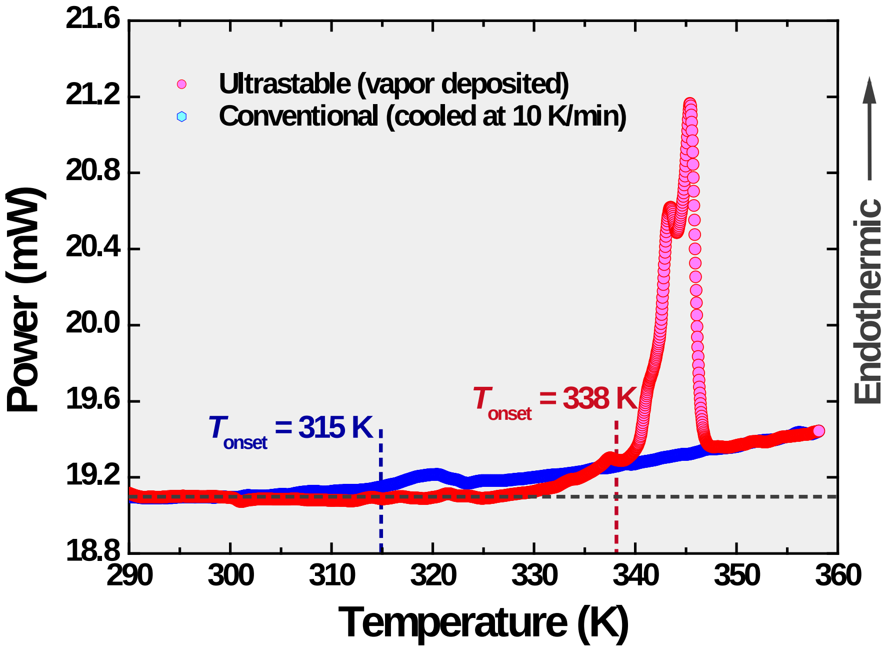

Figure 6.3 Differential Scanning Calorimetry of conventional and ultrastable glasses of Indomethacin. Dependence of the heat flow with temperature in which endothermic signals correspond to growing power values. The glass transition temperatures of the conventional and ultrastable glasses are determined by the onset in the heat flow curve, T_g^{conv} = 315 K and T_{onset}^{ultr} = 338 K.

The ultrastable samples used for the low-temperature specific heat measurements had thicknesses of several tens of micrometers, typically 50 – 60 μm. These thicknesses are large in order to increase the mass of the sample, necessary to have enough heat capacity contribution at very low temperatures. Typical thicknesses employed in the study of vapor deposited thin films of organic molecules vary from from micrometers down to a few nanometers, for which nanocalorimetry is required [Leon09][Leon10][Kearns10] [Tress10]. In the measurement procedure followed in Figure 6.3, first an ultrastable sample 50 μm thick was vapor-deposited onto a silicon substrate in UHV conditions. After stabilizing the ultrastable sample at room temperature, it was removed from the UHV chamber and taken to the DSC set up. The sample was measured from 290 K up to 358 K at a rate of 10 K/min. A huge endothermic peak at the glass transition T_g^{ultr} = 338 K is found as a result of the extraordinary stability achieved in the vapor-deposition process. Once the sample was driven to the liquid state, it was cooled at 10 K/min in order to obtain the conventional glass. The DSC curve of the ordinary glass was determined up to 358 K in order to check reproducibility in the liquid comparing to the curve of the ultrastable sample. The glass transition of the conventional glass was found at T_g^{conv} = 315 K as previously seen in Figure 6.2.

Due to the low glass-transition temperature of the indomethacin, especially in the case of the conventional glass, the sample can crystallize if the sample is heated above room temperature. Moreover, the absorption of water in the indomethacin glass has negative repercussions for our interests: (i) in the case of the conventional glass, the presence of water accelerates the crystallization of the sample; (ii) in the ultrastable sample, water produces, in a first step, a loss of stability, pushing the glass transition temperature towards lower temperatures and decreasing the endothermic signal observed around T_g (see Figure 6.3), what can after derive in the crystallization of the sample. In order to prevent both crystallization and loss of stability in the indomethacin glasses, samples are stored in vacuum conditions or controlled N_2 atmosphere.

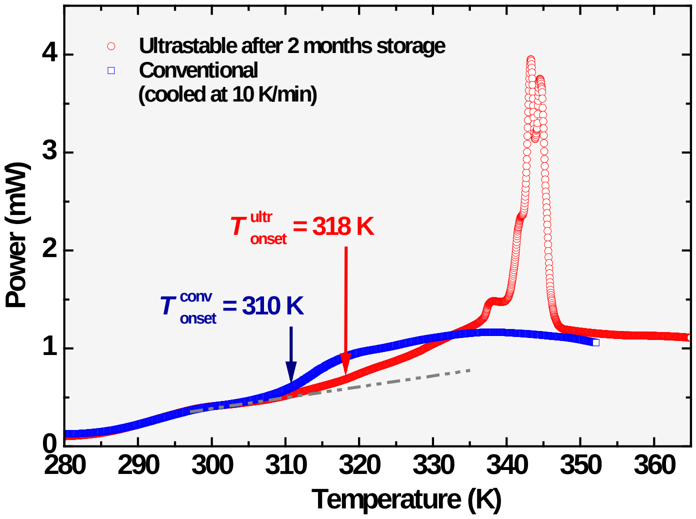

Figure 6.4 Differential Scanning Calorimetry of the ultrastable sample shown in Figure 6.3 with water absorbed, after storing it under poor vacuum conditions at 278 K for two months, and the conventional glass obtained after cooling the liquid at 10 K/min. The effects of the water contamination are observed in the considerable decrease of the onset temperature both in the ultrastable and the conventional glasses T'_{ultr} = 318 K, T'_{conv} = 310 K, as well as in a broadening and a reduction of the endothermic signal in the ultrastable sample.

In the case of the ultrastable indomethacin, the samples were stored under poor vacuum conditions and temperature $T \approx 278$ K. The prolonged storage (above one month) of the ultrastable samples in the above mentioned conditions produced a reduction of the stability, as can be seen in Figure 6.4 compared to the conventional and the ultrastable glasses in Figure 6.3. A reduction in the onset temperature in the ultrastable sample $\Delta T_{\mathrm{onset}}^{\mathrm{ultr}} \approx 20$ K is found, and in the conventional glass $\Delta T_{\mathrm{onset}}^{\mathrm{conv}} \approx 5$ K.

6.3 Low-temperature specific heat of ultrastable glasses

The indomethacin samples used in the low-temperature specific-heat study were all grown on silicon substrate of dimensions 12 x 12 mm^2 and mass $m \approx 125$ mg, what enables the handling of the samples as well as optimal attachment and thermal contact to the calorimetric cell used in the ^{4}He and the ^{3}He - ^{4}He dilution refrigerator cryostats (described in Section 3.5.1). Due to the versatility of the low-temperature calorimeter employed, the same experimental setup was used in both cryostats. This allowed us to measure in a fast and easy way the specific-heat curves of the conventional and the ultrastable glasses, as well as the crystalline phase, in the temperature range $0.18\ \mathrm{K} \leq T \leq 32$ K. The calorimeter was calibrated using a clean silicon substrate, in order to accurately determine the empty-cell contribution to the total heat capacity curves for the indomethacin experiments, as shown in Figure 6.5.

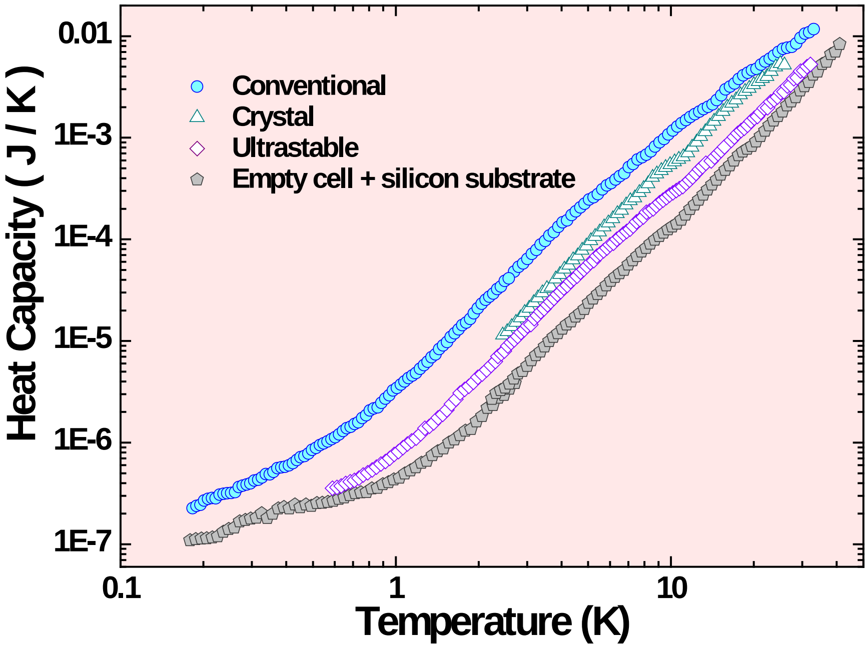

Figure 6.5 Heat capacity contributions of the different indomethacin samples compared to the addenda (empty cell + silicon substrate). The masses of the samples are: m_{conv} = 45 mg, m_{ultr} = 7.6 mg, m_{cryst} = 39 mg. The silicon substrate mass is m_{subs} = 125 mg.

The specific heat of two ultrastable samples was measured at low temperature. A third sample of the same batch as the one showed in Figure 6.5 was measured at low temperature after storing it two months under poor vacuum conditions and temperature T = 278 K, which presented water absorption and a loss of stability (see Figure 6.4). In Figure 6.5 only one of the ultrastable samples is shown for clarity, to illustrate the sample contribution to the total heat capacity. The masses of the indomethacin samples measured range from $m_{\mathrm{ultr}} \approx 8$ - 11 mg typically for the ultrastable samples, up to m_{conv} = 45 mg in the case of the conventional sample. The mass of the crystal was m_{cryst} = 39 mg. Contributions of the sample to the total heat capacity (sample + addenda) vary from 30% up to 90%, depending on the temperature range and the amount of indomethacin employed.

The heat capacity contribution of the empty cell was determined using a clean silicon substrate of mass m_{subs} = 125 mg attached to the calorimeter, in order to directly measure accurately the addenda contribution. The differences between the masses of the silicon substrates used for all the samples and the reference was $\Delta m_{subs} < 5$ mg. Corrections to the heat capacity were done using the polynomial for silicon $C_P(T) = 2.58 \cdot 10^{-7}$ J/g·K$^4 \cdot T^3$, which were found to be negligible. Variations in the apiezon grease used in the sample measurements and the empty cell calibration $\Delta m_{ap} < 0.2$ mg were corrected using the apiezon polynomial given in [Swen99][Wun75], introducing heat-capacity deviations $\Delta C < 2\%$.

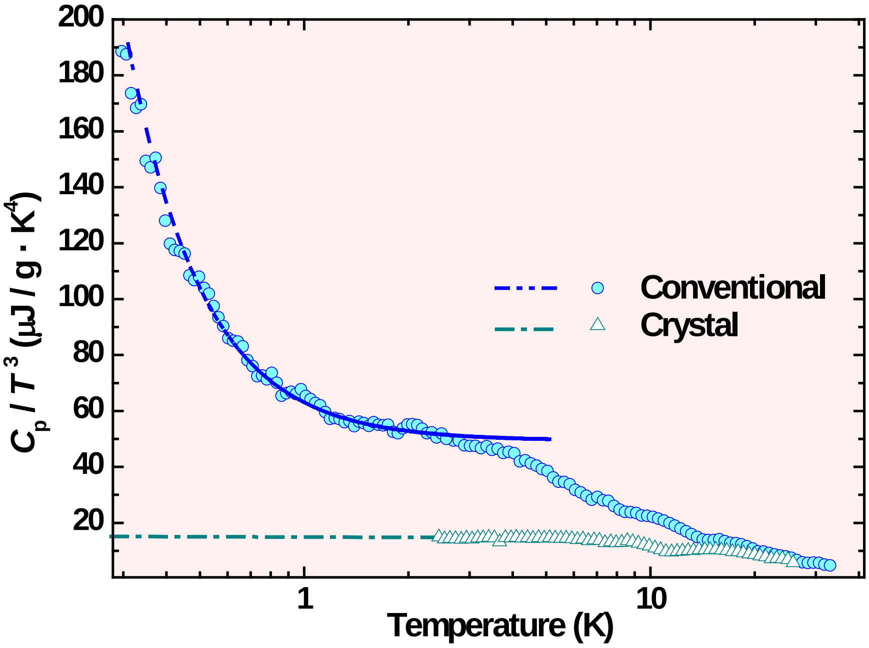

Figure 6.6 C_P/T^3 versus T representation for the crystal and conventional glass of indomethacin. The Debye level from the crystal $C_{Debye} = 15.0 \pm 0.3$ μJ / g·K^4 is shown as a dashed green line. A $C = c_{TLS} \cdot T + c_D \cdot T^3$ fit is shown in dashed blue line for the conventional glass, calculated for data in the temperature range $0.18 \text{ K} \leq T \leq 1.95$ K: $c_{TLS} = 13.6 \pm 0.2$ μJ/g·K^2, $c_D = 49.4 \pm 0.2$ μJ / g·K^4.

Comparison of the specific heat between the conventional glass and the crystal in the reduced C_P/T^3 representation in Figure 6.6 shows an enhancement of the Debye-like contribution in the glass, being the linear dependence of C_P

below 1 K (corresponding to the two-level systems contribution) clearly observed. However, no signature of the boson peak appears above 1 K, but only a *shoulder*. This peculiar absence of the boson peak in the low-temperature specific heat of a glass has been previously reported for other fragile glasses like *o*-terphenyl [ChBe72], and related to the analog behavior observed by inelastic neutron scattering [KBDF92]. This fact is coherent with the large increase of the Debye level in the conventional glass of indomethacin, what involves a softening of the lattice in the glassy phase, and therefore, a high fragility. A possible explanation of this has been given by Sokolov *et al.* [SRKQ93] in terms of the fragility *m* of the glass, which would be associated with a lower vibrational contribution compared to the relaxational one the higher *m*. The fragile character of the indomethacin glass is given by the absence of strong directional bonds between molecules in its network, also ocurring in *o*-terphenyl.

A fit of the form $C = c_{\mathrm{TLS}} \cdot T + c_{\mathrm{D}} \cdot T^3$ for the specific heat of the conventional glass of indomethacin was calculated in the temperature range $0.18\ \mathrm{K} \leq T \leq 1.95\ \mathrm{K}$, shown in Figure 6.6 (in dashed blue line). This allowed us to quantify both the linear term of the specific heat below 1 K $c_{\mathrm{TLS}} = 13.6 \pm 0.2\ \mu\mathrm{J/g{\cdot}K^2}$ (due to tunneling states) and the acoustic contribution $c_{\mathrm{D}} = 49.4 \pm 0.2\ \mu\mathrm{J / g{\cdot}K^4}$. The Debye contribution calculated from our calorimetric measurements agrees with that obtained from the sound velocity and mass density for the conventional glass [Kearns10B] at room temperature $v_{\mathrm{L}}^{\mathrm{conv}} = 2400$ m/s, $v_{\mathrm{T}}^{\mathrm{conv}} = 1080$ m/s and $\rho_{\mathrm{conv}} = 1.31\ \mathrm{g/cm^3}$, thus $c_{\mathrm{D}}^{\mathrm{elas}} \approx 51\ \mu\mathrm{J / g{\cdot}K^4}$ (no correction factor to extrapolate to zero Kelvin was attempted). Attempts to fit the specific heat in that temperature range to the basic Soft Potential Model prediction (with an additional $C \sim T^5$ term) result in negative contributions of the soft-modes term, hence meaningless. The reduced C_{P}/T^3 representation of the crystal is nearly constant below 9 K with a value $C_{\mathrm{Debye}} = 15.0 \pm 0.3\ \mu\mathrm{J/g \cdot K^4}$.

The specific heat of two ultrastable indomethacin samples was measured in the temperature range $0.6\ \mathrm{K} \leq T \leq 32\ \mathrm{K}$, as shown in Figure 6.5. A third ultrastable sample was measured in the temperature range $2.4 \leq T \leq 37$ K, showing good reproducibility with the other two ultrastable samples in Figure 6.7. Putting together the specific heat of the ultrastable indomethacin in the reduced C_{P}/T^3 representation and that of the conventional and crystalline samples, a slight decrease of the Debye level in the ultrastable samples is observed compared to the conventional glass. The same shoulder-like behavior as in the ordinary glass appears below ~ 5 K. Nevertheless, the most surprising behavior in the ultrastable sample is the dissapearance of the linear term of the specific heat ascribed to the tunneling states, clearly seen as a flattening of the C_P/T^3 curve below 2 K compared to the conventional glass in Figure 6.7.

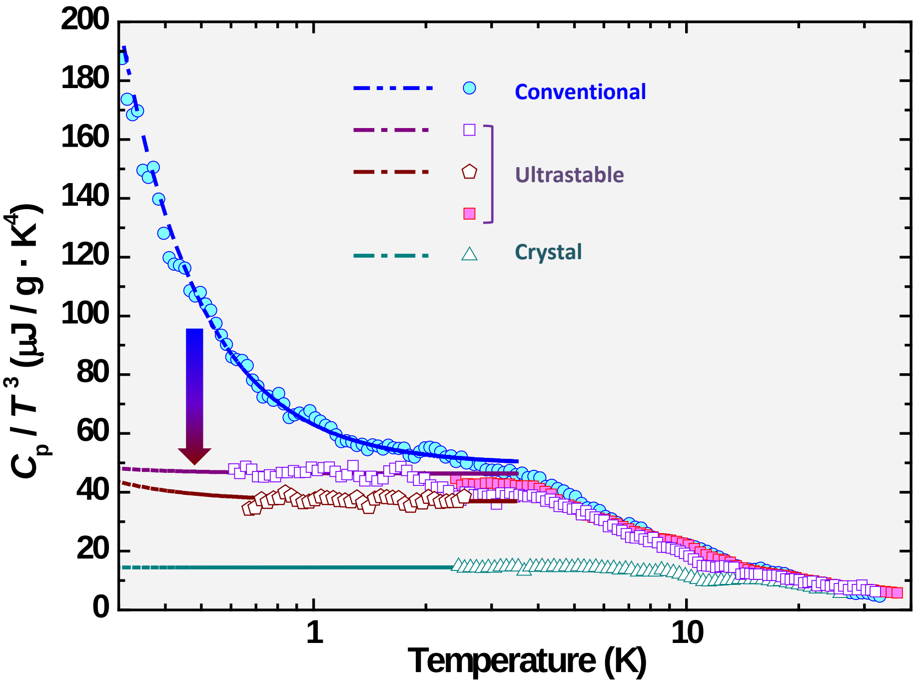

Figure 6.7 C_P/T^3 versus T representation for the ultrastable indomethacin 50 µm- and 80µm-thin films (~8 mg and ~ 11.5 mg respectively), compared to the crystalline phase and the conventional glass. The arrow indicates the disappearance of the linear term in the specific heat comparing the ultrastable thin film to the ordinary indomethacin glass. Deviation between the linear terms of the two glasses is illustrated by the large difference in the $C = c_{TLS} \cdot T + c_D \cdot T^3$ fits below 1 K.

A fit of the specific heat data for the ultrastable indomethacin in the temperature range $0.6 \text{ K} \leq T \leq 1.95 \text{ K}$ of the form $C = c_{TLS} \cdot T + c_D \cdot T^3$ is shown in dashed purple and dashed maroon lines in Figure 6.7, revealing the considerable deviation with the behavior of the conventional glass (solid blue circles).

The linear fit done in the C_P/T versus T^2 representation of Figure 6.8 clearly shows the suppressed contribution of the tunneling states in the ultrastable samples, evidenced by the zero crossing of its extrapolated specific heat c_{TLS}^{ultr} = 0.2 ± 0.9 μJ/g·K^2 and c_{TLS}^{ultr} = 0.6 ± 0.7 μJ/g·K^2. The uncertainty in the contribution introduced by the tunneling states is due to the smaller temperature range available for the fit in the case of the ultrastable indomethacin samples of mass m_{ultr1} = 7.8 mg and m_{ultr2} = 11.5 mg, respectively.

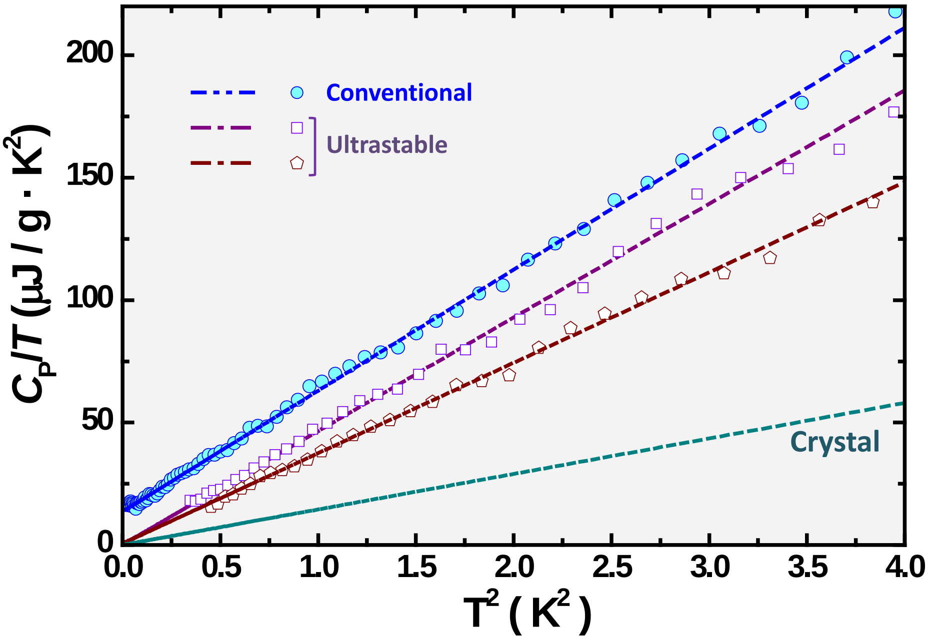

Figure 6.8 Specific-heat comparison between the ultrastable (open purple square and open brown pentagon) and conventional (solid circle) indomethacin glasses in the C_P/T versus T^2 representation at very low temperatures. The fits of the form $C = c_{TLS} \cdot T + c_D \cdot T^3$ done in this representation correspond to the dashed violet and dashed brown (blue) lines for the ultrastable (conventional) indomethacin samples. The values of the tunneling states and acoustic contributions for both samples are: C_P^{conv} = (13.6 ± 0.2) μJ/g·K^2· T + (49.4 ± 0.2) μJ/g·K^4 · T^3, (open purple circles) C_P^{ultr1} = (0.2 ± 0.9) μJ/g·K^2· T + (46.4 ± 0.6) μJ/g·K^4 · T^3 and (open brown pentagons) C_P^{ultr2} = (0.02 ± 0.8) μJ/g·K^2· T + (36.9 ± 0.4) μJ/g·K^4 · T^3. The crystal is shown in dashed green-bluish line as reference.

This suppression of the tunneling states we have observed in the indomethacin glass when growing the ultrastable sample, has been previously reported for two exceptional cases, namely, in hydrogenated amorphous silicon measured by internal friction experiments by Liu *et al.* [LWPI97] and in SiO_2 thin films by Gaganidze *et al.* [GKEZ97]. Unsuccessful attempts have been also done to observe the possible suppression of the two-level systems in amorphous solids reducing the thickness of amorphous SiO_2 films [WhPo96]: the minimum size of 2.2 nm reached for this films was argued to be considerably larger than the size of the tunneling entities involved [RaBu97]. The values of the Debye contribution calculated for the two ultrastable samples measured at very low temperature $c_D^{ultr1} = 46.4 \pm 0.6$ μJ/g·K^4 and $c_D^{ultr2} = 36.9 \pm 0.4$ μJ/g·K^4 again agree well with the values obtained from elastic measurements at room temperature [Kearns10B], in which $v_L^{ultr} = 2550$ m/s, $v_T^{ultr} = 1150$ m/s and $\rho_{ultr} = 1.336$ g/cm^3, thus $c_D^{elas} \approx 41$ μJ / g·K^4.

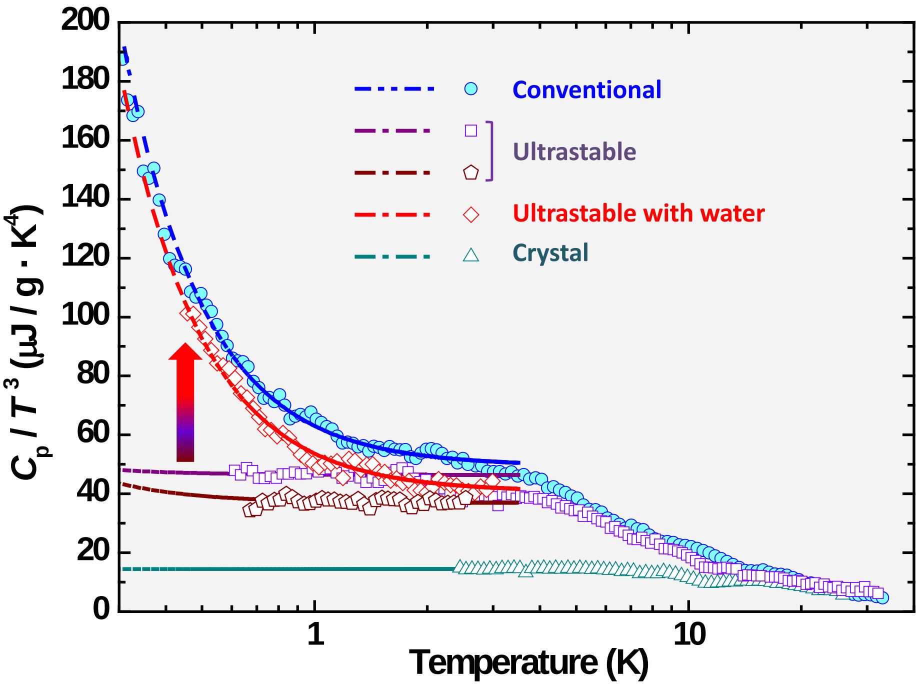

Figure 6.9 Specific heat in the reduced C_P/T^3 representation of the indomethacin samples in the conventional and ultrastable glassy states and the crystal phase. An ultrastable sample with water absorbed in it (red open diamonds) is presented, for which the tunneling states contribution (linear term of C_P) has increased to the values of the conventional glass, as indicated by the red arrow.

The effects of water absorption in the low-temperature glassy properties of ultrastable indomethacin were also studied. An ultrastable sample of the same batch as the one shown in Figure 6.7 (open purple squares) and Figure 6.8 was stored under poor vacuum conditions at a temperature of 278 K during two months. After this time, the low-temperature specific heat was measured in the temperature range 0.45 K ≤ T ≤ 3 K, as shown in Figure 6.9. The reduced stability in the ultrastable sample implies an increase in the two-level systems contribution to the specific heat to the values of the conventional glass, as indicated by the red arrow in Figure 6.9.

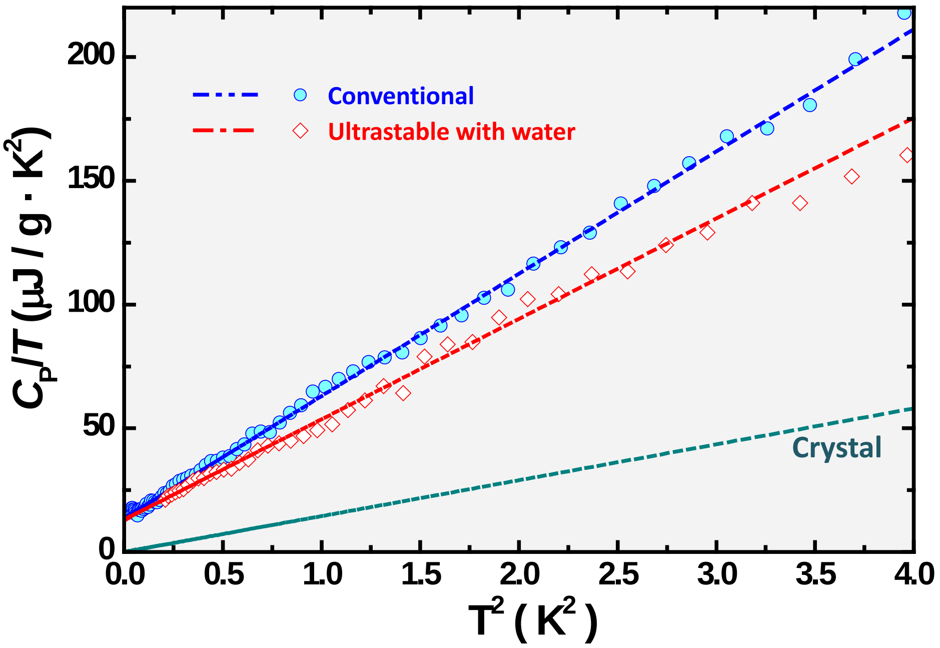

Figure 6.10 C_P/T versus T^2 of the conventional and the ultrastable (with absorbed water) indomethacin samples, together with their corresponding linear fits: $C_P^{\text{ultr'}} = (13.0 \pm 0.7)\ \mu\text{J/g}\cdot\text{K}^2 \cdot T + (40.6 \pm 0.5)\ \mu\text{J/g}\cdot\text{K}^4 \cdot T^3$. The crystal is shown in dashed green-bluish line as reference.

Quantification of the two-level systems contribution to the specific heat is done again by calculating the linear fit of C_P / T versus T^2 in the temperature range 0.45 K ≤ T ≤ 1.95 K, as illustrated in Figure 6.10. It is observed that the independent term of the linear fit corresponding to the ultrastable sample with water absorbed is the same as for the conventional glass within our experimental error $c_{TLS}^{\text{ultr'}} = 13.0 \pm 0.7$ μJ/ g · K^2, with $c_{TLS}^{\text{conv}} = 13.7 \pm 0.3$ μJ/ g · K^2. The cubic term of the specific heat in the water-contaminated ultrastable sample shows a lower value than in the conventional and the ultrastable glasses $c_D^{\text{ultr'}} = 40.6 \pm 0.5\ \mu\text{J/ g} \cdot \text{K}^2$.

Comparing the evolution of the low-temperature anomalies with increasing thermodynamic and kinetic stability observed in two different samples as amber and indomethacin, the discrepancy is obvious. As seen in Chapters 4 and 5 for Dominican and Spanish ambers, respectively, no change in the density of tunneling states is observed between the pristine (hyperaged and extraordinarily stable) and the rejuvenated (conventional) amber glasses, calculated from the specific-heat measurements. Nevertheless, we saw that the enthalpy curves of the Spanish amber samples evidenced a strong increase of the stability with hypergeing, comparable to that observed in indomethacin samples [SKMK07][KSEW08].

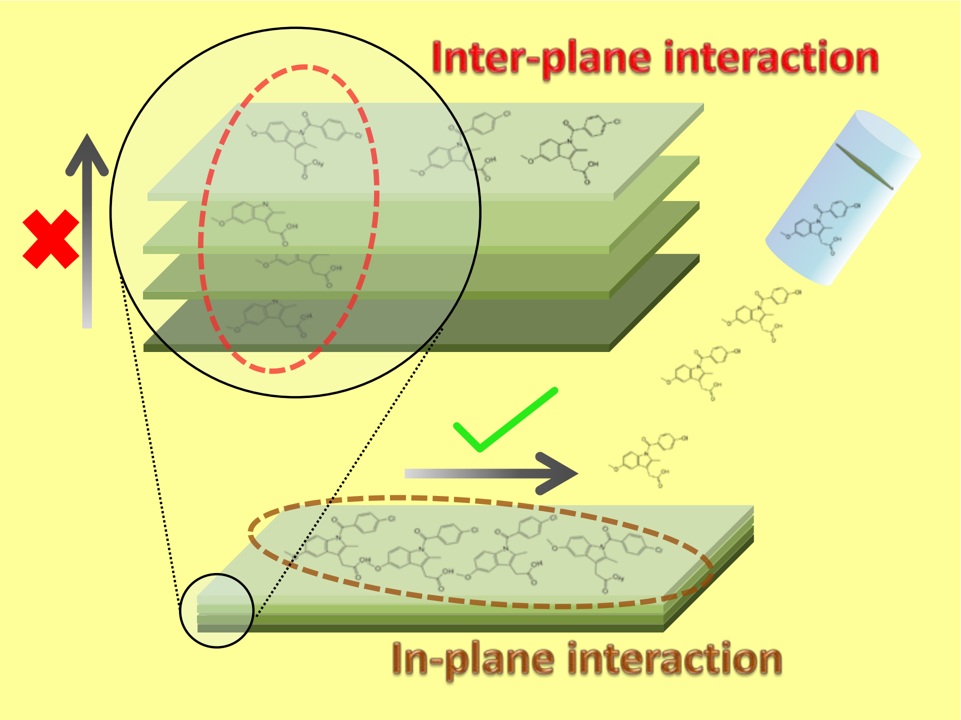

Figure 6.11 Loss of interaction between indomethacin molecules in the perpendicular direction (the growth direction) in the ultrastable samples grown by vapor deposition. This mechanism could explain the reduction in the density of tunneling states, since the basic units which give rise to these excitations would be frustrated by the growth procedure.

Such a discrepancy between two glasses which have in common an extraordinary stability, though achieved in two different ways, tells us that ultrastability cannot be the responsible of the strong reduction/disappearance of the tunneling states. From our point of view, the possible explanation for this effect is given in terms of the key difference between hyperaged amber and ultrastable indomethacin: *dimensionality*. A similar effect was observed by Liu *et at.* [LWPI97] in amorphous silicon films by changing their chemical composition: introducing hydrogen in small concentration. In our ultrastable indomethacin samples there is no chemical composition variation, but it is the loss of interaction between molecules what could induce the disappearance of the low-energy excitations. The samples studied here were grown at rates of 0.1 nm/s onto a substrate at T = 0.85 T_g = 266 K. The enhanced mobility of the surface molecules [KSEW08] allow them to achieve very stable configurations in small periods of time [SLGR11] compared to the bulk glasses. It is possible that this enhanced mobility and rapidly acquired stability could also remove the interaction among the surface molecules, thus producing the complete disappearance of the tunneling states observed in the conventional bulk glass of indomethacin.

6.4 Conclusions

We have presented in this chapter the first study on the low-temperature anomalies of indomethacin glasses, both in the conventional and the ultrastable state. We observed that the linear dependence of the specific heat at very low temperature (as predicted by the Tunneling Model) vanishes in the ultrastable sample, indicating the disappearance of the tunneling states with enhanced stability. Nevertheless, comparison with the amber glass studied in this thesis, which also presents extraordinary kinetic and thermodynamic stabilities, shows different phenomenology. The low-energy glassy excitations in hyperaged amber remain (almost) the same as in the conventional glass, obtained after removing the ageing signal of the pristine sample (rejuvenation). This essential difference in the behavior of the two glasses suggests that the disappearance of the tunneling states could not be explained by the enhanced stability. It could be, though, the vapor deposition procedure which originates the ultrastability, the responsible for removing the tunneling states in the glassy indomethacin. The enhanced mobility of the surface molecules that allow them to rapidly acquire stable configurations would reduce the interaction or coupling necessary for the presence of the extra excitations in glasses. The two-level systems and the soft modes in glasses are thought to comprise of the order of 20 to 100 atomic units [BPND86], what means length scales ranging from few angstroms to few nanometers. This is coherent with the presence of these glassy anomalies in hyperaged glasses, like amber, given its bulk behavior.

The suppression of the tunneling states in the ultrastable indomethacin thin films would be then produced, from our point of view, by the *effective* reduced dimensionality of the samples grown by vapor deposition. The term *effective* is used in order to define the loss of interaction among the indomethacin molecules which rapidly achieve high stabilities in the vapor-deposited thin films. This would confer the final (bulk) sample a two-dimensional-like behavior in terms of the frustrated interaction necessary for the tunneling states in glasses. This fact suggests that the vapor-deposited ultrastable glasses may lead to the formation of new 2D low-energy structures, not representative of the isotropic bulk liquid state, answering to the question stated by Singh *et al.* in [SiEP13] regarding the dimensionality and anisotropy of the glasses so grown.

This observation opens the possibility to understand, from a microscopic point of view, the nature of the interactions which give rise to the excess density of states in amorphous solids at low-temperatures/energies. A combined study of the sample stability, the possible anisotropy derived from the vapor deposition and the low-temperature anomalies would be able to clarify many unsolved questions in glasses. Although in the case of indomethacin no maximum in the reduced C_P/T^3 representation is observed, by extending this study to other systems that may present a well-defined boson peak, a definite understanding of the excess vibrational states in glasses could be addressed, as well as their possible connection with the lower-energy tunneling states.

[BPND86] U. Buchenau, M. Prager, N. Nücker, A. J. Dianoux, N. Ahmad and W. Phillips, “Low-frequency modes in vitreous silica”, *Physical Review B*, vol. 34, no. 8, pp. 5665–5673, 1986.

[ChBe72] S. S. Chang and A. B. Bestul, “Heat Capacity and Thermodynamic Properties of o-Terphenyl Crystal, Glass, and Liquid”, *The Journal of Chemical Physics*, vol. 56, no. 1, pp. 503 – 516, 1972.

[GKEZ97] E. Gaganidze, R. König, P. Esquinazi, K. Zimmer and A. Burin, “Low Temperature Sound Velocity of Thin SiO2 Films”, *Physical Review Letters*, vol. 79, p. 5038, 1997.

[KBDF92] M. Kiebel, E. Bartsch, O. Debus, F. Fujara, W. Petry and H. Sillescu, “Secondary relaxation in the glass-transition regime of ortho-terphenyl observed by incoherent neutron scattering”, *Physical Review B*, vol. 45, no. 18, pp. 1–5, 1992.

[Kearns10] K. L. Kearns, K. R. Whitaker, M. D. Ediger, H. Huth and C Schick, “Observation of low heat capacities for vapor-deposited glasses of indomethacin as determined by AC nanocalorimetry”, The Journal of Chemical Physics, vol. 133, 014702, 2010.

[Kearns10B] K. L. Kearns, T. Still, G. Fytas and M. D. Ediger, "High-Modulus Organic Glasses Prepared by Physical Vapor Deposition", Advanced Materials, vol. 22, pp. 39 - 42, 2010.

[KSEW07] K. L. Kearns, S. F. Swallen, M. D. Ediger, T. Wu and L. Yu, “Influence of substrate temperature on the stability of glasses prepared by vapor deposition”, *The Journal of Chemical Physics*, vol. 127, no. 15, p. 154702, 2007.

[KSEW08] K. L. Kearns, S. F. Swallen, M. D. Ediger, T. Wu, Y. Sun and L. Yu, “Hiking down the energy landscape: progress toward the Kauzmann temperature via vapor deposition”, *The Journal of Physical Chemistry B*, vol. 112, no. 16, pp. 4934 – 4942, Apr. 2008.

[Leon09] E. León-Gutiérrez, G. García, M. T. Clavaguera-Mora and J. Rodríguez-Viejo, "Glass transition in vapor deposited thin films of toluene", Thermochimica Acta, vol. 492, no. 1-2, 2009.

[Leon10] E. León-Gutiérrez, G. García, A. F. Lopeandía, M. T. Clavaguera-Mora and J. Rodríguez-Viejo, "Size Effects and Extraordinary Stability of Ultrathin Vapor Deposited Glassy Films of Toluene", The Journal of Physical Chemistry Letters, vol. 1, no. 1, 2010.

[LGLF08] E. León-Gutierrez, G. Garcia, A. F. Lopeandía, J. Fraxedas, M. T. Clavaguera-Mora and J. Rodríguez-Viejo, “In situ nanocalorimetry of thin glassy organic films”, *The Journal of chemical physics*, vol. 129, no. 18, p. 181101, 2008.

[LWPI97] X. Liu, J. . B. White, R. Pohl, E. Iwanizcko, K. Jones, A. Mahan, B. Nelson, R. Crandall and S. Veprek, “Amorphous Solid without Low Energy Excitations”, *Physical Review Letters*, vol. 78, no. 23, pp. 4418–4421, 1997.

[PEBT05] R. D. Priestley, C. J. Ellison, L. J. Broadbelt and J. M. Torkelson, “Structural relaxation of polymer glasses at surfaces, interfaces, and in between”, *Science*, vol. 309, no. 5733, pp. 456–9, 2005.

[PRBR10] J. E. Pye, K. a. Rohald, E. a. Baker and C. B. Roth, “Physical Aging in Ultrathin Polystyrene Films: Evidence of a Gradient in Dynamics at the Free Surface and Its Connection to the Glass Transition Temperature Reductions”, *Macromolecules*, vol. 43, no. 19, pp. 8296–8303, 2010.

[Prie09] R. D. Priestley, “Physical aging of confined glasses”, *Soft Matter*, vol. 5, no. 5, pp. 919–926, 2009.

[RaBu97] M. A. Ramos and U. Buchenau, “Low-temperature thermal conductivity of glasses within the soft-potential model”, *Physical Review B*, vol. 55, no. 9, pp. 5749 – 5754, 1997.

[SiEP13] S. Singh, M. D. Ediger and J. J. de Pablo, “Ultrastable glasses from in silico vapour deposition”, *Nature Materials*, vol. 12, no. 1, pp. 1–6, 2013.

[SKMK07] S. F. Swallen, K. L. Kearns, M. K. Mapes, Y. S. Kim, R. J. McMahon, M. D. Ediger, T. Wu, L. Yu and S. Satija, “Organic glasses with exceptional thermodynamic and kinetic stability”, *Science*, vol. 315, no. 5810, pp. 353–6, 2007.

[SLGR11] A. Sepúlveda, E. Leon-Gutierrez, M. Gonzalez-Silveira, C. Rodríguez-Tinoco, M. Clavaguera-Mora and J. Rodríguez-Viejo, “Accelerated Aging in Ultrathin Films of a Molecular Glass Former”, *Physical Review Letters*, vol. 107, no. 2, p. 025901, 2011.

[SRKQ93] A. Sokolov, E. Rössler, A. Kisliuk and D. Quitmann, “Dynamics of strong and fragile glass formers: Differences and correlation with low-temperature properties”, *Physical Review Letters*, vol. 71, no. 13, pp. 1–4, 1993.

[Swen99] C. A. Swenson, “Specific heat (C_p) of Apiezon N grease (1 to 108 K) and calorimetry: C_p of copper below 30 K”, *Review of Scientific Instruments*, vol. 70, no. 6. pp. 2728–2731, 1999.

[Tress10] M. Tress, M. Erber, E. U. Mapesa, H. Huth, J. Müller, A. Serghei, C. Schick, K. J. Eichborn, B. Voit and F. Kremer, "Glassy Dynamics and Glass Transition in Nanometric Thin Layers of Polystyrene", Macromolecules, vol. 43, pp. 9937-9944, 2010

[WhPo96] B. E. White Jr. and R. O. Pohl, “How do two-level-systems come about?”, *Physica B: Condensed Matter*, vol. 219–220, no. 0, pp. 267–269, 1996.

[Wun75] M. Wun, “Low temperature specific heat of Apiezon N grease”, *Cryogenics*, vol. 15, no. 1, pp. 36–37, 1975.

BIBLIOGRAPHY

6

GENERAL CONCLUSIONS

The work done in this thesis establishes the basis to study glasses with extraordinary stability in the framework of the low-temperature physics. We have focused our efforts on finding how extreme thermal histories in glasses affect their universal properties at low temperatures. For this purpose, we have employed calorimetric techniques to investigate the phenomenology both around the glass transition and at low temperatures, where the excess excitations in glasses above the Debye-expected contribution appear. In particular, we have studied two systems which allow us to access highly-stable glassy states as well as their corresponding conventional (ordinary) glasses in completely different ways: amber, the fossilized natural resin, and ultrastable thin-film glasses of indomethacin (an organic molecule commonly used in pharmaceuticals).

Our first step to access the physics of these extreme glasses was designing and building a versatile calorimeter for the temperature range from 50 mK to 40 K. In Chapter 3 we have presented a complete description of all the elements necessary in our very low-temperature calorimetric set up. We have combined the use of a ^{4}He cryostat and a dilution refrigerator to accomplish the specific heat measurements in such a wide temperature range. Determining the temperature in cryogenics requires a careful mounting and accurate calibration of the sensors employed, together with the election of the correct electronics to optimize the reading signals without inducing self-heating to the thermometers. The geometries and the materials employed in the calorimeter have been deeply discussed taking into account the temperature range and the heat capacities involved. Illustrative examples and practical considerations have been exposed to serve as future reference. The performance of our calorimeter has enabled us to resolve heat capacity values from few tens of nJ/K to several tens of mJ/K by using three quasi-adiabatic calorimetric methods, namely, the standard relaxation, an alternative fast relaxation (previously developed in our laboratory), and a continuous method. The validity of the last method at temperatures down to 2 K has been also verified in this thesis, providing accurate measurements in short times. Our development of specific calorimetric software which implements the three methods mentioned above has certainly improved the applicability of our low-temperature calorimeter.

The second technical contribution of this thesis consists on the implementation of a protocol for the accurate determination in absolute values of the specific heat for glasses using commercial Differential Scanning Calorimetry (DSC). The Modulated Temperature Differential Scanning Calorimetry (MT-DSC) technique is introduced in Chapter 3 for the study of thermodynamic and kinetic stability in glasses, and extensively discussed in Appendix A with all the practical recommendations and the information which can be derived from the experimental data.

As already said before, the aim of the work done in this thesis was the study of how the universal low-temperature properties of amorphous solids are affected by extreme thermal histories, in our case, glasses with extraordinary high stabilities. The main system we have studied is natural amber, a glass which has reached a highly stable state by means of ageing during tens of million years.

The results on amber samples from the Dominican Republic (~ 20 million years old) have evidenced the efficiency of this extreme ageing process (hyperageing) in driving the system towards more stable states, as clearly determined in the huge enthalpy relaxation $\Delta H \approx 5$ J/g present around its devitrification temperature $T_{\mathrm{dev}} = 389$ K. The low-temperature specific-heat measurements in the range $0.6 \text{ K} \leq T \leq 26$ K unambiguously show that glassy excitations remain after extreme stabilization processes, as the $C \sim T$ dependence below 1 K and the $C \sim T^5$ increase above 1K prove. Besides, we observed that the hyperaged amber also has a strong boson peak (in the reduced C_P/T^3 representation) if compared to its Debye level, which was independently determined from elasto-acoustic measurements by High Resolution Brillouin Scattering (HRBS). The appearance of an exothermic signal slightly above the glass transition in the pristine sample may indicate further polymerization processes when first driving this amber to the supercooled liquid state, causing a small decrease in the height of the boson peak, already reported for chemical glasses with increasing polymerization.

The second natural amber studied proceeds from Spain, in El Soplao deposit. Two types of amber are found in this deposit, attending to the differences in its chemical composition derived from their different arboreal origin. This amber samples have undergone an ageing process during 110 million years at temperatures in the range from 300 K to 340 K approximately, far below their glass transitions, which are located at 402 K and 423 K. The extraordinary stabilization achieved in this hyperageing results in an enthalpy release of 8 – 10 J/g, what implies fictive temperature shifts of up to 36 K. The specific heat study done in these samples around T_g using the Modulated Temperature-DSC allowed us to separately follow the evolution of the devitrification temperature (obtained from the reversible part of the specific heat). We have found a drastic kinetic-stability enhancement with hyperageing, experimentally observed in a shift of the devitrification temperature towards higher temperatures of $\Delta T_{dev} = 15$ K.

After the complete characterization of the thermodynamics and kinetics of the Spanish amber, we have studied the effects of the increasing stability on its low-temperature specific-heat, varying from the hyperaged (highly stable) sample to the rejuvenated (conventional) glass. We found two remarkable aspects regarding the excess glassy excitations in glasses, namely, (i) the density of tunneling states remain unaltered under extreme relaxation processes, (ii) the small increase of the boson peak height from the hyperaged to the rejuvenated sample does not imply a variation in the position of the maximum $T_{max} = 3.4$ K or minimum $T_{min} = 1.2$ K in the reduced C_P/T^3 representation. This invariability of both the two-level systems and (to a lesser extent) the boson peak with extreme stabilization processes strongly support the idea that the universal glassy properties are independent of the frozen-in disorder at the glass transition and of the energy stability.

The other system we have studied is indomethacin glass, which acquires extraordinary stability when thin films of this organic compound are grown by physical vapor deposition under specific conditions, also called ultrastable glasses (found as well for other organic molecules as toluene or celecoxib®). We have measured the low-temperature specific heat of the crystalline phase and the conventional and ultrastable glass, which reveal the high fragility of the amorphous solid, considering the negligible existence of excess vibrational modes derived from the absence of the boson peak in the C_P/T^3 representation (previously observed in other organic compounds like *o*-terphenyl). The specific heat of the ultrastable indomethacin sample manifests a strong reduction (if not disappearance) of the tunneling states density, given by the drastic decrease in a factor ~ 14 of the linear term in C_P compared to the conventional glass. This peculiar phenomenon has been previously reported in two cases: hydrogenated amorphous silicon (due to the change in chemical composition) and thin SiO_2 films (ascribed to dimensionality). We consider that the effect we find in the ultrastable thin films of indomethacin is due to the reduced-dimensionality (quasi 2D behaviour) of this glass when grown by vapor deposition, what supports the idea of a phonon mediated interaction between tunneling systems, proposed by Yu and Leggett in 1988.

CONCLUSIONES GENERALES

El trabajo que se ha desarrollado en esta tesis establece la base para el estudio de las propiedades térmicas a bajas temperaturas de vidrios con una extraordinaria estabilidad. Hemos centrado nuestros esfuerzos en encontrar cómo la historia térmica extrema en vidrios afecta a sus propiedades universales de bajas temperaturas. Para llevar a cabo esta tarea hemos utilizado la calorimetría como técnica principal, que nos ha permitido investigar la fenomenología de estos vidrios tanto alrededor de su transición vítrea como a bajas temperaturas, en donde las excitaciones en exceso sobre el nivel de Debye aparecen. En particular nos hemos interesado por dos sistemas que permiten acceder a estados vítreos muy estables así como a sus correspondientes vidrios ordinarios (no estables) de formas completamente distintas: el ámbar, la resina natural fosilizada, y las películas delgadas ultraestables de vidrio a partir de indometacina (una molécula orgánica usada como antiinflamatorio).

El primer paso que hemos dado para investigar la física de estos vidrios extremos ha sido el diseño y montaje de un calorímetro versátil para baja temperatura, útil en el rango de 50 mK a 40 K. En el Capítulo 3 hemos presentado una descripción completa de todos los elementos necesarios en nuestro montaje calorimétrico de muy baja temperatura. Hemos combinado el empleo de un criostato de ^{4}He con el de un refrigerador de dilución ^{3}He - ^{4}He para acceder al calor específico de nuestras muestras en este amplio rango de temperaturas. Dado que la determinación de la temperatura en nuestros estudios es fundamental, se ha hecho especial énfasis en los distintos montajes utilizados y las calibraciones de los sensores necesarias, así como la descripción de la electrónica adecuada para optimizar las lecturas de temperatura sin inducir autocalentamiento en los termómetros. Se han discutido las geometrías de nuestros calorímetros y los materiales que hemos usado en su montaje, teniendo en cuenta el rango de temperatura y las capacidades caloríficas que intervienen en las medidas. Hemos dado ejemplos ilustrativos de la calorimetría de bajas temperaturas, así como consideraciones prácticas que puedan servir de referencia en el futuro. El funcionamiento de nuestro calorímetro nos ha permitido determinar capacidades caloríficas desde unas pocas decenas de nJ/K hasta centenares de mJ/K, usando tres métodos calorimétricos quasiadiabáticos, que son el método de relajación estándar, un método alternativo de relajación (previamente desarrollado en el laboratorio) y un método continuo. Se ha validado asimismo este último método para el estudio de calor específico a bajas temperaturas (hasta 2 K) en esta tesis, encontrándose que proporciona una gran precisión y resolución en las medidas con tiempos experimentales cortos. Además, nuestro desarrollo e implementación de software específico para los tres métodos calorimétricos mencionados ha aumentado la posibilidad de utilizar nuestro calorímetro de baja temperatura en un amplio abanico de muestras.

La segunda contribución técnica hecha en esta tesis consiste en la implementación de un protocolo para determinar de forma precisa, en valor absoluto, el calor específico de vidrios utilizando Calorimetría (DSC por sus siglas en inglés). Más concretamente, la técnica de Calorimetría Diferencial con modulación en temperatura (MT-DSC) ha sido introducida en el Capítulo 3 con el objetivo de estudiar la estabilidad termodinámica y cinética en nuestros vidrios de ámbar, y ha sido discutida en mayor profundidad en el Apéndice A, donde se incluyen las recomendaciones prácticas y el modo de analizar los resultados experimentales.

Como ya hemos dicho anteriormente, el objetivo del trabajo hecho en esta tesis es el estudio de cómo se ven influidas las propiedades universales de bajas temperaturas en los sólidos amorfos sometidos a historias térmicas extremas, en nuestro caso, vidrios con estabilidad extraordinariamente alta. El sistema principal estudiado es el ámbar, un vidrio que ha alcanzado esta estabilidad gracias al envejecimiento que ha experimentado durante decenas de millones de años.

Los resultados obtenidos de las muestras de ámbar procedentes de la República Dominicana (de unos 20 millones de edad) muestran la eficiencia que ha tenido este proceso de envejecimiento extremo (hiperenvejecimiento) al llevar el sistema a estados vítreos más estables, como indican las liberaciones entálpicas

$\Delta H \approx 5$ J/g medidas alrededor de la transición vítrea $T_g = 389$ K. El calor específico a bajas temperaturas, medido en el rango $0.6\ K \leq T \leq 26$ K, demuestra de forma clara la permanencia de las excitaciones vítreas tras procesos de estabilización extremos, visible en la contribución lineal del calor específico por debajo de 1 K y el incremento como $C \sim T^5$ por encima de esta temperatura. Hemos observado, asimismo, que el vidrio hiperenvejecido posee un pico bosónico *fuerte* (en la representación C_P/T^3), comparando su altura con el nivel de Debye que fue determinado independientemente a partir de medidas elasto-acústicas mediante Dispersión Brillouin de Alta Resolución (HRBS de sus siglas en inglés). La existencia de una señal exotérmica ligeramente por encima de la transición vítrea en la muestra de ámbar original, parece indicar un proceso de polimerización residual la primera vez que el vidrio transita al líquido sobreenfriado. Esto explicaría el leve descenso en la altura del máximo del pico bosónico, tal y como se ha visto en vidrios químicos con la polimerización.

El segundo ámbar natural que hemos estudiado procede de España, concretamente del yacimiento de El Soplao. Existen dos tipos de ámbar en este depósito atendiendo a la composición química derivada de su origen arbóreo. En el caso del ámbar de El Soplao, las muestras han sufrido procesos de envejecimiento de 112 millones de años a temperaturas que han oscilado entre 300 K y 340 K, bastante por debajo de su transición vítrea, que se encuentra a 402 K y 423 K. La extraordinaria estabilización resultante de este hiperenvejecimiento se traduce en liberaciones entálpicas de 8 – 10 J/g, lo que supone corrimientos en la temperatura ficticia de hasta 36 K. El estudio de calor específico hecho en estas muestras alrededor de T_g usando la técnica de MT-DSC nos ha permitido seguir de forma separada la evolución de la temperatura de devitrificación T_{dev} (obtenida a partir de la parte reversible del calor específico). Hemos encontrado un incremento contundente en la estabilidad cinética de este ámbar como consecuencia del hiperenvejecimiento, tal y como evidencia el corrimiento de 15 K en la T_{dev} hacia temperaturas más altas.

Después de caracterizar la termodinámica y la cinética del ámbar español, hemos estudiado los efectos que esta creciente estabilidad tiene en su calor específico a bajas temperaturas, yendo desde el estado altamente estable (muestra original) hasta el estado ordinario (muestra rejuvenecida). Hemos encontrado dos aspectos remarcables teniendo en cuenta las excitaciones vítreas de bajas temperaturas: (i) por un lado, la densidad de estados de tuneleo permanecen invariables ante procesos de relajación extrema, (ii) hemos observado un incremento moderado en la altura del pico bosónico entre el ámbar original y la muestra rejuvenecida, sin una variación en la posición del máximo $T_{\text{máx}} = 3.4$ K ni del mínimo $T_{\text{mín}} = 1.2$ K en la representación C_P/T^3. La invariabilidad de los estados de tuneleo y (en menor medida) del pico bosónico ante un proceso de estabilización tan extremo apoya la idea de que las propiedades universales de los vidrios son independientes tanto del desorden congelado en la transición vítrea como de la estabilidad energética de estos.

El otro sistema amorfo que hemos estudiado es el vidrio de indometacina, el cual adquiere una alta estabilidad cuando se crecen, en ciertas condiciones, películas delgadas de esta molécula orgánica por deposición física en fase vapor. A los vidrios así crecidos se los denomina ultraestables (también existen ultraestables de otras moléculas orgánicas como el tolueno o el celecoxib®). En este trabajo hemos medido el calor específico a baja temperatura de las fases cristalina y amorfa, ésta última en el estado convencional y ultraestable. De ello hemos podido observar la alta fragilidad del vidrio de indometacina, considerando la escasa contribución de los modos vibracionales en exceso sobre el nivel de Debye, tal y como se deduce de la ausencia de pico bosónico (observado en otros compuestos orgánicos como el *o*-terfenil). El calor específico de la muestra ultraestable de indometacina presenta una reducción drástica (si no la desaparición) de los estados de tuneleo, observada en la fuerte disminución de la contribución lineal al calor específico en un factor ~ 14, comparado con el vidrio convencional. Este fenómeno tan peculiar ha sido reportado previamente en dos sistemas únicamente (silicio amorfo hidrogenado y películas delgadas de SiO_2 amorfo), pero es la primera vez que este efecto es observado en una muestra tridimensional que es crecida por deposición en fase vapor. El modelo que consideramos puede explicar la fuerte reducción de los sistemas de tuneleo es justamente el comportamiento cuasi bidimensional derivado de la alta estabilidad que alcanzan las moléculas al ser depositadas debido a la gran movilidad de éstas en la superficie, y que de alguna manera reduciría la interacción entre moléculas y sucesivas capas, necesaria para la existencia de los estados de tuneleo a bajas energías/temperaturas. Estas observaciones apoyan, desde nuestro punto de vista, la idea de la interacción entre sistemas de tuneleo mediada por fonones, propuesta por Yu y Leggett en 1988.

CONCLUSIONES GENERALES

APPENDICES

A

DIFFERENTIAL SCANNING CALORIMETRY MEASUREMENTS

In this appendix we describe with detail a protocol to determine the specific heat in absolute values with high accuracy using a Differential Scanning Calorimeter (DSC). This protocol was used to measure the specific heat curves of the Spanish amber from *El Soplao* presented in Chapter 5 around the glass transition with high precision and reproducibility, compared to the standard protocol (which does not provide reliable absolute C_P values) used in Chapeter 4 for the Dominican amber. In the experiments discussed in Chapter 5 an exhaustive study on the effects of extreme ageing processes is presented. For this purpose, determination of the enthalpy release present around the glass transition as a consequence of the relaxation processes becomes crucial. Comparison between samples with different thermal histories is only possible if the specific-heat curves are highly reproducible and consistent. Using a DSC model Q100 from TA Instruments (in the SIdI –*Servicio Interdepartamental de Investigación*– facilities) accuracies better than 1 % have been obtained. This protocol should be followed when accurate and highly reproducible values of the specific heat are needed.

In order to optimize the resolution of the equipment some recommendations must be followed. In the experiments performed using the DSC, standard aluminum pans of mass $m \approx 20$ mg are used. The calorimeter uses two of these pans for each experiment, one of which is empty (the reference) and the other one contains the sample to study. It is important to find pans with masses *equal* to the reference, with deviations below 0.1 mg, so that the empty cell contribution to the total heat capacity is well determined. To minimize the error introduced by these deviations, the mass of the sample must be maximized. In the case of our amber samples, the maximum sample mass to employ in each experiment was 10 mg, given the volume of the pan.

Maximizing the mass of the sample is not enough, since a good internal equilibrium is also necessary so that the whole sample contributes to the measurement at the same time. This is achieved by manually milling the sample down to a homogeneus grain size of 50 – 60 μm. It is highly recommendable to use similar sample values in all the experiments (for all the pans) as well, thus ensuring the same experimental conditions of the cell.

Once we have optimized the mass aspects, we start with the measurement. In standard DSC experiments, certified indium is used to calibrate both temperature and enthalpy (given the melting point of indium at T = 429.75 K and melting enthalpy ΔH_{melt} = 3.263 kJ/mol) (see [MeBr09] and [CrRe07] for further technical details). In the measurements performed on amber, Modulated-Temperature DSC (MT-DSC) technique was employed, which provides in a single experiment both the reversible and irreversible contributions to the specific heat separately. This allows us to study independently the kinetic and history-dependent contributions to the total specific heat, which determine the glass transition temperature and the enthalpy released in the relaxation processes, respectively. MT-DSC adds to the standard heating/cooling ramps of the DSC a sinusoidal-modulated heating signal, what enables the study of the in-phase (reversing) and out-of-phase (non-reversing) responses of the sample.

For a good calibration of the MT-DSC curves certified sapphire is used. The specific heat of the sapphire is determined in the same conditions as in the amber measurements. Typical heating/cooling ramps of ± 1 K/ min were applied, with modulating amplitude ± 0.5 K/min every 60 – 80 s. Direct comparison of the experimental curves obtained for the sapphire on each run with the standard curve (provided by the company), provides a correction curve for the specific heat.

The determination of the specific heat of an amber sample implies three heating plus three cooling ramps at rates ± 1 K/min. Only the curves measured in the heating ramps are used for the analysis, since thermal control is optimized under these conditions. The three curves, as already said in Chapters 4 and 5, are necessary to check the differences between the first run and the two others, as well as checking the reproducibility among the second and third runs. Determination of the three curves for a single sample means around 24 hours of continuous measurement, what can introduce deviations in the heating/cooling power of the system.

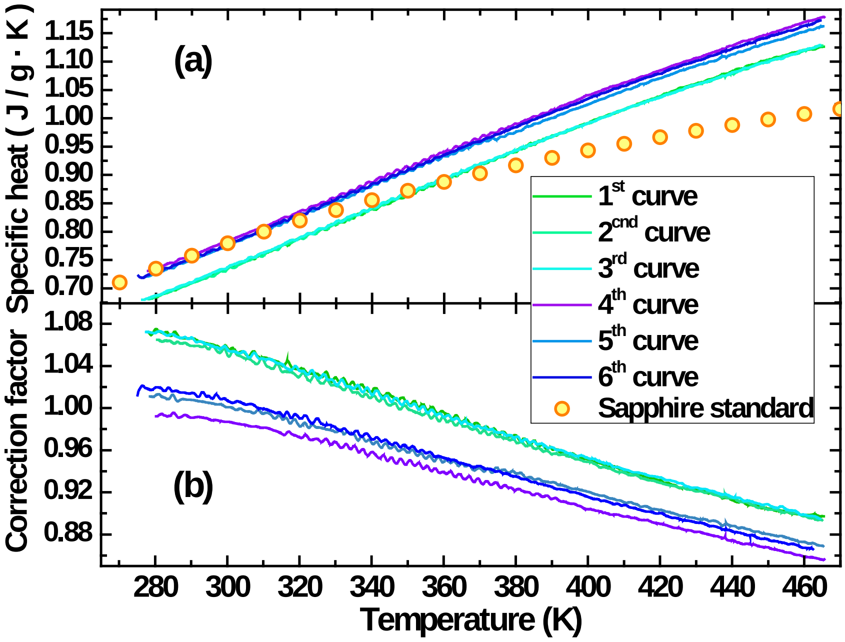

Figure A.1 Example of calibration procedure using sapphire specific heat as standard for the MT-DSC measurements using a Q100 TA Instruments DSC. (a) The six heating curves (three before plus three after the amber measurement) corresponding to the equipment calibration immediately before and after a sample measurement, together with the reference specific heat for sapphire (orange solid circles). In (b) the correction factor $K_{Cp}(T)$ for every curve in (a) is shown, given by the relation between the reference and the experimental curves in Equation (A.1).

To minimize the uncertainty and discard possible systematic errors in the specific heat curves of amber, calibrations of the equipment using sapphire were done before and after every sample measurement. This means that six specific-heat curves for sapphire at heating/cooling rates ± 1 K/min were obtained immediately before and after studying each amber sample. Comparing the experimental values for sapphire to the standard curve provides the correction curves for the amber, as illustrated in Figure A.1 The correction factor $K_{\mathrm{Cp}}(T)$ for the specific heat is given by the relation between the reference specific heat of sapphire and the experimental curves obtained in our measurements

$$\boldsymbol{K}_{\boldsymbol{C}_{\mathbf{p}}}(\boldsymbol{T})=\frac{\boldsymbol{C}_{\mathbf{p}}^{\mathbf{std}}(\boldsymbol{T})}{\boldsymbol{C}_{\mathbf{p}}^{\mathbf{exp}}(\boldsymbol{T})} \qquad \text{(A.1)}$$

The final correction to the specific heat curves of amber are done averaging the two corresponding heating ramps in the two sapphire calibrations (immediately before and after the amber measurement) which appear in the same order. For example, with sapphire curves in Figure A.1, for the first heating ramp of the amber sample we use the average correction factor given by the first and the fourth curves in Figure A.1(b); for the second heating ramp of amber we use the average correction factor given by the second and fifth curves in Figure A.1(b), and so on.

Taking into account all the recommendations given above, specific heat curves around the glass transition were obtained for Spanish amber samples from El Soplao, with accuracy of the order of 1% and high reproducibility, as shown in Figure A.2. These are two essential aspects if a detailed study on the enthalpy effects of the thermal history of the samples is sought.

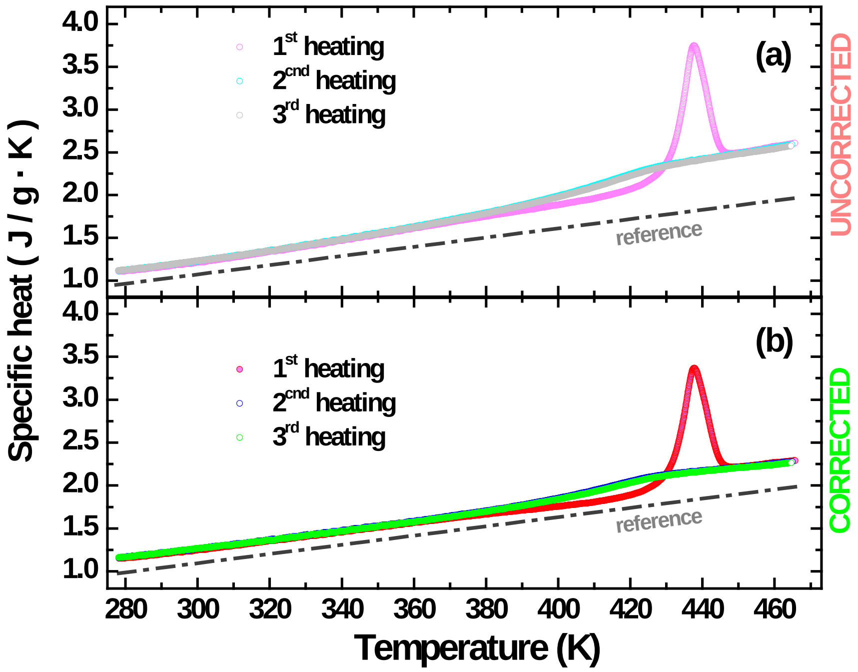

Figure A.2 Example of correction applied to the three heating curves corresponding to a sample measurement, using the correction factor obtained as described in Figure A.1. In (a) the raw data are shown. After applying the sapphire correction factor the curves in (b) are obtained. The dashed dotted line in (a) and (b) is a reference to the eye, in order to notice the changes introduced by the correction factor $K_{Cp}(T)$.

References

[CrRe07] D. Q. M. Craig and M. Reading, *Thermal Analysis of Pharmaceuticals*. Taylor & Francis Group, 2007, p. 400.

[MeBr09] J. D. Menczel and R. Bruce Prime, *Thermal Analysis of Polymers: Fundamentals and Applications*, First Edit. Wiley & Sons, 2009, p. 688.

B

DEVELOPMENT OF A SOFTWARE FOR LOW-TEMPERATURE CALORIMETRY

In the course of this thesis a great effort has been done to design and build a low-temperature calorimeter, with which heat capacity measurements in the broad temperature range going from 0.05 K up to 100 K have been performed. One of the most outstanding results of the work presented in the manuscript is the successful performance of a low- and very-low-temperature calorimeter, which indeed presents a user friendly handling. One of the aspects which undoubtedly make our non-commercial calorimeter robust and *easy* to operate is the automation achieved with the software developed for this purpose.

The measurement procedure of our low-temperature calorimeter makes use of Labview-based programs specifically developed and implemented for this thesis by us, in which the relaxation techniques and a fast quasi-adiabatic continuous method (described in Chapter 3, Sections 3.6.1 and 3.6.2) are implemented. They provide a self-consistent and automated method to measure heat capacity with increasing or decreasing temperature. Control on the parameters involved in the different methods is easily done via the user-interface of the programs, which allow live monitoring and adjustment of the ongoing measurements. Besides, complete record of the experimental conditions facilitates the later analysis of the data.

The philosophy applied to the programs developed for the relaxation techniques consists on the so-called *state machine*, in which the system passes through periodically recurring phases. The basic idea is that, when measuring heat capacity with the relaxation methods, the calorimeter always follows the same procedure:

1. Equilibration at a given temperature of the calorimeter *reservoir* shown in Figure B.1c (see Section 3.5.1), namely, the copper ring from which the cell hangs.

2. After the temperature of the calorimeter is equilibrated, its thermal drift is recorded during a period of time which is referred to as first Palier in Figure B.1a, so that later changes in temperature can be calculated in absolute values using extrapolations of this drift.

3. The calorimetric cell (addenda plus sample) is heated using the heater attached to the sapphire with fixed power P, so that a small increase in the temperature (typically $\Delta T/T$ = 1-2 %) is achieved. When the calorimeter equilibrates in the new temperature (the thermal drift must fulfill a parallelism requisite with the 1st Palier), the heating is switched off.

4. The calorimeter relaxes towards the initial temperature given by the first Palier after the heater is switched off in the right side of Figure B.1a. Since the relaxation obeys an exponential law, taking the logarithm of the temperature decrease (in Figure B.1b), it is easy to check that the relaxation involves only one time constant τ given the linearity in Figure B.1b.

5. Once the relaxation is completed, the system is driven to a new set-point temperature. The system is held at this stage for a period of time, so that good equilibrium is reached, as shown in Figure B.1c.

6. The whole process starts again.

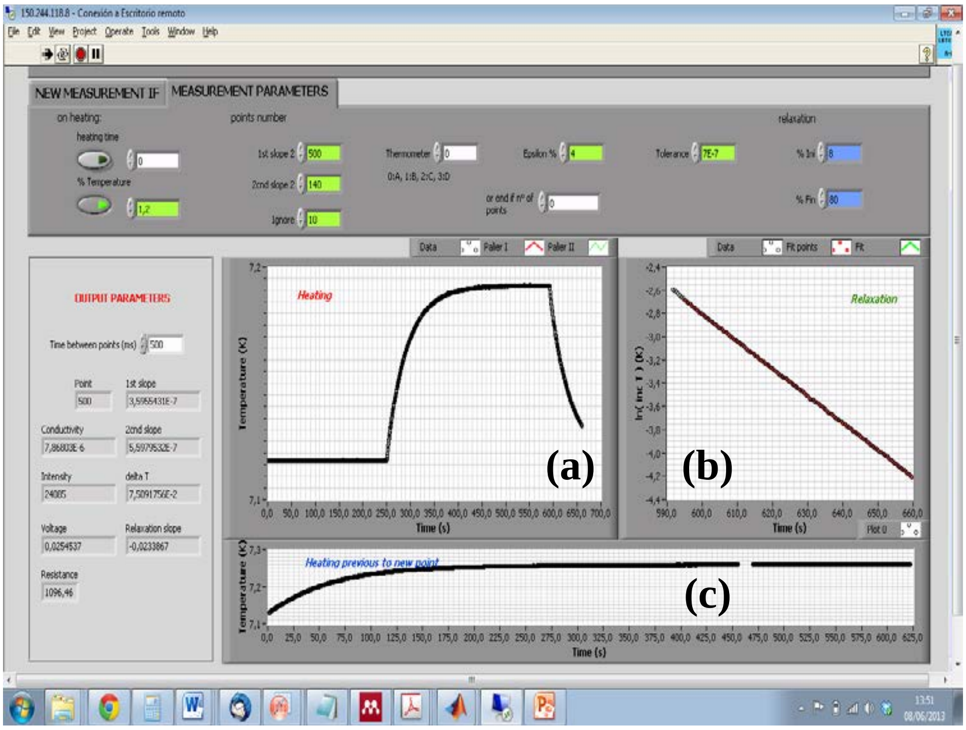

on heating:
heating time 0
% Temperature 1,2

points number
1st slope 2 500
2nd slope 2 140
Ignore 10

Thermometer 0
0:A, 1:B, 2:C, 3:D
Epsilon % 4
or end if nº of points 0
Tolerance 7E-7

relaxation
% Ini 8
% Fin 80

Time between points (ms) 500
Point 500
1st slope 3,5955431E-7
Conductivity 7,86803E-6
2nd slope 5,5979532E-7
Intensity 24085
delta T 7,5091756E-2
Voltage 0,0254537
Relaxation slope -0,0233867
Resistance 1096,46

Figure B.1 Front panel corresponding to the Labview-based program for the standard relaxation method. The control parameters for the measurements which can be modified appear in different tabs for clarity. The output values of the measurement calculated by the program appear on the lower left corner. The measurement is monitored using three graphs: in (a) the curve of temperature versus time $T(t)$ is displayed; the relaxation stage is shown in (b) in a $\log(\Delta T(t))$ versus time representation, so that correct working of the calorimeter can be checked visually (linearity of the $\log(\Delta T(t))$ curve reflects a single relaxation time τ which dominates, what is required in our relaxation method); the temperature control previous to each relaxation point, in which the calorimeter is driven to a new set-point, is displayed in (c).

As can be derived from the points enumerated above, the system repeats a fixed number of stages always in the same order. The parameters involved in the measurement have to do with the thermal drifts required, the temperature increase from the first to the second equilibration temperature within a point, the parallelism requirements between the two thermal drifts, etc. All these parameters are controlled by the user, so that optimization of the measurement conditions is possible at any time. The parameters necessary to calculate the heat capacity at each point are saved, such as the thermal drifts, the thermal conductance of the link, resistance of the heater, the current applied to the heater, the relaxation time, etc. In parallel, the temperature versus time curve is saved, so that later analysis could be performed in case it would be needed.

In the alternative relaxation method an analogous procedure is followed, with a minor change due to the fact that the equilibrium at the second temperature (point 3 in previous page) is not reached, as shown in Figure B.2. Instead, the heating is switched off when the temperature increase reaches a given value (specified by the user), and the system is driven to the relaxation stage. This difference makes the alternative relaxation method much faster than the standard one.

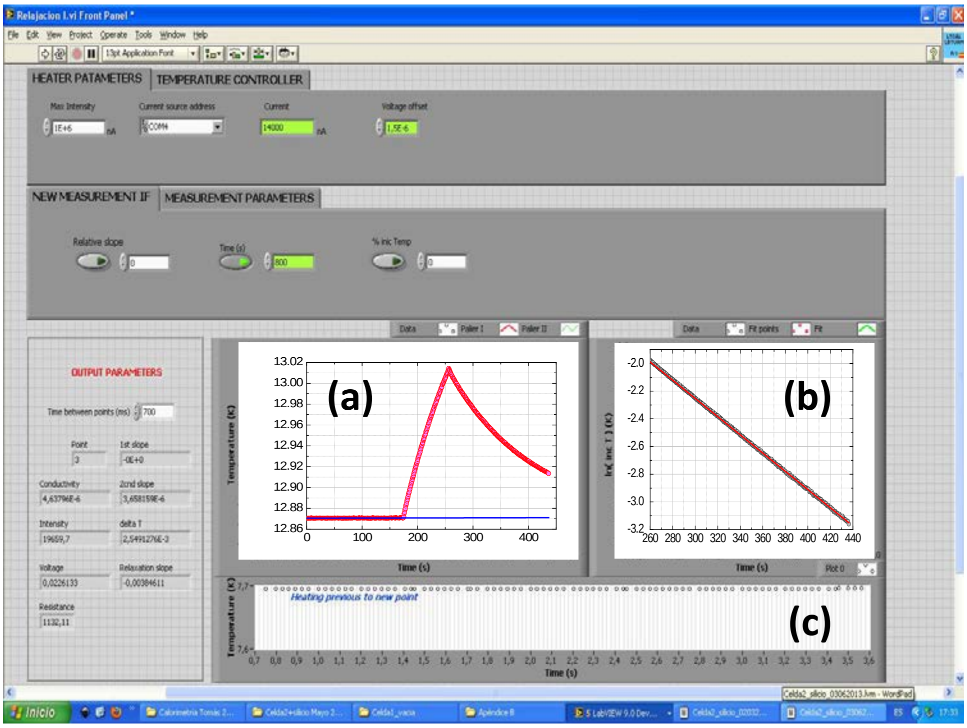

Max Intensity: 1E+6 nA
Current source address: COM4
Current: 14000 nA
Voltage offset: 1,5E-6
Relative slope: 0
Time (s): 800
% inc Temp: 0

OUTPUT PARAMETERS
Time between points (ms): 700
Point: 3
1st slope: -0E+0
Conductivity: 4,63796E-6
2nd slope: 3,658159E-6
Intensity: 19659,7
delta T: 2,5491276E-3
Voltage: 0,0226133
Relaxation slope: -0,00384611
Resistance: 1132,11

Figure B.2 Front panel corresponding to the Labview-based program for the fast relaxation method. There is no equilibration after the temperature jump, as shown in (a). After the temperature jump given by the user (typically 1% - 2 %) is reached, the power to the heater is switched off (right side of (a)). The relaxation is monitored in in (b) in a log($\Delta T(t)$) versus time representation, analogously to what is done in the standard relaxation method. After the measurement, the calorimeter is stabilized in a new temperature (c).

The two programs which control the relaxation methods directly provide the $C(T)$ curves (heat capacity versus time) for the samples measured, without the need of any additional analysis.

In the case of the quasi-adiabatic continuous method described in Section 3.6.2, a simple program to record the temperature evolution in the calorimeter and its surroundings as well as the powers applied to the heater was developed. Further integrated analysis using Matlab software enables the calculation of the heat capacity.

Specific software was also developed in order to calibrate the thermometers used in the low-temperature measurements, both in the ^{4}He cryostat and the ^{3}He–^{4}He dilution refrigerator. This software allowed us to monitor in parallel the resistance values of different sensors as a function of the temperature provided by a previously calibrated thermometer. Subsequent analysis of the resistance versus temperature curves provided us with the calibration curve.

In summary, one of the relevant outcomes derived from the work done during this thesis is a complete set of Labview- and Matlab-based software which allows us to perform calorimetric measurements at low and very low temperatures with integrated analysis. In Figure B.3 a schematic diagram with all the programs developed for the experimental work is shown. Note that the complete ensemble of experimental parameters provided by the programs provides us with optimal information about the experimental conditions and the suitability of the results.

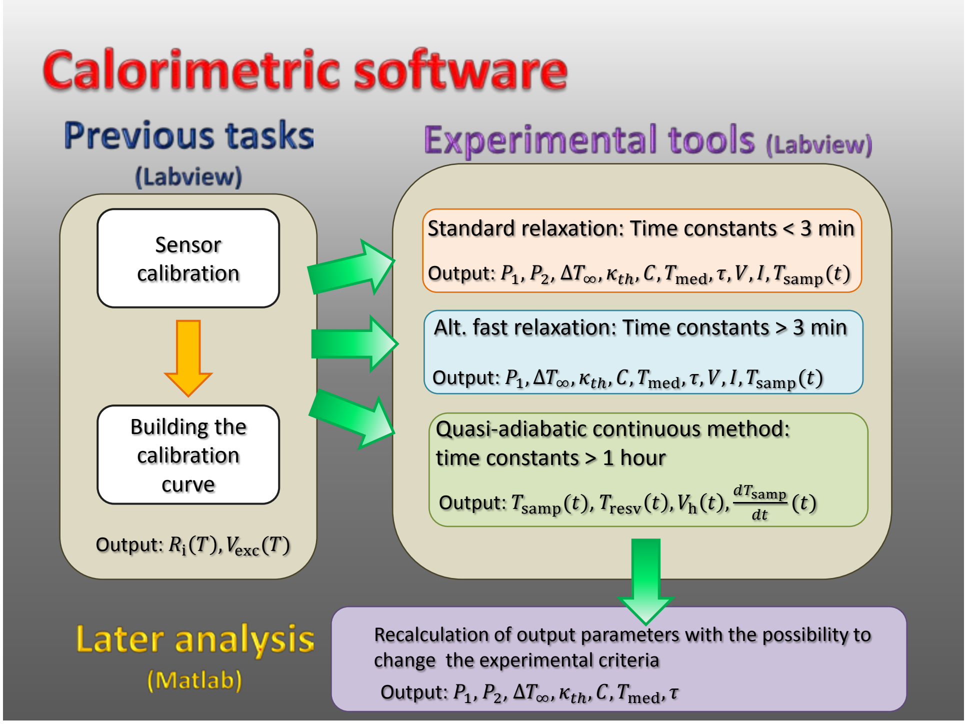

Figure B.3 Schematic diagram of the software developed for the low-temperature calorimetric measurements, which includes the previous sensor calibration procedure and the later integrated analysis. The three calorimetric methods used in the measurements presented in this thesis are shown, with the corresponding output information provided by the respective Labview programs. The later analysis based in Matlab allows us to recalculate the output parameters by varying the same criteria available in the experimental software.

PUBLICATION LIST

[1] Tomás Pérez-Castañeda, Jon Azpeitia, Jan Hanko, Anton Fente, Hermann Suderow and Miguel A. Ramos, *Low-temperature specific heat of graphite and* $CeSb_2$*: Validation of a quasi-adiabatic continuous method*, Journal of Low Temperature Physics 173, pp. 4 – 20 (2013).

[2] Tomás Pérez-Castañeda, Rafael J Jiménez Riobóo and Miguel A Ramos, *Low-temperature thermal properties of a hyperaged geological glass*, Journal of Physics: Condensed Matter 25, 295402 (2013).

[3] Tomás Pérez-Castañeda, Rafael J Jiménez Riobóo and Miguel A Ramos, *Fossilized tunneling states and boson peak in hyperaged amber glasses*. In preparation.

[4] Tomás Pérez-Castañeda, Miguel A Ramos, Cristian Rodríguez-Tinoco, Aitor F Lopeandía and Javier Rodriguez-Viejo, *Low-temperature specific heat of ultrastable glasses of indomethacin*. In preparation.

[5] R. F. Luccas, A. Fente, J. Hanko, T. Pérez-Castañeda, F. Mompean, M. R. Osorio, J. Azpeitia, M. García-Hernández, N. M. Nemes, P. C. Canfield, M. A. Ramos, S. Vieira and H. Suderow, *Charge Density Wave in the* $LaSb_2$ *Ce doped compound*. In preparation.